Doctoral Thesis

Modeling, Identification, and Compensation of Channel Mismatch Errors in Time-Interleaved Analog-to-Digital Converters

Christian Vogel

Faculty of Electrical Engineering and Information Technology
Graz University of Technology, Austria

First Advisor:
Prof. Dr. Gernot Kubin, Graz University of Technology, Austria
Second Advisor:
Prof. Dr. Håkan Johansson, Linköpings universitet, Sweden
Industrial Advisor:
Dr. Dieter Draxelmayr, Infineon Technologies AG, Austria

Graz, July 2005

to my lovely wife Birgit

Zusammenfassung

Moderne Signalverarbeitungsanwendungen, wie sie in der Nachrichtentechnik und Messtechnik verwendet werden, benötigen sehr schnelle Analog-Digital-Umsetzer (ADU), was durch eine räumlich parallele Anordnung von zeitlich versetzt arbeitenden ADUs (ADU-Array) erreicht werden kann. Die zeitliche Verschiebung ermöglicht, im Vergleich zu einem Kanal, eine Erhöhung der Abtastrate um die Anzahl der Kanäle im ADU-Array. Leider werden die Leistungsmerkmale von ADU-Arrays durch Fehlanpassungen zwischen den Kanälen eingeschränkt, weshalb sich diese Arbeit mit der Identifikation und der Kompensation von Fehlanpassungen in ADU-Arrays befasst. Die ADU-Arrays wurden mit nichtlinearen hybriden Filterbänken detailliert modelliert und analysiert. Das Modell umfasst lineare und nichtlineare Fehlanpassungen und vereinheitlicht und erweitert die bereits in der Literatur bestehenden Modelle. Es wurde eine neuartige Vordergrund-Identifikationsmethode zur vollständigen Charakterisierung von dynamischen linearen Fehlanpassungen entwickelt. Eine Hintergrund-Identifikationsmethode liefert genaue Schätzwerte für die Abstastzeitfehlanpassungen. Zum Schluss werden in dieser Arbeit noch leistungseffiziente Kompensationsmethoden präsentiert, die den Einfluss von Fehlanpassungen auf die Leistungsmerkmale eines ADU-Arrays signifikant reduzieren. Dank der vorgestellten Methoden, wird es möglich sein, sehr schnelle ADU-Arrays sowohl für leistungskritische als auch für hochgenaue Anwendungen zu verwenden.

Abstract

Modern signal processing applications emerging in telecommunication and instrumentation industries need high-speed analog-to-digital converters (ADCs), which can be achieved by employing a time-interleaved parallel array of ADCs (time-interleaved ADCs). The time interleaving of the channels allows to increase the sampling rate by the number of channels compared to a single channel. Unfortunately, time-interleaved ADCs suffer from channel mismatches that limit their performance, wherefore this thesis deals with the identification and compensation of channel mismatches in time-interleaved ADCs. By using nonlinear hybrid filter banks, we have modeled and analyzed channel mismatches in detail. The model covers linear and nonlinear channel mismatches, unifies, and extends the channel models found in the literature. A novel foreground channel mismatch identification method has been developed, which can be used to fully characterize dynamic linear mismatches. A background identification method provides accurate timing mismatch estimates. Finally, power-efficient channel mismatch compensation methods, which significantly reduce the impact of channel mismatches on the time-interleaved ADC performance, are presented in this work. Thanks to the presented methods, it will be possible to use high-rate time-interleaved ADCs for power-critical as well as for high-precision applications.

Acknowledgment

Several people made this thesis possible. First of all, I would like to thank my wife Birgit who has convinced me to quit my old job and to start my doctoral studies. Furthermore, I am grateful to Professor Gernot Kubin, whose support throughout my research has led to this thesis and who has shaped my understanding of digital systems. I would like to thank Dr. Dieter Draxelmayr who has helped me with the analog pitfalls of analog-to-digital converters and Professor Håkan Johansson for inspiring discussions and for being my second advisor for this thesis. I would like to thank everybody from the SPSC Lab and especially the people from the CD-Lab for Nonlinear Signal Processing for the discussions and the fun we had. Finally, special thanks goes to Infineon Technologies AG Austria for the funding of this research project.

Graz, July 2005 Christian Vogel

Contents

1 Introduction **1**
1.1 Introduction to Time-Interleaved ADCs . . . 1
1.1.1 The Principle of Time-Interleaved ADCs . . . 1
1.1.2 Mismatch Errors in Time-Interleaved ADCs . . . 3
1.1.3 History and State-of-the-Art Performance . . . 3
1.2 Scope of the Work . . . 6
1.3 Outline of the Thesis and Main Contributions . . . 7

2 Channel Mismatch Modeling **11**
2.1 Introduction . . . 11
2.2 Linear Hybrid Filter Banks . . . 13
2.2.1 Continuous-Time Downsamplers and Discrete-Time Upsamplers . . . 15
2.2.2 Input/Output Relation of Linear Hybrid Filter Banks . . . 17
2.3 Nonlinear Hybrid Filter Banks . . . 19
2.3.1 Static Nonlinearities . . . 19
2.3.2 Input/Output Relation of Nonlinear Hybrid Filter Banks . . . 22
2.4 Fundamental Interval Representation of Hybrid Filter Banks . . . 23
2.4.1 Fundamental Interval Representation of Linear Hybrid Filter Banks 25
2.4.2 Fundamental Interval Representation of Nonlinear Hybrid Filter Banks . . . 27
2.5 Time-Interleaved ADCs Modeled with Nonlinear Hybrid Filter Banks . . . 29
2.6 Conclusion . . . 32

3 Channel Mismatch Error Analysis **35**
3.1 Introduction . . . 35
3.2 The Impact of Channel Mismatches . . . 36
3.2.1 Static Mismatches . . . 36
3.2.2 Dynamic Mismatches . . . 47
3.3 Reducing the Complexity of the Time-Interleaved ADC Representation . . . 55
3.4 Deterministic Analysis of Combined Channel Mismatch Errors . . . 59
3.4.1 Deterministic SINAD for Combined Channel Mismatch Errors . . . 62
3.4.2 Influence of Timing Jitter and Quantization Noise on the SINAD . . . 64
3.4.3 Worst-Case Analysis of Individual Channel Mismatch Errors . . . 67
3.4.4 Numerical Results . . . 68
3.5 Statistical Analysis of Combined Channel Mismatch Errors . . . 71

3.5.1 Expected SINAD for Combined Channel Mismatch Errors 72
3.5.2 Expected SINAD for Individual Channel Mismatch Errors 74
3.5.3 Numerical Results 75
3.6 Conclusion 77

4 Channel Mismatch Identification 83
4.1 Introduction 83
4.2 Matrix Notation for Linear Mismatches 84
4.3 Foreground Identification of Dynamic Linear Mismatches 91
4.3.1 Algorithm Derivation 92
4.3.2 Input Signal Requirements 94
4.3.3 Simulation Results 96
4.4 Background Identification of Timing Mismatches 101
4.4.1 Algorithm Derivation 101
4.4.2 Input Signal Requirements 104
4.4.3 Simulation Results 109
4.5 Conclusion 112

5 Channel Mismatch Compensation 115
5.1 Introduction 115
5.2 Compensation of Nonlinearity Errors and Mismatches 117
5.2.1 Using Complementary Nonlinearities 117
5.2.2 Using Randomization and Complementary Nonlinearities 121
5.3 Timing Mismatch Compensation through Transfer Characteristics Tuning . 123
5.3.1 Analysis of Transfer Characteristics Tuning 126
5.3.2 Simulation Results 128
5.4 Spectral Shaping in Time-Interleaved ADCs 132
5.4.1 Spectral Shaping of Timing Mismatches 133
5.4.2 Combining Randomization and Spectral Shaping 139
5.5 Conclusion 149

6 Concluding Remarks 153

A Simulation Environment for Time-Interleaved ADCs 155
A.1 Introduction 155
A.2 System Modeling 156
A.2.1 Time-Interleaved ADC Model 156
A.2.2 Signal Generation 156
A.2.3 Channel ADC Model 157
A.3 Simulation Results 160
A.4 Conclusion 162

B Channel Mismatch Identification in the Time Domain **165**
B.1 Purely Digital Methods . . . 165
B.1.1 Offset Mismatch Identification . . . 165
B.1.2 Gain Mismatch Identification . . . 167
B.1.3 Timing Mismatch Identification . . . 170
B.2 Methods with a Reference Channel . . . 172
B.2.1 Offset Mismatch Identification . . . 174
B.2.2 Gain Mismatch Identification . . . 175
B.2.3 Timing Mismatch Identification . . . 176
B.3 Conclusion . . . 181

C Signal and System Considerations **183**
C.1 System Classification . . . 183
C.2 Signal Classification . . . 183
C.3 Signal Transforms . . . 184
C.4 Special Signals . . . 185
C.5 Relation between Sampled Continuous-Time Signals and Discrete-Time Signals . . . 185
C.6 Finding the Coefficients of a Static Nonlinearity . . . 186
C.7 Representations of Sampling Time Errors . . . 188

List of Abbreviations and Symbols **189**

Bibliography **193**

List of Figures

1.1 Time-interleaved ADC with M channels 2
1.2 Timing diagram of a time-interleaved ADC with M channels. 2
1.3 Mismatches in time-interleaved ADCs 4

2.1 Discrete-time linear hybrid filter bank with M channels. 13
2.2 Continuous-time linear hybrid filter bank with M channels. 14
2.3 Mathematical model of the quantization error 15
2.4 Sampling of a continuous-time signal with a sampling period $\hat{T}_s = MT_s$ . . 16
2.5 Upsampling of a discrete-time signal by factor M. 16
2.6 Maximally decimated continuous-time linear hybrid filter bank 17
2.7 Schematic illustration of the frequency response of a linear hybrid filter bank 18
2.8 Nonlinear hybrid filter bank (NHFB) 20
2.9 Approximation of the function $f(x)$ through a polynomial 21
2.10 Static nonlinearity 21
2.11 Sampler and static nonlinearity 22
2.12 Output spectrum of a nonlinear hybrid filter bank 24
2.13 Frequency response of a maximally decimated hybrid filter bank 25
2.14 A channel model of the mth channel ADC of a time-interleaved ADC. . . . 29
2.15 Channel of an NHFB representing a channel ADC 30

3.1 Output spectrum of a time-interleaved ADC without mismatches 37
3.2 Output waveform of a time-interleaved ADC with four channels ($M = 4$) without mismatches. 37
3.3 ADC with gain errors 38
3.4 Output spectrum of a time-interleaved ADC with four channels and gain mismatches 39
3.5 Output waveform of a time-interleaved ADC with four channels and gain mismatches 39
3.6 ADC with offset error 41
3.7 Output spectrum of a time-interleaved ADC with four channels and offset mismatches 42
3.8 Output waveform of a time-interleaved ADC with offset mismatches 42
3.9 ADC with INL and DNL error 43
3.10 Output spectrum of a time-interleaved ADC with four channels and nonlinearity mismatches 46

3.11 Output waveform of a time-interleaved ADC with nonlinearity mismatches 46
3.12 The two error sources of timing mismatches. 49
3.13 Explanation of the timing mismatch 50
3.14 Output spectrum of a time-interleaved ADC with timing mismatches 51
3.15 Output waveform of a time-interleaved ADC with timing mismatches . . . 52
3.16 Output spectrum of a time-interleaved ADC with four channels and timing jitter. 54
3.17 Output waveform of a time-interleaved ADC with timing jitter 54
3.18 The impact of magnitude and phase mismatches 57
3.19 The impact of linear-phase and nonlinear-phase mismatches 58
3.20 Mathematical model of a channel ADC 60
3.21 Output spectrum of a time-interleaved ADC 61
3.22 The structure of a meta time-interleaved ADC 66
3.23 Mathematical model of channel ADCs with timing jitter 66
3.24 Comparison between the simulated SINAD and the calculated SINAD . . . 69
3.25 Worst-case estimates for gain and offset mismatches 70
3.26 Comparison of the expected SINAD and the worst-case SINAD 71
3.27 Expected SINAD for Gaussian distributed gain, offset, and timing mismatch errors 76
3.28 The difference between the simulated and the calculated expected SINAD . 78
3.29 Histogram plots of the difference between the expected SINAD and the calculated SINAD for different numbers of realizations 79
3.30 Histogram plots of the difference between the expected SINAD and the calculated SINAD for different numbers of samples 80

4.1 Periodicity of the aliased spectral components. 85
4.2 Spectrum representation using the discrete-time notation of a time-interleaved ADC. 86
4.3 Illustration of the modulo operator $\zeta(\Omega)$. 87
4.4 Impact of the modulo operator $\zeta(\Omega)$. 89
4.5 The figure illustrates the aliasing of $\frac{\Omega_s}{M}$-spaced frequency points in a time-interleaved ADC 90
4.6 Identification with bandlimited input signals 95
4.7 Foreground identification with broadband signals 97
4.8 Foreground identification with a sinusoidal signal 98
4.9 Foreground identification with broadband signals and 10-bit quantization . 99
4.10 Foreground identification with a sinusoidal signal and 10-bit quantization . 100
4.11 Timing mismatch identification with bandlimited input signals 102
4.12 Filter specification used for timing mismatch identification 105
4.13 Illustration of the mismatch band 106
4.14 Bandwidth of the mismatch band against the number of channel ADCs . . . 108
4.15 Background identification of timing mismatches for the average case 110
4.16 Background identification of timing mismatches for the worst case 110
4.17 Background identification of timing mismatches for average and worst cases 111

4.18 Background identification of timing mismatches for the average case with 10-bit quantization . . . 111
4.19 Background identification of timing mismatches for the worst case with 10-bit quantization . . . 112
4.20 Background identification of timing mismatches for average and worst cases with 10-bit quantization . . . 113
4.21 Quantization limits the performance of the identification method but its general behavior is the same with or without quantization. . . . 113

5.1 Two consecutive channel ADCs with complementary transfer curves . . . 118
5.2 Time-interleaved ADC with four channels and nonlinearity mismatches . . 119
5.3 Time-interleaved ADC with nonlinearity mismatches and pairwise complementary nonlinearities . . . 120
5.4 Randomization of the channel ADCs . . . 121
5.5 Randomization with complementary channel ADCs . . . 122
5.6 Time-interleaved ADC with six channels to allow randomization without decreasing the sampling rate. . . . 124
5.7 Time-interleaved ADC with six channels, pairwise complementary nonlinearities, and randomization. . . . 125
5.8 The principle of tuning the transfer characteristics . . . 126
5.9 Comparison of phase responses . . . 127
5.10 Timing deviations which can be corrected by tuning the bandwidth . . . 129
5.11 Comparison of a simulated time-interleaved ADC with two channels ($M = 2$) before and after timing mismatch compensation . . . 130
5.12 Analysis of the magnitude mismatch effects of transfer characteristics tuning 131
5.13 Spectrally shaped output spectrum of a time-interleaved ADC with 32 channels . . . 134
5.14 The principle of shaping timing mismatch error power . . . 135
5.15 The average SINAD in ENOB for spectrally shaped time-interleaved ADCs 139
5.16 The average SFDR for spectrally shaped time-interleaved ADCs . . . 140
5.17 The basic concept of channel randomization . . . 141
5.18 The basic concept of spectrally shaped channel randomization . . . 143
5.19 Output spectrum of a non-randomized time-interleaved ADC with four channels . . . 144
5.20 Effect of spectrally shaped randomization . . . 145
5.21 Performance enhancement due to spectral shaping (average) . . . 147
5.22 Performance enhancement due to spectral shaping (worst-case) . . . 148
5.23 Change the group membership . . . 149

A.1 Basic architecture of the time-interleaved ADC simulation. . . . 155
A.2 Behavioral simulation model of the lth channel ADC. . . . 157
A.3 Illustration of the nonlinear mapping $\mathcal{F}_m^Q$ with a memory of $J = 2$ and a quantization resolution of $Q = 8$ bits. . . . 158

A.4 RBF network approximation of the nonlinear mapping $\mathcal{F}_m$ with a memory of $J = 2$. 159
A.5 Simulation with offset, gain and timing mismatches. 161
A.6 Input filters used for demonstrating the bandwidth mismatch effect. The dashed line indicates half the sampling frequency. 161
A.7 The effect of bandwidth mismatches. 162
A.8 Time-interleaved ADC where each channel ADC has a different INL. . . . 163
A.9 Comparison between the SINAD of a time-interleaved ADC and its worst channel ADC. 163
A.10 Comparison between the SFDR of a time-interleaved ADC and its worst channel ADC. 164

B.1 Average performance of the purely digital offset mismatch identification . . 168
B.2 Worst-case performance of the purely digital offset mismatch identification 168
B.3 Average performance of the purely digital gain mismatch identification . . . 170
B.4 Worst-case performance of the purely digital gain mismatch identification . 171
B.5 Average performance of the purely digital timing mismatch identification . 172
B.6 Worst performance of the purely digital timing mismatch identification . . . 173
B.7 Identification with a reference channel ADC 173
B.8 Timing diagram for the identification with a reference channel ADC 174
B.9 Average offset identification performance with a reference channel 175
B.10 Worst-case offset identification performance with a reference channel . . . 176
B.11 Average gain identification performance with a reference channel 177
B.12 Worst-case gain identification performance with a reference channel 177
B.13 Identification of timing mismatches with a reference channel 178
B.14 Average performance of timing mismatch identification with a reference channel 180
B.15 Performance comparison of time-domain timing mismatch identification methods 180
B.16 Worst-case performance of timing mismatch identification with a reference channel 181

C.1 Representations of Sampling Time Errors 188

List of Tables

1.1 Comparison of reported time-interleaved ADC performances. 6

Chapter 1

Introduction

Modern signal processing applications emerging in the telecommunication and instrumentation industries need high-speed analog-to-digital converters (ADCs), which can be realized by a time-interleaved architecture that can be combined with practically any ADC technology. Recent high-speed ADCs using this time-interleaved technology achieve sampling rates up to 20GSa/s [112]; nevertheless, the time-interleaving concept is not restricted to high-speed applications, but has been successfully applied to high-resolution oversampling ADCs as well [64, 66].

Time-interleaved ADCs suffer from channel mismatches. Channel mismatches limit their performance and prevent the breakthrough of this technology. In recent years, new mismatch compensation concepts have been introduced and time-interleaved ADCs have become a possible alternative. Nevertheless, this additional compensation reduces the advantages of time-interleaved ADC, especially for high-rate low power ADCs. Furthermore, many compensation methods have to interrupt the conversion process for calibration. Therefore, they are suitable for measurement applications but only partially useful for communication applications.

The objective of this work was to develop new background identification and compensation methods, which need a minimum of additional power consumption.

1.1 Introduction to Time-Interleaved ADCs

Time-interleaved ADCs are special cases of converter arrays. A converter array consists of M parallel sampling channels, where it can fulfill the Nyquist criterion by combining the output of all channels. There are many ways to divide the analog input signal into different domains and to combine them on the digital side of the converter. The theoretical background for all these methods was provided by Papoulis' Generalized Sampling Expansion (GSE) [100]. In the following we will introduce time-interleaved ADCs, which are one possible practical realization of the GSE.

1.1.1 The Principle of Time-Interleaved ADCs

A time-interleaved ADC consists of M channel ADCs, which have the same sampling rate but different sampling phases, as if they were a single converter operating at an M times higher sampling rate [8, 7]. Such a time-interleaved architecture is illustrated in Fig. 1.1, where each channel ADC operates at a sampling rate of $\tilde{f}_s = \frac{f_s}{M}$ and where the phase of

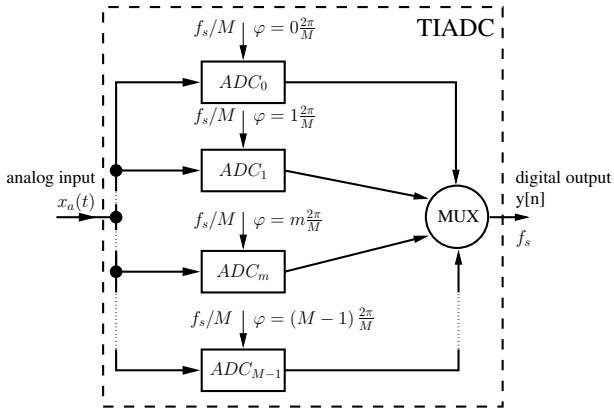

Figure 1.1: Time-interleaved ADC with M channels.

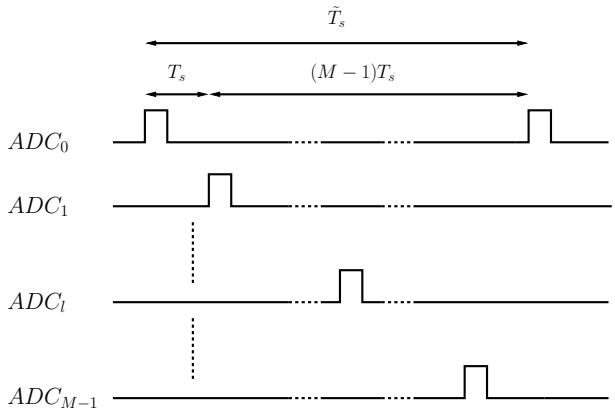

Figure 1.2: Timing diagram of a time-interleaved ADC with M channels.

the clock signal for the mth channel ADC is given by $m\frac{2\pi}{M}$. The analog input signal is alternately sampled by all channel ADCs in a successive order. On the digital side, the sampled data of each channel ADC are merged into one data stream by a digital multiplexer (MUX).

In Fig. 1.2 we see the timing diagram of a time-interleaved ADC. Each channel has a sampling period of $\tilde{T}_s = MT_s$; however, the start times of all conversion processes are interleaved. Hence, each time a sample is taken a digital output is produced, whereby the time-interleaved system achieves a sampling period of $T_s = \frac{\tilde{T}_s}{M}$. This means that we can decrease the sampling period T_s by increasing the number of interleaved channels M. Thereby, we can produce very fast ADCs [112] as well as fast ADCs with very low power consumption [18]. It should be noticed that even though the channel ADC can run at an M-times reduced sampling rate the sampling unit in each channel ADC has to deal with the entire bandwidth of the input signal, otherwise the sampled signal would be distorted.

1.1.2 Mismatch Errors in Time-Interleaved ADCs

From a theoretical point of view, we can increase the sampling rate of a time-interleaved ADC by the number of channel ADCs which work parallel in the system. Ideally, the sampling rate would linearly scale with the number of channels; however, channel mismatches ultimately limit the performance of time-interleaved ADCs.

Each channel ADC in a time-interleaved ADC possesses errors like a conventional ADC, but due to component mismatches among the channel ADCs, additional errors are introduced. These errors are therefore called mismatch errors. This is illustrated in Fig. 1.3, where we can see a matched and an unmatched time-interleaved ADC. The additional spectral components significantly reduce the performance of the time-interleaved ADC, i.e., the signal-to-noise-and-distortion ratio (SINAD) and the spurious-free dynamic range (SFDR) [41, 40].

1.1.3 History and State-of-the-Art Performance

Most time-interleaved ADCs were only developed for academic purposes, although, some were developed for commercial purposes as well. The main problem for using time-interleaved ADCs for commercial applications is to guarantee their performance, especially, when they are used for general purpose applications.

The first published time-interleaved ADC design is from Black [8, 7]. The performance compared to today's ADCs is moderate; however, the four channel time-interleaved ADC works with a sampling rate of 4 MS/s and a resolution of 7 bits. The reported integral nonlinearity (INL) was $\pm 1/2$ LSB (least significant bit).

One of the first commercially applicable time-interleaved ADC designs was invented by Ken Poulton et al. [109, 15]. The four channel time-interleaved ADC works at a sampling rate of 1 GS/s and has a resolution of 6 bits. They first came up with the idea of a two-rank-sampler, i.e., a sampler which runs on the high rate and M samplers in each channel running on the low rate to minimize timing mismatch errors. The power dissipation of the time-interleaved ADC is 7.9 W. The effective number of bits (ENOB) is greater than 5.2 for input frequencies from DC to 1 GHz.

The next highlight in the development of time-interleaved ADCs was constructed by Schiller and Byrne [119]. They invented a two channel time-interleaved ADC with a sampling rate of 4 MS/s, 2-GHz bandwidth, and a resolution of 8 bits. The INL is $\pm 1/2$ LSB. Through a special sample-and-filter method the bandwidth and slew-rate requirements of the ADC are relaxed.

In 1992 Conroy et al. created a 4-channel ADC with mismatch compensation [13, 14]. The sampling rate of the system was 85 MS/s with 8-bit resolution. The INL and differential nonlinearity (DNL) were for a 4 MHz sine wave ± 1.0 LSB and ± 0.8 LSB, respectively. The SINAD was measured as 42 dB or 6.68 ENOB. The power dissipation reported with 820 mW.

In 1997 Ken Poulton et al. developed a 4-channel, 8-GS/s time-interleaved ADC with 8-bit resolution [110]. They reported a resolution of 7.6 ENOB for low input frequencies

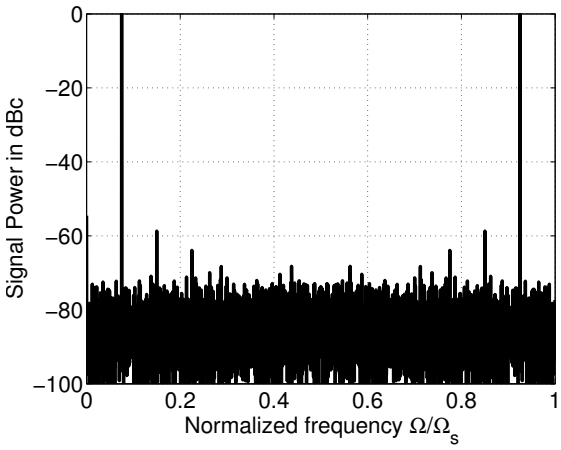

(a) Time-interleaved ADC without channel mismatches

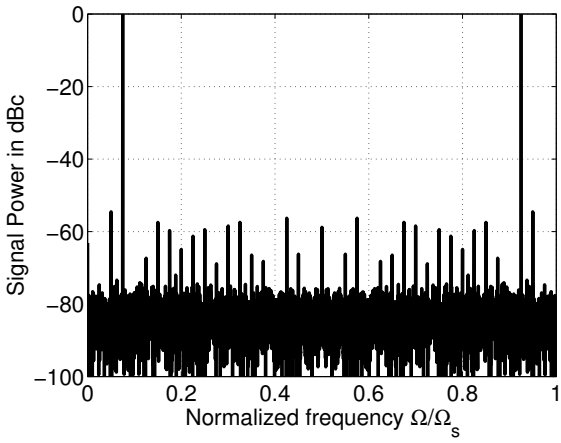

(b) Time-interleaved ADC with channel mismatches

Figure 1.3: These figures show a typical output spectrum of a time-interleaved ADC without mismatches Fig. 1.3(a) and with mismatches Fig. 1.3(b). For both figures we have used a sinusoidal input signal with a frequency of $0.075 f_s$. Fig. 1.3(a) looks like the output of a conventional ADC, whereas Fig. 1.3(b) has additional spurious spectral components, which are caused by channel mismatches and cannot be found in the output of single ADCs.

and 5.3 ENOB for a 2 GHz input signal. The time-interleaved ADC has a power dissipation of 12.5 W, its application area, however, are high-speed oscilloscopes.

In [62] a two channel time-interleaved ADC with 8-bit resolution is reported. It has a conversion rate of 52 MS/s and a power dissipation of 230 mW. Both, the INL and the DNL, are ± 0.4 LSB.

A more sophisticated time-interleaved ADC can be found in [164]. Baiying Yu and C. Black developed a 900-MS/S, 6-bit, 4-channel time-interleaved ADC. The SINAD is 31 dB at an input frequency of 1.1 MHz and the SFDR is 30 dB for an input frequency of 400 MHz.

A 4-channel, 10-bit, and 200-MS/s time-interleaved ADC is presented in [130]. Sumanen et al. use a digital offset compensation method to reduce mismatch errors and achieve a power dissipation of 230 mW. For an input signal of 71.3 MHz they reported a SINAD of 43 dB (6.85 ENOB) and an SFDR of 44 dB. The DNL is given with ± 0.8 LSB and the INL is given with ± 0.9 LSB.

Shafiq Jamal et al. developed a two-channel time-interleaved ADC with digital background calibration [43, 44]. They reported a sampling rate of 120 MS/s with 10-bit resolution. The power dissipation is 234 mW. The nonlinearities are $+0.44/-0.36$ LSB in terms of INL and $+0.6/-0.88$ LSB in terms of DNL. For an input signal with a frequency of 900 kHz the SINAD is measured at 56.8 dB (9.14 ENOB) and the SFDR is measured at 70.2 dB.

Another innovation came from Ken Poulton et al. [111]. Poulton et al. presented a 32-channel, 4-GS/s time-interleaved ADC with 8-bit resolution. They used offline mismatch compensation algorithms to yield 6.1 ENOB at an input frequency of 1 GHz. The compensation of timing mismatches is carried out on the analog side of the time-interleaved ADC whereas the estimation of the parameters is done on the digital side. They also use a look-up table to compensate nonlinearity errors and achieve an INL of ± 0.25 LSB and a DNL of ± 0.2 LSB.

The fastest time-interleaved ADC in CMOS (complementary metal oxide semiconductor) technology so far was introduced by Poulton et al. [112] in 2003. They achieve 20 GS/s and a 6-GHz bandwidth with 8-bit resolution. The INL is ± 0.4 LSB and the DNL is ± 0.3 LSB. At 6 GHz the time-interleaved ADC achieves a SINAD of 26 dB.

A fast time-interleaved ADC with very low power consumption was introduced [18]. It runs at a sampling rate of 600 MHz, has a resolution of 6 bits, and a power consumption of only 10 mW. At an input frequency of 329 MHz the time-interleaved ADC achieves a SINAD of 31 dB.

Tab. 1.1 summarizes the reported results. To make the results more comparable we have used a figure of merit (FOM) given by [142]

$$\text{FOM} = \frac{\text{Power}}{f_s 2^{\text{ENOB}}}, \tag{1.1}$$

where f_s is the sampling rate of the ADC. Since the presented measurement results have been taken at different sampling frequencies this figure of merit only roughly indicates the ADC performances.

YEAR	RATE	RES.	SINAD	POWER	FOM	REF.
1980	4 MS/s	7 bits	39 dB	250 mW	858.41 pJ	[8, 7]
1987	1000 MS/s	6 bits	33 dB	7900 mW	216.51 pJ	[109, 15]
1991	4000 MS/s	8 bits	41 dB	n.a.	n.a.	[119]
1992	85 MS/s	8 bits	42 dB	820 mW	93.80 pJ	[13, 14]
1997	8000 MS/s	8 bits	34 dB	12500 mW	38.16 pJ	[110]
1999	52 MS/s	8 bits	43 dB	230 mW	38.32 pJ	[62]
2001	900 MS/s	6 bits	31 dB	450 mW	17.25 pJ	[163]
2001	200 MS/s	10 bits	43 dB	230 mW	9.96 pJ	[130]
2002	120 MS/s	10 bits	59 dB	234 mW	2.67 pJ	[43, 44]
2002	4000 MS/s	8 bits	39 dB	4600 mW	15.79 pJ	[111]
2003	20000 MS/s	8 bits	26 dB	9000 mW	27.61 pJ	[112]
2004	600 MS/s	6 bits	31 dB	10 mW	0.56 pJ	[18]

Table 1.1: Comparison of reported time-interleaved ADC performances.

1.2 Scope of the Work

The aim of this work is to use digital and mixed signal processing methods to reduce mismatch errors. Since the intended time-interleaved ADC should have a very low power consumption, the signal processing methods should be as power efficient as possible. Another preferable property of the methods should be the ability to work in the background, i.e., without interrupting the normal conversion process.

The methods can be roughly divided in identification and compensation methods. Both should work without any additional analog circuits or, at least, with circuits that are power-aware and can easily be implemented. All these requirements are very contradictory wherefore solutions fulfilling all these requirements cannot be found in the literature.

In order to design such signal processing methods, we have analyzed time-interleaved ADCs and developed system models. One part of our research was to formally understand time-interleaved ADCs and to describe their error (mismatch) behavior. Therefore we have extended the state-of-the-art system description of a time-interleaved ADC to dynamic and static nonlinear elements, we have developed a MATLAB® simulation environment, and we have analyzed the impact of combined channel mismatches and timing jitter on the signal-to-noise ratio. Another fundamental part of our research was concerned with identification algorithms. So far, we have found power-efficient background algorithms, but their entire features and qualities have not been fully investigated yet. The compensation algorithms are as difficult as the identification methods and our recent research on this topic has revealed that combined digital and analog methods are the most promising ones. A more detailed conclusion and a further discussion of the work is given in chapter 6.

1.3 Outline of the Thesis and Main Contributions

In this thesis we discuss time-interleaved ADCs regardless of the channel ADC technology. Thus, we focus on problems of the architecture itself and do not analyze any technology-dependent problems of time-interleaved ADCs. Even though we can advantageously apply many of the investigated methods to time-interleaved sigma-delta converters, we do not discuss them in great detail and refer to the literature [72, 64, 65, 66, 73, 94, 70, 4, 71].

Introduction: In chapter 1 we give an introduction to time-interleaved ADCs and a problem statement.

Channel Mismatch Modeling: In chaper 2 we introduce the concept of nonlinear hybrid filter banks and use this theory to model channel mismatches in time-interleaved ADCs. Since the mathematical treatment of time-interleaved ADCs we have found in the literature [8, 106, 46, 48, 125, 76, 7, 164, 75, 79], was not satisfying, we have formulated, based on the concept of nonlinear hybrid filter banks, a new approach to deal with time-interleaved ADCs and their properties from a system engineering point of view. In particular, we have unified and combined the separate treatment of linear channel mismatches analyzed in [8, 106, 46, 48, 7, 164, 75, 79] and have found a connection to nonlinear channel mismatches investigated in [125, 75]. Our more complete description of a time-interleaved ADC has allowed us to get a deeper insight on how mismatches influence the performance, which is documented in:

- Christian Vogel, Work report on the project Digital Correction of Analog Signal Processing Errors in Fast Analog-to-Digital Converters, Internal Report, Christian Doppler Laboratory for Nonlinear Signal Processing, Graz University of Technology, Austria, May 2003 [147].
- Christian Vogel and Gernot Kubin, Time-Interleaved ADCs in the Context of Hybrid Filter Banks, Proceedings of the 2004 URSI International Symposium on Signals, Systems, and Electronics (ISSSE 2004), Linz (Austria), pp. 214-217, ISBN:3-9501491-4-7, August 2004 [154].
- Christian Vogel and Gernot Kubin, Analysis and Compensation of Nonlinearity Mismatches in Time-Interleaved ADC Arrays, Proceedings of the 2004 IEEE International Symposium on Circuits and Systems (ISCAS 2004), Vancouver (Canada), Vol.1, pp. 593-596, May 2004 [153].
- Christian Vogel, Dieter Draxelmayr and Franz Kuttner, Compensation of Timing Mismatches in Time-Interleaved Analog-to-Digital Converters through Transfer Characteristics Tuning, 47th IEEE International Midwest Symposium On Circuits and Systems (MWSCAS 2004), Hiroshima (Japan), Vol. 1, pp. 349-352, July 2004 [151].
- Christian Vogel and Gernot Kubin, Modeling of Time-interleaved ADCs with Nonlinear Hybrid Filter Banks, AEÜ-International Journal of Electronics and Communications, Vol. 59, Issue 5, pp. 288-296, July 2005 [157].

Channel Mismatch Error Analysis: In chapter 3 we analyze channel mismatches in combination with timing jitter and quantization noise. From these analyses, we can rate the significance of different channel mismatches in order to obtain a simpler system model. The publications to this chapters are:

- Christian Vogel, Comprehensive Error Analysis of Combined Channel Mismatch Effects in Time-Interleaved ADCs, Proceedings of the 20th IEEE Instrumentation and Measurement Technology Conference (IMTC 2003), Vail (USA), Vol.1, pp. 733-738, May 2003 [146].
- Christian Vogel, The Impact of Combined Channel Mismatch Effects in Time-interleaved ADCs, IEEE Transactions on Instrumentation and Measurement, Vol.55, Issue 1, pp. 415-427, February 2005 [149].

Channel Mismatch Identification: In chapter 4 we present channel mismatch identification methods. By introducing a matrix notation for time-interleaved ADCs with linear channel mismatches, we derive a linear channel mismatch identification method and a timing mismatch identification method. The related papers are:

- Christian Vogel, Work report on the project Digital Correction of Analog Signal Processing Errors in Fast Analog-to-Digital Converters, Internal Report, Christian Doppler Laboratory for Nonlinear Signal Processing, Graz University of Technology, Austria, May 2003 [147].
- Christian Vogel, Work report on the project Digital Correction of Analog Signal Processing Errors in Fast Analog-to-Digital Converters, Internal Report, Christian Doppler Laboratory for Nonlinear Signal Processing, Graz University of Technology, Austria, May 2004 [148].

Channel Mismatch Compensation: In chapter 5 we discuss different channel mismatch compensation approaches. One improves the static nonlinearities as well as their mismatch effects in time-interleaved ADCs. Another method compensates timing-mismatches through transfer characteristics tuning. From a theoretical point of view this method is very precise and only needs very little power consumption, since it needs only few additional circuits. Furthermore, we have found an entirely new approach, which is the deterministic optimization of channel ADC sequences. This method is very robust and can significantly improve the signal-to-noise ratio as well as the spurious-free dynamic range. The publications in this field are:

- Christian Vogel and Gernot Kubin, Analysis and Compensation of Nonlinearity Mismatches in Time-Interleaved ADC Arrays, Proceedings of the 2004 IEEE International Symposium on Circuits and Systems (ISCAS 2004), Vancouver (Canada), Vol.1, pp. 593-596, May 2004 [153].
- Dieter Draxelmayr, Christian Vogel, and Franz Kuttner, Compensation of Nonlinearity Mismatches in Time-Interleaved ADCs, pending patent application, Germany and United States, 102004009613.9, February 2004 [20].

- Christian Vogel, Dieter Draxelmayr and Franz Kuttner, Compensation of Timing Mismatches in Time-Interleaved Analog-to-Digital Converters through Transfer Characteristics Tuning, 47th IEEE International Midwest Symposium On Circuits and Systems (MWSCAS 2004), Hiroshima (Japan), Vol. 1, pp. 349-352, July 2004 [151].
- Dieter Draxelmayr, Franz Kuttner, and Christian Vogel, Delay Equalization in Converter Arrays, pending patent application, Germany and United States, 102004009612.9, February 2004 [19].
- Christian Vogel, Dieter Draxelmayr, and Gernot Kubin, Channel Sequence Optimization in Converter Arrays, pending patent application, Germany, 102004049161.5, October 2004 [156].
- Christian Vogel, Dieter Draxelmayr, and Gernot Kubin, Spectral Shaping of Timing Mismatches in Time-Interleaved ADCs, Proceedings of the 2005 IEEE International Symposium on Circuits and Systems (ISCAS 2005), Kobe (Japan), pp. 1394-1397, May 2005 [150].
- Christian Vogel, Viktoria Pammer, and Gernot Kubin, A Novel Channel Randomization Method for Time-Interleaved ADCs , Proceedings of the 22nd IEEE Instrumentation and Measurement Technology Conference (IMTC 2005), Ottawa (Canada), Vol. 1, pp. 150-155, May 2005 [155].

Concluding Remarks: In chapter 6 we discuss further research objectives.

Simulation Environment: In appendix A we discuss the architecture of a MATLAB simulation environment for time-interleaved ADCs. We have developed a MATLAB environment capable of simulating the main characteristics of time-interleaved ADCs as well as of nonlinear hybrid filter banks. We have implemented most of the promising methods and algorithms from the literature and have written test programs to investigate their performance. Furthermore, we have written performance analyses and display tools. The system design of the environment was published in:

- Christian Vogel and Heinz Köppl, Behavioral Modeling of Time-Interleaved ADCs using MATLAB, Proceedings of the Austrochip 2003, Linz (Austria), pp. 45-48, October 2003 [152].

In contrast to other papers about ADC modeling and simulation [53, 89, 3, 9, 115, 2, 12, 92], we have investigated time-interleaved structures and their error behavior explicitly. Furthermore, we have been able to verify many results from the literature, e.g., [46, 107, 76] , as well as to disprove some results, e.g., [125, 75].

Time-Domain Identification: In appendix B we briefly discuss time-domain identification methods including their difficulties. Furthermore, we introduce an advanced time-domain identification concept.

- Dieter Draxelmayr and Christian Vogel, Background Identification of Timing-Mismatches in Converter Arrays, Christian Doppler Laboratory for Nonlinear

Signal Processing (Graz University of Technology, Austria) and Infineon Technologies Austria AG joint invention disclosure, May 2005.

Signals and Systems: In appendix C we define common system and signal properties and discuss representation aspects of sampling errors.

Furthermore, there are publications which are not included in this thesis, which are

- Peter Singerl and Christian Vogel, An Analysis of a Low Complexity Received Signal Strength Indicator for Wireless Applications, Austrochip 2004, Proceedings of the Austrochip 2004, Villach (Austria), pp. 57-60, October 2004 [126].
- Peter Singerl and Christian Vogel, A Fast and Accurate Automatic Gain Control for a Wireless Local Area Network Receiver, accepted for Global Mobile Congress (GMC), Chongqing (China), October 2005 [127].

Chapter 2

Channel Mismatch Modeling

This chapter deals with the problem of modeling channel mismatches in time-interleaved ADCs. The starting point of our investigation is that time-interleaved ADCs are special cases of hybrid filter banks [105]. Since hybrid filter banks are based on multirate systems, which are well understood, the analysis of time-interleaved ADCs can be unified and simplified. However, time-interleaved ADCs also possess nonlinear mismatches, which have no counterpart in the well-known linear hybrid filter banks. For this reason, linear hybrid filter banks are extended by static nonlinearities in each channel to obtain nonlinear hybrid filter banks, i.e., a comprehensive system to model time-interleaved ADCs.

In Sec. 2.1 we introduce time-interleaved ADC modeling and review existing literature. Sec. 2.2 establishes linear hybrid filter banks and in Sec. 2.3 we extend linear hybrid filter banks to nonlinear hybrid filter banks. Sec. 2.4 discusses the fundamental interval representation of linear and nonlinear hybrid filter banks and, finally, in Sec. 2.5 we use nonlinear hybrid filter banks to model time-interleaved ADCs.

2.1 Introduction

Analog-to-digital conversion relies on the Nyquist criterion [95] and on Shannon's law [122]. If a continuous-time signal $\Omega(t)$ fulfills the Nyquist criterion that is [99]

$$X_a(j\Omega) = 0 \quad |\Omega| \geq \frac{\Omega_s}{2}, \tag{2.1}$$

where $X_a(j\Omega)$ is the continuous-time Fourier transform (CTFT) (cf. Sec. C.3) of $x_a(t)$, Ω_s is the sampling frequency given by $\Omega_s = \frac{2\pi}{T_s}$, and T_s is the sampling period, it can be perfectly reconstructed from its samples $x_a(nT_s)$.

The idea of a time-interleaved ADC is that each channel ADC in a system of M parallel channels alternately takes one sample, whereas the sampling frequency of one channel $\frac{\Omega_s}{M}$ does not need to fulfill the Nyquist criterion [8, 7]. However, when in the digital domain all samples merge into one sequence we obtain an overall sampling frequency Ω_s which fulfills the Nyquist criterion given in (2.1). Thus, sampling with an ideal time-interleaved ADC with M channels is equivalent to sampling with an ideal ADC with an M times higher sampling rate.

This is a simple interpretation of an ideal time-interleaved ADC, but Shannon's law is more than 50 years old and today's sampling theory has many new findings, e.g., [51, 137,

140], which allow a more general interpretation of a time-interleaved ADC, which also includes its non-ideal behavior.

One of the most remarkable findings is the Generalized Sampling Expansion (GSE) found by Papoulis [100]. He proves that a band-limited signal $x_a(t)$ is uniquely determined by the samples $g_m(nT_s)$, which are the responses of M linear systems with input $x_a(t)$, sampled at $\frac{1}{M}$ the Nyquist rate. A simple example of such a system is the sampling of the signal $x_a(t)$ and its derivative $\frac{dx_a(t)}{dt}$ at half the Nyquist rate. In [100] Papoulis only gives a proof of the existence of such systems but does not investigate the reconstruction process itself in terms of stability and causality. Vaidyanathan provides similar results for discrete-time systems with his work about multirate systems [141, 139]. Moreover, perfect reconstruction for maximally decimated filter banks is the digital counterpart of Papoulis' GSE. Brown [10, 11] was one of the first who discovered the link between multirate systems and the GSE and combined both worlds by introducing multi-channel sampling. All these efforts lead to the area of hybrid filter banks (HFB) [105, 139, 124, 32, 144, 96, 83, 31, 82], which can be seen as the engineer's point of view of new sampling innovations, which allow for practical considerations such as causality, quantization noise, and filter length. Based on hybrid filter bank sampling concepts, new ADC designs, called hybrid filter bank ADCs (HFB ADCs), have been introduced in the literature [104, 106, 145, 97, 143, 108, 85]. This new hybrid filter bank ADCs also found their way from the academic world to industrially manufactured ADCs [17].

Although a time-interleaved ADC is a special form of such a hybrid filter bank [144], only few people use this unified framework of HFBs to investigate time-interleaved ADCs. In [107] the authors use the hybrid filter bank approach to model gain and offset mismatches in time-interleaved ADCs. They have been limited to such static errors since they use discrete-time HFBs for their investigation. A dynamic mismatch effect like the timing mismatch has been first investigated and modeled by Jenq [46], where he starts from a time-domain representation of sampling errors in order to derive the frequency behavior. Similar approaches to model offset, gain, and timing mismatches can be found in [55, 35, 164, 25]. All those papers do not exploit the relation to hybrid filter banks. In [77, 76] the authors introduce for the first time bandwidth mismatches, which can be interpreted as dynamic gain and nonlinear-phase mismatches. Unfortunately, they neither use the hybrid filter bank approach and, therefore, cannot clearly present the connection between gain and magnitude mismatches and timing and phase mismatches.

A special problem of ADCs is their nonlinear behavior. This behavior has no counterpart in linear hybrid filter banks and, therefore, the possibility of modeling the nonlinear behavior of time-interleaved ADCs with hybrid filter banks has not even been mentioned in the literature. Outside the scope of hybrid filter banks, first investigations on nonlinear behavior in time-interleaved ADCs can be found in [38]. The authors do not use a unified modeling approach nor do they stress the impact of nonlinear mismatches. In [125] the authors use statistical analysis rather than a nonlinear deterministic model. For this reason their analysis is somehow imprecise and the conclusions they draw inadequate. A quantitative investigation of nonlinear mismatches can be found in [75], where the authors only propose properties of such mismatches without presenting a detailed time-interleaved

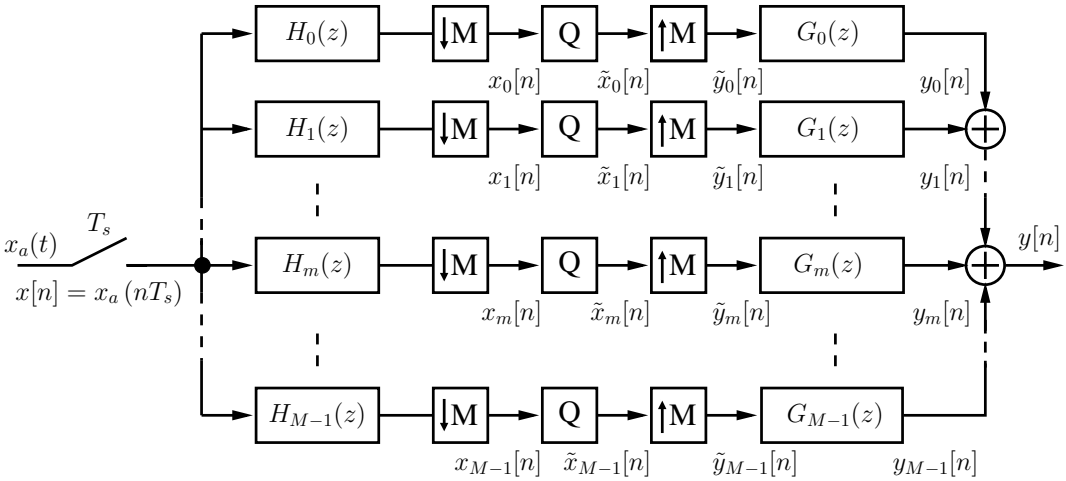

Figure 2.1: Discrete-time linear hybrid filter bank with M channels.

ADC model. A paper on time-interleaved ADC modeling including nonlinear mismatches is [69]. Here, the authors also include strong nonlinear effects such as clipping of the input signal. Nevertheless, the modeling approach is hard to unify and generalize.

A first comprehensive investigation of time-interleaved ADCs in the context of hybrid filter banks can be found in [154, 151]. There, a linear hybrid filter bank is used to model offset, gain, timing, magnitude, and phase mismatches, where gain mismatches are the static special case of the overall magnitude mismatches and timing mismatches are linear-phase contributions to the overall phase mismatches. Modeling nonlinearities of time-interleaved ADCs with nonlinear hybrid filter banks was introduced in [153]. An entirely comprehensive time-interleaved ADC model exploiting nonlinear hybrid filter banks is presented in [157]. All those papers do not include the quantization noise in their models, since as long as we assume that the quantization noise is identical in each channel ADC, the overall behavior does not differ from a single channel sampling system. Since practical implementations of time-interleaved ADCs use the same quantization resolution for all channel ADCs, this assumption is therefore satisfied. Thus, all quantization characteristics from single sampling systems are valid for multi-channel systems as well. A deterministic analysis of quantization can be found in [5, 6] and a statistical analysis of quantization noise is given in [162].

2.2 Linear Hybrid Filter Banks

A linear hybrid filter bank (LHFB) is usually referred to as a system with continuous-amplitude analysis filters and discrete-time synthesis filters. If, in addition, the analysis filters are discrete-time we denote the system as discrete-time hybrid filter bank (DT LHFB), otherwise, if the filters are continuous-time we denote the system as continuous-time hybrid filter bank (CT LHFB). If the number of channels is M and the sampling rate in each

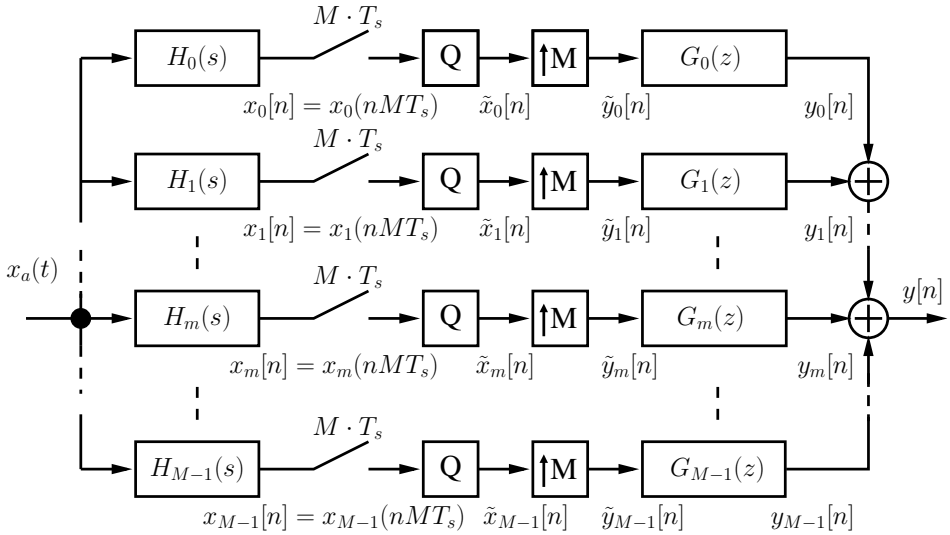

Figure 2.2: Continuous-time linear hybrid filter bank with M channels.

channel is $\frac{f_s}{M}$ we call the system a maximally decimated linear hybrid filter bank [139, 82].

Discrete-time linear hybrid filter bank ADCs [106], pictured in Fig. 2.1, were the first natural development out of the theory of multirate filter banks [139]. The input signal $x_a(t)$ is sampled at the Nyquist rate. The sampled signal goes into a synthesis filter bank, which divides the frequency band of the input signal $X_a(j\Omega)$ into M subbands, where all subbands together have to cover the entire input signal frequency band. The subbands can be quantized with different resolutions, which can be higher than for quantizers covering the complete input signal frequency spectrum. The advantage of using discrete-time filters, e.g., switched-capacitor or charge-coupled devices, is that they can usually be implemented with much higher accuracy than continuous-time filters. Furthermore, such filter bank ADCs can be completely described in the discrete-time domain and we can use the entire design theory of multirate systems [139]. The main disadvantage of discrete-time filters are their limited switching frequencies, which do not allow fast ADC designs. The first DT HFB have been presented in [106], where the authors have used a quadrature mirror filter (QMF) bank consisting of switched-capacitor analysis filters for analog-to-digital conversion.

The principle of a continuous-time linear hybrid filter bank ADC is shown in Fig. 2.2. In CT HFB ADCs the analysis filters are analog, i.e., continuous-time and continuous-amplitude. As for most analog devices it is much harder to implement given design requirements than for discrete-time devices. On the other hand they can handle much higher frequencies. Therefore, they are used for new analog-to-digital conversion concepts [143, 85]. The implementation problem of analog filters is minimized by asymmetric filter architectures. Thus, the digital filter inherits much more complexity to minimize the implementation uncertainties of the analog filters [82]. However, it is also possible to use more restricted filter designs on the analog side because of, for example, power or speed considerations. For

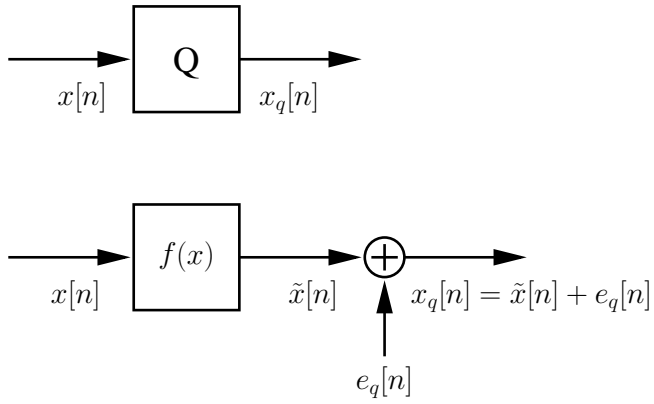

Figure 2.3: Mathematical model of the quantization error. In a statistical approach, ideal quantization can be represented by the continuous-time signal $\tilde{x}[n]$ plus an additive stationary white noise process $e_q[n]$ with variance σ_q. To further represent continuous deviations from the ideal transfer curve, the function $f(x)$ changes the amplitudes of the input signal $x[n]$.

such designs, the analog filters have to be designed very carefully and the chip production process has to be very precise.

For the further discussion we have to investigate the quantization process in more detail. The mathematical model is shown in Fig. 2.3. The discrete-amplitude output signal $x_q[n]$ can be described by the continuous-amplitude input signal $\tilde{x}[n]$ plus the quantization error $e_q[n]$. Strictly speaking, quantization is a strong nonlinear operation which is difficult to describe in a convenient way. In many cases [98, 114], however, we can treat the quantization error $e_q[n]$ as an additive stationary white noise process with variance σ_q. Furthermore, we see from Fig. 2.3 the function $f(x)$ which takes nonideal quantization steps into account. This is represented by the function $f(x)$, which changes the signal amplitudes of the continuous-amplitude signal $x[n]$, i.e, compresses or expands them, before they become ideally quantized. With this function, we can describe continuous changes of the transfer curve of the quantizer, which result in different quantization step sizes.

For the following discussion, we will first include the function $f(x)$ in our descriptions but omit the quantization error of the ideal quantizer, which is described in a statistical way. In Sec. 3.4.2, however, we will include the quantization error as well and analyze its impact on the performance of a time-interleaved ADC.

2.2.1 Continuous-Time Downsamplers and Discrete-Time Upsamplers

We consider the process of reducing (downsampling) and increasing (upsampling) the sampling rate of signals.

The principle of a sampling rate reduction (downsampling) of a continuous-time signal is shown in Fig. 2.4, where we sample the signal $x(t)$ with an M times larger sampling period than the Nyquist sampling period T_s. A continuous-time signal $x(t)$ sampled with such a

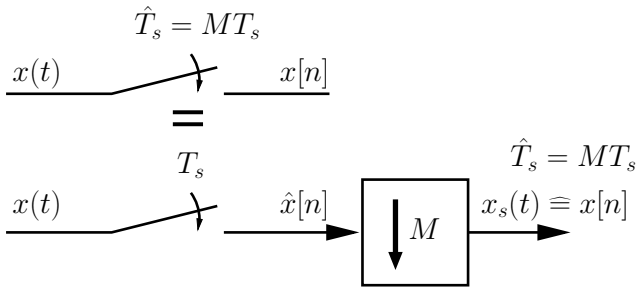

Figure 2.4: Sampling of a continuous-time signal with a sampling period $\hat{T}_s = MT_s$. This is the same as first sampling a continuous-time signal with T_s and digitally downsampling the resulting discrete-time signal by the factor M afterwards.

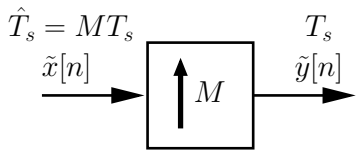

Figure 2.5: Upsampling of a discrete-time signal by factor M.

sampling period MT_s can be expressed as [83, 98]

$$x_s(t) = \sum_{n=-\infty}^{\infty} x(t)\,\delta(t - nMT_s)\,. \tag{2.2}$$

The sampled signal $x_s(t)$ has an equivalent discrete-time representation $x[n]$, where $x[n]$ is a sequence of values representing the sampling values of $x(t)$ at $t = nMT_s$ [98]. Thus, for further discussion, we use $x_s(t)$ and $x[n]$ synonymously. It should be noticed, however, that these two representations are not completely identical and cannot be interchanged arbitrarily. The representation $x_s(t)$ can be only evaluated in an integral form, whereas the representation $x[n]$ does not have that constraint. The continuous-time Fourier transform (cf. Sec. C.3) of (2.2) is therefore (cf. Sec. C.5)

$$\begin{aligned} X\left(e^{j\Omega MT_s}\right) &= X_s(j\Omega M) \\ &= \frac{1}{MT_s}\sum_{p=-\infty}^{\infty} X\left(j\left(\Omega - p\frac{\Omega_s}{M}\right)\right). \end{aligned} \tag{2.3}$$

This is identical to sampling a signal with a sampling period T_s and taking every Mth sample, i.e., digitally downsampling the sampled signal (cf. [141, 98]).

The upsampling of a discrete-time signal $\tilde{x}[n]$ by factor M, which is illustrated in Fig. 2.5,

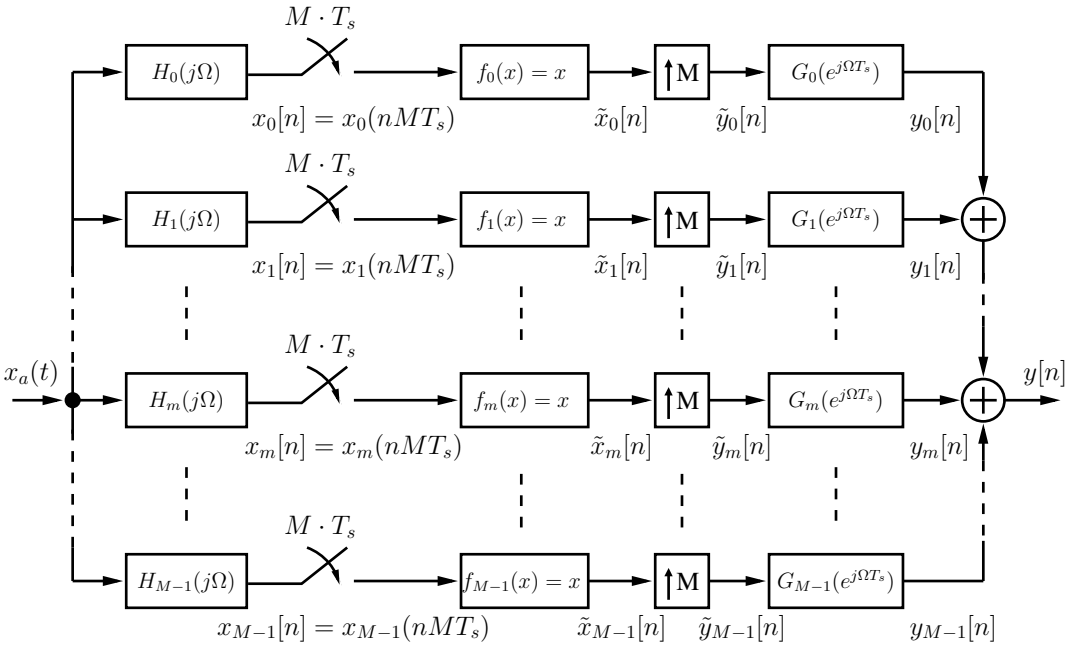

Figure 2.6: Maximally decimated continuous-time linear hybrid filter bank with analysis filters $H_m(j\Omega)$ and synthesis filters $G_m(e^{j\Omega T_s})$

gives [98]

$$\tilde{y}[n] = \begin{cases} \tilde{x}[n/M] & \text{for } n = 0, \pm M, \pm 2M, \ldots \\ 0 & \text{otherwise,} \end{cases} \tag{2.4}$$

where the Fourier transform of the upsampled signal can be written as [83, 98]

$$\tilde{Y}\left(e^{j\Omega T_s}\right) = \tilde{X}\left(e^{j\Omega \hat{T}_s}\right) = \tilde{X}\left(e^{j\Omega M T_s}\right). \tag{2.5}$$

2.2.2 Input/Output Relation of Linear Hybrid Filter Banks

From Fig. 2.6 we see that the output $Y(e^{j\Omega T_s})$ of the linear hybrid filter bank (LHFB) is given by the sum of the channel outputs $Y_m\left(e^{j\Omega T_s}\right)$, which can be expressed as

$$\begin{aligned} Y\left(e^{j\Omega T_s}\right) &= \sum_{m=0}^{M-1} Y_m\left(e^{j\Omega T_s}\right) \\ &= \sum_{m=0}^{M-1} G_m(e^{j\Omega T_s}) \tilde{Y}_m\left(e^{j\Omega T_s}\right). \end{aligned} \tag{2.6}$$

In order to determine the output of each channel, we have to concatenate the input/output relation of the blocks we have determined in Sec. 2.2.1.

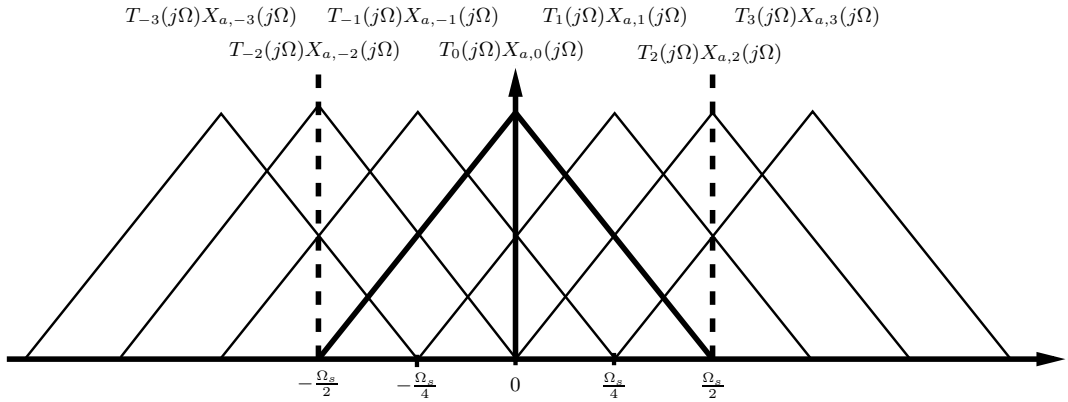

Figure 2.7: Schematic illustration of the frequency response of a maximally decimated linear hybrid filter bank with four channels ($M = 4$). Each spectrum is weighted by the complex distortion function $T_p\left(j\Omega\right)$. For the illustration we use the abbreviation $X_{a,p}(j\Omega) = X_a\left(j\left(\Omega - p\frac{\Omega_s}{M}\right)\right)$.

First, the input signal $X_a(j\Omega)$ is connected to the analysis filters $H_m\left(j\Omega\right)$, which results in the output

$$X_m\left(j\Omega\right) = X_a(j\Omega)H_m\left(j\Omega\right). \tag{2.7}$$

The next block is the continuous-time sampler, which is given by (2.3). The output of the sampler can be written as

$$\begin{aligned} X_m\left(e^{j\Omega MT_s}\right) &= X_{s,m}\left(j\Omega M\right) \\ &= \frac{1}{MT_s}\sum_{p=-\infty}^{\infty} X_m\left(j\left(\Omega - p\frac{\Omega_s}{M}\right)\right), \end{aligned} \tag{2.8}$$

where the following identity function $f_m(x) = x$ has no influence on the signal $X_m\left(e^{j\Omega MT_s}\right)$. For an LHFB we can omit the function $f_m(x)$, but to be consistent with the representation of an NHFB we use the identity function $f_m(x) = x$ instead. This gives

$$\tilde{X}_m\left(e^{j\Omega MT_s}\right) = X_m\left(e^{j\Omega MT_s}\right). \tag{2.9}$$

Finally, we have the discrete-time upsampler, where we can use the relation given with (2.5) to rewrite (2.6) as

$$Y(e^{j\Omega T_s}) = \sum_{m=0}^{M-1} G_m(e^{j\Omega T_s})\tilde{X}_m(e^{j\Omega MT_s}), \tag{2.10}$$

where the complete description of $\tilde{X}_m(e^{j\Omega MT_s})$ can be obtained by substituting (2.7)

into (2.8), which gives

$$\begin{aligned}\tilde{X}_m\left(e^{j\Omega MT_s}\right) &= X_{s,m}\left(j\Omega M\right) \\ &= \frac{1}{MT_s}\sum_{p=-\infty}^{\infty} X_a\left(j\left(\Omega - p\frac{\Omega_s}{M}\right)\right) H_m\left(j\left(\Omega - p\frac{\Omega_s}{M}\right)\right).\end{aligned} \tag{2.11}$$

We can also rewrite (2.10) and (2.9) as

$$Y(e^{j\Omega T_s}) = \frac{1}{T_s}\sum_{p=-\infty}^{\infty} T_p(j\Omega) X_a\left(j\left(\Omega - p\frac{\Omega_s}{M}\right)\right), \tag{2.12}$$

where

$$T_p(j\Omega) = \frac{1}{M}\sum_{m=0}^{M-1} H_m\left(j\left(\Omega - p\frac{\Omega_s}{M}\right)\right) G_m\left(e^{j\Omega T_s}\right). \tag{2.13}$$

In Fig. 2.7 we see the output spectrum given by (2.12).

2.3 Nonlinear Hybrid Filter Banks

In this section we derive the input/output relation of a nonlinear hybrid filter bank (NHFB) [153], which is shown in Fig. 2.8. An NHFB is a continuous-time linear hybrid filter bank [143, 82] extended by a static nonlinearity $f_m(x)$ in each channel. Therefore, an NHFB consists of continuous-time analysis filters $H_m(j\Omega)$, continuous-time samplers with a sampling period MT_s, static nonlinearities $f_m(x)$, discrete-time upsamplers with a factor of M, and discrete-time synthesis filters $G_m(e^{j\omega})$. In order to find the input/output relation for NHFBs we use the same procedure as for LHFBs. The difference between LHFBs and NHFBs is the static nonlinearity $f_m(x)$, which differs from the identity function $f_m(x) = x$ for the case of an NHFB. In principle, we can extend static nonlinearities to dynamic nonlinearities as well, but their usefulness for modeling time-interleaved ADCs is not clear. Moreover, by combining analysis filters, static nonlinearities, and synthesis filters we can model at least a subset of dynamic nonlinearities represented by special Volterra systems [158, 118, 138]. We start with the analysis of static nonlinearities.

2.3.1 Static Nonlinearities

Any continuous real-valued static (memoryless) nonlinearity $f(x)$ on the interval $[a, b]$ for a given error bound $\varepsilon > 0$ can be approximated by a univariate polynomial $p(x)$ of degree $K - 1$ such that

$$|f(x) - p(x)| < \varepsilon \quad x \in [a, b] \tag{2.14}$$

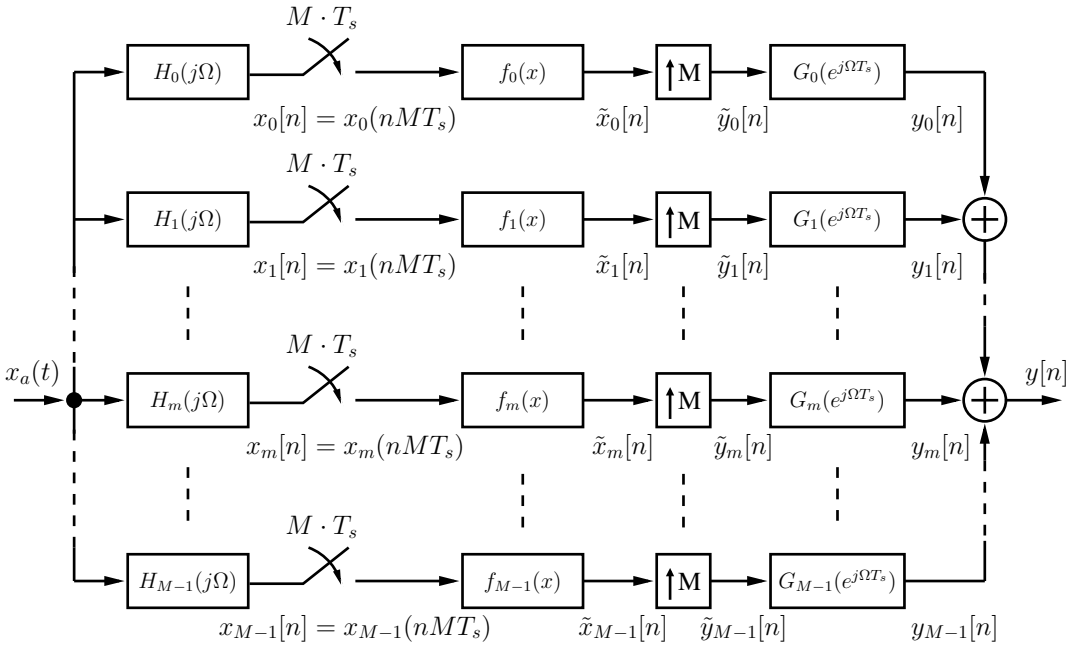

Figure 2.8: A nonlinear hybrid filter bank (NHFB) with analysis filters $H_m(j\Omega)$, continuous-time samplers with sampling period MT_s, static nonlinearities $f_m(x)$, discrete-time upsamplers with factor of M, and synthesis filters $G_m(e^{j\omega})$.

holds [74]. A univariate polynomial with constant coefficients of order $K-1$ is a polynomial in a single variable and is given by

$$\begin{aligned} p(x) &= c_0x^0 + c_1x^1 + \ldots + c_{K-2}x^{K-2} + c_{K-1}x^{K-1} \\ &= \sum_{k=0}^{K-1} c_k x^k. \end{aligned} \tag{2.15}$$

Thus, any continuous function $f(x)$ on a closed and bounded interval $[a, b]$ can be uniformly approximated on that interval by a polynomial $p(x)$ to any degree of accuracy (cf. Fig. 2.9), which is known as the Weierstrass approximation theorem [74]. By employing the Weierstrass approximation theorem we can assume for the further discussion that we have found a polynomial $p(x)$ which approximates the static nonlinearity as closely as desired.

When the static nonlinearity $f(x)$ is driven by a time-dependent signal $x(t)$ it produces a time-dependent output (cf. Fig. 2.10), which can be written with (2.15) as [102, 153]

$$\tilde{x}(t) = \sum_{k=0}^{K-1} c_k x^k(t). \tag{2.16}$$

For the Fourier transform of (2.16) we obtain [153]

$$\tilde{X}(j\Omega) = \sum_{k=0}^{K-1} c_k X^{(*k)}(j\Omega), \tag{2.17}$$

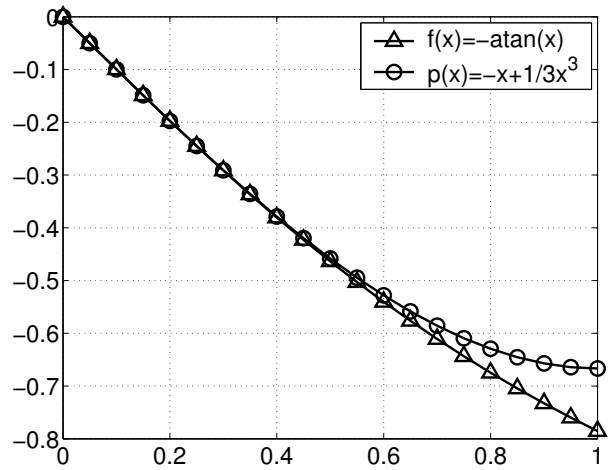

Figure 2.9: Approximation of the function $f(x)$ through a polynomial of order $K - 1 = 3$. The coefficients have been determined by a Taylor series approximation around 0 (Maclaurin series).

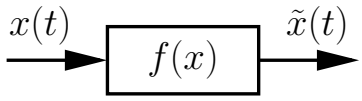

Figure 2.10: The continuous-time signal $x(t)$ runs through the static nonlinearity and produces the output signal $\tilde{x}(t)$.

where $X^{(*k)}(j\Omega)$ is the (k-1)-fold convolution with itself:

$$X^{(*k)}(j\Omega) = \begin{cases} 2\pi\delta\left(\Omega\right) & \text{for } k = 0 \\ X\left(j\Omega\right) & \text{for } k = 1 \\ \frac{1}{2\pi}\int_{-\infty}^{\infty} X\left(j\lambda\right) X\left(j\left(\Omega - \lambda\right)\right) d\lambda & \text{for } k = 2 \\ \left(\frac{1}{2\pi}\right)^{k-1} (\underbrace{X * X * \ldots * X}_{(k-1)-\text{convolutions}})(j\Omega) & \text{for } k > 2 \end{cases}$$

Thereby, we have found a deterministic input-output relation of a static nonlinearity excited with a continuous-time signal $x(t)$ in the time as well as in the frequency domain.

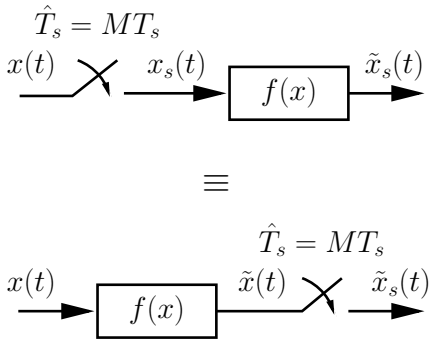

Figure 2.11: Since we have a static (memoryless) nonlinearity $f(x)$ we can change the order of the nonlinearity and the sampler [120].

2.3.2 Input/Output Relation of Nonlinear Hybrid Filter Banks

From Fig. 2.8 we see that the output $Y(e^{j\Omega T_s})$ of the NHFB is given by the sum of the channel outputs $Y_m\left(e^{j\Omega T_s}\right)$, which can be expressed as

$$\begin{aligned} Y\left(e^{j\Omega T_s}\right) &= \sum_{m=0}^{M-1} Y_m\left(e^{j\Omega T_s}\right) \\ &= \sum_{m=0}^{M-1} G_m(e^{j\Omega T_s})\tilde{Y}_m\left(e^{j\Omega T_s}\right). \end{aligned} \tag{2.18}$$

In order to determine the output of each channel, we have to concatenate the input/output relation of the blocks we have determined in the last two sections.

First, the input signal $X_a(j\Omega)$ is connected to the analysis filters $H_m\left(j\Omega\right)$, which results in the output

$$X_m\left(j\Omega\right) = X_a(j\Omega)H_m\left(j\Omega\right). \tag{2.19}$$

The next block is the continuous-time sampler followed by the static nonlinearity $f_m(x)$. Since this is a static nonlinearity, we can change the order of the static nonlinearity and the continuous-time sampler [120], which is shown in Fig. 2.11. This simplifies the notation, since by using (2.17) and (2.3) the output can be written as

$$\begin{aligned} \tilde{X}_m\left(e^{j\Omega MT_s}\right) &= X_{s,m}\left(j\Omega M\right) \\ &= \frac{1}{MT_s}\sum_{p=-\infty}^{\infty}\sum_{k=0}^{K-1} c_{k,m}X_m^{(*k)}\left(j\left(\Omega - p\frac{\Omega_s}{M}\right)\right), \end{aligned} \tag{2.20}$$

where the operator $(*k)$ is defined in (2.18). Finally, we have the discrete-time upsampler, where we can use the relation (2.5) to rewrite (2.18) as

$$Y(e^{j\Omega T_s}) = \sum_{m=0}^{M-1} G_m(e^{j\Omega T_s})\tilde{X}_m(e^{j\Omega MT_s}), \tag{2.21}$$

where the complete description of $\tilde{X}_m(e^{j\Omega MT_s})$ can be obtained by substituting (2.19) in (2.20), which gives

$$\begin{aligned}\tilde{X}_m\left(e^{j\Omega MT_s}\right) &= X_{s,m}\left(j\Omega M\right) \\ &= \frac{1}{MT_s}\sum_{p=-\infty}^{\infty}\sum_{k=0}^{K-1} c_{k,m}\left(X_a(j\Omega)H_m(j\Omega)\right)^{(*k)}\Big|_{j\Omega=j\left(\Omega-p\frac{\Omega_s}{M}\right)}.\end{aligned} \tag{2.22}$$

To show the relation to linear hybrid filter banks [143, 82], we rewrite (2.21) and (2.22) as

$$Y(e^{j\Omega T_s}) = \frac{1}{T_s}\sum_{k=0}^{K-1}\sum_{p=-\infty}^{\infty} T_{p,k}(j\Omega), \tag{2.23}$$

where

$$T_{p,k}(j\Omega) = \frac{1}{M}\sum_{m=0}^{M-1} c_{k,m}\left(X_a\left(j\Omega\right)H_m\left(j\Omega\right)\right)^{(*k)}\Big|_{j\Omega=j\left(\Omega-p\frac{\Omega_s}{M}\right)} G_m\left(e^{j\Omega T_s}\right). \tag{2.24}$$

In Fig. 2.12 we have illustrated the output of an NHFB with four channels ($M = 4$). For $k = 1$ we get the linear case of an HFB, which is

$$Y(e^{j\Omega T_s}) = \frac{1}{T_s}\sum_{p=-\infty}^{\infty}\tilde{T}_p(j\Omega)X_a\left(j\left(\Omega - p\frac{\Omega_s}{M}\right)\right) \tag{2.25}$$

where

$$\tilde{T}_p(j\Omega) = \frac{1}{M}\sum_{m=0}^{M-1} c_{1,m}H_m\left(j\left(\Omega - p\frac{\Omega_s}{M}\right)\right)G_m\left(e^{j\Omega T_s}\right). \tag{2.26}$$

Only the constant coefficients $c_{1,m}$ differ from the typical LHFB representation [82], which can be avoided by setting $c_{1,m} = 1$ for all m with a corresponding rescaling of the analysis filters $H_m\left(j\Omega\right)$ or synthesis filters $G_m\left(e^{j\Omega T_s}\right)$.

2.4 Fundamental Interval Representation of Hybrid Filter Banks

To represent the fundamental interval of the output spectrum $]-\frac{\Omega_s}{2},\frac{\Omega_s}{2}]$ we can omit most of the aliased terms of our output relations given with (2.12) for LHFBs and (2.23) for NHFBs, respectively. The representation of the fundamental interval allows us to easily qualify the reconstruction properties of LHFBs and NHFBs. In the following we clarify how many p-terms we have to include in order to describe the fundamental interval of LHFBs as well as NHFBs.

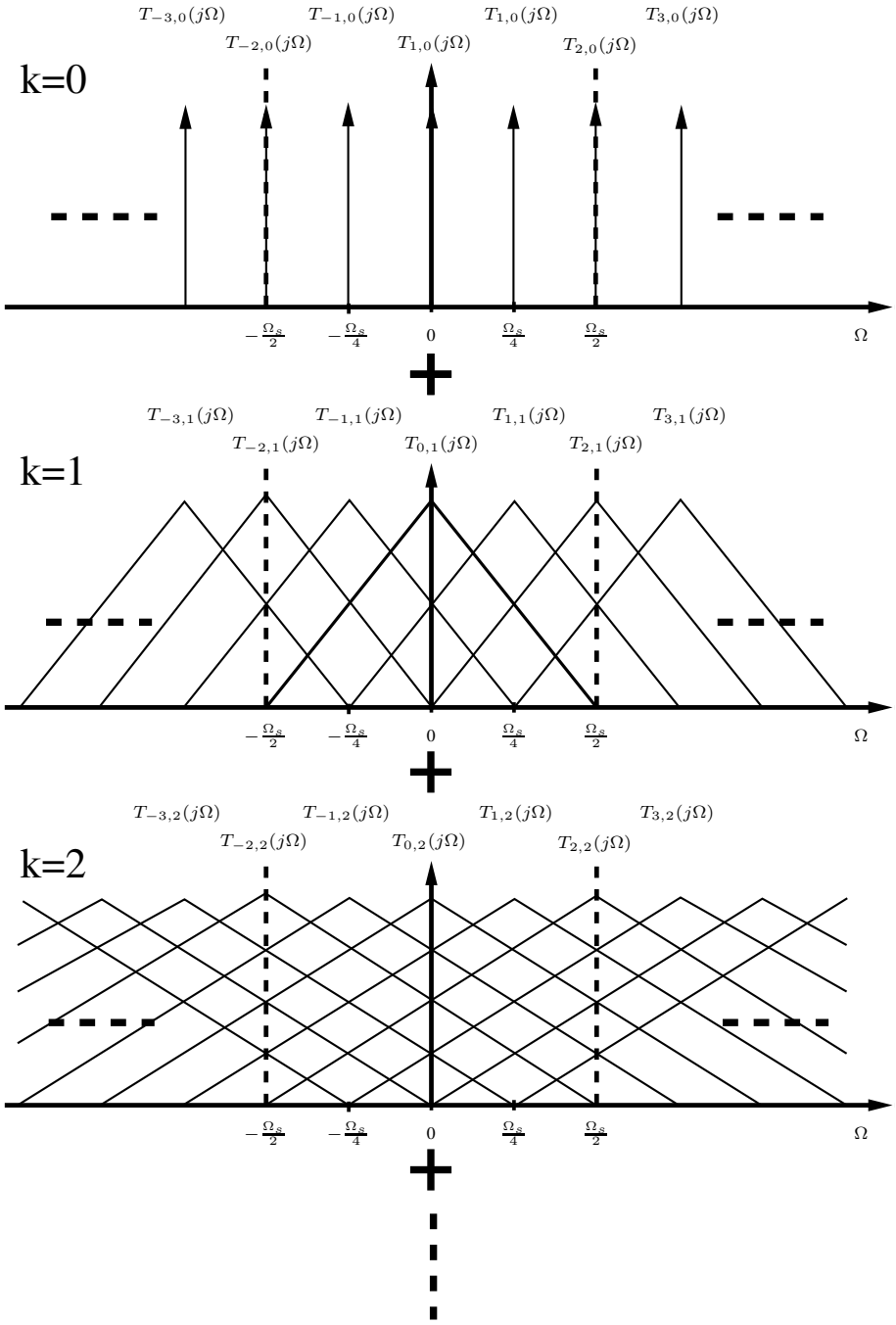

Figure 2.12: We show the K separated spectral components of a nonlinear hybrid filter bank with four channels ($M = 4$). For $k = 0$ we only have Dirac delta impulses and no dependency on the input signal $X_a(j\Omega)$. For $k = 1$ we have the case of an LHFB and for $k > 1$ we obtain the higher order nonlinear cases. The observable output spectrum of an NHFB is the sum of all $k = 0, 1, \ldots, K - 1$ spectral components.

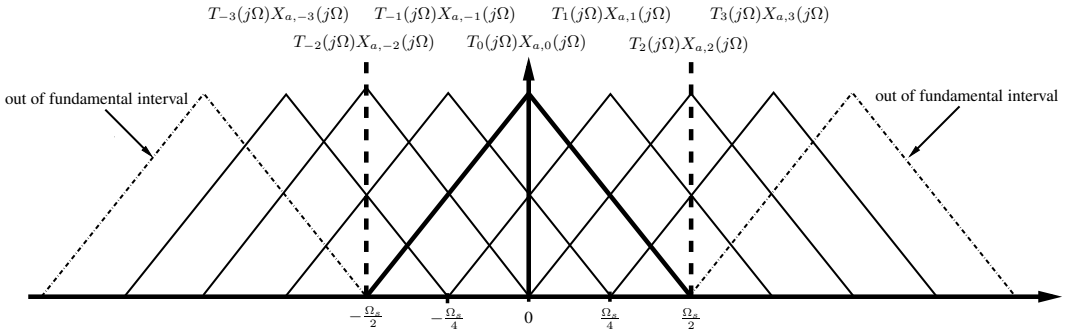

Figure 2.13: Frequency response of a maximally decimated hybrid filter bank with four channels (M=4). We see that we have to include more than $M = 4$ aliased terms to obtain the correct fundamental interval representation out of (2.12) The dash-dotted copies of the input spectrum $X_a(j\Omega)$ are outside the fundamental interval and need not be included.

2.4.1 Fundamental Interval Representation of Linear Hybrid Filter Banks

When we assume that the input signal is bandlimited, i.e. $X_a(j\Omega) = 0$ for $|\Omega| \geq \frac{\Omega_s}{2}$, a DT HFB equals a discrete-time multirate system where it is well known that we have to consider M aliased terms to obtain a complete fundamental interval representation [139, 141]. However, in a CT HFB we have to consider more than M terms because the input signal $X_a\,(j\Omega)$ and the analog filters $H_m(j\Omega)$ are in contrast to the discrete-time synthesis filters $G_m(e^{j\Omega T_s})$ not implicitly periodic with Ω_s. This can be seen by considering Fig. 2.13 and (2.12). The input signal (signal between $|\Omega| \leq \frac{\Omega_s}{2}$ with strong lines) is copied into the frequency spectrum with spacing $\Omega - p\frac{\Omega_s}{M}$. To obtain a complete description of the fundamental interval we need 7 aliased spectral components although we have an HFB with $M = 4$ channels.

In order to obtain the general number of terms we need for a complete fundamental interval representation, we determine the lower and upper bound on p. In principal we can choose an arbitrary frequency band with range Ω_s as fundamental interval, but it is convenient to choose it between

$$-\frac{\Omega_s}{2} < \Omega \leq \frac{\Omega_s}{2}. \tag{2.27}$$

To get the lower bound we have to determine the smallest p for which

$$X_a\left(j\left(-\frac{\Omega_s}{2} - p\frac{\Omega_s}{M}\right)\right) = 0 \tag{2.28}$$

holds, i.e., to find the first p-term which does not contribute to the fundamental interval. For example, in Fig. 2.13 the dash-dotted spectral components are the first components outside the fundamental interval and, therefore, we need not include these corresponding p-terms of (2.12) to obtain a complete fundamental interval representation. Since $X_a\,(j\Omega)$

is bandlimited, (2.28) is fulfilled if

$$\begin{aligned} \frac{\Omega_s}{2} + p\frac{\Omega_s}{M} &\leq -\frac{\Omega_s}{2} \\ p &\leq -M. \end{aligned} \tag{2.29}$$

Thus, the first term contributing to the considered frequency band is

$$p = -(M-1). \tag{2.30}$$

The upper bound can be found by selecting all p for which

$$X_a\left(j\left(\frac{\Omega_s}{2} - p\frac{\Omega_s}{M}\right)\right) = 0 \tag{2.31}$$

holds. Therefore, we can write

$$\begin{aligned} -\frac{\Omega_s}{2} + p\frac{\Omega_s}{M} &\geq \frac{\Omega_s}{2} \\ p &\geq M, \end{aligned} \tag{2.32}$$

and recognize that the last term contributing to the considered frequency band is

$$p = M - 1. \tag{2.33}$$

Thus we can express the fundamental interval spectrum of an LHFB as

$$Y\left(e^{j\Omega T_s}\right) = \frac{1}{T_s}\sum_{p=-(M-1)}^{M-1} T_p\left(j\Omega\right) X_{a,p}\left(j\Omega\right) \quad \text{for } -\frac{\Omega_s}{2} < \Omega \leq \frac{\Omega_s}{2}, \tag{2.34}$$

where

$$T_p(j\Omega) = \frac{1}{M}\sum_{m=0}^{M-1} H_m\left(j\left(\Omega - p\frac{\Omega_s}{M}\right)\right) G_m\left(e^{j\Omega T_s}\right). \tag{2.35}$$

A more comprehensive investigation on the frequency spectrum and the number of aliased terms for the fundamental interval representation can be found in [82, 83].

With the fundamental interval representation we can qualify the reconstruction property of the linear HFB. In Fig. 2.13 we see the original input signal $X_a\left(j\Omega\right)$ weighted by a complex factor $T_0\left(j\Omega\right)$ and additional copies $X_a\left(j\left(\Omega - p\frac{\Omega_s}{M}\right)\right)$ of the input spectrum weighted by the complex factors $T_p\left(j\Omega\right)$. For perfect reconstruction all complex factors $T_p\left(j\Omega\right)$ for $p \neq 0$ must be zero and the factor $T_0\left(j\Omega\right)$ has to be a linear-phase behavior (time delay) with a constant amplitude (scaling). Thus, a linear HFB is a perfect reconstruction system if the output signal fulfills [141]

$$T_p\left(j\Omega\right) = \begin{cases} ce^{j\Omega\Delta t} & \text{for } p = 0 \\ 0 & \text{for } p \neq 0 \end{cases} \quad \text{for } 0 < \Omega < \Omega_s. \tag{2.36}$$

Thus, a perfect reconstruction HFB responds with a time-delayed ($e^{j\Omega\Delta t}$) and scaled version (c) of the input signal.

2.4.2 Fundamental Interval Representation of Nonlinear Hybrid Filter Banks

In our description, (2.23), of an NHFB with static nonlinearities we treat an infinite frequency spectrum. Like for the linear case, it is enough to look at the fundamental interval, since the other parts of the spectrum are simply copies of it. In Fig. 2.12 a typical spectrum of an HFB is shown. We see the fundamental interval, which is the sum of the scaled original spectrum $X_a(j\Omega)$ weighted by some factor $T_{0,1}$ and additional spectral components which arise due to different channel properties. To determine the number of aliased spectral components, i.e., the number of p-terms we have to include in (2.23), we assume that $X_a(j\Omega)$ is bandlimited and seek all p for which

$$\left(X_a\left(j\Omega\right)H_m\left(j\Omega\right)\right)^{(*k)}\Big|_{j\Omega=j\left(-\frac{\Omega_s}{2}-p\frac{\Omega_s}{M}\right)}=0 \tag{2.37}$$

holds. Contrary to the linear case, we have to deal with non-bandlimited signals in the nonlinear case, since each convolution of the input signal and the analysis filters with themselves increases the bandwidth. The bandwidth increases with the order of nonlinearity, i.e., with $k\Omega$ for k convolutions. Nevertheless, for a given order k we can determine the number of terms as for the linear case. Therefore, the lower bound on p for $k \neq 0$ is given by the smallest p which satisfies (2.37), that is

$$\begin{aligned} k\frac{\Omega_s}{2}+p\frac{\Omega_s}{M} &\leq -\frac{\Omega_s}{2} \\ p &\leq -\frac{M}{2}(k+1). \end{aligned} \tag{2.38}$$

Thus, the first term contributing to the considered frequency band is

$$p=-\left(\left\lceil\frac{M}{2}(k+1)\right\rceil-1\right). \tag{2.39}$$

The upper bound on p for $k \neq 0$ can be found by finding all p for which

$$\left(X_a\left(j\Omega\right)H_m\left(j\Omega\right)\right)^{(*k)}\Big|_{j\Omega=j\left(\frac{\Omega_s}{2}-p\frac{\Omega_s}{M}\right)}=0 \tag{2.40}$$

holds. Accordingly, we can write

$$\begin{aligned} -k\frac{\Omega_s}{2}+p\frac{\Omega_s}{M} &\geq \frac{\Omega_s}{2} \\ p &\geq \frac{M}{2}(k+1), \end{aligned} \tag{2.41}$$

and recognize that the last term contributing to the considered frequency band is

$$p=\left\lceil\frac{M}{2}(k+1)\right\rceil-1. \tag{2.42}$$

So far, we have omitted the case $k = 0$ (cf. (2.18)), where we deal with Dirac delta impulses, which have very special properties (cf. C.2). One property is that they concentrate their whole signal power on a single frequency point. This could be a problem if one is exactly located on our considered interval boundary at $\frac{\Omega_s}{2}$, which is the case for an even number of channels M. According to (2.42) we would not include this Dirac delta impulse, although it would be within our fundamental interval. Hence, for $k = 0$ we have to modify the relation operator of (2.42) to

$$\begin{aligned} p\frac{\Omega_s}{M} &> \frac{\Omega_s}{2} \\ p &> \frac{M}{2} \end{aligned} \tag{2.43}$$

and obtain

$$p = \left\lfloor \frac{M}{2} \right\rfloor . \tag{2.44}$$

Consequently, (2.21) becomes for the fundamental interval

$$\begin{aligned} Y(e^{j\Omega T_s}) &= \frac{1}{T_s} \sum_{p=-\left(\left\lceil \frac{M}{2} \right\rceil - 1\right)}^{\left\lfloor \frac{M}{2} \right\rfloor} T_{p,0}(j\Omega) \\ &\quad + \frac{1}{T_s} \sum_{k=1}^{K-1} \sum_{p=-\left(\left\lceil \frac{M}{2}(k+1) \right\rceil - 1\right)}^{\left\lceil \frac{M}{2}(k+1) \right\rceil - 1} T_{p,k}(j\Omega) \qquad \text{for } -\frac{\Omega_s}{2} < \Omega \leq \frac{\Omega_s}{2}, \end{aligned} \tag{2.45}$$

where

$$T_{p,k}(j\Omega) = \frac{1}{M} \sum_{m=0}^{M-1} c_{k,m} \left(X_a\left(j\Omega\right) H_m\left(j\Omega\right) \right)^{(*k)} \Big|_{j\Omega = j\left(\Omega - p\frac{\Omega_s}{M}\right)} G_m\left(e^{j\Omega T_s}\right). \tag{2.46}$$

To obtain an NHFB with perfect reconstruction we require that

$$T_{p,k}(j\Omega) = \begin{cases} c e^{j\Omega\Delta t} X_a(j\Omega) & \text{for } p = 0 \text{ and } k = 1 \\ 0 & \text{for all } p \neq 0 \text{ and all } k \neq 1 \end{cases} \tag{2.47}$$

From (2.47) and (2.45) we realize that we cannot achieve perfect reconstruction if we have a static nonlinearity different from $f_m(x) = x$. To achieve perfect reconstruction, we have to find inverse nonlinear systems [117, 118, 136] to compensate for the static nonlinearities. Nevertheless, since our primary purpose was to model time-interleaved ADCs, we did not investigate methods for finding inverse nonlinear systems in great detail.

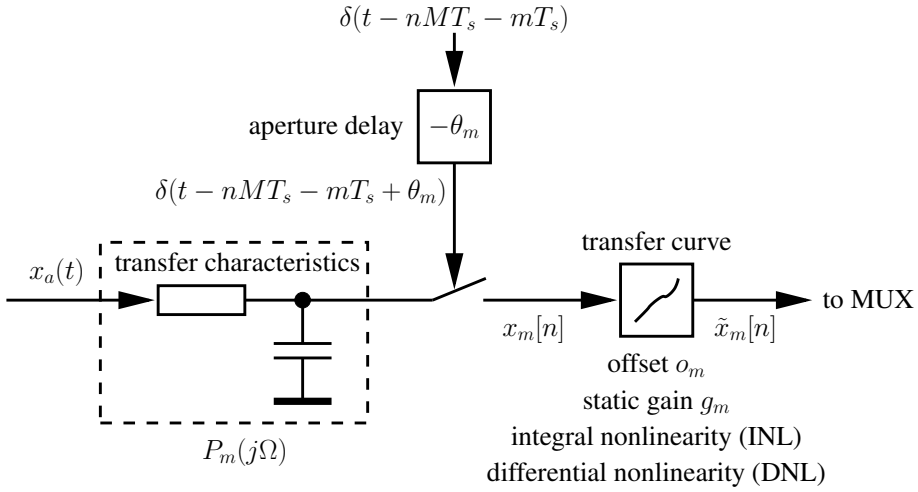

Figure 2.14: A channel model of the mth channel ADC of a time-interleaved ADC.

2.5 Time-Interleaved ADCs Modeled with Nonlinear Hybrid Filter Banks

To model a time-interleaved ADC we use the NHFB presented in Section 2.3. We cover the well-known offset, gain, and timing mismatches. Additionally, we model transfer characteristics mismatches and nonlinearity mismatches. We do not consider quantization noise and jitter effects like clock jitter, which have been extensively treated in [69, 149].

In Fig. 2.14 we see a model of the mth channel ADC of a time-interleaved ADC, which includes transfer characteristics, aperture delay, offset, gain, and nonlinearity mismatches. The transfer characteristics of the channel ADC is determined by the sample-and-hold in hold mode. If we do not consider any nonlinear sample-and-hold effects we can describe the transfer characteristics by the frequency response $P_m(j\Omega)$ of a continuous-time filter [151]. Furthermore, the sample-and-hold has an aperture delay θ_m, where the aperture delay is defined as the time difference between the clock signal triggering a sampling event and the moment the real sample is taken [41]. After the sample-and-hold we see the nonlinear continuous transfer function of the channel ADC, which covers offset o_m, gain g_m, and nonlinearity errors often measured as integral nonlinearity (INL) and differential nonlinearity (DNL) errors [41]. Finally, the output signal of the mth channel ADC goes to a digital multiplexer, which merges the information from all channel ADCs into one output signal (cf. Fig. 1.1).

In Fig. 2.15 we see the corresponding NHFB channel, which takes all parameters of the channel ADC model into account. The continuous-time analysis filters $H_m(j\Omega)$ of the NHFB channel are given by

$$H_m(j\Omega) = P_m(j\Omega)e^{-j\Omega\theta_m}e^{j\Omega T_s m}. \tag{2.48}$$

Beside the transfer characteristics mismatches $P_m(j\Omega)$, we notice two additional terms that

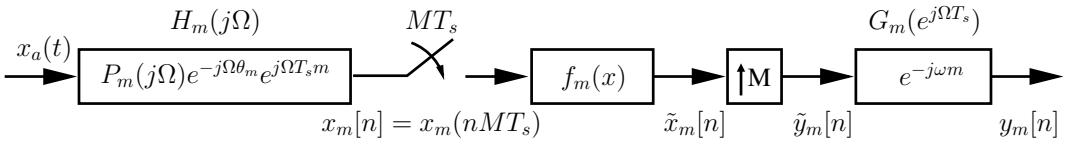

Figure 2.15: The mth channel of an NHFB representing the mth channel ADC shown in Fig. 2.14.

do not appear in the signal path of the channel ADC model (cf. Fig. 2.14). We have moved the aperture delays θ_m and the time shifts $T_s m$, which are due to time interleaving, from the clock path to the signal path. This is an equivalent representation of the system, since a clock signal advance in the clock path means an input signal delay in the signal path and vice versa. Thus, when we move a time shift from one signal path to the other we have to change the signs of that time shift. The nonlinearity of our channel ADC model is described by the power series representing the nonlinearity $f_m(x)$ of the NHFB channel. The discrete-time synthesis filters $G_m(e^{j\Omega T_s})$ are given by

$$G_m(e^{j\Omega T_s}) = e^{-j\omega m}|_{\omega=\Omega T_s} = e^{-j\Omega T_s m}, \tag{2.49}$$

where we model the multiplexing operation by the upsampler and the corresponding time shifts in each channel of the NHFB. Thus, at each time instant n only one channel ADC provides information different from zero, which is equivalent to the multiplexing operation. It should be noticed that ω is the discrete-time angular frequency and Ω is the continuous-time angular frequency.

When we extend the description from the mth channel to an NHFB with M (cf. Fig. 2.8) channels we obtain the input/output relation of a time-interleaved ADC. To this end, we substitute the analysis filters (2.48) and synthesis filters (2.49) in (2.21), which results in

$$Y(e^{j\Omega T_s}) = \frac{1}{T_s}\sum_{k=0}^{K-1}\sum_{p=-\infty}^{\infty} T_{p,k}(j\Omega), \tag{2.50}$$

where

$$\begin{aligned} T_{p,k}\left(j\Omega\right) &= \frac{1}{M}\sum_{m=0}^{M-1} c_{k,m} \\ &\left(X_a\left(j\Omega\right)P_m\left(j\Omega\right)e^{-j\Omega\theta_m}e^{j\Omega T_s m}\right)^{(*k)}\Big|_{j\Omega=j\left(\Omega-p\frac{\Omega_s}{M}\right)} e^{-j\Omega T_s m}. \end{aligned} \tag{2.51}$$

To gain more insight into (2.50) and (2.51) we can reshape their notation. We split the frequency response $P_m(j\Omega)$, which characterizes the transfer characteristics of the mth channel, into magnitude response and phase response, which gives

$$P_m(j\Omega) = A_m(\Omega)e^{j(-\tau_m\Omega+\phi_m(\Omega))}, \tag{2.52}$$

where $e^{-j\tau_m\Omega}$ is the linear part and $^{j\phi_m(\Omega)}$ is the nonlinear part of the phase response.

Consequently, the convolution in (2.51) consists, including the new frequency response representation, of three linear phase terms: $e^{-j\Omega\tau_m}$, $e^{-j\Omega\theta_m}$, and $e^{j\Omega T_s m}$. All these linear phase terms can be factored out of the convolution, which can be seen in the time-domain representation, where we can write $(x(t) * \delta(t-\Delta t))^k = x^k(t-\Delta t) = x^k(t) * \delta(t-\Delta t)$. Thus, we can rewrite (2.50) as

$$Y(e^{j\Omega T_s}) = \frac{1}{T_s}\sum_{k=0}^{K-1}\sum_{p=-\infty}^{\infty} T_{p,k}\left(j\left(\Omega - p\frac{\Omega_s}{M}\right)\right), \tag{2.53}$$

and (2.51) as

$$T_{p,k}\left(j\Omega\right) = \frac{1}{M}\sum_{m=0}^{M-1} c_{k,m}\left(X_a\left(j\Omega\right)A_m(\Omega)e^{j\phi_m(\Omega)}\right)^{(*k)} e^{-j\Omega(\theta_m+\tau_m)}e^{-jpm\frac{2\pi}{M}}. \tag{2.54}$$

From (2.54) we see an inherent property of time-interleaved ADCs. We always have to deal with a discrete Fourier transform (DFT) over all channels from $m = 0$ to $M-1$, where the related exponential factor is $e^{-jpm\frac{2\pi}{M}}$. So the "frequency domain" corresponding to the channel index m is actually the spectral aliasing index p. The DFT is the outcome of the two fundamental operations of a time-interleaved ADC, which are time interleaving and multiplexing of the channels. Thus, the weighting coefficients $T_{p,k}\left(j\Omega\right)$ are the result of a DFT of all considered channel properties and the input signal.

We can further simplify the representation by expressing the aperture delays θ_m as

$$\theta_m = \theta_R + \Delta\theta_m, \tag{2.55}$$

where θ_R is some kind of reference delay, e.g., the average of all aperture delays, and $\Delta\theta_m$ is the deviation of the mth channel from the reference delay. Equivalently, we can rewrite the linear phase response τ_m of the transfer characteristics as

$$\tau_m = \tau_R + \Delta\tau_m, \tag{2.56}$$

where τ_R is some reference linear phase and $\Delta\tau_m$ is the deviation of the mth channel from it. With these definitions, we can introduce the total timing mismatch which we define as

$$\Delta t_m = \Delta\theta_m + \Delta\tau_m. \tag{2.57}$$

and obtain for (2.54)

$$\begin{aligned} T_{p,k}\left(j\Omega\right) &= \frac{1}{M}e^{-j\Omega(\theta_R+\tau_R)}\sum_{m=0}^{M-1} c_{k,m} \\ &\quad \left(X_a\left(j\Omega\right)A_m(\Omega)e^{j\phi_m(\Omega)}\right)^{(*k)} e^{-j\Omega\Delta t_m}e^{-jpm\frac{2\pi}{M}}. \end{aligned} \tag{2.58}$$

This new representation consists of a global linear phase shift $e^{-j\Omega(\theta_R+\tau_R)}$, which is independent from the channel m and the degree of nonlinearity k. A global linear phase shift only delays the output samples of the time-interleaved ADC but does not introduce any distortions, i.e., it fulfills the perfect reconstruction property [141]. Thus, we do not need to consider the global linear phase shift any further and can drop it to simplify the equation.

So far, we have not explicitly introduced the offsets o_m and the gains g_m of the channels. The DC offset is defined as the output signal of an ADC when no input signal is applied [41]. Hence, the coefficients $c_{0,m}$ correspond to the DC offset of the channel ADCs and we can rewrite the coefficients as $c_{0,m} = o_m$. Similarly, we can rewrite the coefficients $c_{1,m}$ as gains g_m. However, the gain of an ADC is not as well defined as its offset, since it depends on the input signal and the measurement method we apply [41] when we deal with nonlinearities. Nevertheless, we can write for (2.53) and (2.58)

$$\begin{aligned} Y(e^{j\Omega T_s}) &= \frac{1}{T_s}\sum_{p=-\infty}^{\infty}\Bigg[\beta_p 2\pi\delta\left(\Omega - p\frac{\Omega_s}{M}\right) \\ &\quad +\alpha_p\left(j\left(\Omega - p\frac{\Omega_s}{M}\right)\right)X_a\left(j\left(\Omega - p\frac{\Omega_s}{M}\right)\right) \\ &\quad +\sum_{k=2}^{K-1}T_{p,k}\left(j\left(\Omega - p\frac{\Omega_s}{M}\right)\right)\Bigg] \end{aligned} \tag{2.59}$$

where

$$\beta_p = \frac{1}{M}\sum_{m=0}^{M-1} o_m e^{-jpm\frac{2\pi}{M}} \tag{2.60}$$

$$\alpha_p(j\Omega) = \frac{1}{M}\sum_{m=0}^{M-1} g_m A_m(\Omega)\, e^{-j\Omega\Delta t_m} e^{j\phi_m(\Omega)} e^{-jpm\frac{2\pi}{M}} \tag{2.61}$$

$$T_{p,k}(j\Omega) = \frac{1}{M}\sum_{m=0}^{M-1} c_{k,m}\left(X_a(j\Omega)\, A_m(\Omega) e^{j\phi_m(\Omega)}\right)^{(*k)} e^{-j\Omega\Delta t_m} e^{-jpm\frac{2\pi}{M}}, \tag{2.62}$$

and explicitly show the important offset mismatches β_p (k=0) and linear mismatches $\alpha_p(j\Omega)$ (k=1). Finally, we have obtained a complete input/output relation for a time-interleaved ADC modeled with an NHFB.

2.6 Conclusion

We have modeled time-interleaved ADCs with nonlinear hybrid filter banks. In our time-interleaved ADC model we utilize for each channel ADC a linear analysis filter $H_m(j\Omega)$, a static nonlinearity $f_m(x)$, and again a linear synthesis filter $G_m(e^{j\Omega T_s})$. This structure represents an LNL cascade model, which can approximate a large class of Volterra systems [138, 158]. With this model, we have introduced a comprehensive input/output relation for time-interleaved ADCs including combined static gain, offset, aperture delay,

transfer characteristics and nonlinearity mismatches. This input/output relation can easily be adapted to a given number of channels and to arbitrary analysis and synthesis filter characteristics. It is an extendable starting point for profound analyses of time-interleaved ADC behavior.

Chapter 3

Channel Mismatch Error Analysis

In this chapter we analyze channel mismatch errors in time-interleaved ADCs. We analyze the different mismatches as well as their combined impact on the system performance. We develop a deterministic and a statistical error model, which enables us to determine the amount of error power different kinds of mismatch errors produce and how they affect the system performance.

In Sec. 3.1 we give an introduction to the error analysis of time-interleaved ADCs. Sec. 3.2 defines and characterizes the most important channel mismatches and in Sec. 3.3 we compare different mismatches and their impact on the time-interleaved ADC performance. Thereby we can simplify the ADC representation we have found in Sec. 2.5, which leads to the combined error analyses carried out in Sec. 3.4 and Sec. 3.5. In Sec. 3.4 we develop a deterministic error model of combined offset, gain, and timing mismatches and in Sec. 3.5 we derive a statistical model of these mismatches.

3.1 Introduction

Each channel ADC in a time-interleaved ADC possesses errors like a single channel ADC. However, component mismatches among the channels of a time-interleaved ADC add further to these errors. Accordingly, they are called mismatch errors. Mismatches are the primary error source in time-interleaved ADCs and significantly reduce the performance of the time-interleaved ADC, i.e., the signal-to-noise-and-distortion ratio (SINAD) and the spurious-free dynamic range (SFDR) [41].

A lot of research has been done on analyzing individual mismatch errors and the first investigations on that subject can be found in [8, 7]. Gain and offset mismatches are extensively treated in [107], where Gaussian distributed mismatches have been assumed for the statistical analysis. The impact of gain and offset mismatches in time-interleaved oversampling converters is studied in [65]. A profound analysis of timing mismatches can be found in [46]. In addition to timing mismatches in time-interleaved ADCs the authors in [50, 121, 116] also investigate the digital-to-analog conversion with a time-interleaved DAC.

In [79] the authors derive probability density functions for Gaussian distributed individual mismatch errors in order to calculate the SINAD. The same authors also found SFDR probability functions for individual mismatch errors in [80]. The merged and extended contents of both papers can be found in [81]. In [164, 35] the main research results for individual mismatch errors are summarized. An analysis of gain and timing mismatches in the context

of hybrid filter banks is given in [84]. In [77, 76] closed-form expressions for calculating the explicit SINAD for most mismatch errors together are given for the case where these errors are known deterministically, but the equations are rather involved and difficult to extend to an arbitrary number of channels. A detailed analysis of channel mismatches can also be found in [25]. In [125] the authors provide a first analysis of nonlinearity mismatches and in [75] some features of nonlinearity mismatches are presented. Timing jitter for single channel systems has been treated in [48, 123, 129, 39, 132, 68, 45].

However, a complete and unified mathematical treatment of combined channel mismatches and timing jitter has been missing. This chapter is an extended version, which includes parts of already published papers [146, 149, 157].

3.2 The Impact of Channel Mismatches

A time-interleaved ADC is a dynamic nonlinear system. To understand how different channel mismatches influence the time-interleaved ADC performance we classify the channel mismatches. We distinguish between linear and nonlinear and between static and dynamic channel mismatches (cf. Sec. C.1).

To illustrate the different mismatch errors in time-interleaved ADCs we use numerical simulations (cf. chapter A). For all simulations we use the same basic time-interleaved ADC configuration. The considered time-interleaved ADC, with a resolution of 8 bits, consists of four channels ($M = 4$), and provides a full scale range (FSR) of 2. The time-interleaved ADC is driven by a zero-mean sinusoidal input signal with an amplitude $A = 0.9$ and a frequency $\Omega_0 = 53\frac{\Omega_s}{4096}$. From this input signal we take 4096 samples with a sampling frequency of $\Omega_s = 2\pi$, i.e., $T_s = 1$, and plot the output spectrum and the first period of the sampled signal. With this time-interleaved ADC configuration and no mismatches we obtain an output spectrum as in Fig. 3.1 and a time plot as in Fig. 3.2.

3.2.1 Static Mismatches

Static mismatches can be divided into gain, offset, and higher nonlinearity mismatches, which will turn out to be the general case of gain and offset mismatches.

3.2.1.1 Gain Mismatches

Gain mismatches appear as soon as the gain errors in each channel of a time-interleaved ADC differ. Gain errors are caused by the non-ideal overall slope of the transfer curve of an ADC, which is depicted in Fig. 3.3. Gain errors should not be confused with gain mismatches, since gain mismatches are errors of the system, which only occur if the channel ADCs have different gain errors. Hence, we can have a time-interleaved ADC with gain errors but without gain mismatches, if all channel ADCs have identical gain errors.

When we only consider gain mismatches g_m, (2.59) reduces to

$$Y(e^{j\Omega T_s}) = \frac{1}{T_s} \sum_{p=-\infty}^{\infty} \alpha_p X_a \left(j \left(\Omega - p\frac{\Omega_s}{M} \right) \right) \tag{3.1}$$

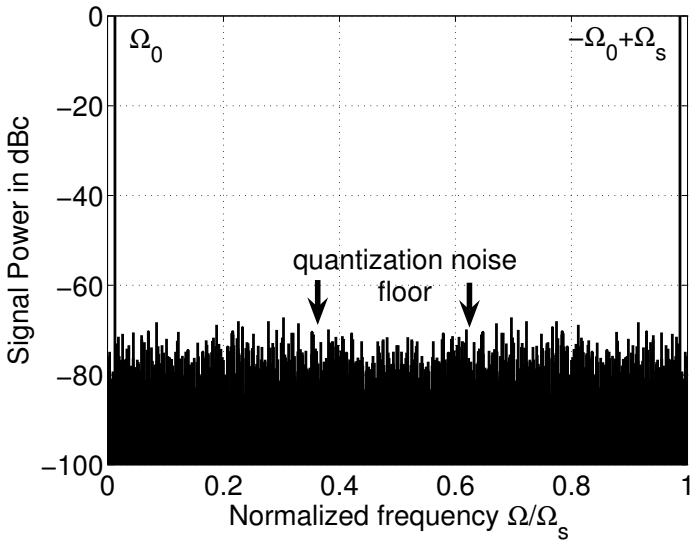

Figure 3.1: Output spectrum of an 8-bit time-interleaved ADC with four channels ($M = 4$) without mismatches and a full scale range (FSR) of two. The time-interleaved ADC is driven by a sinusoidal input signal with amplitude $A = 0.9$ and frequency $\Omega_0 = 53\frac{\Omega_s}{4096}$. The sampling frequency of the time-interleaved ADC is $\Omega_s = 2\pi$ and 4096 samples are used to generate the plot. The signal power is given in dBc, where decibels (below) carrier measures the relative signal strength between main lobe and spurs.

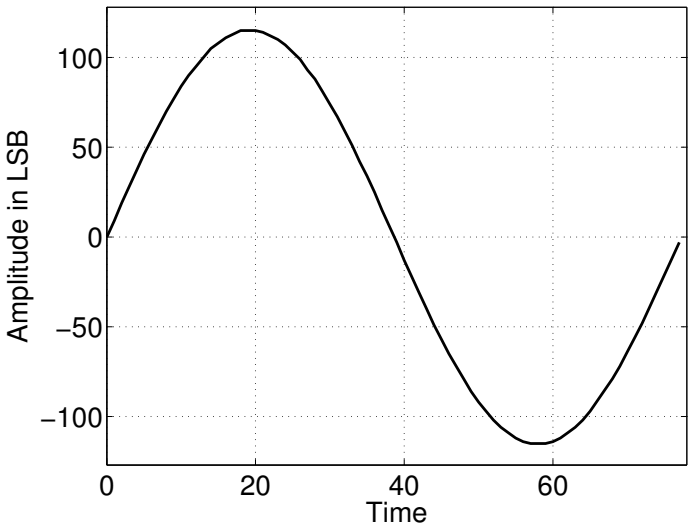

Figure 3.2: Output waveform of a time-interleaved ADC with four channels ($M = 4$) without mismatches. The plot shows 77 samples of the first period of the sampled sinusoidal input signal shown in Fig. 3.1. The samples are interpolated with straight lines for display purposes only.

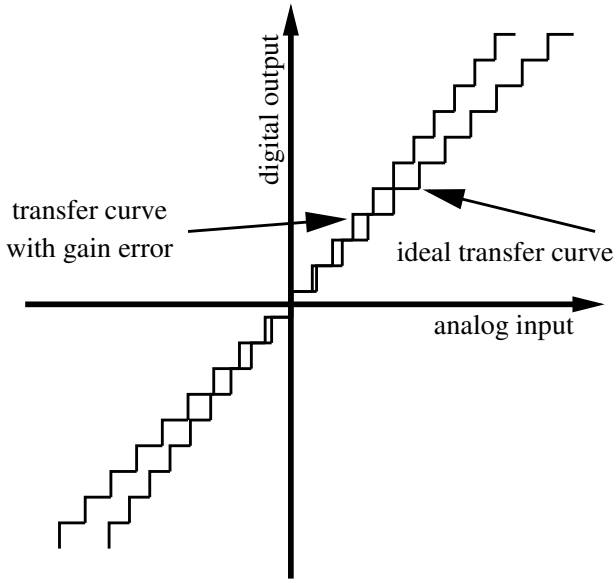

Figure 3.3: ADC with gain error. The slope of the transfer curve with gain errors is different from the ideal transfer curve.

and (2.60) becomes

$$\alpha_p = \frac{1}{M} \sum_{m=0}^{M-1} g_m e^{-jpm\frac{2\pi}{M}}. \tag{3.2}$$

Hence, each aliased spectral component of the output spectrum $X_a\left(j\left(\Omega - p\frac{\Omega_s}{M}\right)\right)$ is weighted by α_p, the DFT of the gains g_m. It should be noticed that even the fundamental spectrum is weighted by α_0, i.e., it is amplified by the average of the gains. The locations of the spectral components are given by $\Omega + p\frac{\Omega_s}{M}$, where Ω is defined for $X_a(\Omega) \neq 0$.

To illustrate the effect of gain mismatches we use the time-interleaved ADC configuration of Fig. 3.1 including gain mismatches. In Fig. 3.4 we see the output spectrum of the simulated time-interleaved ADC. To further investigate the shown output spectrum we insert the Fourier transform of a sinusoidal input signal $X_a(j\Omega) = -\frac{A\pi}{j}\left[\delta(\Omega - \Omega_0) - \delta(\Omega + \Omega_0)\right]$ in (3.1), which results in

$$Y(e^{j\Omega T_s}) = \frac{1}{T_s} \sum_{p=-\infty}^{\infty} \alpha_p \frac{A}{2j} \left[2\pi\delta\left(\Omega - \Omega_0 - p\frac{\Omega_s}{M}\right) - 2\pi\delta\left(\Omega + \Omega_0 - p\frac{\Omega_s}{M}\right)\right], \tag{3.3}$$

where α_p is given in (3.2). From Fig. 3.4 and (3.3) we recognize that for a sinusoidal input signal we obtain $2M$ spectral peaks in the output spectrum, i.e., 8 peaks for $M = 4$, if the gains among the channels do not match. Two peaks are the input signal at $\pm\Omega_0$ and all other peaks are aliasing distortions at $\pm\Omega_0 + p\frac{\Omega_s}{M}$. Since the gains do not depend on the frequency, the weighting factor α_p and the error power introduced by the gain mismatches do not depend on the input signal frequency.

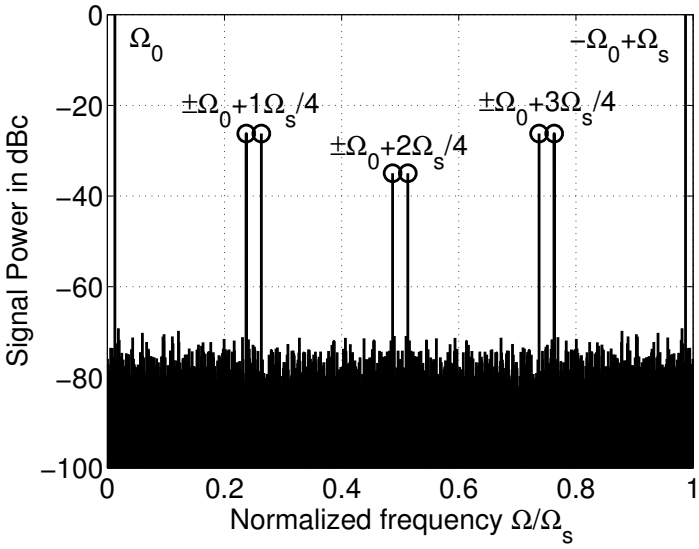

Figure 3.4: Output spectrum of a time-interleaved ADC with four channels ($M = 4$) and gain mismatches. The gains of the channels are $\boldsymbol{g}$=[1.06 1.04 0.88 0.97]. All other time-interleaved ADC features are identical to the ones in Fig. 3.1.

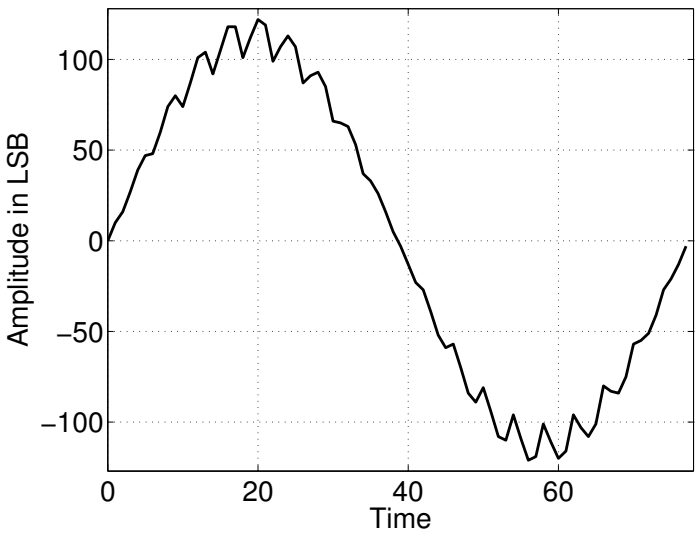

Figure 3.5: Output waveform of a time-interleaved ADC with four channels and gain mismatches. The plot shows the first period of the sampled signal shown in Fig. 3.4.

In Fig. 3.5 we see the impact of gain mismatches in the time domain. The absolute output error, $y(t) - x_a(t)$, becomes amplitude dependent; hence, we see larger oscillations for higher amplitudes and hardly no oscillations for smaller amplitudes. In contrast, the relative error $\frac{y(t)-x_a(t)}{x_a(t)}$ is constant. In the time-domain we can write the output signal with gain mismatches as

$$y(t) = \sum_{n=-\infty}^{\infty} g_{\langle n \rangle_M} x_a(t)\delta(t - nT_s), \tag{3.4}$$

where the operator $\langle n \rangle_M$ means that all indices n are taken modulo M and $\delta(t)$ is the Dirac delta impulse (cf. Sec. C.4). Consequently, we get a sampled amplitude modulated signal, where the gains $\langle n \rangle_M$ produce M carrier frequencies [0, 1 $\frac{\Omega_s}{M}$, 2 $\frac{\Omega_s}{M}$, ..., $M - 1$ $\frac{\Omega_s}{M}$] in the fundamental interval, which are modulated by the input signal $x_a(t)$. To obtain the original input signal $x_a(t)$ out from (3.4) we have to use an ideal reconstruction filter [114, 99, 98], which eliminates all frequency components outside the fundamental interval.

3.2.1.2 Offset Mismatches

Offset mismatches are caused by channel ADCs with different offset errors. A transfer curve with an offset error is shown in Fig. 3.6. The curve is shifted from its origin; hence, it produces an output without an input signal and returns a digital zero for a non-zero analog input signal. Analog components in ADCs like amplifiers and comparators have an inherent offset voltage and an offset current, which can cause such offset errors [142].

If an ADC is used to convert signals without any low-frequency components, the impact of an offset error on the performance of the ADC is not significant, since in the frequency spectrum the offset error power is at frequency $\Omega = 0$ and can easily be eliminated. Only the input dynamic, i.e., the maximal allowed input signal level, is reduced. In contrast, mismatches of offset errors cause a significant performance loss in any case.

When we only consider offset mismatches o_m, (2.59) can be written as

$$Y(e^{j\Omega T_s}) = \frac{1}{T_s} \sum_{p=-\infty}^{\infty} \left[\beta_p 2\pi\delta\left(\Omega - p\frac{\Omega_s}{M}\right) + \alpha_p X_a\left(j\left(\Omega - p\frac{\Omega_s}{M}\right)\right)\right] \tag{3.5}$$

where

$$\begin{aligned} \beta_p &= \frac{1}{M}\sum_{m=0}^{M-1} o_m e^{-jpm\frac{2\pi}{M}} \\ \alpha_p &= \frac{1}{M}\sum_{m=0}^{M-1} e^{-jpm\frac{2\pi}{M}} \\ &= \delta\left[\langle p \rangle_M\right], \end{aligned} \tag{3.6}$$

where $\delta\left[\langle p \rangle_M\right]$ is the discrete-time impulse (cf. Sec. C.2). According to (3.5), the output spectrum $Y(e^{j\Omega T_s})$ consists of the input signal spectrum $X_a\left(j\left(\Omega - p\frac{\Omega_s}{M}\right)\right)$ and M additional spectral spurs $2\pi\delta\left(\Omega - p\frac{\Omega_s}{M}\right)$. The spur at frequency $\Omega = 0$ is the average offset of

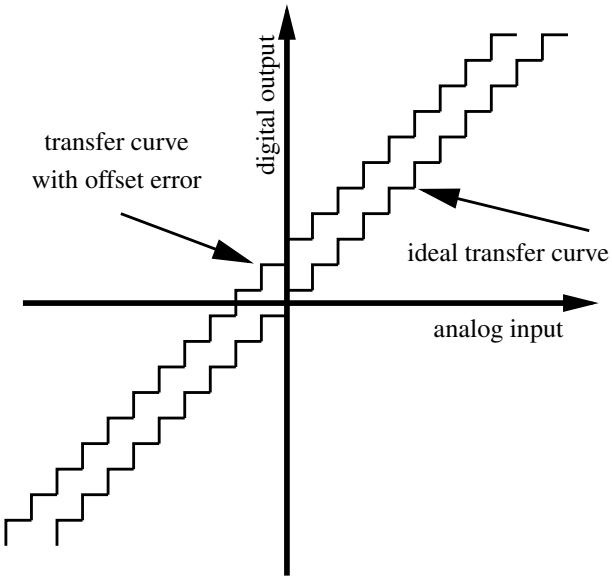

Figure 3.6: ADC with offset error. The transfer curve with offset is a shifted version of the ideal transfer curve.

all channels. The other spurs, which are located at $p\frac{\Omega_s}{M}$, are given by the DFT of the offsets. It should be noticed that the spurs are completely determined by the channel ADC offsets o_m and do not depend on the input signal $X_a(\Omega)$.

In Fig. 3.7 we see the output spectrum of a simulated time-interleaved ADC ($M = 4$) with offset mismatches, where we have used again the same time-interleaved ADC configuration as in Fig. 3.1. The shown output spectrum can be described by inserting the Fourier transform of a sinusoidal input signal $X_a(j\Omega) = -\frac{A\pi}{j}\left[\delta(\Omega - \Omega_0) - \delta(\Omega + \Omega_0)\right]$ in (3.5), which results in

$$\begin{aligned} Y(e^{j\Omega T_s}) &= \frac{1}{T_s}\sum_{p=-\infty}^{\infty}\left[\beta_p 2\pi\delta\left(\Omega - p\frac{\Omega_s}{M}\right) + \alpha_p\frac{A}{2j}2\pi\delta\left(\Omega - \Omega_0 - p\frac{\Omega_s}{M}\right) - \right. \\ &\quad \left. - \alpha_p\frac{A}{2j}2\pi\delta\left(\Omega + \Omega_0 - p\frac{\Omega_s}{M}\right)\right], \end{aligned} \tag{3.7}$$

where β_p and α_p are given in (3.6). Beside the sinusoidal input signal at Ω_0 and $-\Omega_0 + \Omega_s$ we can see in Fig. 3.7 M additional unwanted spectral lines at $p\frac{\Omega_s}{M}$ caused by offset mismatches. This agrees with (3.7).

In Fig. 3.8 we see the impact of offset mismatches in the time domain. As the offset mismatch does not depend on the input signal, the error pattern does not change with the amplitude as for the gain mismatch. In the time-domain we can express the output signal of a time-interleaved ADC with offset mismatches as

$$y(t) = \sum_{n=-\infty}^{\infty}\left[o_{\langle n\rangle_M} + x_a(t)\right]\delta(t - nT_s). \tag{3.8}$$

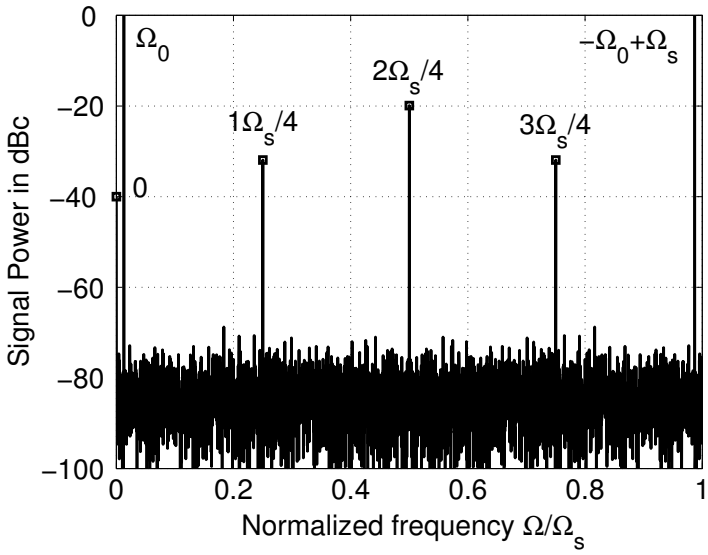

Figure 3.7: Output spectrum of a time-interleaved ADC with four channels ($M = 4$) and offset mismatches. The offsets of the channels are $\boldsymbol{o}$=[0.03 -0.03 0.052 -0.07]. All other time-interleaved ADC features are identical to the ones in Fig. 3.1.

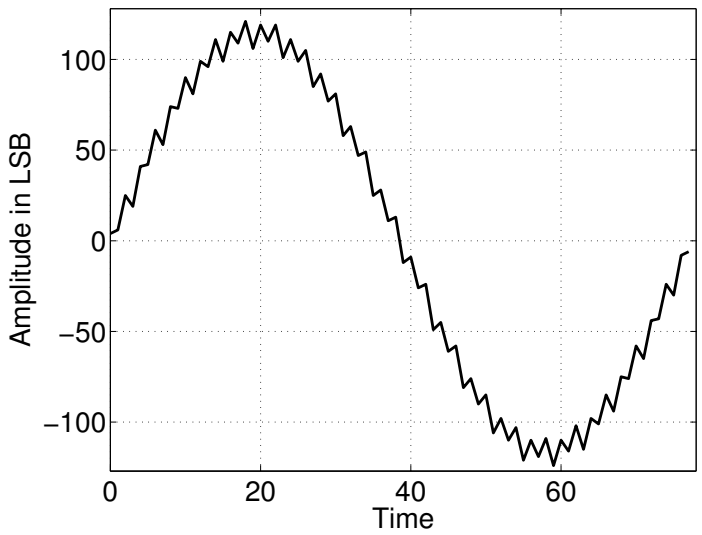

Figure 3.8: Output waveform of a time-interleaved ADC with four channels and offset mismatches. The plot shows the first period of the sampled signal shown in Fig. 3.7.

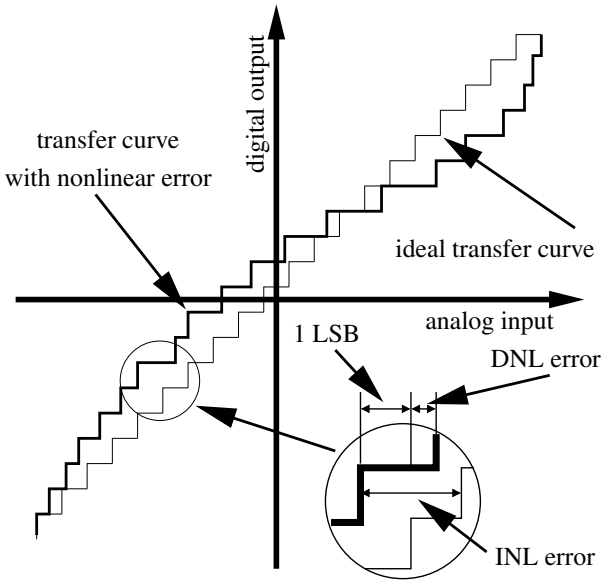

Figure 3.9: ADC with integral nonlinearity (INL) and differential nonlinearity (DNL) errors. INL errors are the deviations of the real transfer curve from the ideal transfer curve at each code transition. In contrast, the DNL error is the deviation of the real transfer curve from the ideal LSB step at each code transition. Therefore, the INL error is the integral of the DNL error.

Thus the output signal consists of the sampled input signal $x_a(t)$ and a sampled amplitude modulated signal with M carrier frequencies [0, 1 $\frac{\Omega_s}{M}$, 2 $\frac{\Omega_s}{M}$, ..., $M-1$ $\frac{\Omega_s}{M}$] in the fundamental interval, which are produced by the offsets $o_{\langle n \rangle_M}$. The difference to the gain mismatch is the modulation signal that constantly equals 1. Hence, we only see the carrier frequencies in the output spectrum and the original input signal.

3.2.1.3 Nonlinearity Mismatches

Nonlinearity errors occur when the transfer curve of the ADC, neglecting the quantization, is not a straight 45° line. To characterize the linearity of an ADC the integral nonlinearity (INL) and the differential nonlinearity (DNL) are measured, which is illustrated in Fig. 3.9. The INL error is the deviation from the ideal transfer curve, whereas the DNL error is the deviation from the ideal quantization step [142]. For sinusoidal input signals, INL errors produce visible harmonic distortions in the output spectrum. In contrast, distortions caused by DNL errors only, i.e., without accumulating to large INL errors, are distributed over many different frequencies in the spectrum, wherefore DNL distortions are similar to noise. When the nonlinearities in a time-interleaved ADC do not match we are confronted with nonlinearity mismatches. Hence, we usually have nonlinearity errors and nonlinearity mismatches in a time-interleaved ADC.

We have modeled the nonlinearities in time-interleaved ADCs by the means of polynomials (cf. Sec. 2.3.1). With this approach we can model INL like nonlinearity errors, but

we can neither represent quantization effects nor the quantization related DNL measure. Statistical and deterministic discussions of quantization errors can be found in [5, 6, 162].

When we only consider nonlinearity mismatches, (2.59) and (2.60) can be written as

$$\begin{aligned} Y(e^{j\Omega T_s}) &= \frac{1}{T_s}\sum_{p=-\infty}^{\infty}\left[\beta_p 2\pi\delta\left(\Omega - p\frac{\Omega_s}{M}\right) + \alpha_p X_a\left(j\left(\Omega - p\frac{\Omega_s}{M}\right)\right)\right. \\ &\quad \left. + \sum_{k=2}^{K-1} T_{p,k} X_a^{(*k)}\left(j\left(\Omega - p\frac{\Omega_s}{M}\right)\right)\right] \end{aligned} \tag{3.9}$$

where

$$\beta_p = \frac{1}{M}\sum_{m=0}^{M-1} o_m e^{-jpm\frac{2\pi}{M}} \tag{3.10}$$

$$\alpha_p = \frac{1}{M}\sum_{m=0}^{M-1} g_m e^{-jpm\frac{2\pi}{M}} \tag{3.11}$$

$$T_{p,k} = \frac{1}{M}\sum_{m=0}^{M-1} c_{k,m} e^{-jpm\frac{2\pi}{M}}. \tag{3.12}$$

We see that the gains g_m and the offsets o_m are only special cases of the coefficients $T_{p,k}$ describing the higher-order nonlinearities. Consequently, the higher-order nonlinearity terms introduce additional spectral components given by $k\Omega - p\frac{\Omega_s}{M}$. Thus, because the higher-order nonlinearities cause a convolution of the input signal with itself, the bandwidth increases and we get $KM - 1$ aliased spectral components instead of $M - 1$ when we only have gain mismatches.

To show this effect we have simulated a time-interleaved ADC with nonlinearity errors and mismatches, which is shown in Fig. 3.10. Again we have used the basic time-interleaved ADC configuration of Fig. 3.1. The output spectrum in Fig. 3.10 can be described by substituting a sinusoidal input signal in (3.9). A representation for the k-times convolved sinusoidal input signal, which is the kth power of the input signal in the time domain, can be found by using the relation

$$\sin(\Omega_0 t) = \frac{1}{2j}\left(e^{j\Omega_0 t} - e^{-j\Omega_0 t}\right) \tag{3.13}$$

and the binomial theorem

$$(x+a)^k = \sum_{n=0}^{k}\binom{k}{n} x^n a^{k-n}. \tag{3.14}$$

Therefore, we can write the kth power of the input signal $x_a(t)$ as

$$x_a^k(t) = \left(\frac{A}{2j}\right)^k \sum_{n=0}^{k}\binom{k}{n}(-1)^{k-n} e^{j\Omega_0(2n-k)t} \tag{3.15}$$

and obtain for the Fourier transform

$$X_a^{(*k)}(j\Omega) = \left(\frac{A}{2j}j\right)^k \sum_{n=0}^{k} \binom{k}{n} (-1)^{k-n} 2\pi\delta\left(\Omega - \Omega_0 (2n-k)\right). \tag{3.16}$$

Substituting (3.16) in (3.9) leads to

$$\begin{aligned} Y(e^{j\Omega T_s}) \;=\; & \frac{1}{T_s} \sum_{p=-\infty}^{\infty} \Bigg[\beta_p 2\pi\delta\left(\Omega - p\frac{\Omega_s}{M}\right) \\ & + \frac{A}{2j}\alpha_p \left[2\pi\delta\left(\Omega - \Omega_0 - p\frac{\Omega_s}{M}\right) - 2\pi\delta\left(\Omega + \Omega_0 - p\frac{\Omega_s}{M}\right)\right] \\ & + \sum_{k=2}^{K-1} \frac{T_{p,k}}{k!} \left(\frac{A}{2j}\right)^k \\ & \sum_{n=0}^{k} \binom{k}{n} (-1)^{k-n} 2\pi\delta\left(\Omega - \Omega_0 (2n-k) - p\frac{\Omega_s}{M}\right)\Bigg]. \end{aligned} \tag{3.17}$$

When we only consider the coefficients β_p and $\alpha_p(j\Omega)$ and their corresponding tones in the spectrum, we obtain the relation for the well-analyzed offset and gain mismatches. As already discussed in Sec. 3.2.1.1 and Sec. 3.2.1.2 the offset mismatches are located at $p\frac{\Omega_s}{M}$ and the gain mismatches are given by $\pm\Omega_0 + p\frac{\Omega_s}{M}$. We notice that both mismatches have different locations for all p as long as $\Omega_0 \neq 0$.

The picture changes when we also consider the higher-order nonlinearity mismatches ($k > 1$). As soon as the coefficients $c_{k,m}$ are different from zero and mismatch, we get tones at $\pm k\Omega_0 + p\frac{\Omega_s}{M}$, which agree very well with offset ($k = 0$) and gain ($k = 1$) mismatches. However, because of the convolution in (3.16), we get, for a given k not only tones at $\pm k\Omega_0 + p\frac{\Omega_s}{M}$ but also additional tones at

$$\pm l\Omega_0 + p\frac{\Omega_s}{M} \begin{cases} \text{where } l = 0, 2, 4, \ldots, k-2 \text{ for even k} \\ \text{where } l = 1, 3, 5, \ldots, k-2 \text{ for odd k,} \end{cases} \tag{3.18}$$

where $l = (2n - k)$. We see that higher-order nonlinearities possibly contribute to the same frequency locations as lower order nonlinearities do. Thus, contrary to cases where we only consider offset and gain mismatches, we lose the exact correspondence between the weighting coefficients β_p, α_p, and $T_{p,k}$ and the amount of mismatch power at a particular frequency location for sinusoidal input signals [153]. This can influence the accuracy of channel mismatch identification algorithms.

In Fig. 3.11 we see the impact of nonlinearity mismatches in the time domain. As the nonlinearity mismatch depends on the amplitude of the input signal, the error of the output signal changes with the input signal. Contrary to gain mismatches, both, absolute and relative errors, change with the input signal amplitude. In the time-domain we can

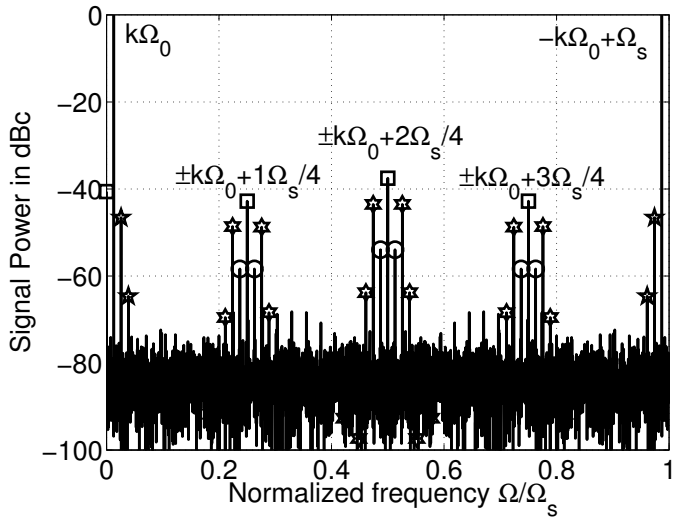

Figure 3.10: Output spectrum of a time-interleaved ADC with four channels ($M = 4$) and nonlinearity mismatches (marked as stars). The power series coefficients of the channels are $\boldsymbol{c_0}$=[0 1 0.01 0.008], $\boldsymbol{c_1}$=[0 1 -0.01 -0.004], $\boldsymbol{c_2}$=[0 1 0.04 0.004], $\boldsymbol{c_3}$=[0 1 0.0011 0.003]. All other time-interleaved ADC features are identical to the ones in Fig. 3.1. Although we have not specified any offset ($c_{0,m} = 0$ for $m = 0, \ldots, M-1$) or gain mismatches ($c_{1,m} = 1$ for $m = 0, \ldots, M-1$), we have gain (circles) and offset (squares) like spurs in the output. This is because the power series representations of the transfer curves are not unique [74, 136].

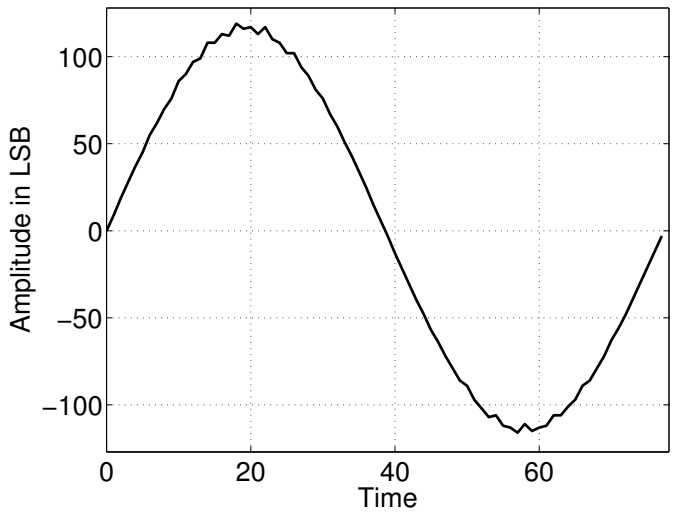

Figure 3.11: Output waveform of a time-interleaved ADC with four channels and nonlinearity mismatches. The plot shows the first period of the sampled signal shown in Fig. 3.10.

express the output signal of a time-interleaved ADC with nonlinearity mismatches as

$$y(t) = \sum_{n=-\infty}^{\infty} f_{\langle n \rangle_M}(x_a(t))\,\delta(t - nT_s), \tag{3.19}$$

where the operator $\langle n \rangle_M$ means that all indices n are taken modulo M. With our polynomial approach discussed in Sec. 2.3.1 we can further express (3.19) as

$$y(t) = \sum_{n=-\infty}^{\infty} \sum_{k=0}^{K-1} c_{k,\langle n \rangle_M} x_a^k(t)\delta(t - nT_s). \tag{3.20}$$

According to the gain and the offset case, we get a sampled modulated signal, where we have MK carrier frequencies all located at [0, 1 $\frac{\Omega_s}{M}$, 2 $\frac{\Omega_s}{M}$, ..., $M-1$ $\frac{\Omega_s}{M}$] in the fundamental interval and K modulation signals [1, $x_a(t)$, $x_a^2(t)$, ..., $x_a^{K-1}(t)$]. Again we see that offset and gain mismatches are special cases of nonlinearity mismatches.

To summarize, the output spectrum of a time-interleaved ADC with nonlinearity mismatches depends on the channel parameters o_m, g_m, and $c_{k,m}$ but also on the input signal, and for sinusoidal input signals we lose the exact correspondence between the error power at a particular frequency location and the weighting factors β_p, α_p, and $T_{p,k}$.

3.2.2 Dynamic Mismatches

In ADCs most dynamic errors are caused by the sample and hold (S/H) architecture [16, 37, 160, 142]. Dynamic errors are errors which depend on temporary memory effects and whose behavior changes with the frequency. When this errors differ among the channels of a time-interleaved ADC we obtain dynamic mismatches. In this section we consider dynamic linear mismatches, i.e., frequency response mismatches.

We can distinguish between magnitude response and phase response mismatches. Although both kinds of mismatches are connected, they have a different influence on the time-interleaved ADC performance. Thus, we will first discuss the more important phase mismatches and afterwards the magnitude mismatches.

3.2.2.1 Phase Response Mismatches

Phase response mismatches depend on the input frequency. We distinguish between linear-phase mismatches, which linearly depend on the frequency and nonlinear-phase mismatches, which nonlinearly depend on the frequency. A linear phase results in a constant time-shift in the time domain, whereas a nonlinear phase results in frequency dependent time shifts in the time domain.

The influence of linear-phase mismatches on the time-interleaved ADC performance increases with the frequency but this does not need to be true for nonlinear-phase mismatches. Thus, the mismatches among the phases are the reason that the time-interleaved ADC produces error power. However, since typically ADCs have linear-phase transfer characteristics the impact of linear-phase mismatches is much more significant than the one of nonlinear-phase mismatches and the term linear-phase mismatch or timing mismatch roughly characterizes the system equally well.

Linear-Phase Response Mismatches When we consider timing mismatches, we see from our time-interleaved ADC model and its representation (2.59) that two error sources contribute to them: aperture-delay mismatches $\Delta\theta_m$ and the linear parts $\Delta\tau_m$ of the phase-response mismatches. By only considering the output signal we cannot distinguish between these two different mismatch error sources contributing to the timing mismatch Δt_m. Due to this and an often inadequate modeling of time-interleaved ADCs, the terms aperture delay and timing mismatch (also known as clock skew mismatch) have been used synonymously in the past. In Fig. 3.12 the difference between aperture-delay mismatches and linear-phase input mismatches is illustrated for the mth channel ADC. An aperture delay mismatch causes time shifts of the clock signal. Therefore, the sample is taken at the wrong sampling instant and we obtain a value, which does not correspond to the basic assumption of uniform sampling. In contrast, the linear-phase input mismatches shift the input signal itself. Thus, even when we take the sample at the ideal sampling instant we obtain the wrong sampling value. Typically, we have a combination of both effects. The time shift of the input signal and the time shift of the clock signal merge into one time shift, which results in the timing mismatch. For the example shown in Fig. 3.12 these two time shifts add up but they can also cancel each other. This effect can be exploited for a very power efficient timing mismatch compensation method [151], which is presented in Sec. 5.3.

Nevertheless, since both effects add up we can also describe timing mismatches as in Fig. 3.13.

When we only consider timing mismatches, (2.59) becomes

$$Y(e^{j\Omega T_s}) = \frac{1}{T_s}\sum_{p=-\infty}^{\infty} \alpha_p\left(j\left(\Omega - p\frac{\Omega_s}{M}\right)\right) X_a\left(j\left(\Omega - p\frac{\Omega_s}{M}\right)\right) \tag{3.21}$$

where

$$\alpha_p(j\Omega) = \frac{1}{M}\sum_{m=0}^{M-1} e^{-j\Omega\Delta t_m} e^{-jpm\frac{2\pi}{M}}. \tag{3.22}$$

The spectral components of timing mismatches are located at $\Omega + p\frac{\Omega_s}{M}$. Hence, they contribute to the same frequency locations as gain mismatches do (cf. Sec. 3.2.1.1).

The impact of timing mismatches is shown in Fig. 3.14, where we have simulated a time-interleaved ADC with timing mismatches. All other time-interleaved ADC features are identical to the ones in Fig. 3.1. As expected, the output spectrum of the simulated time-interleaved ADC shows additional tones at $\pm\Omega_0 + p\frac{\Omega_s}{M}$. We can describe the output spectrum by applying the Fourier transform of the sinusoidal input signal $X_a(j\Omega) = -\frac{A\pi}{j}\left[\delta\left(\Omega - \Omega_0\right) - \delta\left(\Omega + \Omega_0\right)\right]$ in (3.21) and obtain

$$\begin{aligned} Y(e^{j\Omega T_s}) \;=\; & \frac{1}{T_s}\sum_{p=-\infty}^{\infty} \frac{A}{2j}\left[\alpha_p\left(j\left(\Omega - \Omega_0 - p\frac{\Omega_s}{M}\right)\right) 2\pi\delta\left(\Omega - \Omega_0 - p\frac{\Omega_s}{M}\right)\right. \\ & \left. -\alpha_p\left(j\left(\Omega + \Omega_0 - p\frac{\Omega_s}{M}\right)\right) 2\pi\delta\left(\Omega + \Omega_0 - p\frac{\Omega_s}{M}\right)\right] \end{aligned} \tag{3.23}$$

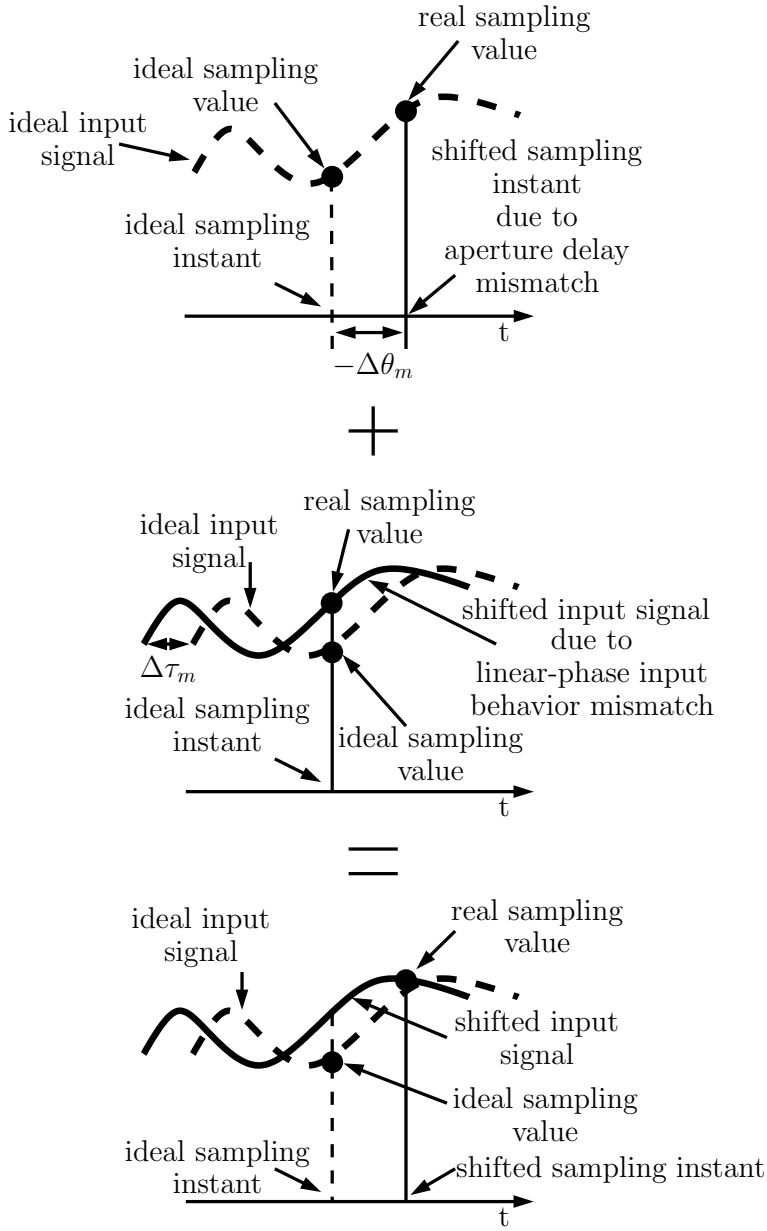

Figure 3.12: The pictures illustrate the two contributions to timing mismatches for the mth channel ADC. The first shows the aperture delay mismatch, where the sample is taken at the wrong sampling instant. The second picture shows the linear-phase mismatch of the transfer characteristics. We see that the input signal itself is time-shifted and we obtain the wrong sampling value although we have taken the sample at the ideal sampling instant. The final picture shows the result of both time shifts, which is the timing mismatch.

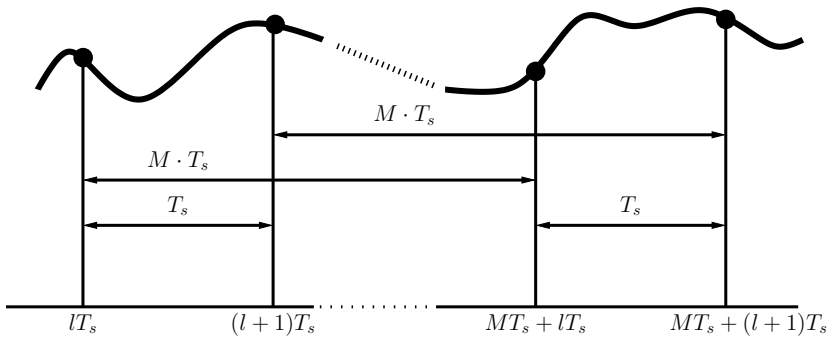

(a) Sampling with an ideal time-interleaved ADC.

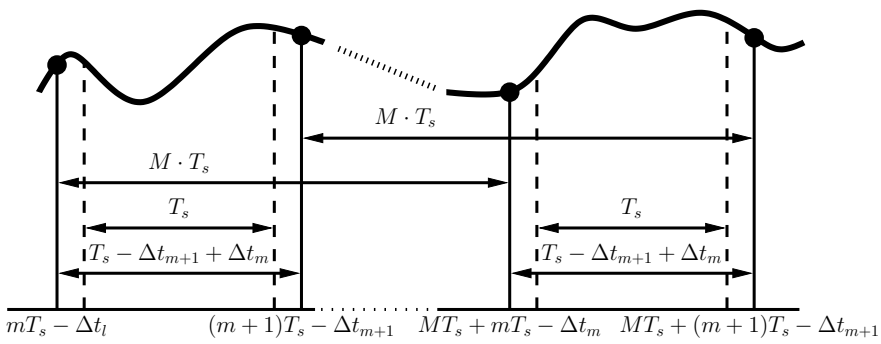

(b) Sampling with a time-interleaved ADC with timing-mismatches. The dashed line indicates the ideal sampling.

Figure 3.13: The timing mismatch is the deterministic deviation between the ideal sampling period [Fig. 3.13(a)] and the real sampling period [Fig. 3.13(b)]. It only affects the sampling process if several channel ADCs are combined.

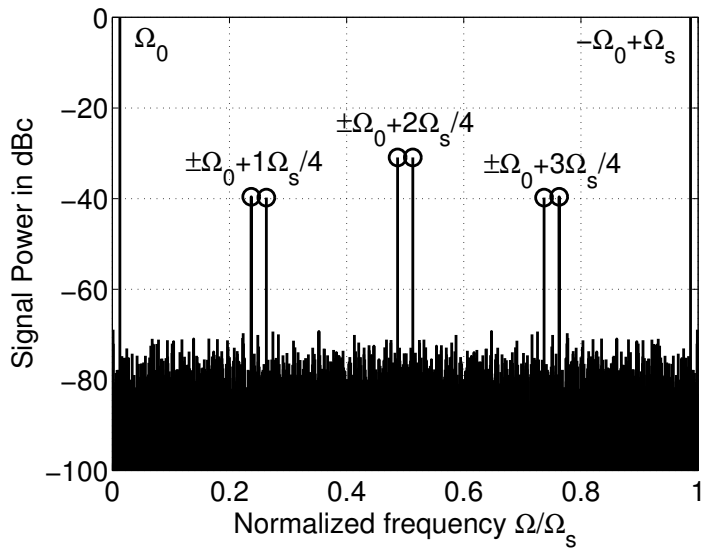

Figure 3.14: Output spectrum of a time-interleaved ADC with four channels ($M = 4$) and timing mismatches. The timing mismatches of the channels are $\boldsymbol{\Delta t}$=[0.5 -0.5 0.4 0.0]T_s. The aliased spurs that are due to timing mismatches are at the same frequency locations as for the gain mismatch (cf. Fig. 3.4).

where

$$\alpha_p(j\Omega) = \frac{1}{M}\sum_{m=0}^{M-1} e^{-j\Omega\Delta t_m} e^{-jpm\frac{2\pi}{M}}. \tag{3.24}$$

The peaks in the spectrum are weighted by the coefficients $\alpha_p(j\Omega)$, where the $\alpha_p(j\Omega)$ are the DFT of the timing mismatches $e^{-j\Omega\Delta t_m}$.

In Fig. 3.15 we see the output signal in the time domain. For slowly varying amplitudes the timing-mismatch dependent oscillations are smaller than for fast amplitude changes like in the zero crossing regions. For typical timing mismatches, these differences are not visible for such a low input frequency, but for our simulation we have used huge timing mismatches to clearly present the effect. We can express the output signal of a time-interleaved ADC with timing mismatches in the time-domain as

$$y(t) = \sum_{n=-\infty}^{\infty} x(t - \Delta t_{<n>_M})\delta(t - nT_s). \tag{3.25}$$

Thus, timing mismatches produce a phase modulation of input signals $x_a(t)$, for which the continuous Fourier transform [99] exists, where we circularly switch among M different phases [76].

Nonlinear-Phase Response Mismatches Most of the above discussion is true for nonlinear-phase mismatches as well; moreover, as long as we only consider sinusoidal in-

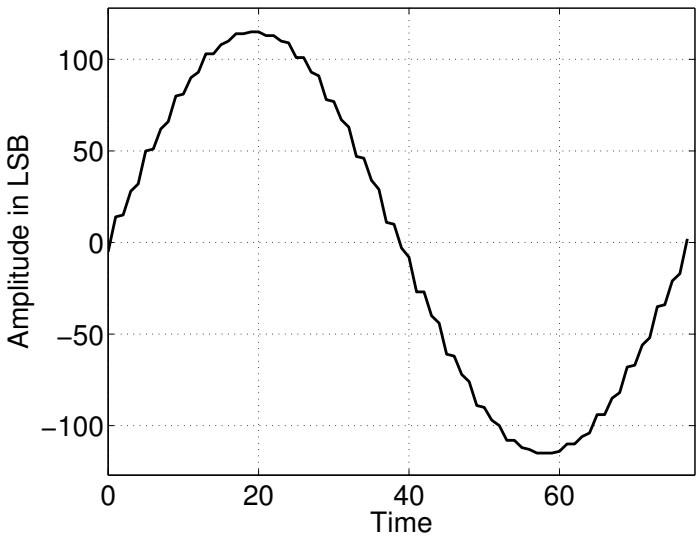

Figure 3.15: Output waveform of a time-interleaved ADC with four channel ADCs and timing mismatches. The plot shows the first period of the sampled signal shown in Fig. 3.14.

put signals, nonlinear-phase mismatches behave just like linear-phase mismatches. However, when we consider broadband signals we see that the nonlinear phase of an ADC also introduces group delay problems, which distort the output signal in addition to the mismatches. For this reason ADCs are designed to have a linear phase. Therefore, linear phase mismatches have much more impact on the time-interleaved ADC performance than the nonlinear-phase mismatches (cf. Sec. 3.3).

3.2.2.2 Timing Jitter

Timing jitter is strongly related to timing mismatches. Both timing errors are deviations from the ideal sampling instant. Timing mismatches are deviations caused by different channel properties among all channels of a time-interleaved ADC. Thus, they have a periodicity of M, which is the number of channels. In contrast, timing jitter (time uncertainty, clock jitter) is the deviation from the ideal sampling instant, which changes for every sampling instant in a random manner. Thus, timing jitter is a common error feature of all channels without a channel depending periodicity. Therefore, we can describe timing jitter only in a statistical way. Nevertheless, we can use our deterministic model to derive properties of this stochastic process, which has been first investigated in [48] and further developed in [149]. It should be noticed that we assume that all channels generate timing jitter with the same statistical properties and we have no timing jitter mismatches. This implies that the following analysis can be applied to ADCs with a single channel as well as to time-interleaved ADCs.

From the above description we see that timing mismatches and timing jitter are very similar. Moreover, if we had a time-interleaved ADC with an infinite number of channels, we would not be able to distinguish both effects. Hence, we can approximate the effect of timing jitter by describing it by a time-interleaved ADC with a large number of channels N. Thereby, we obtain an approximate representation but, by increasing the number of channels N, we can increase the accuracy to any requirement. Once again, for the timing jitter analysis we only exploit the time-interleaved architecture with N channels as an efficient mathematical approximation to describe timing jitter, which could be the timing jitter of a single physical ADC as well as of a time-interleaved ADC. In Sec. 3.4 we will show how we can combine the representation of timing jitter with gain, timing, and offset mismatches of a time-interleaved ADC.

By using the equation for timing mismatches, (3.21), and by setting the number of channels M to N we can approximate a sampled signal with timing jitter in the frequency domain as

$$Y(e^{j\Omega T_s}) = \frac{1}{T_s} \sum_{p=-\infty}^{\infty} \alpha_p \left(j \left(\Omega - p\frac{\Omega_s}{N} \right) \right) X_a \left(j \left(\Omega - p\frac{\Omega_s}{N} \right) \right) \tag{3.26}$$

where

$$\alpha_p(j\Omega) = \frac{1}{N} \sum_{n=0}^{N-1} e^{-j\Omega\delta_n T_s} e^{-jpn\frac{2\pi}{N}}. \tag{3.27}$$

We have replaced the symbol for timing mismatch Δt_n by the symbol for timing jitter $\delta_n T_s$ to clearly distinguish both phenomena, where δ_n denotes the normalized jitter (in percent of the sampling period T_s) for sampling time n. From (3.26) and (3.27) we recognize that, by increasing the number of samples, we also increase the number of aliased spectral components $X_a\left(j\left(\Omega - p\frac{\Omega_s}{N}\right)\right)$ but decrease the power of each spectrum because of the factor $\frac{1}{N}$ in (3.27). Furthermore, since the timing jitter samples $\delta_n T_s$ are drawn from a stochastic process, we get uniformly distributed spectral components.

When we use a sinusoidal input signal we can write for (3.26)

$$\begin{aligned} Y(j\Omega) &= \frac{1}{T_s} \sum_{p=-\infty}^{\infty} \left[\alpha[p] \frac{A}{2j} 2\pi\delta \left(\Omega - \Omega_0 - p\frac{\Omega_s}{N} \right) \right. \\ &\quad \left. -\alpha^*[N-p] \frac{A}{2j} 2\pi\delta \left(\Omega + \Omega_0 - p\frac{\Omega_s}{N} \right) \right] \end{aligned} \tag{3.28}$$

and for (3.27)

$$\alpha[p] = \frac{1}{N} \sum_{n=0}^{N-1} e^{-j\Omega_0\delta_n T_s} e^{-jpn\frac{2\pi}{N}}. \tag{3.29}$$

In Fig. 3.16 we have plotted the output of a time-interleaved ADC with a sinusoidal input signal and timing jitter. We see the two peaks of the input signal and an increased noise floor, which agrees very well with (3.28) and (3.29). By comparing Fig. 3.1 and Fig. 3.16

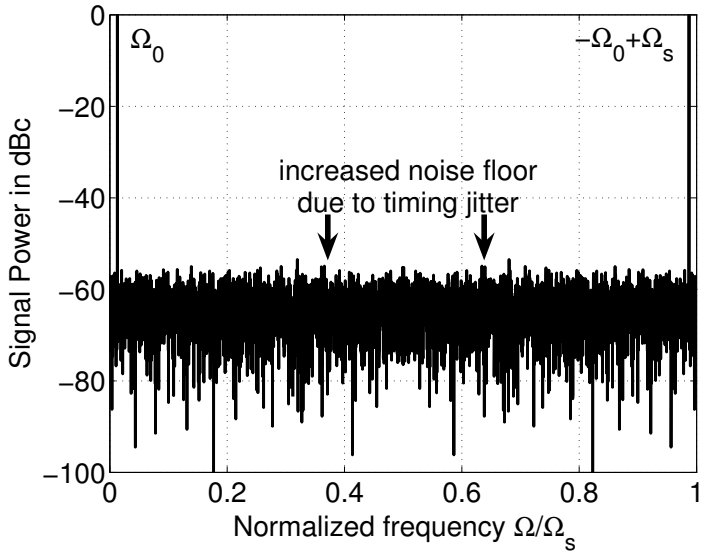

Figure 3.16: Output spectrum of a time-interleaved ADC with four channels ($M = 4$) and timing jitter. The timing jitter is normally distributed with a standard deviation of $\sigma_{\tilde{r}} = 0.4T_s$.

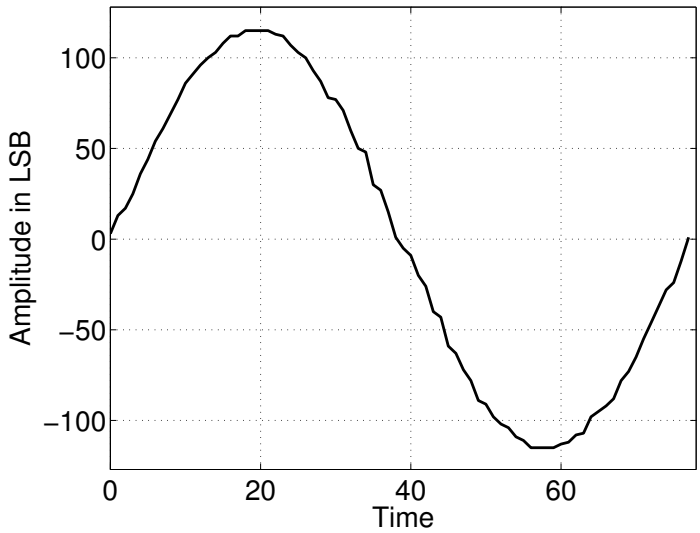

Figure 3.17: Output waveform of a time-interleaved ADC with four channels and timing jitter.

we see that the noise floor has increased by about 20dB because of timing jitter. Due to the factor $\Omega_0 \delta_n T_s$ in (3.29), the timing jitter scales with the input frequency and is the limiting factor of many ADC designs [159]. This can be seen by developing $e^{-j\Omega_0 \delta_n T_s}$ in a Taylor series, which gives

$$\mathcal{T}\{e^{-j\Omega_0 \delta_n T_s}\} = 1 - j\Omega_0 \delta_n T_s - \frac{1}{2}\Omega_0^2 \delta_n^2 T_s^2 + \dots . \tag{3.30}$$

In [48] it is shown that the noise floor will drop by 6dB, if the input frequency is reduced by half and the jitter is dominating. From the time-domain plot shown in Fig. 3.17 we can conclude that the amount of produced error power depends on the derivative of the input signal, i.e., fast changing signals are more influenced by timing jitter.

3.2.2.3 Magnitude Response Mismatches

Except for changing their values with the frequency, magnitude response mismatches behave like gain mismatches. Hence, for a fixed frequency gain and magnitude response mismatches cannot be distinguished. Therefore, the sinusoidal input signal plots shown in Fig. 3.4 and Fig. 3.5 are also valid for magnitude response mismatches.

By only considering magnitude response mismatches, we can write for (2.59)

$$Y(e^{j\Omega T_s}) = \frac{1}{T_s} \sum_{p=-\infty}^{\infty} \alpha_p \left(j \left(\Omega - p\frac{\Omega_s}{M} \right) \right) X_a \left(j \left(\Omega - p\frac{\Omega_s}{M} \right) \right) \tag{3.31}$$

and for (2.60)

$$\alpha_p(j\Omega) = \frac{1}{M} \sum_{m=0}^{M-1} A_m(\Omega)\, e^{-jpm\frac{2\pi}{M}}, \tag{3.32}$$

and see the similarity to the representation of gain mismatches given by (3.1) and (3.2). The only difference are the frequency dependent weighting factors $\alpha_p(j\Omega)$, since they are the result of the DFT of the frequency dependent magnitudes $A_m(\Omega)$.

3.3 Reducing the Complexity of the Time-Interleaved ADC Representation

In Sec. 2.5 we have introduced a mathematical representation for time-interleaved ADCs. In the last two sections, Sec. 3.2.1 and Sec. 3.2.2, we have discussed different error sources and their characteristics. In order to simplify the further investigation of combined channel mismatch errors we reduce the complexity of the time-interleaved ADC representation. The objective is to neglect mismatch errors, which contribute only little power compared to the total mismatch error power. From (2.23) and (2.59) we see that the frequency response $P_m(j\Omega)$, which models phase and magnitude response mismatches, increases in combination with the nonlinearity the representation complexity and makes the combined mismatch error analysis difficult. Fortunately, as we will show, these errors have a low impact on the

time-interleaved ADC performance and we can often neglect them to reduce the representation complexity and simplify the combined analysis.

To further analyze the influence of frequency response mismatches, i.e., phase response mismatches and magnitude response mismatches, on the time-interleaved ADC performance, we assume first-order RC low-pass characteristics for the S/Hs (sample and hold circuits) in sampling mode, which is roughly valid for a wide range of S/H designs [21, 142]. Hence, the frequency response $P_m(j\Omega)$, characterizing the S/Hs, can be written as

$$P_m(j\Omega) = \frac{1}{1 + j\Omega\tau_m}. \tag{3.33}$$

The inverse of the time constant τ_m is the angular cut-off frequency of the mth channel, where the signal power is attenuated 3dB below the nominal signal power. The time constant τ_m is given by

$$\tau_m = R_m C_m, \tag{3.34}$$

where R_m is the resistance and C_m is the capacitance of the S/H in the channel m, while it is in sampling mode.

The magnitude response becomes therefore

$$A_m(\Omega) = \frac{1}{\sqrt{1 + (\Omega\tau_m)^2}} \tag{3.35}$$

and the phase response is (cf. (2.52))

$$-\Omega\tau_m + \phi_m(\Omega) = -\mathrm{atan}(\Omega\tau_m). \tag{3.36}$$

From (3.34) to (3.36) we realize that as soon as the resistances R_m or the capacitances C_m mismatch, we get different time constants τ_m, which cause mismatches of the magnitude responses $A_m(\Omega)$ and phase responses $-\Omega\tau_m + \phi_m(\Omega)$.

To see the relation between the input frequency and the time constant τ_m we develop (3.35) and (3.36) in Taylor series. The magnitude response thereby becomes

$$\mathcal{T}\{A_m(\Omega)\} = 1 - \frac{1}{2}(\Omega\tau_m)^2 + \frac{3}{8}(\Omega\tau_m)^4 - \cdots \tag{3.37}$$

and the phase response results in

$$\mathcal{T}\{-\arctan(\Omega\tau_m)\} = -(\Omega\tau_m) + \underbrace{\frac{1}{3}(\Omega\tau_m)^3 - \frac{1}{5}(\Omega\tau_m)^5 + \cdots}_{\phi_m(\Omega)}, \tag{3.38}$$

where the radius of convergence is $|\Omega\tau_m| < 1$. For low input frequencies Ω or small time constants τ_m we notice that the magnitude response is mainly constant while the phase response linearly depends on the frequency. Furthermore, the nonlinear-phase response $\phi_m(\Omega)$ is a third-order effect and should have little impact compared to linear-phase responses. Thus, we can expect that linear-phase mismatches have much more impact on the

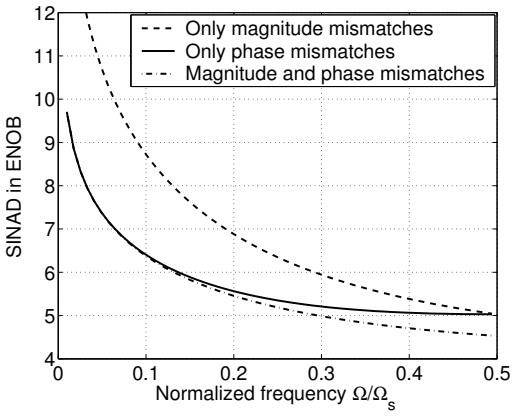

(a) $\Omega_s \tau_R = 2$

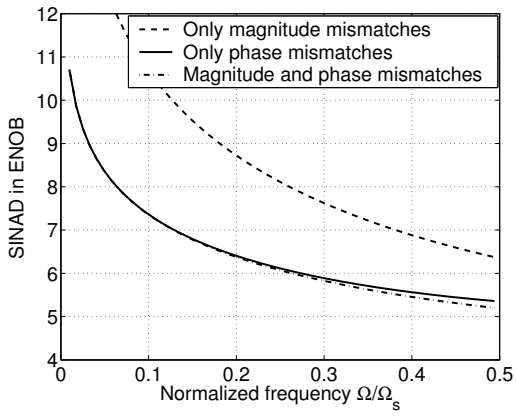

(b) $\Omega_s \tau_R = 1$

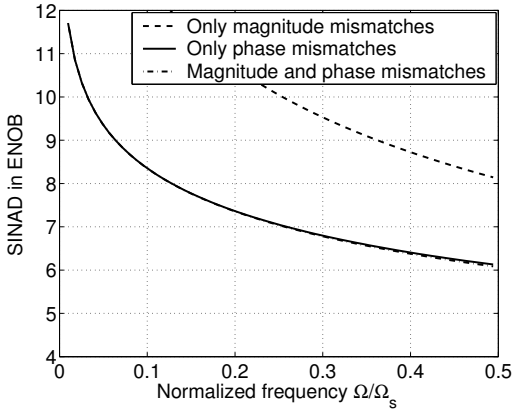

(c) $\Omega_s \tau_R = 0.5$

Figure 3.18: The impact of magnitude and phase mismatches for three different reference time constants τ_R. The figures show the signal-to-noise and distortion ratio (SINAD) of a simulated time-interleaved ADC in effective number of bits (ENOB) against the normalized input frequency Ω/Ω_s. In each plot we have simulated a time-interleaved ADC with two channels (M=2), where for the first channel the time constant τ_0 equals 95 percent of τ_R and for the second channel the time constant τ_1 equals 105 percent of τ_R. Each line in the figure represents another mismatch configuration. The dash-dotted lines have been generated for frequency responses $P_m(j\Omega)$ given by (3.33), which produce both magnitude and phase mismatches. The solid lines have been generated for frequency responses $P_m(j\Omega) = e^{-j\Omega\tau_m + j\phi_m(\Omega)}$, where we have only considered phase mismatches, i.e., linear-phase and nonlinear-phase mismatches, and, finally, the dashed lines have been generated for frequency responses $P_m(j\Omega) = A_m(\Omega)$, where we have only considered magnitude mismatches. The figures show that phase mismatches have much more influence on the SINAD than magnitude mismatches.

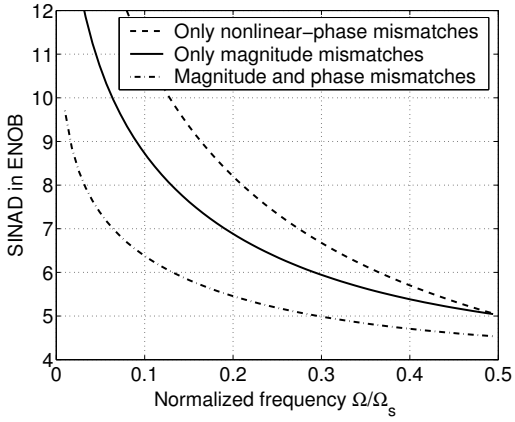

(a) $\Omega_s \tau_R = 2$

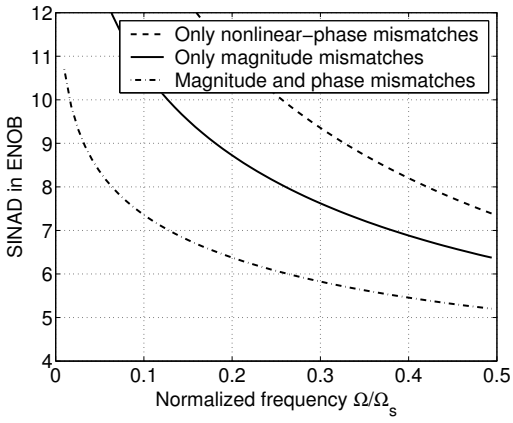

(b) $\Omega_s \tau_R = 1$

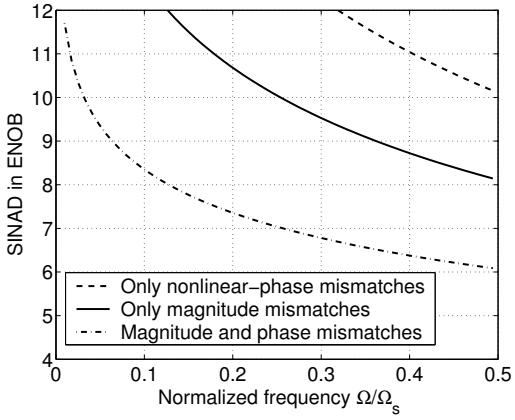

(c) $\Omega_s \tau_R = 0.5$

Figure 3.19: The impact of linear-phase and nonlinear-phase mismatches for three different reference time constants τ_R. The figures show the signal-to-noise and distortion ratio (SINAD) of a simulated time-interleaved ADC in effective number of bits (ENOB) against the normalized input frequency Ω/Ω_s. In each plot we have simulated a time-interleaved ADC with two channels (M=2), where for the first channel the time constant τ_0 equals 95 percent of τ_R and for the second channel the time constant τ_1 equals 105 percent of τ_R. Each line in the figure represents another mismatch configuration. The dash-dotted lines have been generated for frequency responses $P_m(j\Omega)$ given by (3.33), which produce both magnitude and phase mismatches. The solid lines have been generated for frequency responses $P_m(j\Omega) = A_m(\Omega)$, where we have only considered magnitude mismatches and, finally, the dashed lines have been generated for frequency responses $P_m(j\Omega) = e^{j\phi_m(\Omega)}$, where we have only considered nonlinear-phase mismatches . The figures show that magnitude mismatches have much more influence on the SINAD than nonlinear-phase mismatches.

time-interleaved ADC performance than magnitude mismatches and that magnitude mismatches have more impact than nonlinear-phase mismatches.

This is confirmed in Fig. 3.18 and in Fig. 3.19 for three different reference time constants τ_R, defined as $\tau_R = \tau_m - \Delta\tau_m$ (cf. (2.56)), where the two channels of the simulated time-interleaved ADC differ from the reference time constant by $\frac{\Delta\tau_0}{\tau_R} = +5\%$ and $\frac{\Delta\tau_1}{\tau_R} = -5\%$. As expected from our analysis, the influence of phase mismatches is considerably higher than the influence of magnitude mismatches (cf. Fig. 3.18). With a decreasing reference time constant τ_R this trend becomes more and more evident. Equivalently, the impact of nonlinear-phase mismatches is smaller than the impact of magnitude mismatches (cf. Fig. 3.19).

Since linear-phase mismatches have a much greater impact than the other dynamic mismatches, i.e., nonlinear-phase and magnitude mismatches, we will neglect the latter in the following to obtain a reduced time-interleaved ADC representation for the error analysis, which can be written as

$$\begin{aligned} Y(e^{j\Omega T_s}) &= \frac{1}{T_s}\sum_{p=-\infty}^{\infty}\Bigg[\beta_p 2\pi\delta\left(\Omega - p\frac{\Omega_s}{M}\right) \\ &\quad +\alpha_p\left(j\left(\Omega - p\frac{\Omega_s}{M}\right)\right)X_a\left(j\left(\Omega - p\frac{\Omega_s}{M}\right)\right) \\ &\quad +\sum_{k=2}^{K-1}T_{p,k}\left(j\left(\Omega - p\frac{\Omega_s}{M}\right)\right)X_a^{(*k)}\left(j\left(\Omega - p\frac{\Omega_s}{M}\right)\right)\Bigg] \end{aligned} \tag{3.39}$$

where

$$\beta_p = \frac{1}{M}\sum_{m=0}^{M-1} o_m e^{-jpm\frac{2\pi}{M}} \tag{3.40}$$

$$\alpha_p(j\Omega) = \frac{1}{M}\sum_{m=0}^{M-1} g_m e^{-j\Omega\Delta t_m} e^{-jpm\frac{2\pi}{M}} \tag{3.41}$$

$$T_{p,k}(j\Omega) = \frac{1}{M}\sum_{m=0}^{M-1} c_{k,m} e^{-j\Omega\Delta t_m} e^{-jpm\frac{2\pi}{M}}. \tag{3.42}$$

Since we neglect the magnitude response mismatches and the nonlinear-phase mismatches the convolved input signal can be pulled out of the DFT, which greatly simplifies the representation and gives a more consistent structure.

3.4 Deterministic Analysis of Combined Channel Mismatch Errors

In the following we analyze the influence of channel mismatches, timing jitter, and quantization noise on the SINAD of time-interleaved ADCs. We analyze the SINAD for given channel mismatches of a time-interleaved ADC. Thus, from the measurement of gain, offset,

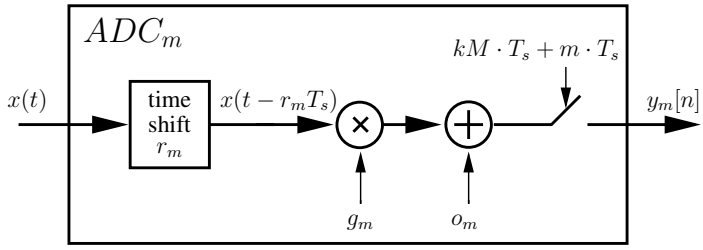

Figure 3.20: Mathematical model of a channel ADC. The input signal $x(t)$ is time-shifted by $\Delta t_m = r_m T_s$, amplified by g_m, added to an offset o_m, and finally sampled with a sampling period of $M \cdot T_s$ and a constant time shift of $m \cdot T_s$.

and timing mismatches we would like to calculate the SINAD. Therefore, we use the term deterministic analysis. The objective is to understand how different mismatches influence each other and contribute to the total noise power. We extend our analysis by considering the influence of timing jitter and quantization noise as well. Hence, the term "deterministic" only refers to the channel mismatches and not to the additionally considered timing jitter and quantization noise.

The main spurious frequencies of a time-interleaved ADC system are caused by gain, offset, and timing mismatches [107, 46]. When we only consider these mismatches we have a channel model as shown in Fig. 3.20. In Fig. 3.20 we have used the relative timing mismatch $r_m = \frac{\Delta t_m}{T_s}$, which is the absolute timing mismatch Δt_m normalized by the sampling period T_s. If the parameters of the model mismatch, spurious tones appear in the spectrum as shown in Fig. 3.21, where a sinusoidal input signal $x_a(t) = A\sin(\Omega_0 t)$ has been coherently sampled. The output spectrum of Fig. 3.21 can be represented by (3.39), where we only consider offset, gain, and timing mismatches, which results in

$$\begin{aligned} Y(e^{j\Omega T_s}) &= \frac{2\pi}{T_s} \sum_{p=-\infty}^{\infty} \left[\alpha_p \delta\left(\Omega - \Omega_0 - p\frac{\Omega_s}{M}\right) - \alpha^*_{M-p} \delta\left(\Omega + \Omega_0 - p\frac{\Omega_s}{M}\right) \right. \\ &\quad \left. + \beta_p \delta\left(\Omega - p\frac{\Omega_s}{M}\right) \right], \end{aligned} \tag{3.43}$$

where

$$\begin{aligned} \alpha_p &= \frac{A}{j2M} \sum_{m=0}^{M-1} g_m e^{-j\omega_0 r_m} e^{-jpm\frac{2\pi}{M}} \\ \beta_p &= \frac{1}{M} \sum_{m=0}^{M-1} o_m e^{-jpm\frac{2\pi}{M}}. \end{aligned} \tag{3.44}$$

The symbol $*$ in (3.43) marks complex conjugation.

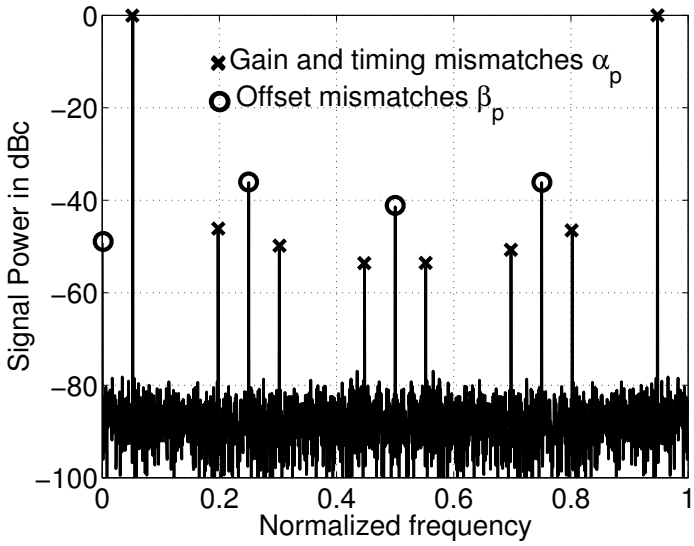

Figure 3.21: Output spectrum of a time-interleaved ADC. We have simulated a time-interleaved ADC with 10-bit resolution and a full-scale range (FSR) [41] of 2 consisting of four channels ($M = 4$) with gain ($\boldsymbol{g}$ = [0.994 0.989 1.009 0.996]), offset ($\boldsymbol{o}$ =[-0.002 0.0033 -0.0021 -0.004]), and timing mismatches ($\boldsymbol{r}$ =[-0.009 -0.002 -0.008 0.004]). Additionally, we have used Gaussian distributed timing jitter with a standard deviation of $\sigma_{\tilde{\delta}} = 0.01$ for the simulation. Furthermore, we have applied a sinusoidal input signal with an amplitude $A = 0.99$ and a frequency $\Omega_0 = 107\frac{\Omega_s}{2048}$ (coherent sampling) from which 2048 sampling points have been taken. The normalized frequency corresponds to $\frac{\omega}{2\pi} = \frac{\Omega T_s}{2\pi}$.

3.4.1 Deterministic SINAD for Combined Channel Mismatch Errors

In order to calculate the SINAD as defined in [41] we use the coefficients α_p, β_p from (3.44). First we neglect quantization noise and timing jitter and later on we show how to add both quantities. We see that the coefficients α_0 and α_M^* represent the original sinusoidal signal, i.e., the scaled input signal power P_S^{gr}, whereas all other coefficients represent additional unwanted tones, i.e., the mismatch error power P_N^{gro}. It should be noted that the scaled input signal power P_S^{gr} itself is influenced by mismatch effects and differs from the original input signal power P_S. Nevertheless, the standard [41] uses only the measured signal power for determining the SINAD, which is, from a measurement point of view, quite reasonable for an ADC. The superscripts in the power symbols P_N and P_S, e.g. g and r, indicate these influences of different error sources gain, relative timing, and offset mismatch on the power. When we substitute the scaled input signal power and the mismatch error power into the definition of the SINAD we get an explicit formula, which combines all three mismatch effects

$$\begin{aligned} SINAD &= 10\log_{10}\left(\frac{P_S^{gr}}{P_N^{gro}}\right) \\ &= 10\log_{10}\left(2|\alpha_0|^2\right) - 10\log_{10}\left(2\sum_{p=1}^{M-1}|\alpha_p|^2 + \sum_{p=0}^{M-1}|\beta_p|^2\right). \end{aligned} \tag{3.45}$$

The equation given in (3.45) unifies and extends the equations found in [76]. It can handle an arbitrary number of channels and can easily be evaluated.

To get a deeper insight, we rewrite (3.45). The scaled input signal power P_S^{gr} can be written as

$$\begin{aligned} P_S^{gr} &= 2|\alpha_0|^2 \\ &= \frac{A^2}{2}\left|\frac{1}{M}\sum_{m=0}^{M-1} g_m e^{-j\omega_0 r_m}\right|^2 \\ &= \frac{A^2}{2}\left|\frac{1}{M}\sum_{m=0}^{M-1} g_m \cos\left(\omega_0 r_m\right) - j\frac{1}{M}\sum_{m=0}^{M-1} g_m \sin\left(\omega_0 r_m\right)\right|^2 \\ &= \frac{A^2}{2}\left(\overline{\gamma_1}^2 + \overline{\gamma_2}^2\right), \end{aligned} \tag{3.46}$$

where

$$\overline{\gamma_1} = \frac{1}{M}\sum_{m=0}^{M-1} g_m \cos\left(\omega_0 r_m\right) \tag{3.47}$$

$$\overline{\gamma_2} = \frac{1}{M}\sum_{m=0}^{M-1} g_m \sin\left(\omega_0 r_m\right). \tag{3.48}$$

The derivation shows that a global timing deviation does not influence the signal power. Hence, for determining the SINAD we can always assume that

$$\sum_{m=0}^{M-1} r_m = 0. \tag{3.49}$$

The mismatch error power P_N^{gro} consists of two terms. The gain and timing mismatch error power $P_N^{gr} = 2\sum_{p=1}^{M-1} |\alpha_p|^2$ and the offset mismatch error power $P_N^o = \sum_{p=0}^{M-1} |\beta_p|^2$. The offset mismatch error power P_N^o can be rewritten using Parseval's theorem

$$\sum_{p=0}^{M-1} |X_p|^2 = M \sum_{m=0}^{M-1} |x[m]|^2, \tag{3.50}$$

where $x[m]$ and X_p are arbitrary DFT pairs, resulting in

$$P_N^o = \sum_{p=0}^{M-1} |\beta_p|^2 = \frac{1}{M} \sum_{m=0}^{M-1} |o_m|^2 = \overline{|o|^2}. \tag{3.51}$$

The gain and timing mismatch error power P_N^{gr} can be split into $2\sum_{p=0}^{M-1} |\alpha_p|^2 - 2|\alpha_0|^2$, where we have already evaluated the second term with (3.46). Using again Parseval's theorem, the first term can be rewritten as

$$\begin{aligned} 2\sum_{p=0}^{M-1} |\alpha_p|^2 &= \frac{A^2}{2M} \sum_{m=0}^{M-1} \left| g_m e^{-j\omega_0 r_m} \right|^2 \\ &= \frac{A^2}{2} \frac{1}{M} \sum_{m=0}^{M-1} g_m^2 = \frac{A^2}{2} \overline{g^2}. \end{aligned} \tag{3.52}$$

Combining (3.46) and (3.52) results in

$$P_N^{gr} = \frac{A^2}{2} \left(\overline{g^2} - \left(\overline{\gamma_1}^2 + \overline{\gamma_2}^2 \right) \right). \tag{3.53}$$

If we combine the simplified terms (3.46), (3.51), and (3.53), we obtain from (3.45)

$$\begin{aligned} SINAD &= 10\log_{10}\left(\frac{P_S^{gr}}{P_N^{gr} + P_N^o} \right) \\ &= 10\log_{10}\left(\frac{A^2}{2} \left(\overline{\gamma_1}^2 + \overline{\gamma_2}^2 \right) \right) - 10\log_{10}\left(\frac{A^2}{2} \left(\overline{g^2} - \left(\overline{\gamma_1}^2 + \overline{\gamma_2}^2 \right) \right) + \overline{|o|^2} \right) \\ &= 10\log_{10}\left(\frac{P_S^{gr}}{\frac{A^2}{2}\overline{g^2} - P_S^{gr} + P_N^o} \right), \end{aligned} \tag{3.54}$$

which explicitly indicates how gain and timing mismatches interact.

3.4.2 Influence of Timing Jitter and Quantization Noise on the SINAD

To complete our description, we analyze the influence of additional timing jitter and quantization noise on the SINAD. Therefore, we assume that both quantities are mutually independent. Although timing jitter is a statistical quantity we first describe it in a deterministic way in order to see its influence on the other channel mismatches. To derive the influence of timing jitter, we use a special arrangement of time-interleaved ADCs, illustrated in Fig. 3.22. On the left side we see a prototype time-interleaved ADC. With this prototype time-interleaved ADC we build a structure of N identical time-interleaved ADCs, all of which sample in a time-interleaved manner. The first time-interleaved ADC takes M samples, then the second one takes M samples and so forth, until the N-th time-interleaved ADC takes M samples and the first time-interleaved ADC starts again. Therefore, the scaled input signal power of such a structure can be written as (cf. (3.46))

$$P_S^{gr} = \frac{A^2}{2} \left| \frac{1}{N} \sum_{n=0}^{N-1} \frac{1}{M} \sum_{m=0}^{M-1} g_m e^{-j\omega_0 r_m} \right|^2 , \tag{3.55}$$

where the scaled input signal power is, due to the repetitive structure of time-interleaved ADCs, identical to the case of a single time-interleaved ADC given by (3.46). Next, we consider a structure of N identical time-interleaved ADCs, where each time-interleaved ADC channel has an additional relative timing deviation δ_{n+m} (Fig. 3.23) which is not repetitive but varies among all channels, which results in

$$P_S^{gr} = \frac{A^2}{2} \left| \frac{1}{N} \sum_{n=0}^{N-1} \frac{1}{M} \sum_{m=0}^{M-1} g_m e^{-j\omega_0 r_m} e^{-j\omega_0 \delta_{n+m}} \right|^2 . \tag{3.56}$$

If we assume that the stochastic process underlying the additional relative timing deviations δ_{n+m} is ergodic [101], then its time average is an unbiased estimator [63] of its expected value defined as

$$\mu_{\tilde{\delta}} = E\left\{\tilde{\delta}\right\} := \int_{-\infty}^{\infty} x f_{\tilde{\delta}}(x) dx, \tag{3.57}$$

where $f_{\tilde{\delta}}$ is the probability density function of the random variable $\tilde{\delta}$ [101] associated with the observations δ_{n+m}. Therefore, we can write (3.56) as

$$\begin{aligned} \lim_{N\to\infty} P_S^{gr} &= \frac{A^2}{2} \left| \frac{1}{N} \sum_{n=0}^{N-1} \frac{1}{M} \sum_{m=0}^{M-1} g_m e^{-j\omega_0 r_m} e^{-j\omega_0 \delta_{n+m}} \right|^2 \\ &= \frac{A^2}{2} \left| E\left\{ \frac{1}{M} \sum_{m=0}^{M-1} g_m e^{-j\omega_0 r_m} e^{-j\omega_0 \tilde{\delta}} \right\} \right|^2 \end{aligned} \tag{3.58}$$

and finally obtain

$$\begin{aligned} P_S^{gr\delta} &= \frac{A^2}{2} \left(\overline{\gamma_1}^2 + \overline{\gamma_2}^2 \right) \left| E\left\{ e^{-j\omega_0 \tilde{\delta}} \right\} \right|^2 \\ &= \frac{A^2}{2} \left(\overline{\gamma_1}^2 + \overline{\gamma_2}^2 \right) |\Phi_{\tilde{\delta}}(\omega_0)|^2. \end{aligned} \tag{3.59}$$

The expression $\Phi_{\tilde{\delta}}(\omega_0)$ is the characteristic function of the random variable $\tilde{\delta}$ defined by $\Phi_{\tilde{\delta}}(\omega) = E\left\{e^{j\omega\tilde{\delta}}\right\} = \int_{-\infty}^{\infty} f_{\tilde{\delta}}(x)e^{j\omega x}dx$ [101]. Thus, we have extended our structure of time-interleaved ADCs to infinity, whereby each sample is taken by a different channel with a different additional timing deviation, which models the timing jitter of the system. From (3.54) we see that this modified signal power completely describes the time-interleaved ADC. Hence, we can write for a time-interleaved ADC with timing jitter

$$\begin{aligned} SINAD &= 10\log_{10}\left(\frac{P_S^{gr\delta}}{\frac{A^2}{2}\overline{g^2} - P_S^{gr\delta} + P_N^o}\right) \\ &= 10\log_{10}\left(\frac{A^2}{2}\left(\overline{\gamma_1}^2 + \overline{\gamma_2}^2\right)|\Phi_{\tilde{\delta}}(\omega_0)|^2\right) - \\ &- 10\log_{10}\left(\frac{A^2}{2}\left(\overline{g^2} - \left(\overline{\gamma_1}^2 + \overline{\gamma_2}^2\right)|\Phi_{\tilde{\delta}}(\omega_0)|^2\right) + \overline{|o|^2}\right) \\ &= 10\log_{10}\left(\frac{P_S^{gr\delta}}{P_N^{gr\delta} + P_N^o}\right). \end{aligned} \tag{3.60}$$

When we assume that the quantization noise is independent from all other effects, (3.60) becomes

$$SINAD = 10\log_{10}\left(\frac{P_S^{gr\delta}}{P_N^{gr\delta} + P_N^o + P_N^q}\right), \tag{3.61}$$

where $P_N^q = \frac{\Delta^2}{12}$. The symbol Δ is the quantization step size, which is given for an B bit converter by $\Delta = \frac{FSR}{2^B}$, where FSR is the full-scale range [41]. With (3.61) we have derived an explicit combined mismatch description, which also takes timing jitter and quantization noise into account.

Unfortunately, the mismatch error power and the timing jitter power are coupled; nevertheless, they can be separated by using some simplifications. By assuming Gaussian distributed timing jitter we can evaluate the characteristic function $|\Phi_{\tilde{\delta}}(\omega_0)|^2$ to $e^{-{\omega_0}^2{\sigma_{\tilde{\delta}}}^2}$ [cf. (3.84)], where $\sigma_{\tilde{\delta}}$ is the standard deviation of the timing jitter. The Taylor series expansion of $e^{-{\omega_0}^2{\sigma_{\tilde{\delta}}}^2}$ gives $1-{\omega_0}^2{\sigma_{\tilde{\delta}}}^2+\frac{1}{2}{\omega_0}^4{\sigma_{\tilde{\delta}}}^4-\ldots$, where we see that the higher-order terms are small compared to the first two and can be neglected. Therefore, we can express (3.61) as

$$\begin{aligned} SINAD &= 10\log_{10}\left(\frac{A^2}{2}\left(\overline{\gamma_1}^2 + \overline{\gamma_2}^2\right)\left(1 - {\omega_0}^2{\sigma_{\tilde{\delta}}}^2\right)\right) - \\ &- 10\log_{10}\left(\frac{A^2}{2}\left(\overline{g^2} - \left(\overline{\gamma_1}^2 + \overline{\gamma_2}^2\right)\left(1 - {\omega_0}^2{\sigma_{\tilde{\delta}}}^2\right)\right) + \overline{|o|^2} + \frac{\Delta^2}{12}\right) \\ &= 10\log_{10}\left(\frac{P_S^{gr} - P_N^{\delta}}{P_N^{gr} + P_N^{\delta} + P_N^o + P_N^q}\right), \end{aligned} \tag{3.62}$$

where $P_N^{\delta} = \frac{A^2}{2}\left(\overline{\gamma_1}^2 + \overline{\gamma_2}^2\right)\left({\omega_0}^2{\sigma_{\tilde{\delta}}}^2\right)$. Through these simplifications, we have separated the mismatch error power from the jitter noise error power. When we neglect the mismatch effects the result is comparable to the results in [68, 123].

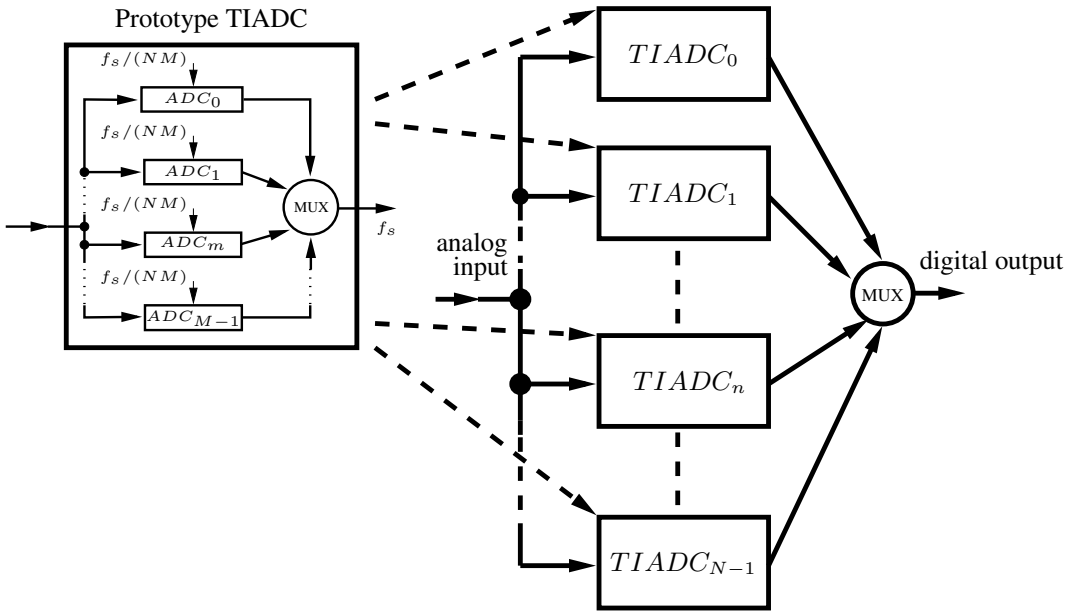

Figure 3.22: To determine the effect of timing jitter we build a structure of time-interleaved ADCs by repeating one prototype time-interleaved ADC with M channels each N times. The structure itself samples in a time-interleaved manner. Thereby we obtain "time-interleaved time-interleaved ADCs" (a meta time-interleaved ADC with a total of $N \cdot M$ channels). All time-interleaved ADCs in the meta time-interleaved ADC have the same properties (gain, offset, timing deviation of the channel ADCs). Only an additional timing deviation (cf. Fig. 3.23) varies among all channels of the meta time-interleaved ADC. When we let the number of time-interleaved ADCs N go to infinity, we get a meta time-interleaved ADC, which is identical in its behavior to the prototype time-interleaved ADC, except for the additional timing deviations which model the non-deterministic timing jitter.

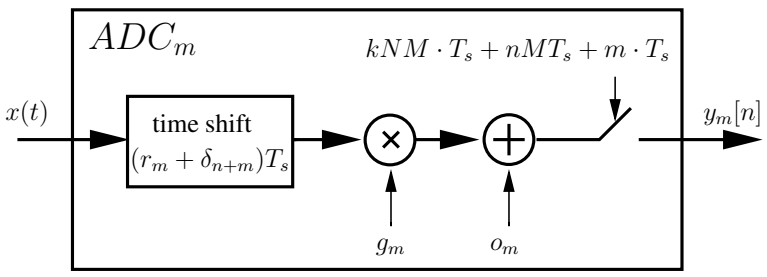

Figure 3.23: Mathematical model of the channel ADCs used for Fig. 3.22. The additional timing deviation $\delta_{n+m}T_s$ will lead to timing jitter.

3.4.3 Worst-Case Analysis of Individual Channel Mismatch Errors

To obtain the worst cases for individual mismatch errors we set upper and lower bounds for the parameters $x_m \in [x_{min}, x_{max}]$, where x_m stands for a certain parameter g_m, o_m, or r_m. We neglect timing jitter and quantization noise and further assume an even number of ADCs M.

We first start with the special case where timing and offset mismatches are negligible (e.g., $r_m = 0$ and $o_m = 0$), so that we can write for (3.54)

$$SINAD = 10 \log_{10} \left(\frac{\frac{A^2}{2} \overline{g}^2}{\frac{A^2}{2} \left(\overline{g^2} - \overline{g}^2 \right)} \right). \tag{3.63}$$

With the relation

$$\sum_{m=0}^{M-1} {g_m}^2 - \frac{1}{M} \left(\sum_{m=0}^{M-1} g_m \right)^2 = \sum_{m=0}^{M-1} (g_m - \overline{g})^2 \tag{3.64}$$

the worst case for (3.54) is obtained as

$$SINAD = 20 \log_{10} \left(\frac{\overline{g}}{\Delta g_{max}} \right), \tag{3.65}$$

where $\Delta g_{max} = \frac{g_{max} - g_{min}}{2}$. Thus, the worst case occurs if all g_m are either g_{min} or g_{max} and the average $\overline{g}$ of all g_m is $\frac{g_{min} + g_{max}}{2}$.

Second, if gain and offset mismatches are negligible (e.g., $g_m = \overline{g}$ and $o_m = 0$), we can express (3.54) as

$$SINAD = 20 \log_{10} \left(\frac{\frac{A^2}{2} \overline{g}^2 \left(\overline{\phi_1}^2 + \overline{\phi_2}^2 \right)}{\frac{A^2}{2} \overline{g}^2 \left(1 - \left(\overline{\phi_1}^2 + \overline{\phi_2}^2 \right) \right)} \right), \tag{3.66}$$

where

$$\overline{\phi_1} = \frac{1}{M} \sum_{m=0}^{M-1} \cos(\omega_0 r_m) \tag{3.67}$$

$$\overline{\phi_2} = \frac{1}{M} \sum_{m=0}^{M-1} \sin(\omega_0 r_m). \tag{3.68}$$

To obtain the worst case we simplify (3.66) to

$$SINAD = 20 \log_{10} \left(\frac{1}{\left(\frac{1}{\left(\overline{\phi_1}^2 + \overline{\phi_2}^2 \right)} - 1 \right)} \right) \tag{3.69}$$

and recognize that we can minimize (3.69) by minimizing the term $\left(\overline{\phi_1}^2 + \overline{\phi_2}^2\right)$. Since both quantities $\overline{\phi_1}$ and $\overline{\phi_2}$ are squared, their smallest possible value is zero. According to (3.49) and the cosines in (3.67) the quantity $\overline{\phi_1}$ has its minimum if all r_m are either r_{max} or r_{min}. The quantity $\overline{\phi_2}$ is zero for $r_m \equiv 0$ or if the number of $r_m = r_{max}$ equals the number of $r_m = r_{min}$. Therefore, the worst case for (3.54) reduces to

$$SINAD = 20\log_{10}\left(\frac{1}{\omega_0 \Delta r_{max}}\right), \tag{3.70}$$

where $\Delta r_{max} = \frac{r_{max}-r_{min}}{2}$. Again, the worst case occurs if all r_m are either r_{min} or r_{max} and the average $\overline{r}$ of all r_m is $\frac{r_{min}+r_{max}}{2}$.

Third, if gain and timing mismatches are negligible (e.g., $g_m = \overline{g}$ and $r_m = 0$), the worst case for (3.54) is

$$SINAD = 20\log_{10}\left(\frac{A\overline{g}}{\sqrt{2}\hat{o}_{max}}\right), \tag{3.71}$$

where all $o_m = \hat{o}_{max} = max\left(|o_{min}|, |o_{max}|\right)$. However, from (3.43) we see that for this special case the power is concentrated in $\Omega = 0$ and is not caused by a mismatch effect. In fact, we are confronted with a global offset. Thus, we can simply filter this error power by subtracting the arithmetic mean value from the output signal of the time-interleaved ADC. Thereby we get the reduced worst case for offset mismatches

$$SINAD = 20\log_{10}\left(\frac{A\overline{g}}{\sqrt{2}\Delta o_{max}}\right), \tag{3.72}$$

where $\Delta o_{max} = \frac{o_{max}-o_{min}}{2}$, which is more consistent with the other worst cases. Hence, all o_m are either o_{min} or o_{max} and the average $\overline{o}$ of all o_m is $\frac{o_{min}+o_{max}}{2}$.

3.4.4 Numerical Results

Numerical time-domain simulations have been carried out to compare the results of the derived equations and the simulation results [152].

The difference between the SINAD of a simulated time-interleaved ADC with 10bit resolution, combined channel mismatches and timing jitter and the SINAD calculated according to (3.61) and (3.62) is shown in Fig. 3.24. We see that even for these strong mismatch errors and the strong timing jitter the calculated SINAD is, except for quantization and jitter uncertainties, identical to the simulated one. Moreover, even the approximate SINAD (3.62), where all error sources are separated, only slightly deviates from the simulation results.

In Fig. 3.25 we show the applicability of the worst-case analyses for dominating offset [Fig. 3.25(a)] and dominating gain [Fig. 3.25(b)] mismatches with uniform distributions. For both plots we have generated 10000 realizations and determined the SINAD with a coherently sampled sinusoidal input signal. We see how accurately the worst-case analyses (dashed lines) determine the lower bound of the SINAD for both examples.

In Fig. 3.26 we compare the expected and the worst-case SINAD for timing mismatches. For the expected SINAD we assume Gaussian distributed timing mismatches (3.88) with

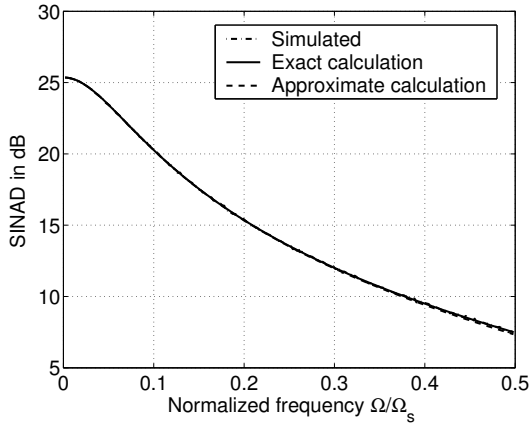

(a) Comparison between the simulated SINAD and the SINAD calculated according to (3.61) (exact) and (3.62) (approximated), respectively. All three curves are essentially coincide.

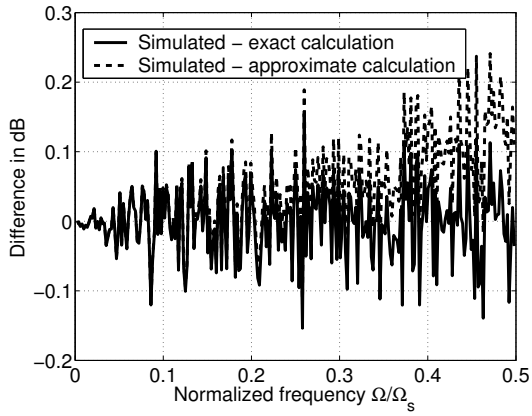

(b) Difference between the simulated and the exactly calculated SINAD (solid line) and between the simulated and the approximated SINAD (dashed line).

Figure 3.24: Simulation of a time-interleaved ADC with 10-bit resolution and an FSR of 2 consisting of four channels (M=4) with gain (g = [1.01 0.95 1.03 0.97]), offset (o =[0.01 -0.03 -0.04 0.02]) and timing mismatches (r =[0.1 -0.09 0.05 -0.07]). Additionally, Gaussian distributed timing jitter ($\sigma_{\tilde{\delta}}$=0.1) and sinusoidal input signals with an amplitude $A = 0.9$ are used, where each signal has been sampled with 16348 sampling points through coherent sampling. The exact SINAD calculation (3.61) yields very accurate results; however, even the approximated SINAD calculation (3.62), where the timing jitter power is separated from the other power sources, only slightly deviates from the simulated one.

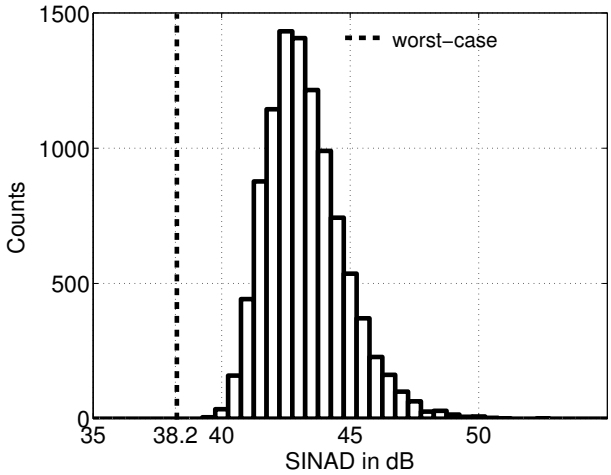

(a) Dominating offset mismatches with a uniform distribution.

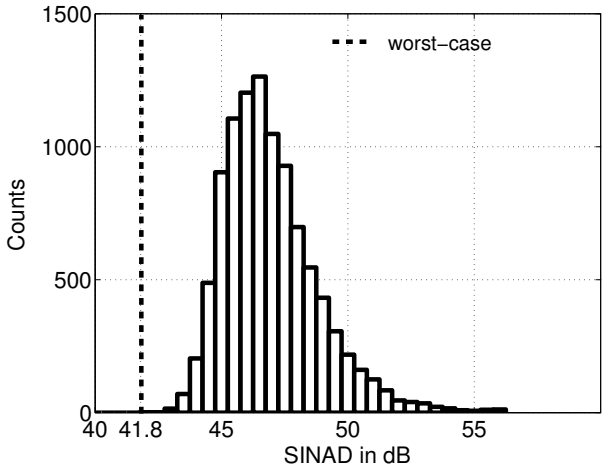

(b) Dominating gain mismatches with a uniform distribution.

Figure 3.25: The histogram plots show the SINAD of an eight channel time-interleaved ADC ($M = 8$) for 10000 realizations with 1024 samples. The sinusoidal input signal with $A = 1$ has been coherently sampled with $f_0 = \frac{307}{1024} f_s$. In (a) dominating offset mismatches with a uniform distribution are shown, where $\mu_{\tilde{o}} = 0$ and $\sigma_{\tilde{o}} = 0.005$, whereas in (b) dominating gain mismatches with a uniform distribution are shown, where $\mu_{\tilde{g}} = 1$ and $\sigma_{\tilde{g}} = 0.005$. The dashed line marks the worst case for (a) according to (3.72) and for (b) according to (3.65).

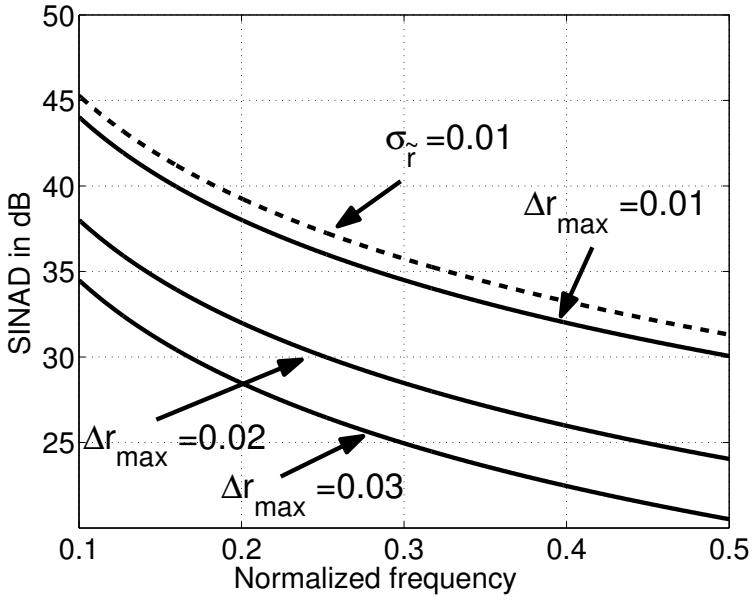

Figure 3.26: Comparison of the expected SINAD and the worst-case SINAD for a time-interleaved ADC consisting of four channels with dominating timing mismatches. The dashed line shows the expected SINAD for Gaussian distributed timing mismatches (3.86) with $\sigma_{\tilde{r}} = 0.01$. The other lines show the worst-case SINAD (3.70) if we set the maximum deviation from the ideal sampling period to three different hard bounds ($\Delta r_{max} = 0.01$, $\Delta r_{max} = 0.02$ and $\Delta r_{max} = 0.03$).

$\sigma_{\tilde{r}} = 0.01$ and for the corresponding worst-case SINAD (3.70) we set different maximum deviations from the ideal sampling period $\Delta r_{max} = 0.01$, $\Delta r_{max} = 0.02$, and $\Delta r_{max} = 0.03$. This is the case when we discard all time-interleaved ADC realizations that have a channel ADC with a relative timing deviation smaller than r_{min} or greater than r_{max}. When we compare the expected SINAD and the worst-case SINAD we see that the worst cases are significantly worse. The worst cases are not very likely to occur and their probability decreases with the number of channels. However, they are the true lower bounds of the SINAD and should, therefore, be considered, too.

3.5 Statistical Analysis of Combined Channel Mismatch Errors

So far, we are able to calculate the signal and the error power of a time-interleaved ADC if the explicit parameters g_m, r_m, o_m of each channel ADC and its timing jitter distribution are known. However, if only the probability distributions of the mismatch parameters are known, e.g., for a particular production process, we need to derive formulas for the expected signal and error power. In Sec. 3.4.2 we have shown how timing jitter and quantization noise power can be separated. Therefore, we only analyze the statistical behavior of offset, gain, and timing mismatches.

3.5.1 Expected SINAD for Combined Channel Mismatch Errors

We replace the scaled input signal power and the mismatch error power by their expected values, as defined in (3.57), and substitute the explicit parameters by corresponding random variables $\tilde{g}_m$, $\tilde{r}_m$, $\tilde{o}_m$. Furthermore, we assume that all mismatch effects are mutually independent and get

$$\begin{aligned} SINAD &= 10\log_{10}\left(\frac{E\left\{P_S^{\tilde{g}\tilde{r}}\right\}}{E\left\{P_N^{\tilde{g}\tilde{r}\tilde{o}}\right\}}\right) \\ &= 10\log_{10}\left(\frac{E\left\{P_S^{\tilde{g}\tilde{r}}\right\}}{E\left\{\frac{A^2}{2}\overline{\tilde{g}^2} - P_S^{\tilde{g}\tilde{r}}\right\} + E\left\{P_N^{\tilde{o}}\right\}}\right). \end{aligned} \tag{3.73}$$

We reduce (3.73) in three steps. First, we simplify the expected scaled input signal power $E\left\{P_S^{\tilde{g}\tilde{r}}\right\}$. Then, we focus on the combined gain and timing mismatch error power $E\left\{\frac{A^2}{2}\overline{\tilde{g}^2} - P_S^{\tilde{g}\tilde{r}}\right\}$ and finally, we evaluate the offset mismatch error power $E\left\{P_N^{\tilde{o}}\right\}$.

The scaled input signal power can be expressed as

$$\begin{aligned} E\left\{P_S^{\tilde{g}\tilde{r}}\right\} &= \frac{A^2}{2}\left|\frac{1}{M}\sum_{m=0}^{M-1}\tilde{g}_m e^{-j\omega_0\tilde{r}_m}\right|^2 \\ &= \frac{A^2}{2M^2}\sum_{m=0}^{M-1}\sum_{l=0}^{M-1} E\left\{\tilde{g}_m\tilde{g}_l e^{-j\omega_0\tilde{r}_m}e^{j\omega_0\tilde{r}_l}\right\}. \end{aligned} \tag{3.74}$$

In order to simplify (3.74), we distinguish between two cases. For the first one we set $m = l$ and for the second one we set $m \neq l$. After evaluating both cases, we can add the results. This leads us to

$$\begin{aligned} m = l \quad &\Rightarrow \quad \frac{A^2}{2M^2}\sum_{m=0}^{M-1} E\left\{\tilde{g_m}^2 e^{-j\omega_0(\tilde{r}_m-\tilde{r}_m)}\right\} \\ &= \quad \frac{A^2}{2M}(\mu_{\tilde{g}}^2 + \sigma_{\tilde{g}}^2) \end{aligned} \tag{3.75}$$

$$\begin{aligned} m \neq l \quad &\Rightarrow \quad \frac{A^2}{2M^2}\sum_{m=0}^{M-1}\sum_{l=0,l\neq m}^{M-1} E\left\{\tilde{g}_m\right\}E\left\{\tilde{g}_l\right\} \\ &\qquad E\left\{e^{-j\omega_0\tilde{r}_m}\right\}E\left\{e^{j\omega_0\tilde{r}_l}\right\} \\ &= \quad \frac{A^2}{2M}((M-1)\mu_{\tilde{g}}^2|\Phi_{\tilde{r}}(\omega_0)|^2) \end{aligned} \tag{3.76}$$

and finally results in

$$\begin{aligned} E\left\{P_S^{\tilde{g}\tilde{r}}\right\} &= (3.75) + (3.76) \\ &= \frac{A^2}{2M}\left(\mu_{\tilde{g}}^2((M-1)|\Phi_{\tilde{r}}(\omega_0)|^2 + 1) + \sigma_{\tilde{g}}^2\right). \end{aligned} \tag{3.77}$$

The symbol $\mu_{\tilde{g}}$ denotes the mean value and the symbol $\sigma_{\tilde{g}}$ the standard deviation of the gain mismatch variable $\tilde{g}$. The expression $\Phi_{\tilde{r}}(\omega_0)$ is the characteristic function of the random variable $\tilde{r}$.

A simplified form of the gain and timing mismatch error power in (3.73) can be found by

$$\begin{aligned} E\left\{\frac{A^2}{2}\overline{\tilde{g}^2} - P_S^{\tilde{g}\tilde{r}}\right\} &= \frac{A^2}{2}\left({\mu_{\tilde{g}}}^2 + {\sigma_{\tilde{g}}}^2\right) - \frac{A^2}{2M}({\mu_{\tilde{g}}}^2((M-1)|\Phi_{\tilde{r}}(\omega_0)|^2+1) + {\sigma_{\tilde{g}}}^2) \\ &= \frac{A^2}{2M}(M-1)\left({\mu_{\tilde{g}}}^2\left(1-|\Phi_{\tilde{r}}(\omega_0)|^2\right) + {\sigma_{\tilde{g}}}^2\right). \end{aligned} \tag{3.78}$$

The offset mismatch error power in (3.73) can be reduced to

$$\begin{aligned} E\left\{P_N^{\tilde{o}}\right\} &= \frac{1}{M}\sum_{m=0}^{M-1} E\left\{|\tilde{o}_m|^2\right\} \\ &= ({\mu_{\tilde{o}}}^2 + {\sigma_{\tilde{o}}}^2). \end{aligned} \tag{3.79}$$

When we combine all three simplified parts and substitute them in (3.73) we obtain

$$\begin{aligned} SINAD &= 10\log_{10}\left(\frac{E\left\{P_S^{\tilde{g}\tilde{r}}\right\}}{E\left\{P_N^{\tilde{g}\tilde{r}\tilde{o}}\right\}}\right) \\ &= 10\log_{10}\left(\frac{A^2}{2M}\left({\mu_{\tilde{g}}}^2((M-1)|\Phi_{\tilde{r}}(\omega_0)|^2+1) + {\sigma_{\tilde{g}}}^2\right)\right) - \\ &- 10\log_{10}\left(\frac{A^2}{2M}(M-1)\left({\mu_{\tilde{g}}}^2\left(1-|\Phi_{\tilde{r}}(\omega_0)|^2\right) + {\sigma_{\tilde{g}}}^2\right) + \left({\mu_{\tilde{o}}}^2 + {\sigma_{\tilde{o}}}^2\right)\right). \end{aligned} \tag{3.80}$$

In order to evaluate (3.80) we need the expected value $\mu_{\tilde{g}}$ and the standard deviation $\sigma_{\tilde{g}}$ of the gain probability distribution, the expected value $\mu_{\tilde{o}}$ and the standard deviation $\sigma_{\tilde{o}}$ of the offset probability distribution, and the characteristic function $\Phi_{\tilde{r}}(\omega_0)$ of the timing deviation probability distribution. Estimates of the expected value and the standard deviation of an unknown probability distribution can be determined by measuring an appropriate number of samples. What remains difficult is the evaluation of the characteristic function, which generally cannot be solved in closed form.

We evaluate the characteristic function for two cases of special interest where closed forms are available. First, we assume that the timing mismatch is uniformly distributed. Therefore, the probability density function (PDF) is

$$f_{\tilde{r}}(x) = \begin{cases} \frac{1}{b-a} & a \le x \le b \\ 0 & \text{otherwise.} \end{cases} \tag{3.81}$$

Furthermore, we use the relation $\frac{b-a}{2} = \sigma_{\tilde{r}}\sqrt{3}$. Therefore, the characteristic function becomes [46]

$$\begin{aligned} |\Phi_{\tilde{r}}(\omega_0)|^2 &= \left|\int_{-\infty}^{\infty} f_{\tilde{r}}(x)e^{j\omega_0 x}dx\right|^2 \\ &= \operatorname{sinc}^2\left(\omega_0\sigma_{\tilde{r}}\sqrt{3}\right), \end{aligned} \tag{3.82}$$

where $\mathrm{sinc}(x) = \frac{\sin(x)}{x}$.

In the same way, we can carry out the calculations for Gaussian distributed timing mismatches. With the PDF of a Gaussian distribution

$$f_{\tilde{r}}(x) = \frac{1}{\sqrt{2\pi\sigma_{\tilde{r}}^2}} e^{-\frac{(x-\mu_{\tilde{r}})^2}{2\sigma_{\tilde{r}}^2}} \tag{3.83}$$

and the relation $\int_{-\infty}^{\infty} e^{-\frac{x^2}{2}} dx = \sqrt{2\pi}$ we get the characteristic function

$$\begin{aligned} |\Phi_{\tilde{r}}(\omega_0)|^2 &= \left| \int_{-\infty}^{\infty} f_{\tilde{r}}(x) e^{j\omega_0 x} dx \right|^2 \\ &= e^{-{\omega_0}^2 {\sigma_{\tilde{r}}}^2}. \end{aligned} \tag{3.84}$$

3.5.2 Expected SINAD for Individual Channel Mismatch Errors

The combined description given by (3.80) can be specialized to derive the expected SINAD for individual errors. As for the combined description, we need not know the probability distribution of the gain or the offset mismatches in order to determine the expected SINAD. It is sufficient to know the mean value and the standard deviation. Only for the timing mismatch we have to assume some kind of probability distribution. Assuming a Gaussian distribution for the timing mismatch and assuming further that $\mu_{\tilde{o}} = 0$, (3.80) reduces to

$$\begin{aligned} & SINAD = \\ = \; & 10\log_{10}\left(\frac{A^2}{2M}\left({\mu_{\tilde{g}}}^2((M-1)e^{-{\omega_0}^2{\sigma_{\tilde{r}}}^2}+1)+{\sigma_{\tilde{g}}}^2\right)\right) - \\ - \; & 10\log_{10}\left(\frac{A^2}{2M}(M-1)\left({\mu_{\tilde{g}}}^2\left(1-e^{-{\omega_0}^2{\sigma_{\tilde{r}}}^2}\right)+{\sigma_{\tilde{g}}}^2\right)+{\sigma_{\tilde{o}}}^2\right). \end{aligned} \tag{3.85}$$

We can show that several known equations for individual mismatch errors are special cases of (3.85). If $\sigma_{\tilde{o}} = 0$ and $\sigma_{\tilde{r}} = 0$ only gain mismatch errors occur and we get (cf. [107, 164, 35])

$$\begin{aligned} SINAD &= 10\log_{10}\left(\frac{{\mu_{\tilde{g}}}^2 M + {\sigma_{\tilde{g}}}^2}{(M-1){\sigma_{\tilde{g}}}^2}\right) \\ &\simeq 20\log_{10}\left(\frac{\mu_{\tilde{g}}}{\sigma_{\tilde{g}}}\right) - 10\log_{10}\left(1-\frac{1}{M}\right). \end{aligned} \tag{3.86}$$

For $\sigma_{\tilde{g}} = 0$ and $\sigma_{\tilde{r}} = 0$ we obtain an expression for offset mismatch errors exclusively (cf. [107, 164, 35])

$$\begin{aligned} SINAD &= 10\log_{10}\left(\frac{{\mu_{\tilde{g}}}^2 M}{\frac{2M}{A^2}{\sigma_{\tilde{o}}}^2}\right) \\ &= 20\log_{10}\left(\frac{A\mu_{\tilde{g}}}{\sqrt{2}\sigma_{\tilde{o}}}\right). \end{aligned} \tag{3.87}$$

For $\sigma_{\tilde{o}} = 0$, $\sigma_{\tilde{g}} = 0$, and by using a Taylor series expansion we get for Gaussian distributed timing mismatch errors only (cf. [46])

$$\begin{aligned} SINAD &= 10\log_{10}\left(\frac{(M-1)e^{-\omega_0{}^2\sigma_{\tilde{r}}{}^2}+1}{(M-1)\left(1-e^{-\omega_0{}^2\sigma_{\tilde{r}}{}^2}\right)}\right) \\ &\simeq 20\log_{10}\left(\frac{1}{\omega_0\sigma_{\tilde{r}}}\right) - 10\log_{10}\left(1-\frac{1}{M}\right). \end{aligned} \tag{3.88}$$

3.5.3 Numerical Results

Numerical time-domain simulations have been carried out to compare the results of the derived equations and the simulation results [152].

Next, we consider the equations for the expected SINAD. To compare it with the averaged SINAD of simulations, we have to average the scaled input signal power and the error power of all simulated realizations, which is

$$SINAD = 10log_{10}\left(\frac{\overline{P_S^{gr}}}{\overline{P_N^{gro}}}\right), \tag{3.89}$$

where

$$\overline{P_S^{gr}} = \frac{1}{K}\sum_{k=0}^{K-1}\left(P_S^{gr}\right)_k$$

and

$$\overline{P_N^{gro}} = \frac{1}{K}\sum_{k=0}^{K-1}\left(P_N^{gro}\right)_k.$$

The symbol K denotes the number of realizations, whereas the index k refers to one particular realization.

In Fig. 3.27 we illustrate the variation of the expected SINAD for the case of Gaussian distributed gain, offset, and timing mismatches (3.85) as a function of two independent parameters. Fig. 3.27(a) shows the three-dimensional surface of the SINAD that appears when $\sigma_{\tilde{g}}$ and $\sigma_{\tilde{r}}$ are varied and all other parameters, especially $\sigma_{\tilde{o}}$, are fixed. Fig. 3.27(b) plots the corresponding isolines of Fig. 3.27(a). The cross marks the distribution parameters for a given production process. Let us assume that in order to improve the SINAD we could either develop some method to reduce the gain mismatch $\sigma_{\tilde{g}}$ (case 1) or the timing mismatch $\sigma_{\tilde{r}}$ (case 2). We see that for the first case we only insignificantly improve the expected SINAD no matter how sophisticated our gain mismatch compensation method will be. This is due to the fact that in our example the timing mismatch limits the performance of the time-interleaved ADC. Thus, to improve the expected SINAD we first have to find a timing mismatch compensation method (case 2). Afterwards it makes sense to think about a gain mismatch compensation method. To sum up, we see that the optimization of one parameter (e.g., $\sigma_{\tilde{g}}$) does not necessarily improve the SINAD if the other parameters

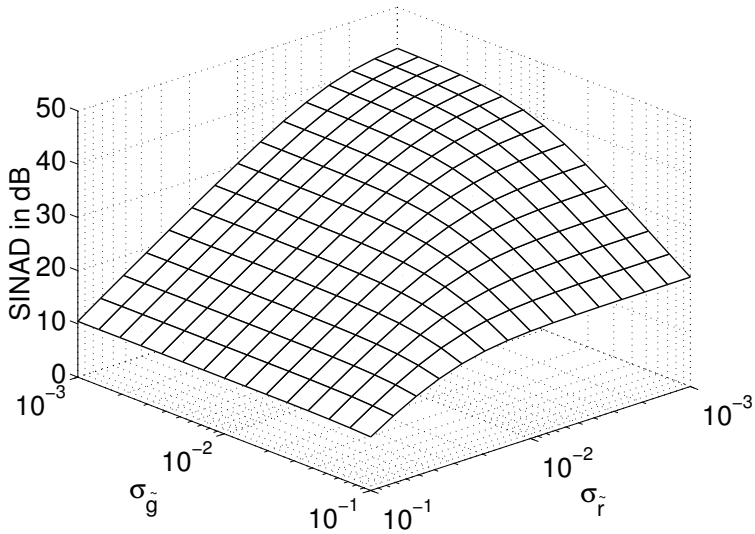

(a) Plot of the expected SINAD

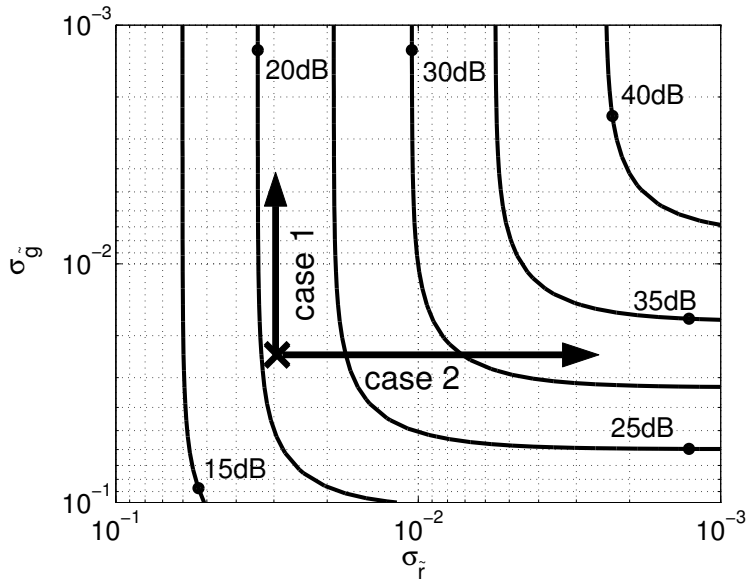

(b) Isolines of the expected SINAD from Fig. 3.27(a).

Figure 3.27: Expected SINAD for Gaussian distributed gain, offset, and timing mismatch errors ($A = 1$, $M = 8$, $f_0 = 1/2f_s$, $\mu_{\tilde{g}} = 1$, $\sigma_{\tilde{o}} = 0.005$, $\mu_{\tilde{o}} = 0$). For the shown example an optimization of the timing mismatches (case 2) has a much more positive impact on the SINAD than an optimization of the gain mismatches (case 1).

are too large. In our example, we only consider the expected SINAD as a function of two independent parameters, since more dimensions are hard to visualize. However, in Fig. 3.27(b) we can also observe the influence of the parameter $\sigma_{\tilde{o}}$. For very small $\sigma_{\tilde{g}}$ and $\sigma_{\tilde{r}}$ the surface flattens because the fixed offset mismatch $\sigma_{\tilde{o}}$ prevents a further improvement of the expected SINAD. Hence, in order to find efficient optimization priorities we have to consider all parameters simultaneously.

In Fig. 3.28 we can see the difference between the calculated expected SINAD and the SINAD of simulated time-interleaved ADCs, which has been obtained by averaging over one hundred realizations. Even for this rather small number of samples the differences between the calculation and the simulation become less than ± 0.5dB.

To see how the deviation from the averaged SINAD to the expected SINAD develops, we have illustrated the difference between these two parameters in Fig. 3.29 for different numbers of realizations. For each plot in Fig. 3.29 we have carried out 1000 trials, where in each trial we have averaged over 10 [Fig. 3.29(a)], 100 [Fig. 3.29(b)], and 1000 [Fig. 3.29(c)] simulated realizations according to (3.89) before we have determined the difference. For each realization we have taken 4096 sampling points through coherent sampling. It can be seen that the averaged values become more accurate with an increasing number of trials.

In Fig. 3.30 we compare the expected and the averaged SINAD for different numbers of samples and for a fixed number of simulated realizations. In particular, we have carried out 1000 trials and have averaged for each trial over 100 simulated realizations. For each realization we have taken 1024 samples [Fig. 3.30(a)], 4096 samples [Fig. 3.30(b)], and 16384 samples [Fig. 3.30(c)], through coherent sampling. We see that the number of samples does not significantly influence the difference between the expected and the averaged SINAD.

3.6 Conclusion

We have investigated channel mismatches in time-interleaved ADCs. First, we have analyzed possible mismatches separately and explained their major properties. Then we have compared the influence of different mismatches and derived a reduced time-interleaved ADC model. Based on this reduced model, we have analyzed combined channel mismatch errors including timing jitter and quantization noise. We have derived formulas for calculating the explicit SINAD for given parameters and the expected SINAD for given parameter distributions. The equation given in (3.45) unifies and extends the equations found in [76] for calculating the explicit SINAD. Its rearranged version (3.54) clarifies how offset, gain, and timing mismatches interact. Moreover, for the first time we have introduced the concept of a meta time-interleaved ADC, which allows us to consider the mutual influence of timing jitter and combined mismatch errors for an arbitrary number of channels (3.61). We have shown a way to separate timing jitter power and mismatch error power with (3.62). Furthermore, we have performed worst-case analyses for individual errors. We have derived the worst-cases for offset (3.72), gain (3.65), and timing mismatches (3.70). With (3.80) we have presented a closed-form expression for the expected SINAD, which combines arbitrarily distributed offset, gain, and timing mismatch errors. This combined error description allows us to consider the mutual dependencies of these errors and we can determine the

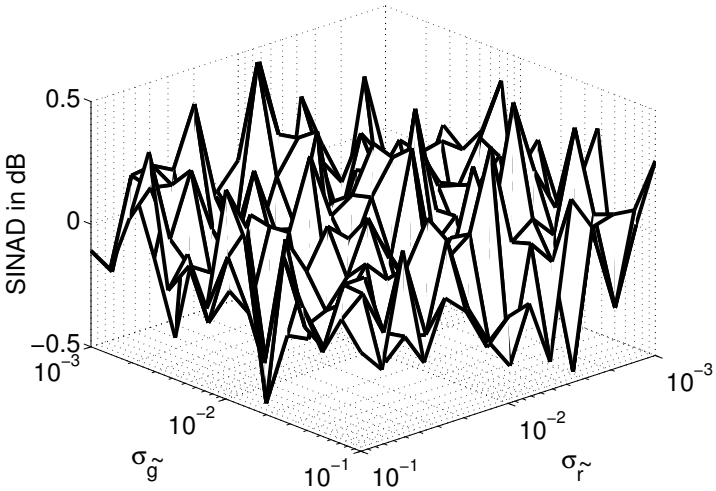

(a) Difference between the expected and the simulated SINAD.

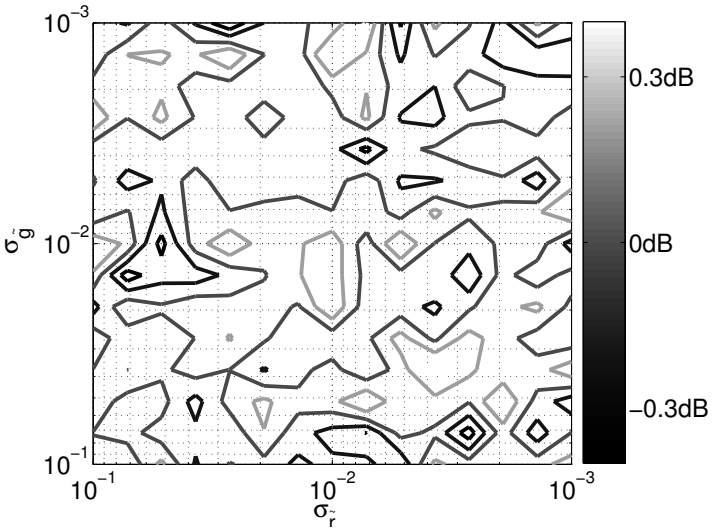

(b) Isolines of the difference between the expected and the simulated SINAD from Fig. 3.28(a).

Figure 3.28: The difference between the expected SINAD calculated with (3.85) and the SINAD of simulated time-interleaved ADCs, which have been obtained by averaging over 100 realizations determined according to (3.89), where for each realization we have taken 8192 samples. The time-interleaved ADC and the distribution parameters have been $A = 1$, $M = 8$, $f_0 = 1/2f_s$, $\mu_{\tilde{g}} = 1$, $\sigma_{\tilde{o}} = 0.005$, $\mu_{\tilde{o}} = 0$, hence, the same as in Fig. 3.27. The difference between the calculated and the simulated and averaged SINAD is less than ± 0.5dB.

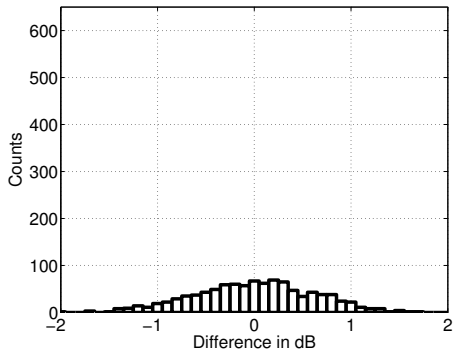

(a) 10 realizations per trial

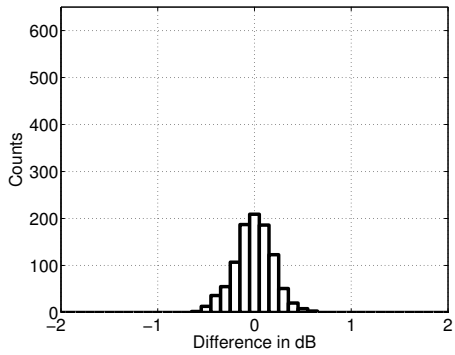

(b) 100 realizations per trial

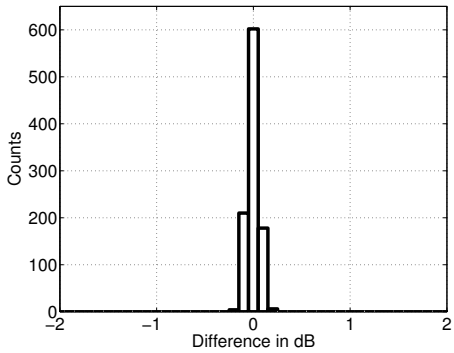

(c) 1000 realizations per trial

Figure 3.29: The histogram plots show the distribution of the difference between the expected SINAD calculated with (3.85) and the averaged SINAD of simulated time-interleaved ADCs calculated with (3.89). For each plot 1000 trials have been carried out, but in (a) we have averaged over 10 realizations, in (b) we have averaged over 100 realizations, and in (c) we have averaged over 1000 realizations for each trial. For each realization 4096 sampling points have been taken. We have used a time-interleaved ADC with 8 channels and a sinusoidal input signal according to $A = 1$ and $f_0 = \frac{2039}{4096} f_s$. The parameters of the Gaussian distributions have been $\mu_{\tilde{g}} = 1$ and $\sigma_{\tilde{g}} = 0.05$ for the gain, $\mu_{\tilde{o}} = 0$ and $\sigma_{\tilde{o}} = 0.005$ for the offset, and $\sigma_{\tilde{r}} = 0.03$ for the timing mismatches. The deviation from the expected SINAD becomes smaller when we average more realizations.

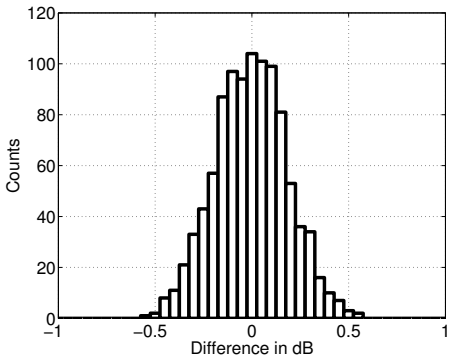

(a) 1024 samples per realization.

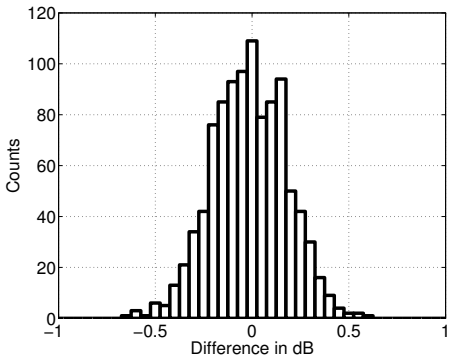

(b) 4096 samples per realization.

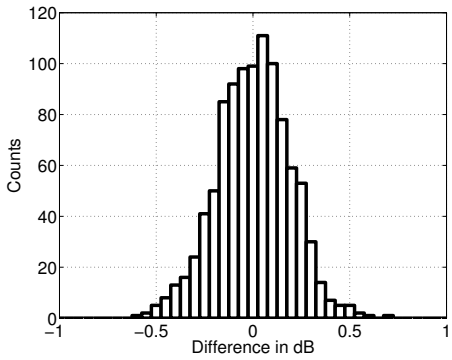

(c) 16384 samples per realization.

Figure 3.30: The histogram plots show the distribution of the difference between the expected SINAD calculated with (3.85) and the averaged SINAD of simulated time-interleaved ADCs calculated with (3.89). For each plot 1000 trials with 100 realizations per trial have been carried out, but in (a) we have used 1024 samples, in (b) we have used 4096 samples, and in (c) we have used 16384 samples for each realization. Signal and distribution parameters have been identical as for Fig. 3.29. From (a) to (c) we realize that the number of samples does not have an observable influence.

one error source which has the main impact on the SINAD. Thus, the equations for the expected SINAD can support engineers in finding the right optimization priorities for their time-interleaved digitizing channels.

Chapter 4

Channel Mismatch Identification

On the one hand identification is the most critical component in the channel mismatch compensation process of time-interleaved ADCs. If the identified parameters are wrong even the best reconstruction algorithms cannot improve the ADC performance. On the other hand, the power consumption of the identification method is not as important as the power consumption of the compensation method. The reason is twofold: first, the identification algorithm does not need to work permanently and, second, it can work on a lower clock rate compared to the sampling rate.

In this chapter we will introduce different identification methods, which differ in implementation complexity and precision, and we will compare their performance. In Sec. 4.2 we will present a matrix notation for linear mismatches. This matrix notation is the key for an accurate foreground channel mismatch identification introduced in Sec. 4.3 and an accurate background identification method for timing mismatches presented in Sec. 4.4.

We have also investigated time-domain methods for background channel mismatch identification. However, since the research on this topic has not been completed, we have included the preliminary results in appendix B.

4.1 Introduction

The first identification procedure for timing mismatches can be found in [47]. There, a sinus wave is used to estimate the timing mismatches in the frequency domain. Because of the special input signal, the method is only suitable for foreground identification, i.e., an identification which interrupts the normal converter operation. However, the method has the advantage of a very high accuracy, which is difficult to achieve with background methods. One background method for timing mismatches is introduced in [26], where the authors use the signal statistics of the time domain signal. The influence of gain mismatches on this identification method is investigated in [28] and performance measurements on the method are carried out in [27]. However, since the timing identification method given in [26] does not provide very accurate estimates, the same authors have used the method within an adaptive system [25]. There, the same timing mismatch identification method is employed to determine the gradient of the timing mismatches and not the mismatches itself, which vastly relaxes the requirements on this method. Unfortunately, the computational complexity of the adaptive solution is very high. With the same adaptive system the authors also show how to correct offset and gain mismatches. A comprehensive investigation of this method can be found in [30]. An analog identification and compensation method for gain and offset

errors is introduced in [22]. The authors use a reference system to calibrate each channel ADC. The same authors present in [33] a digital calibration method for gain and offset mismatches, where they use a reference system as well. A very similar method is introduced in [93]. In [54, 55] a ramp signal is used to identify timing mismatches. Such a ramp signal with the required precision is difficult to generate and is only applicable for foreground methods. A very interesting idea for timing-mismatch identification for two channels is shown in [43, 44]. The authors use the correlation of the input signal and the aliased spectrum to tune the timing mismatch compensation. Unfortunately, the method is limited to two channels. A foreground identification procedure for gain and offset mismatches with a sinusoidal reference signal is given in [103]. The idea is related to Jenq's idea of timing mismatch estimation [47]. A blind identification method for gain and offset mismatches in randomized time-interleaved ADCs is given in [1].

Hence, background calibration methods for timing mismatches are either imprecise, limited to two channels, or they have a huge computational complexity. Foreground calibration methods show a much better performance; the conversion process, however, has to be interrupted. What is still missing, is a background calibration method for timing mismatches with a high accuracy and a maintainable computational complexity and a foreground identification method to determine all linear channel mismatches, i.e., to fully characterize the frequency response mismatch of a time-interleaved ADC.

4.2 Matrix Notation for Linear Mismatches

For the discussion of channel mismatch identification methods in the frequency domain, we introduce a matrix notation for the input/output representation of time-interleaved ADCs. To simplify matters, we exclusively deal with time-interleaved ADCs; nevertheless, the concept can easily be applied to hybrid filter banks as well.

For the further discussion we assume that the input signal $X_a\left(j\Omega\right)$ is bandlimited, i.e.,

$$X_a\left(j\Omega\right) = 0 \quad \text{for } |\Omega| \geq \frac{\Omega_s}{2}. \tag{4.1}$$

When we only consider linear mismatches we can write for the output of a time-interleaved ADC (cf. (2.59) for $k = 1$)

$$Y(e^{j\Omega T_s}) = \frac{1}{T_s} \sum_{p=-\infty}^{\infty} \alpha_p \left(j\left(\Omega - p\frac{\Omega_s}{M}\right)\right) X_a\left(j\left(\Omega - p\frac{\Omega_s}{M}\right)\right). \tag{4.2}$$

where

$$\alpha_p(j\Omega) = \frac{1}{M} \sum_{m=0}^{M-1} g_m A_m\left(\Omega\right) e^{-j\Omega\Delta t_m} e^{j\phi_m(\Omega)} e^{-jpm\frac{2\pi}{M}} \tag{4.3}$$

Since the weighting coefficients $\alpha_p(j\Omega)$ are the outcome of a DFT, they are periodic with M and $\alpha_p(j\Omega) = \alpha_{p_{\langle M\rangle}}(j\Omega)$, where $p_{\langle M\rangle}$ means p modulo M. Even though $\alpha_p(j\Omega)$ is not bandlimited, the product $\alpha_p\left(j\left(\Omega - p\frac{\Omega_s}{M}\right)\right) X_a\left(j\left(\Omega - p\frac{\Omega_s}{M}\right)\right)$ in (4.2) is bandlimited since $X_a\left(j\Omega\right)$ is bandlimited. When we consider (4.2), which is illustrated in Fig. 4.1 for the

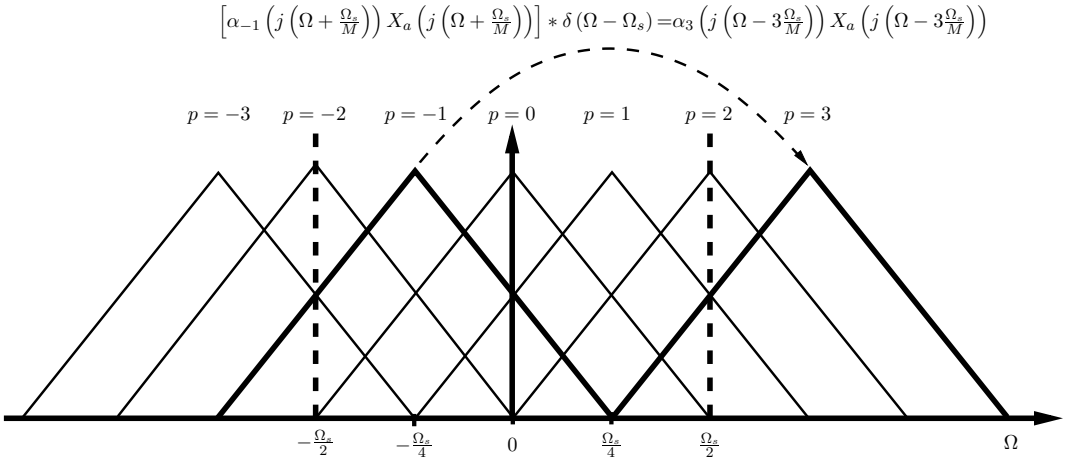

Figure 4.1: Periodicity of the aliased spectral components. All bandlimited spectral components $\alpha_p\left(j\left(\Omega-p\frac{\Omega_s}{M}\right)\right)\ X_a\left(j\left(\Omega-p\frac{\Omega_s}{M}\right)\right)$ have an M-periodicity with respect to p, i.e., apart from a frequency shift of Ω_s they are identical.

case of $M=4$, we recognize that a period of M corresponds to a frequency shift of Ω_s. To show this explicitly, we redefine the index p as

$$p=k+qM \tag{4.4}$$

and rewrite (4.2) as

$$\begin{aligned}
Y(e^{j\Omega T_s}) &= \frac{1}{T_s}\sum_{q=-\infty}^{\infty} \\
&\quad \sum_{k=0}^{M-1}\alpha_{k+qM}\left(j\left(\Omega-(k+qM)\frac{\Omega_s}{M}\right)\right)X_a\left(j\left(\Omega-(k+qM)\frac{\Omega_s}{M}\right)\right) \\
&= \frac{1}{T_s}\sum_{q=-\infty}^{\infty}\sum_{k=0}^{M-1}\alpha_k\left(j\left(\Omega-k\frac{\Omega_s}{M}-q\Omega_s\right)\right)X_a\left(j\left(\Omega-k\frac{\Omega_s}{M}-q\Omega_s\right)\right) \\
&= \sum_{k=0}^{M-1}\alpha_k\left(e^{j\left(\Omega-k\frac{\Omega_s}{M}\right)T_s}\right)X_a\left(e^{j\left(\Omega-k\frac{\Omega_s}{M}\right)T_s}\right)
\end{aligned} \tag{4.5}$$

and (4.3) as

$$\alpha_k(j\Omega)=\frac{1}{M}\sum_{m=0}^{M-1}g_m A_m\left(\Omega\right)e^{-j\Omega\Delta t_m}e^{j\phi_m(\Omega)}e^{-jkm\frac{2\pi}{M}}. \tag{4.6}$$

With (4.5) we obtain a discrete-time representation, where the dependency on $e^{j\Omega T_s}$ indicates the required periodic extension of the fundamental interval defined by the bandlimited input and the mismatches. Furthermore, we explicitly see the M-periodicity with respect to k and the Ω_s-periodicity with respect to Ω. In Fig. 4.2 we have illustrated the new notation

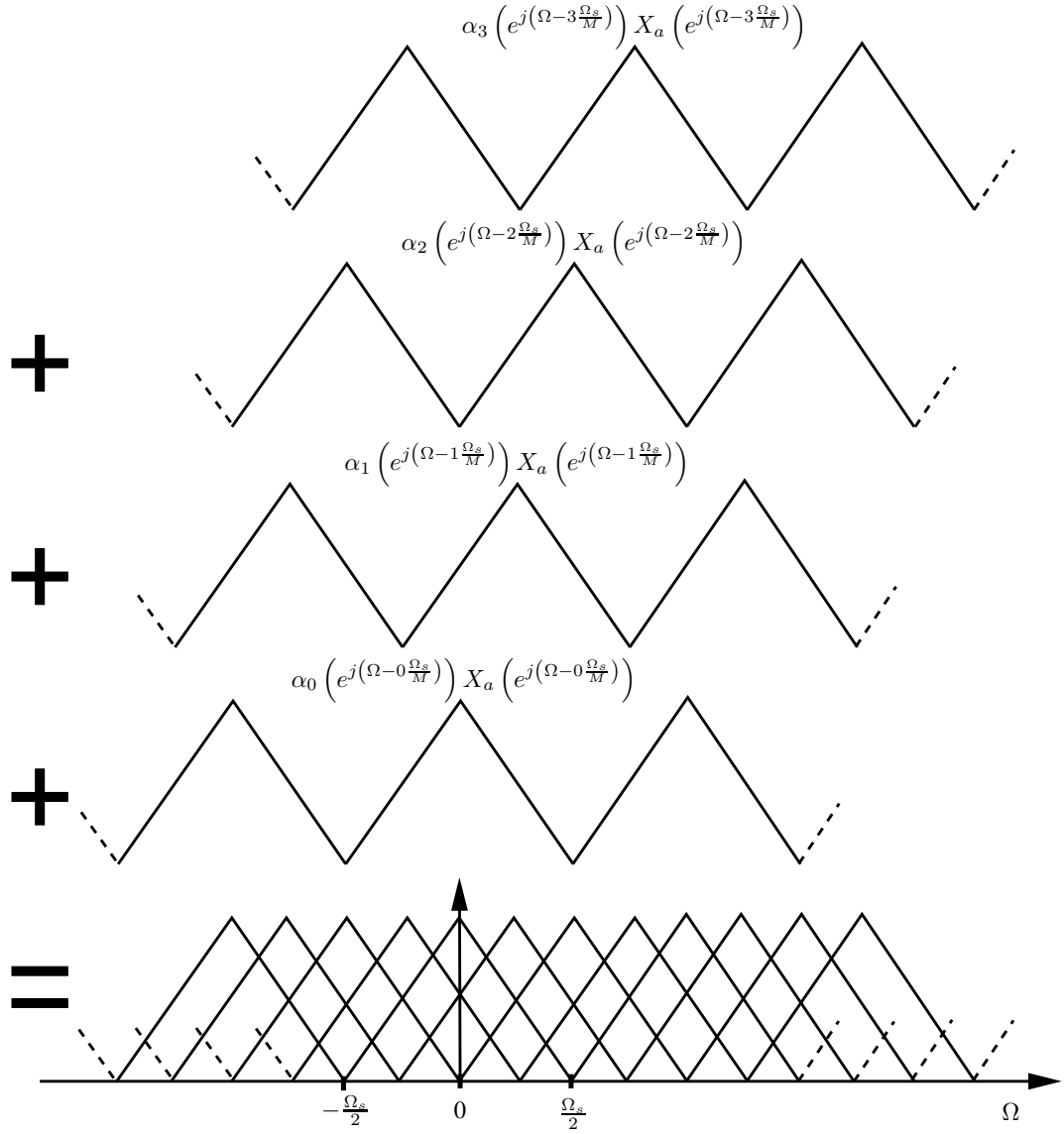

Figure 4.2: Spectrum representation using the discrete-time notation of a time-interleaved ADC with four channels ($M = 4$). We have four periodically extended, shifted spectral components, which are added up to form the entire output spectrum.

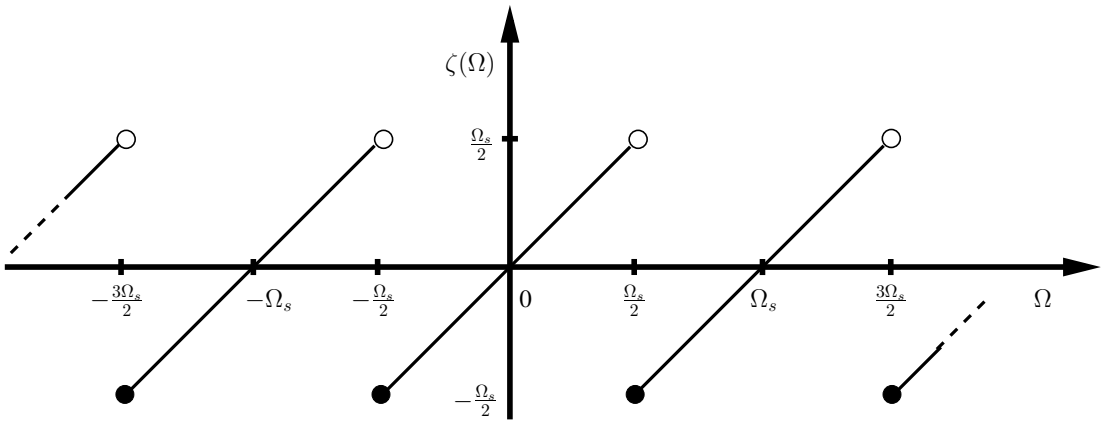

Figure 4.3: Illustration of the modulo operator $\zeta(\Omega)$.

for the case of a four-channel ADC. However, when it comes to evaluating the representation at a particular frequency Ω, we have to work with the continuous-time representation, since the factors of the weighting coefficient $\alpha_k \left(e^{j\left(\Omega - k\frac{\Omega_s}{M}\right)T_s}\right)$ have no bandlimited representations and, in general, we cannot find equivalent discrete-time representations. Therefore, we have to find the corresponding index q of the sum in (4.5) for each considered frequency Ω, i.e., $q = f(\Omega)$ in order to evaluate the continuous-time factors with the correct frequency [82]. In Sec. 2.4 we have done this for the fundamental interval, where we see that we need more than M spectral components to obtain a complete fundamental interval representation. However, to generally represent the entire spectrum and to do computations with the continuous-time factors in (4.6) with a concise representation, we have to find a way for determining the involved spectral components without evaluating the index q each time.

When we consider a sampled bandlimited continuous-time signal (cf. (4.1))

$$\frac{1}{T_s} \sum_{q=-\infty}^{\infty} X_a \left(j \left(\Omega - q\Omega_s\right)\right) \tag{4.7}$$

we see that for a particular frequency Ω we search for a q, which maps $\Omega - q\Omega_s$ in the range of the fundamental interval $]-\frac{\Omega_s}{2}, \frac{\Omega_s}{2}]$, i.e.,

$$\begin{aligned} \frac{\Omega_s}{2} &> \Omega - q\Omega_s \\ -\frac{\Omega_s}{2} &\leq \Omega - q\Omega_s. \end{aligned} \tag{4.8}$$

In fact, we are not interested in the particular index q but in the remaining frequency, which allows us to evaluate the continuous-time components. When we add $\frac{\Omega_s}{2}$ at each

side of (4.8), we can write

$$\begin{aligned}\Omega_s &> \left(\Omega + \frac{\Omega_s}{2}\right) - q\Omega_s \\ 0 &\leq \left(\Omega + \frac{\Omega_s}{2}\right) - q\Omega_s.\end{aligned} \tag{4.9}$$

and realize that (4.9) defines a modulo operation. Thus, we can write

$$\begin{aligned}\Omega_s &> \left(\Omega + \frac{\Omega_s}{2}\right)_{\langle\Omega_s\rangle} \\ 0 &\leq \left(\Omega + \frac{\Omega_s}{2}\right)_{\langle\Omega_s\rangle}.\end{aligned} \tag{4.10}$$

or

$$\begin{aligned}\frac{\Omega_s}{2} &> \left(\Omega + \frac{\Omega_s}{2}\right)_{\langle\Omega_s\rangle} - \frac{\Omega_s}{2} \\ -\frac{\Omega_s}{2} &\leq \left(\Omega + \frac{\Omega_s}{2}\right)_{\langle\Omega_s\rangle} - \frac{\Omega_s}{2}.\end{aligned}$$

With the modulo operator and some algebraic manipulations, we obtain the frequency we can use to evaluate the continuous-time components. Moreover, we can drop the q index, since the particular value is not of interest any more. With this operation we can mix continuous-time and discrete-time representations with a concise notation. To this end, we introduce the frequency transformation $\zeta(\Omega)$, which is given by

$$\zeta(\Omega) = \left(\Omega + \frac{\Omega_s}{2}\right)_{\langle\Omega_s\rangle} - \frac{\Omega_s}{2}, \tag{4.11}$$

where $\langle\Omega_s\rangle$ stands for modulo Ω_s, and which is illustrated in Fig. 4.3. The impact on a bandlimited continuous-time spectrum is shown in Fig. 4.4. The function produces shifted copies of the fundamental interval, whereby the fundamental interval becomes periodic with Ω_s, i.e., it represents the spectrum of a bandlimited continuous-time signal sampled with Ω_s, which can be denoted as

$$\frac{1}{T_s}\sum_{q=-\infty}^{\infty} X_a\left(j\left(\Omega - q\Omega_s\right)\right) = X_a\left(e^{j\Omega T_s}\right) = \frac{1}{T_s}X_a\left(j\zeta\left(\Omega\right)\right). \tag{4.12}$$

Consequently, we can express (4.5) as

$$Y(e^{j\Omega T_s}) = \frac{1}{T_s}\sum_{k=0}^{M-1}\alpha_k\left(j\zeta\left(\Omega - k\frac{\Omega_s}{M}\right)\right)X_a\left(j\zeta\left(\Omega - k\frac{\Omega_s}{M}\right)\right) \tag{4.13}$$

For the further discussion we will maintain this representation. To simplify the notation we use the abbreviations

$$\Omega^{(k)} = \Omega + k\frac{\Omega_s}{M} \tag{4.14}$$

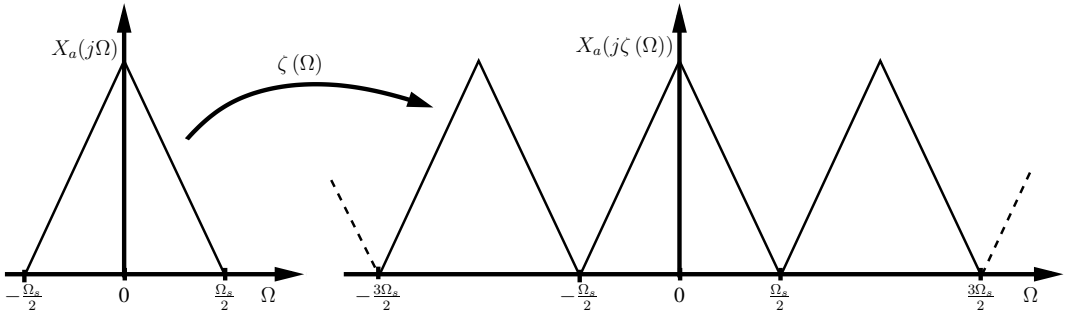

Figure 4.4: Impact of the modulo operator $\zeta(\Omega)$ on a bandlimited continuous-time spectrum $X_a(j\Omega)$. The spectrum becomes periodic with Ω_s

and

$$\check{\Omega}^{(k)} = \zeta\left(\Omega^{(k)}\right). \tag{4.15}$$

Therefore, we can denote (4.13) as

$$Y(e^{j\Omega T_s}) = \frac{1}{T_s}\sum_{k=0}^{M-1}\alpha_k\left(j\check{\Omega}^{(-k)}\right)X_a\left(j\check{\Omega}^{(-k)}\right). \tag{4.16}$$

When we now consider M frequency locations of the output spectrum spaced at multiples of $\frac{\Omega_s}{M}$, i.e., $\Omega = \Omega^{(p)}$ with $p = 0, 1, \ldots, M-1$, we can write (4.16) as

$$Y(e^{j\Omega^{(p)}T_s}) = \frac{1}{T_s}\sum_{k=0}^{M-1}\alpha_k\left(j\check{\Omega}^{(p-k)}\right)X_a\left(j\check{\Omega}^{(p-k)}\right). \tag{4.17}$$

The equation describes M frequency locations of the output spectrum, where at each frequency location the input spectrum and $M-1$ aliased spectral components overlap. This is illustrated in Fig. 4.5 for the case of $M = 4$ channel ADCs and a specific input frequency $\Omega = \Omega_0$. From Fig. 4.5 and (4.17) we see that we can relate M frequency locations of the output spectrum with M frequency locations of the input spectrum. When we express the indices p and k as

$$l = p - k \tag{4.18}$$

we can rewrite (4.17) as

$$Y(e^{j\Omega^{(p)}T_s}) = \frac{1}{T_s}\sum_{l=p-(M-1)}^{p}\alpha_{p-l}\left(j\check{\Omega}^{(l)}\right)X_a\left(j\check{\Omega}^{(l)}\right), \tag{4.19}$$

whereby the input spectrum components $X_a\left(j\check{\Omega}^{(l)}\right)$ and the output spectrum components $Y(e^{j\Omega^{(p)}T_s})$ only depend on one frequency index each. Because all indices are periodic with M, we can write for (4.19)

$$Y(e^{j\Omega^{(p)}T_s}) = \frac{1}{T_s}\sum_{l=0}^{M-1}\alpha_{p-l}\left(j\check{\Omega}^{(l)}\right)X_a\left(j\check{\Omega}^{(l)}\right), \tag{4.20}$$

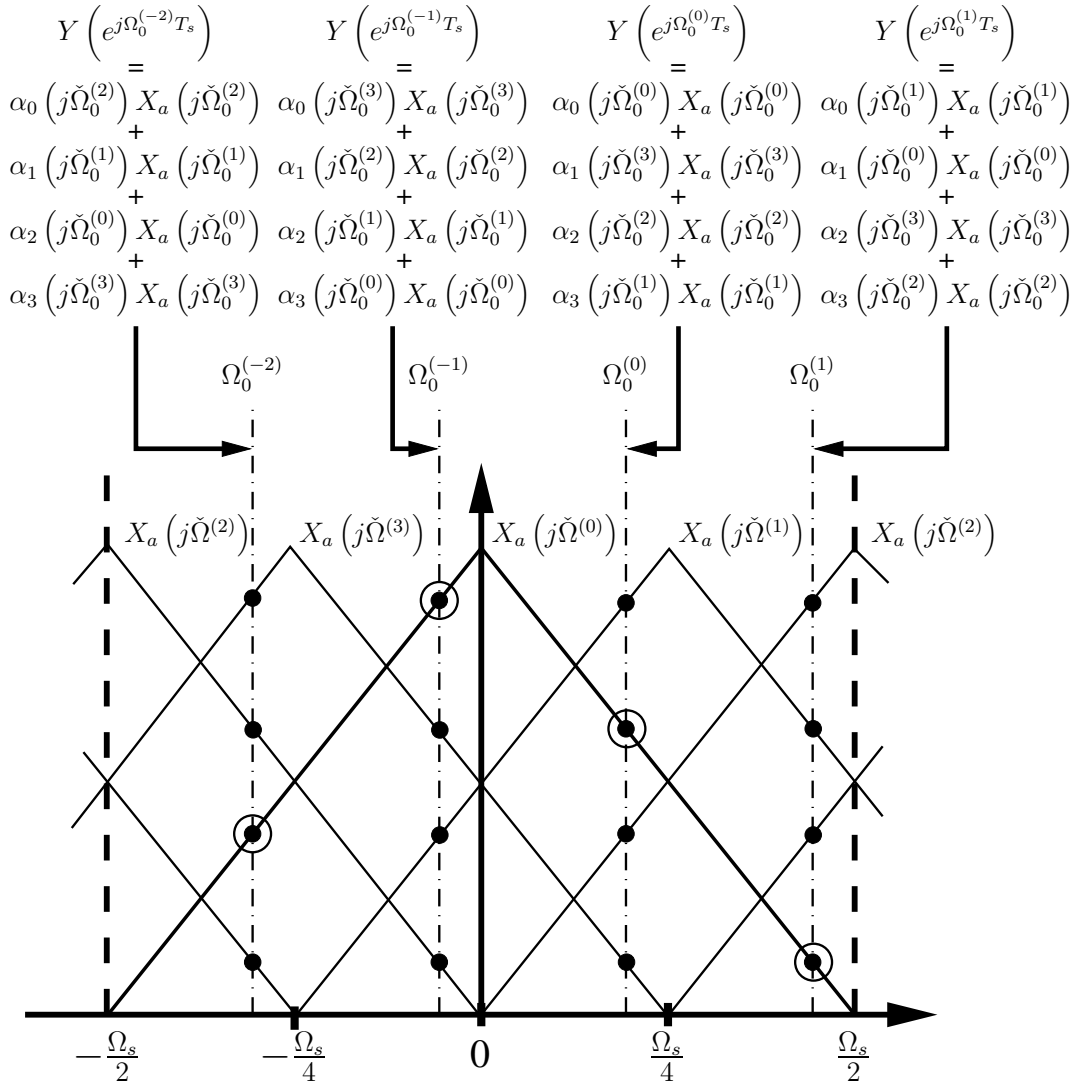

Figure 4.5: The figure illustrates the aliasing of $\frac{\Omega_s}{M}$-spaced frequency points in time-interleaved ADCs with four channels ($M = 4$). Each frequency point $Y\left(e^{j\Omega^{(p)}T_s}\right)$ of the output spectrum is the summation of the weighted input spectrum and three weighted, aliased spectral components. The original frequency points (points with borders) interact through aliasing to produce the output frequency points indicated by dashed-dotted lines. In general, the input spectrum and $M-1$ spectral components, i.e., altogether the number of channels, contribute to one particular frequency point of the output spectrum $Y\left(e^{j\Omega T_s}\right)$. Hence, we can relate M points of the input spectrum with $\frac{\Omega_s}{M}$ spacing with M points of the output spectrum with $\frac{\Omega_s}{M}$ spacing. Note that the modulo operator $\zeta(\Omega)$ allows to write the interaction of the original spectrum plus 6 aliased spectral components (altogether $6+1 = 7$ components) of the input as the interaction of only $4 = M$ periodically extended spectral components.

which can be easily rewritten in a matrix notation.

We define the output spectrum points as

$$\mathbf{y}\left(\mathbf{\Omega}\right) = \left[Y\left(e^{j\Omega^{(0)}T_s}\right), \ldots, Y\left(e^{j\Omega^{(p)}T_s}\right), \ldots, Y\left(e^{j\Omega^{(M-1)}T_s}\right)\right]^T \tag{4.21}$$

and the input spectrum points as

$$\mathbf{x}\left(\check{\mathbf{\Omega}}\right) = \frac{1}{T_s}\left[X_a\left(j\check{\Omega}^{(0)}\right), \ldots, X_a\left(j\check{\Omega}^{(l)}\right), \ldots, X_a\left(j\check{\Omega}^{(M-1)}\right)\right]^T. \tag{4.22}$$

To relate the output vector (4.21) and the input vector (4.22), we use the *channel mismatch matrix*, which is

$$\mathbf{A}\left(\check{\mathbf{\Omega}}\right) = \begin{bmatrix} \alpha_0\left(j\check{\Omega}^{(0)}\right) & \ldots & \alpha_{M-l}\left(j\check{\Omega}^{(l)}\right) & \ldots & \alpha_1\left(j\check{\Omega}^{(M-1)}\right) \\ \vdots & \ddots & \vdots & \ddots & \vdots \\ \alpha_p\left(j\check{\Omega}^{(0)}\right) & \ldots & \alpha_{p-l}\left(j\check{\Omega}^{(l)}\right) & \ldots & \alpha_{p-M+1}\left(j\check{\Omega}^{(M-1)}\right) \\ \vdots & \ddots & \vdots & \ddots & \vdots \\ \alpha_{M-1}\left(j\check{\Omega}^{(0)}\right) & \ldots & \alpha_{M-1-l}\left(j\check{\Omega}^{(l)}\right) & \ldots & \alpha_0\left(j\check{\Omega}^{(M-1)}\right) \end{bmatrix}. \tag{4.23}$$

Unless the coefficients α_p depend on the frequencies $\check{\Omega}^{(l)}$ this matrix would be a Toeplitz matrix. Finally, we can relate (4.21) and (4.22) by (4.23), which results in

$$\mathbf{y}\left(\mathbf{\Omega}\right) = \mathbf{A}\left(\check{\mathbf{\Omega}}\right)\mathbf{x}\left(\check{\mathbf{\Omega}}\right) \tag{4.24}$$

where each row of $\mathbf{A}\left(\check{\mathbf{\Omega}}\right)$ contributes to a particular frequency location and all columns of $\mathbf{A}\left(\check{\mathbf{\Omega}}\right)$ are connected by the DFT of the channel mismatches. Thus, with this relation we can determine the output spectrum if we know the input spectrum and the linear mismatches, e.g., gain, timing mismatches, magnitude, and nonlinear phase mismatches. Moreover, we can also invert the operation and calculate the input spectrum from the output spectrum. Since we have a matrix representation we can simply invert the matrix $\mathbf{A}\left(\check{\mathbf{\Omega}}\right)$ to obtain the input signal from the output signal, which is

$$\mathbf{x}\left(\check{\mathbf{\Omega}}\right) = \mathbf{A}^{-1}\left(\check{\mathbf{\Omega}}\right)\mathbf{y}\left(\mathbf{\Omega}\right) \tag{4.25}$$

Hence, for a fixed number of input frequencies, which is, for example, the case when we consider a finite number of samples, we can exactly calculate the input signal and compensate linear mismatches. Therefore, the matrix notation given by (4.24) and its inverse given by (4.25) are a generalization of the equations found in [49], which are addressing timing mismatches only.

4.3 Foreground Identification of Dynamic Linear Mismatches

We have just derived a very precise representation of channel mismatches. This representation can be used to identify channel mismatches in the frequency domain.

4.3.1 Algorithm Derivation

We start with the general characterization of dynamic linear channel mismatches. Therefore, the weighting coefficient is given by

$$\begin{aligned}\alpha_p(j\Omega) &= \frac{1}{M}\sum_{m=0}^{M-1} g_m A_m(\Omega)\, e^{-j\Omega\Delta t_m} e^{j\phi_m(\Omega)} e^{-jpm\frac{2\pi}{M}} \\ &= \frac{1}{M}\sum_{m=0}^{M-1} \Upsilon_m(\Omega)\, e^{j\vartheta_m(\Omega)} e^{-jpm\frac{2\pi}{M}},\end{aligned} \tag{4.26}$$

where we define

$$\Upsilon_m(\Omega) = g_m A_m(\Omega) \tag{4.27}$$

as the total magnitude response and

$$\vartheta_m(\Omega) = -\Omega\Delta t_m + \phi_m(\Omega). \tag{4.28}$$

as the total phase response of the mth channel ADC. From (4.20) and (4.24) we see that an input signal given by

$$X_a\left(j\check{\Omega}^{(l)}\right) \begin{cases} \neq 0 & \text{for } l = 0 \\ = 0 & \text{for } l \neq 0, \end{cases} \tag{4.29}$$

where $\check{\Omega} \neq 0$, greatly simplifies the identification process, since the input vector given by (4.22) becomes

$$\mathbf{x}\left(\check{\mathbf{\Omega}}\right) = \frac{1}{T_s}\left[X_a\left(j\check{\Omega}\right), \ldots, 0, \ldots, 0\right]^T. \tag{4.30}$$

Consequently, the output vector given by (4.24) reduces to

$$\mathbf{y}(\mathbf{\Omega}) = X_a\left(j\check{\Omega}\right)\left[\alpha_0\left(j\check{\Omega}\right), \ldots, \alpha_p\left(j\check{\Omega}\right), \ldots, \alpha_{M-1}\left(j\check{\Omega}\right)\right]^T. \tag{4.31}$$

From (4.31) we realize that the coefficients of the output vector $\mathbf{y}(\mathbf{\Omega})$ are related by the coefficients $\alpha_p\left(j\check{\Omega}\right)$, which are the outcome of a DFT of the linear mismatches, to the input signal $X_a\left(j\check{\Omega}\right)$. Hence, we can use the IDFT to calculate the linear mismatches from the output vector $\mathbf{y}(\mathbf{\Omega})$, which results in

$$\mathrm{IDFT}(\mathbf{y}(\mathbf{\Omega})) = \frac{1}{M} X_a\left(j\check{\Omega}\right) \begin{bmatrix} \Upsilon_0\left(\check{\Omega}\right) e^{j\vartheta_0\left(\check{\Omega}\right)}, \\ \vdots, \\ \Upsilon_m\left(\check{\Omega}\right) e^{j\vartheta_m\left(\check{\Omega}\right)}, \\ \vdots, \\ \Upsilon_{M-1}\left(\check{\Omega}\right) e^{j\vartheta_{M-1}\left(\check{\Omega}\right)} \end{bmatrix} \tag{4.32}$$

Note that the input spectrum $X_a\left(j\check{\Omega}\right)$ does not depend on the vector index p and is therefore just a constant multiplier regarding the IDFT computation. To explicitly obtain the magnitude mismatches we take the absolute value of (4.32), which gives

$$\left|\mathrm{IDFT}(\mathbf{y}(\mathbf{\Omega}))\right| = \frac{1}{M}\left|X_a\left(\check{\Omega}_0\right)\right|\left[\Upsilon_0\left(\check{\Omega}\right), \ldots, \Upsilon_m\left(\check{\Omega}\right), \ldots, \Upsilon_{M-1}\left(\check{\Omega}\right)\right]^T \tag{4.33}$$

and in order to explicitly obtain the phase mismatches we take the angle of (4.32), which is

$$\angle\left(\mathrm{IDFT}\left(\mathbf{y}\left(\boldsymbol{\Omega}\right)\right)\right) = \angle\left(X_a\left(\check{\Omega}_0\right)\right) + \left[\vartheta_0\left(\check{\Omega}\right), \ldots, \vartheta_m\left(\check{\Omega}\right), \ldots, \vartheta_{M-1}\left(\check{\Omega}\right)\right]^T. \quad (4.34)$$

From (4.33) and (4.34) it becomes clear that we need to know the input signal to determine the magnitude and the phase response of each channel ADC. However, since we are only interested in the channel response mismatches and not in their absolute values, we can normalize (4.33) by the average magnitude that is

$$\begin{aligned}
\overline{\left|\mathrm{IDFT}\left(\mathbf{y}\left(\boldsymbol{\Omega}\right)\right)\right|} &= \frac{1}{M}\sum_{m=0}^{M-1}\left|\mathrm{IDFT}\left(\mathbf{y}\left(\boldsymbol{\Omega}\right)\right)\right| \\
&= \frac{1}{M}\left|X_a\left(\check{\Omega}\right)\right|\frac{1}{M}\sum_{m=0}^{M-1}\Upsilon_m\left(\check{\Omega}\right) \\
&= \frac{1}{M}\left|X_a\left(\check{\Omega}\right)\right|\overline{\Upsilon}\left(\check{\Omega}\right), \qquad (4.35)
\end{aligned}$$

which results in

$$\begin{aligned}
\boldsymbol{\Upsilon}\left(\check{\boldsymbol{\Omega}}\right) &= \left|\mathrm{IDFT}\left(\mathbf{y}\left(\boldsymbol{\Omega}\right)\right)\right| / \overline{\left|\mathrm{IDFT}\left(\mathbf{y}\left(\boldsymbol{\Omega}\right)\right)\right|} \\
&= \frac{1}{\overline{\Upsilon}\left(\check{\Omega}\right)}\left[\Upsilon_0\left(\check{\Omega}\right), \ldots, \Upsilon_m\left(\check{\Omega}\right), \ldots, \Upsilon_{M-1}\left(\check{\Omega}\right)\right]^T. \qquad (4.36)
\end{aligned}$$

Thus, the resulting vector contains the magnitude mismatches that are the magnitudes at frequency $\check{\Omega}$ normalized by the average of all magnitudes. It is also possible to normalize the magnitude to one channel, which could be advantageous if one channel has already been calibrated by some other means and can therefore be used as reference.

In a very similar manner we can also obtain the phase mismatches. Therefore, we normalize (4.34) by the average phase mismatches

$$\begin{aligned}
\overline{\angle\left(\mathrm{IDFT}\left(\mathbf{y}\left(\boldsymbol{\Omega}\right)\right)\right)} &= \frac{1}{M}\sum_{m=0}^{M-1}\angle\mathrm{IDFT}\left(\mathbf{y}\left(\boldsymbol{\Omega}\right)\right) \\
&= \frac{1}{M}\left(\sum_{m=0}^{M-1}\angle\left(X_a\left(j\check{\Omega}\right)\right) + \sum_{m=0}^{M-1}\vartheta_m\left(\check{\Omega}\right)\right) \\
&= \angle\left(X_a\left(j\check{\Omega}\right)\right) + \overline{\vartheta}\left(\check{\Omega}\right). \qquad (4.37)
\end{aligned}$$

Hence, phase mismatches become

$$\begin{aligned}
\boldsymbol{\vartheta}\left(\check{\boldsymbol{\Omega}}\right) &= \angle\left(\mathrm{IDFT}\left(\mathbf{y}\left(\boldsymbol{\Omega}\right)\right)\right) - \overline{\angle\left(\mathrm{IDFT}\left(\mathbf{y}\left(\boldsymbol{\Omega}\right)\right)\right)} \\
&= \left[\vartheta_0\left(\check{\Omega}\right), \ldots, \vartheta_m\left(\check{\Omega}\right), \ldots, \vartheta_{M-1}\left(\check{\Omega}\right)\right]^T - \overline{\vartheta}\left(\check{\Omega}\right). \qquad (4.38)
\end{aligned}$$

With (4.36) and (4.38) we can determine the magnitude and the phase mismatch for any frequency in the band of interest.

Since timing and gain mismatches have much more impact on the output spectrum (cf. Sec. 3.3) magnitude and phase mismatches can be simplified in many cases to

$$\alpha_p(j\Omega) = \frac{1}{M}\sum_{m=0}^{M-1} g_m e^{-j\Omega\Delta t_m} e^{-jpm}. \tag{4.39}$$

Therefore, the total magnitude response becomes

$$\Upsilon_m(\Omega) = g_m \tag{4.40}$$

and the total phase response becomes

$$\vartheta_m(\Omega) = -\Omega\Delta t_m. \tag{4.41}$$

With (4.40) we can simplify (4.36) to

$$\begin{aligned} \boldsymbol{g} &= \left|\mathrm{IDFT}\left(\mathbf{y}\left(\boldsymbol{\Omega}\right)\right)\right| / \overline{\left|\mathrm{IDFT}\left(\mathbf{y}\left(\boldsymbol{\Omega}\right)\right)\right|} \\ &= \frac{1}{\overline{g}}\left[g_0, \ldots, g_m, \ldots, g_{M-1}\right]^T, \end{aligned} \tag{4.42}$$

and, thereby, lose the dependency on the frequency Ω. Accordingly, we can average the determined gain mismatches over different frequency locations to reduce possible estimation errors.

Similarly, we can simplify (4.38) with (4.41) to

$$\begin{aligned} -\check{\Omega}\boldsymbol{\Delta t} &= \angle\left(\mathrm{IDFT}\left(\mathbf{y}\left(\boldsymbol{\Omega}\right)\right)\right) - \overline{\angle\left(\mathrm{IDFT}\left(\mathbf{y}\left(\boldsymbol{\Omega}\right)\right)\right)} \\ &= -\check{\Omega}\left[\Delta t_m, \ldots, \Delta t_m, \ldots, \Delta t_{M-1}\right]^T + \check{\Omega}\overline{\Delta t}. \end{aligned} \tag{4.43}$$

and get the timing mismatches from the linear phase mismatches, by dividing the linear phase mismatches by the input signal frequency $\check{\Omega}$, which results in

$$\begin{aligned} \boldsymbol{\Delta t} &= \frac{-\check{\Omega}\boldsymbol{\Delta t}}{-\check{\Omega}} \\ &= \left[\ \Delta t_0, \ldots, \Delta t_m, \ldots, \Delta t_{M-1}\ \right]^T, \end{aligned} \tag{4.44}$$

where $\overline{\Delta t} = 0$, since timing mismatches are mean value free per definition. In (4.44) we evaluate the timing mismatch for one particular frequency $\check{\Omega}$. As for the gain mismatches we can repeat this process for arbitrary frequencies and average the results. Results from high input frequencies should be preferred, since there the measured linear phase mismatches are larger and much more robust against noise and other potential error sources.

4.3.2 Input Signal Requirements

In the last section we have shown that we can determine the dynamic linear mismatches for any particular frequency location. In order to use the presented method, we need a

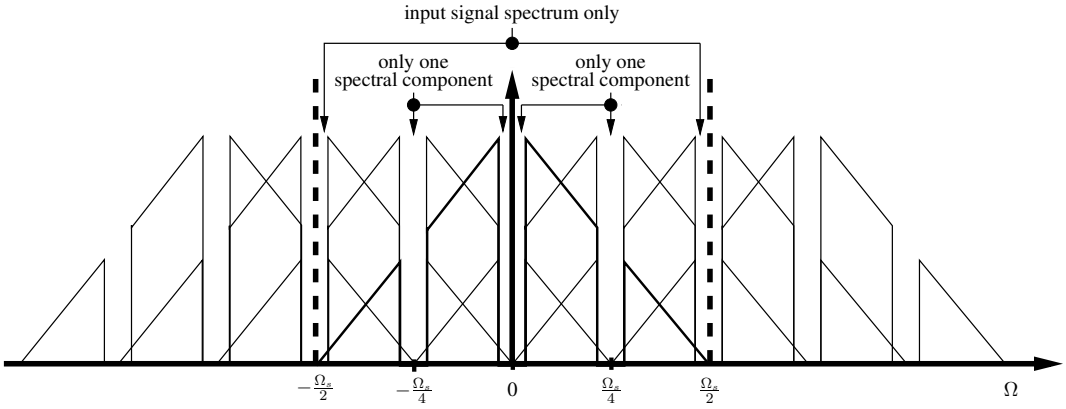

Figure 4.6: The figure shows one special input signal distribution where we can identify the channel mismatches. We see that there are frequency bands spaced by $\frac{\Omega_s}{M}$ where to each band only one aliased spectral component contributes. At the frequency region where we only have the input signal (in this figure close to half the sampling frequency) we can determine the channel mismatches. Theoretically, this band can be arbitrarily small; however, when we work with finite precision output signals, i.e., quantized signals, the signal power in the band is related to its width and can become small compared to the quantization noise power. In such situations the results are inaccurate and we have to increase the bandwidth.

special input signal spectrum, which has to meet the constraint given by (4.29). This is, for example, the case when we limit our input signal bandwidth to

$$X_a\left(j\Omega\right) = 0 \quad \text{for } |\Omega| < \Omega_c \text{ and } |\Omega| \geq \Omega_c + \frac{\Omega_s}{2M}. \tag{4.45}$$

Hence, we have an input signal with a maximum bandwidth of $\frac{\Omega_s}{2M}$. Such signals can easily be generated by low and high pass filters. To obtain the linear mismatches over the entire frequency band, we have to apply at least M such signals with different frequency bands.

Furthermore, we can apply signals with a much broader bandwidth. This is shown in Fig. 4.6, which still fulfills (4.29) for some small frequency bands. We can, however, only determine the mismatches in the frequency band where we have only signal power from the input spectrum and we obtain no characterization outside this frequency band. This is not a problem as long as we only consider mismatches which either linearly depend on the frequency or do not depend on it at all, i.e., timing and gain mismatches, because the identification is, therefore, independent from the frequency band. The generation of such signals is more complicated than in the former strongly bandlimited case given by (4.45). We need comb filters to obtain such input spectra or special known signal distributions.

In practice we will only have a finite number of samples from the time-interleaved ADC. Therefore, it is important to use some kind of windowing for spectrum estimation to minimize leakage effects [36]. Furthermore, it is important that the number of channels M and the number of samples N are related by $N_{<M>} = 0$. Otherwise, the frequency shifts $p\frac{\Omega_s}{M}$ are not coherent with the evaluated frequency bins of the DFT.

4.3.3 Simulation Results

To show the performance of the algorithm we simulate a time-interleaved ADC with eight channels ($M = 8$), which have gain and timing mismatches. The timing mismatches are drawn from a Gaussian distribution with a standard deviation of $0.01T_s$ and zero mean and the gain mismatches are drawn from a Gaussian distribution with a standard deviation of 0.005 and a mean of 1.

We investigate two cases: first, we do not consider any quantization effects and, second, we use a 10-bit quantizer. In each case, we first us a high-pass signal for mismatch identification and, in the second step, we measure the achieved SINAD with a sinusoidal input applied to the mismatch compensated system.

1. We use a high-pass input signal with signal power from $7\frac{\Omega_s}{16}$ to $\frac{\Omega_s}{2}$ consisting of 200 non-harmonic sinusoidal signals. From the input signal we take 16384 samples with the time-interleaved ADC, where the uncompensated output power spectrum of the time-interleaved ADC is shown in Fig. 4.7(a). To identify the mismatches, we calculate the DFT from the windowed (Blackman) sampled input signal [36] and take those 20 frequency bins with the highest signal power. For each frequency bin we determine the corresponding gain mismatches according to (4.42) and the corresponding timing mismatches according to (4.43). Finally, we take the average over the gain mismatches and the average over the timing mismatches for all bins to increase the estimation accuracy. We compensate the identified timing mismatches by using a perfect reconstruction method [49] to avoid any influences from the reconstruction. In Fig. 4.7(b) we see the result and recognize that we have removed all aliased spectral components below 100 dB and only see the input signal.

   For Fig. 4.8 we use the same time-interleaved ADC configuration as for Fig. 4.7, but a single sinusoidal input signal close to half the sampling frequency to precisely determine the SINAD. In Fig. 4.8(a) we see the output signal of the time-interleaved ADC without compensation. In order to remove the aliased signal components we use the channel mismatches we have identified with the broadband signal shown in Fig. 4.7(a). As for Fig. 4.7(b) we use the reconstruction method of Jenq [49] and obtain the output spectrum shown in Fig. 4.8(b). The SINAD for the uncompensated case, Fig. 4.8(a), is 4.6 ENOB and increases for the compensated case, Fig. 4.8(b), to 21.1 ENOB.

2. For the next simulation, we use a time-interleaved ADC with a 10-bit quantizer. The uncompensated output spectrum is shown in Fig. 4.9(a), where we have used the same time-interleaved ADC configuration and the same input signal as for generating Fig. 4.7. In Fig. 4.9(b) we have identified the mismatches and have compensated them. All aliased spectral components are removed and we only see the input signal spectrum and the quantization noise floor. To measure the performance of the identification method including quantization, we use a sinusoidal input signal to determine the SINAD. With the same time-interleaved ADC configuration as in Fig. 4.9 we obtain the output spectrum depicted in Fig. 4.10(a). The shown signal

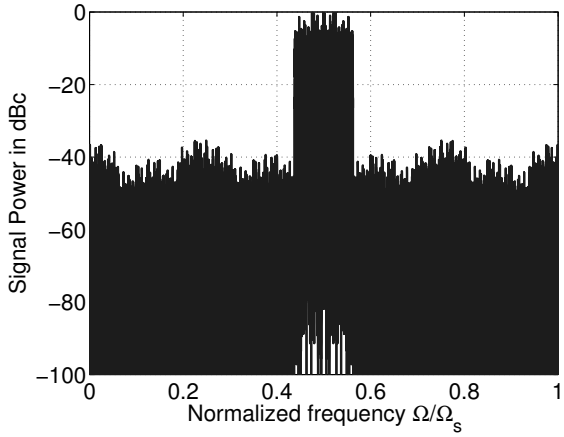

(a) Uncompensated output spectrum

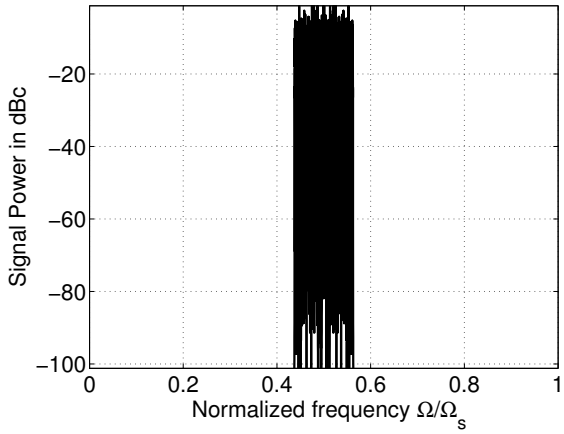

(b) Compensated output spectrum

Figure 4.7: The uncompensated output power spectrum of the time-interleaved ADC is shown in Fig. 4.7(a). After we have identified the mismatches we compensate them with a perfect reconstruction method [49] to avoid any reconstruction influence. In Fig. 4.7(b) we see the result and realize that we have removed all aliased spectral components below 100 dB.

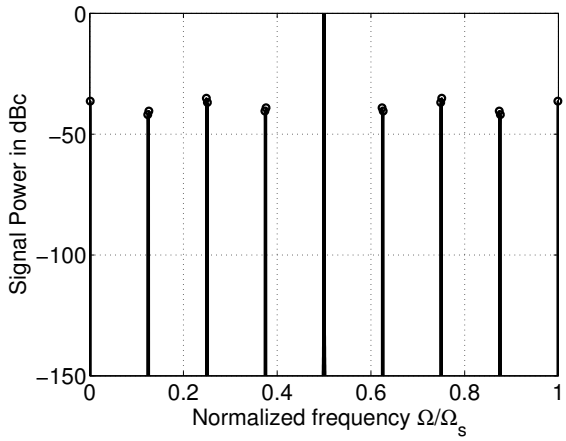

(a) Uncompensated output spectrum

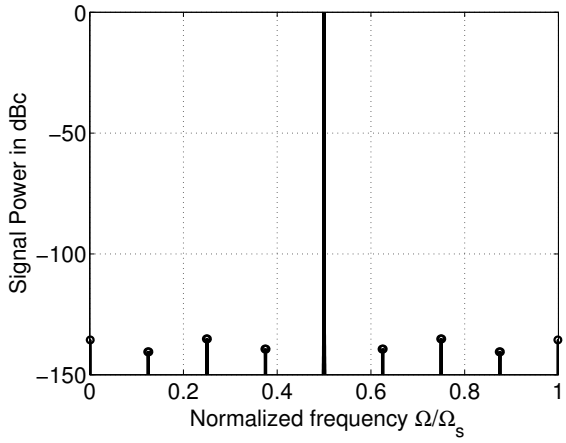

(b) Compensated output spectrum

Figure 4.8: SINAD measurement for the same time-interleaved ADC configuration as in figure Fig. 4.7. In Fig. 4.8(a) the output signal of the time-interleaved ADC for a sinusoidal input signal is close to half the sampling frequency. To compensate the aliased signal components we use the channel mismatches we have identified with the broadband signal shown in Fig. 4.7(a). The compensated output spectrum shown in Fig. 4.8(b) is produced by the method of Jenq [49]. The SINAD for the uncompensated case (cf. Fig. 4.8(a)) is 4.6 ENOB and increases for the compensated case to 21.1 ENOB (cf. Fig. 4.8(b)).

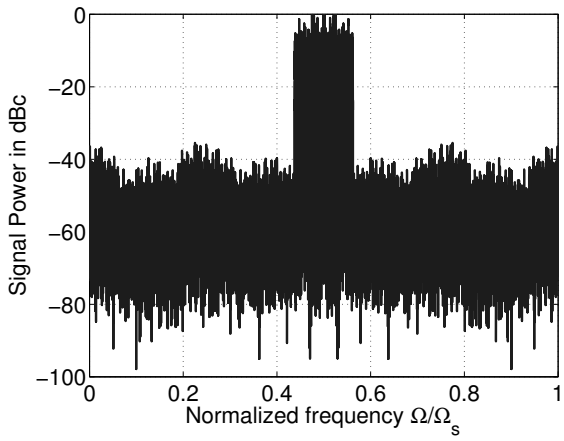

(a) Uncompensated output spectrum

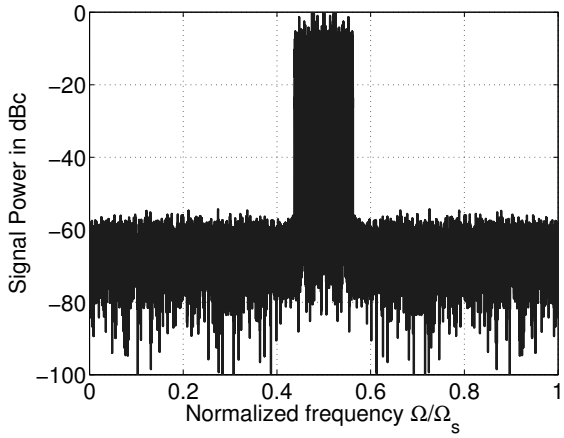

(b) Compensated output spectrum

Figure 4.9: Output spectrum of a time-interleaved ADC with and without compensation. The ADC configuration as well as the input signal are the same as in Fig. 4.7. Only the resolution of the time-interleaved ADC is 10 bits. After we have compensated the mismatches, we only see the input signal spectrum and the quantization noise floor.

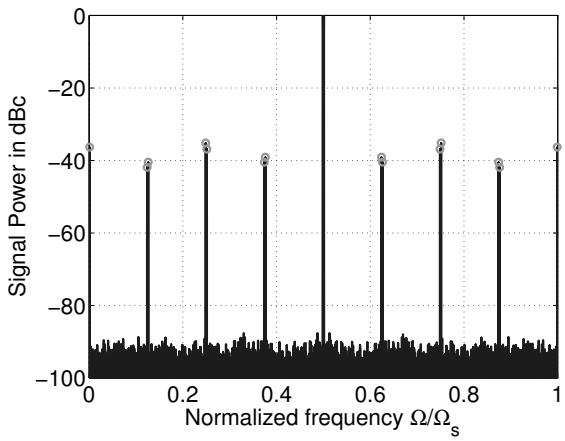

(a) Uncompensated output spectrum

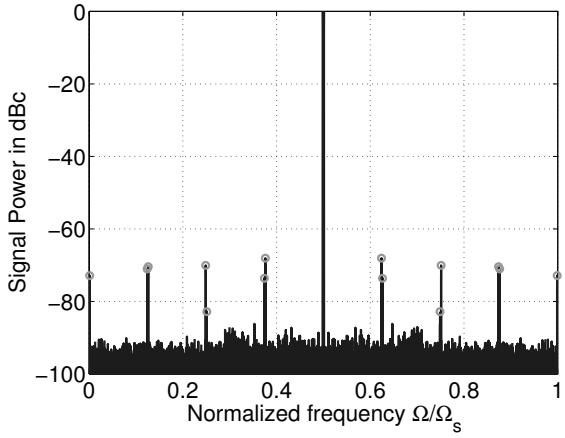

(b) Compensated output spectrum

Figure 4.10: SINAD measurement with a sinusoidal input signal. For the same time-interleaved ADC configuration as in Fig. 4.9, the output spectrum is depicted in Fig. 4.10(a). The signal shows a SINAD of 4.6 ENOB, which equals the non quantized case (cf. Fig. 4.8), since the error power is mainly determined by the mismatches. To obtain the output spectrum shown in Fig. 4.10(b), we have used the mismatches identified in Fig. 4.9 and a perfect reconstruction method [49]. The SINAD is 9.5 ENOB which is very close to an ideal 10-bit time-interleaved ADC.

has a SINAD of 4.6 ENOB, which equals the time-interleaved ADC without quantization (cf. Fig. 4.8), since the error power is mainly determined by the mismatches. To obtain the output spectrum shown in Fig. 4.10(b), we have used the mismatches identified in Fig. 4.9 and a perfect reconstruction method [49]. The SINAD is 9.5 ENOB which is very close to an ideal 10-bit time-interleaved ADC.

4.4 Background Identification of Timing Mismatches

The channel mismatch identification method introduced in Sec. 4.3 even works for bandlimited broadband signals, where the input spectrum has notch-filtered regions at $p\frac{\Omega_s}{M}$. For this special case, this method is close to a background calibration method. However, we have requirements on the input signal, which can be fulfilled for special applications only.

It is much easier to require and guarantee a low-pass filtered input signal, which can be achieved by low-pass filtering and/or oversampling the input signal. However, to obtain such an identification method we have to simplify our model and, therefore, lose the accuracy we can achieve with the method introduced in Sec. 4.3.

4.4.1 Algorithm Derivation

When we only consider timing mismatches, we can express the weighting factor $\alpha_p(j\Omega)$ of (4.3) as

$$\alpha_p(j\Omega) = \frac{1}{M}\sum_{m=0}^{M-1} e^{-j\Omega\Delta t_m} e^{-jpm\frac{2\pi}{M}}. \tag{4.46}$$

Furthermore, we can develop the linear phase mismatches $e^{-j\Omega\Delta t_m}$ in Taylor series and obtain

$$\begin{aligned} \mathcal{T}\{e^{-j\Omega\Delta t_m}\} &= 1 - j\Omega\Delta t_m - \frac{1}{2}\Omega^2\Delta t_m^2 - \dots \\ &\cong 1 - j\Omega\Delta t_m. \end{aligned} \tag{4.47}$$

Hence, for small timing mismatches Δt_m, the linear phase mismatch $e^{j\Omega\Delta t_m}$ can be approximated by a real constant part and an imaginary part $-j\Omega\Delta t_m$, which linearly scales with the input frequency.

This step simplifies the structure of the weighting coefficients $\alpha_p(j\Omega)$, which can be written with (4.47) as

$$\begin{aligned} \alpha_p(j\Omega) &= \frac{1}{M}\sum_{m=0}^{M-1} e^{-j\Omega\Delta t_m} e^{-jpm\frac{2\pi}{M}} \\ &\cong \frac{1}{M}\sum_{m=0}^{M-1} (1 - j\Omega\Delta t_m)\, e^{-jpm\frac{2\pi}{M}} \\ &\cong \delta[p_{\langle M\rangle}] - j\frac{\Omega}{M}\sum_{m=0}^{M-1} \Delta t_m e^{-jpm\frac{2\pi}{M}} \\ &\cong \delta[p_{\langle M\rangle}] - j\Omega\Delta T_p, \end{aligned} \tag{4.48}$$

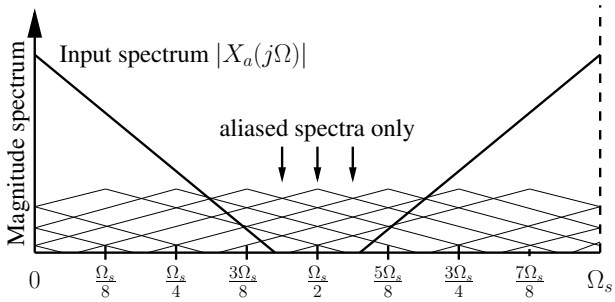

Figure 4.11: Timing mismatch identification with bandlimited input signals.

where

$$\Delta T_p = \frac{1}{M} \sum_{m=0}^{M-1} \Delta t_m e^{-jpm\frac{2\pi}{M}}. \tag{4.49}$$

The simplification of the weighting factors leads to a simplification of the channel mismatch matrix given in (4.23) as well. We can rewrite the channel mismatch matrix as

$$\hat{\mathbf{A}} = \begin{bmatrix} 1 & \dots & -j\Delta T_{M-l} & \dots & -j\Delta T_1 \\ \vdots & \ddots & \vdots & \ddots & \vdots \\ -j\Delta T_p & \dots & -j\Delta T_{p-l} & \dots & -j\Delta T_{p-M+1} \\ \vdots & \ddots & \vdots & \ddots & \vdots \\ -j\Delta T_{M-1} & \dots & -j\Delta T_{M-1-l} & \dots & 1 \end{bmatrix}, \tag{4.50}$$

where we have additionally factored out the frequency factors $\check{\Omega}^{(l)}$ and have moved them to the input vector $\hat{\mathbf{x}}\left(\check{\mathbf{\Omega}}\right)$. We obtain a Toeplitz matrix, where the rows and columns are given by a DFT of the timing mismatches. To relate the input signal and the output signal we have to modify the input vector as

$$\hat{\mathbf{x}}\left(\check{\mathbf{\Omega}}\right) = \frac{1}{T_s}\left[X_a\left(j\check{\Omega}^{(0)}\right), \dots, X_a\left(j\check{\Omega}^{(l)}\right)\check{\Omega}^{(l)}, \dots, X_a\left(j\check{\Omega}^{(M-1)}\right)\check{\Omega}^{(M-1)}\right]^T. \tag{4.51}$$

and can write

$$\mathbf{y}\left(\mathbf{\Omega}\right) = \hat{\mathbf{A}} \cdot \hat{\mathbf{x}}\left(\check{\mathbf{\Omega}}\right) \quad \Omega^{(k)} < \check{\Omega} < \Omega^{(k+1)}, k \in \mathcal{Z} \tag{4.52}$$

where $\mathbf{y}\left(\mathbf{\Omega}\right)$ is given by (4.21).

We can further express the first element of the resulting vector in (4.52) as

$$Y\left(e^{j\Omega^{(0)}T_s}\right) = \frac{1}{T_s}\left[1, \dots, -j\Delta T_{M-l}, \dots, -j\Delta T_1\right] \cdot \hat{\mathbf{x}}\left(\check{\mathbf{\Omega}}\right). \tag{4.53}$$

When we now assume a bandlimited input signal $X_a\left(j\Omega\right)$, where $X_a\left(j\Omega\right) = 0$ for $\Omega_{st_1} \leq |\Omega| \leq \Omega_{st_2}$ and $|\Omega| \geq \frac{\Omega_s}{2}$ (cf. Fig. 4.11 where $\Omega_{st_2} = \frac{\Omega_s}{2}$), and only consider outputs

$Y\left(e^{j\Omega^{(0)}T_s}\right)$ where $\Omega_{st_1} \leq |\check{\Omega}^{(0)}| \leq \Omega_{st_2}$, we can reduce (4.53) to

$$Y\left(e^{j\Omega^{(0)}T_s}\right) = \frac{1}{T_s} - j\left[\Delta T_{M-1}, \ldots, \Delta T_{M-l}, \ldots, \Delta T_1\right] \cdot \begin{bmatrix} X_a\left(j\check{\Omega}^{(1)}\right)\check{\Omega}^{(1)} \\ \vdots \\ X_a\left(j\check{\Omega}^{(l)}\right)\check{\Omega}^{(l)} \\ \vdots \\ X_a\left(j\check{\Omega}^{(M-1)}\right)\check{\Omega}^{(M-1)} \end{bmatrix}. \tag{4.54}$$

Thus, we reduce the number of elements of the vector by one and realize by considering Fig. 4.11 and (4.54) that the resulting output signal $Y\left(e^{j\Omega^{(0)}T_s}\right)$ consists of aliased spectral components only.

From our error analysis in Sec. 3.4 we know that the power of the fundamental aliased input spectrum, which is the input spectrum weighted by the average channel properties $\hat{\alpha}_0$, is much bigger than the aliased spectral components weighted by $\hat{\alpha}_p$, where $p \neq 0, \pm M, \pm 2M, \ldots$. Hence, we can approximate the input signal spectrum by the output signal spectrum

$$Y\left(e^{j\Omega^{(l)}T_s}\right) \cong \frac{1}{T_s} X_a\left(j\check{\Omega}^{(l)}\right), \tag{4.55}$$

which leads us to

$$Y\left(e^{j\Omega^{(0)}T_s}\right) = -j\left[\Delta T_{M-1}, \ldots, \Delta T_{M-l}, \ldots, \Delta T_1\right] \cdot \begin{bmatrix} Y\left(e^{j\Omega^{(1)}T_s}\right)\check{\Omega}^{(1)} \\ \vdots \\ Y\left(e^{j\Omega^{(l)}T_s}\right)\check{\Omega}^{(l)} \\ \vdots \\ Y\left(e^{j\Omega^{(M-1)}T_s}\right)\check{\Omega}^{(M-1)} \end{bmatrix}. \tag{4.56}$$

Since the input signal is bandlimited (4.56) holds for any set of K discrete frequencies $\check{\Omega}_k^{(0)}$ fulfilling $\Omega_{st_1} \leq |\check{\Omega}_k^{(0)}| \leq \Omega_{st_2}$, where k is an index number, i.e., $k = 0, 1, \ldots, K-1$, to distinguish between different frequencies. When we take those K frequencies, we can define

$$\boldsymbol{Y}^{(0)} = \left[Y\left(e^{j\Omega_0^{(0)}T_s}\right), \ldots, Y\left(e^{j\Omega_k^{(0)}T_s}\right), \ldots, Y\left(e^{j\Omega_{K-1}^{(0)}T_s}\right)\right]^T \tag{4.57}$$

and the $K \times (M-1)$ matrix

$$\boldsymbol{\Lambda} = \begin{bmatrix} Y\left(e^{j\Omega_0^{(1)}T_s}\right)\check{\Omega}^{(1)} & \ldots & Y\left(e^{j\Omega_0^{(l)}T_s}\right)\check{\Omega}^{(l)} & \ldots & Y\left(e^{j\Omega_0^{(M-1)}T_s}\right)\check{\Omega}^{(M-1)} \\ \ldots & \ddots & \ldots & \ddots & \ldots \\ Y\left(e^{j\Omega_k^{(1)}T_s}\right)\check{\Omega}^{(1)} & \ldots & Y\left(e^{j\Omega_k^{(l)}T_s}\right)\check{\Omega}^{(l)} & \ldots & Y\left(e^{j\Omega_k^{(M-1)}T_s}\right)\check{\Omega}^{(M-1)} \\ \ldots & \ddots & \ldots & \ddots & \ldots \\ Y\left(e^{j\Omega_{K-1}^{(1)}T_s}\right)\check{\Omega}^{(1)} & \ldots & Y\left(e^{j\Omega_{K-1}^{(l)}T_s}\right)\check{\Omega}^{(l)} & \ldots & Y\left(e^{j\Omega_{K-1}^{(M-1)}T_s}\right)\check{\Omega}^{(M-1)} \end{bmatrix}, \tag{4.58}$$

which leads to a system of equations given by

$$\boldsymbol{Y}^{(\mathbf{0})} = \boldsymbol{\Lambda} \cdot \begin{bmatrix} -j\Delta T_{M-1} \\ \vdots \\ -j\Delta T_{M-l} \\ \vdots \\ -j\Delta T_1 \end{bmatrix}, \tag{4.59}$$

which can be solved in the least square sense by

$$\begin{bmatrix} -j\Delta T_{M-1} \\ \vdots \\ -j\Delta T_{M-l} \\ \vdots \\ -j\Delta T_1 \end{bmatrix} = \left(\boldsymbol{\Lambda}^T \boldsymbol{\Lambda}\right)^{-1} \boldsymbol{\Lambda}^T \boldsymbol{Y}^{(\mathbf{0})}. \tag{4.60}$$

From (4.60) we notice that we have two costly operations: the construction of the square matrix $\boldsymbol{\Lambda}^T\boldsymbol{\Lambda}$ and its inverse. The matrix can be generated in $O(K(M-1)^2)$ time and its inverse can be calculated in $O((M-1)^3)$ time. Hence, the final complexity of the method depends on the number of channel ADCs M and the number of different frequencies K we use. When we assume that the matrix $\boldsymbol{\Lambda}^T\boldsymbol{\Lambda}$ is invertible, i.e., it has full rank, we can determine all coefficients $-j\Delta T_{M-l}$, which can be used to calculate the timing mismatches as (cf. (4.49))

$$\begin{aligned} -\Im\left(M \sum_{p=0}^{M-1} -j\Delta T_p e^{jpm\frac{2\pi}{M}}\right) &= -\Im\left(-j\Delta t_m\right) \\ &= \Delta t_m, \end{aligned} \tag{4.61}$$

where $\Delta T_0 = 0$ because $\sum_{m=0}^{M-1} \Delta t_m = 0$.

The matrix condition number depends on the frequency locations $Y\left(e^{j\Omega_k^{(l)} T_s}\right)$, where $k = 0, \ldots, K-1$ and $l = 1, \ldots, M-1$, and their input signal power. How much power is required to obtain a full rank matrix depends on the input signal power distribution, the noise level and the timing mismatches. For general input signals, these requirements are difficult to fulfill for only $K = M-1$ frequencies and therefore the number of considered frequencies should be quite large, i.e., $K \gg M-1$.

4.4.2 Input Signal Requirements

In the last section, we have obtained a least-squares problem for identifying the timing mismatches. In order to solve (4.60) we have to ensure that the matrix is well-conditioned. Since we have to deal with arbitrary input signal spectra, we cannot generally satisfy this requirement. However, we can avoid cases where the matrix would be always ill-conditioned.

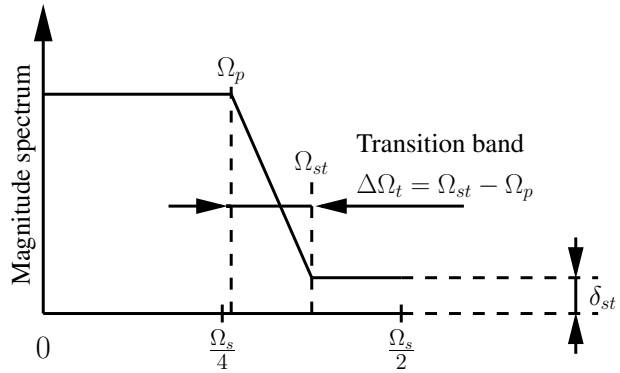

Figure 4.12: The drawing illustrates the filter specification we use in the text. The passband frequency is Ω_p, the stopband frequency is Ω_{st}, and the residual stopband amplitude is δ_{st}.

In the last section we show that we can use an arbitrary band within 0 and $\frac{\Omega_s}{2}$ to identify the timing mismatches. Nevertheless, to simplify matters we focus on the case of a low-pass bandlimited input signal. Hence, we assume a bandlimited input signal given by

$$|X_a(j\Omega)| < \delta_{st} \quad \Omega \geq \Omega_{st}, \tag{4.62}$$

where Ω_{st} is the stopband frequency, i.e., the frequency where the input filter attenuates the input signal to δ_{st}. This is illustrated in Fig. 4.12. This assumption can be fulfilled for many practical applications, where we have an anti-aliasing filter before the ADC anyway. Furthermore, we see the passband frequency Ω_p and the transition band $\Delta\Omega_t$, which is the difference between the stopband and the passband frequency, that is

$$\Delta\Omega_t = \Omega_{st} - \Omega_p. \tag{4.63}$$

To identify mismatches, the stopband attenuation of the input spectrum should be significantly larger than the difference between the input spectrum and the aliased spectral components. Furthermore, we assume that the input spectrum is rich enough so that (4.60) can be solved, e.g., a signal uniformly distributed over the frequency band.

From (4.60) we notice that we need information from each aliased spectral component in order to calculate the timing mismatches in the input signal free band. According to that, the band of interest has to fulfill two conditions: it has to be input signal free and all aliased spectral components have to contribute significant error power. If one of these conditions is not satisfied the matrix in (4.60) cannot be inverted.

To further investigate these two properties we assume ideal input filters, which leads to $\Omega_p = \Omega_{st}$ and $\Delta\Omega_t = 0$. Hence, the input signal is bandlimited to

$$\Omega_p < \frac{\Omega_s}{2} \tag{4.64}$$

and contributes even with the aliased component at $\frac{(M-1)}{M}\Omega_s$ to the input signal free band,

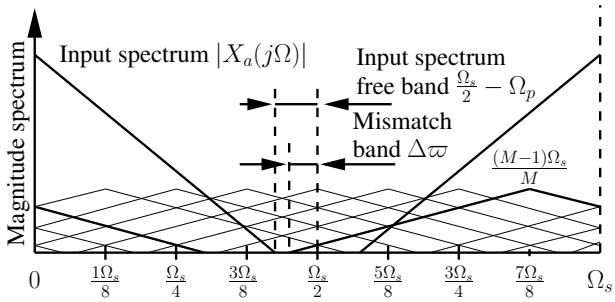

Figure 4.13: The output spectrum of a time-interleaved ADC with eight channels ($M = 8$). Because the input signal is bandlimited to Ω_p (ideal filter with transition band $\Delta\Omega_t = 0$), we obtain an input signal free band of $\frac{\Omega_s}{2} - \Omega_p$ in the output spectrum. The aliased spectral components with the largest distance of its center frequency to this input signal free band is located at $\frac{M-1}{M}\Omega_s$. If this aliased component contributes to the signal free band all other aliased components will contribute as well. Therefore, the aliased component at $\frac{M-1}{M}\Omega_s$ determines the mismatch band, which is the band where all aliased spectral components contribute but not the input spectrum itself.

if

$$\begin{aligned} \frac{(M-1)}{M}\Omega_s - \Omega_p &< \frac{\Omega_s}{2} \\ \Omega_p &> \frac{(M-2)}{M}\frac{\Omega_s}{2} \end{aligned} \tag{4.65}$$

is satisfied, which is depicted in Fig. 4.13 for the case of eight channels ($M = 8$). We see that the bandwidth of the input signal in conjunction with the aliased component at $\frac{(M-1)}{M}\Omega_s$ determines the bandwidth $\Delta\varpi$ where we can identify the channel mismatches. We will call this band the *mismatch band*, i.e., the band where we have no input signal but a superposition of all aliased spectral components. The bandwidth of the mismatch band is given by

$$\Delta\varpi = \min\left(\frac{\Omega_s}{2} - \Omega_p, \frac{\Omega_s}{2} - \frac{(M-1)}{M}\Omega_s + \Omega_p\right). \tag{4.66}$$

Hence, the bandwidth $\Delta\varpi$ becomes larger for increasing Ω_p up to a certain frequency and then decreases for increasing Ω_p, where the bounds on Ω_p are given by (4.65) and (4.64). Therefore, the maximum bandwidth is given when the frequency Ω_p of the input spectrum equals the frequency $\frac{(M-1)}{M}\Omega_s - \Omega_p$ of the spectral component at $\frac{(M-1)}{M}\Omega_s$, i.e.,

$$\begin{aligned} \frac{(M-1)}{M}\Omega_s - \Omega_p &= \Omega_p \\ \Omega_p &= \frac{(M-1)}{M}\frac{\Omega_s}{2}. \end{aligned} \tag{4.67}$$

The maximum bandwidth of the mismatch band $\Delta\varpi$ is therefore

$$\max_{\Omega_p} \Delta\varpi = \frac{\Omega_s}{2M}. \tag{4.68}$$

When we use a real filter we need some transition band $\Delta\Omega_t$ for the filter, which further reduces the maximum possible bandwidth of the mismatch band. When we require that the transition band and the channel mismatch band do not overlap, the stopband frequency Ω_{st} of the input filter is given by the aliased passband frequency $\frac{(M-1)}{M}\Omega_s - \Omega_p$ of the spectral component at $\frac{(M-1)}{M}\Omega_s$, i.e.,

$$\begin{aligned}\Delta\Omega_t &= \Omega_{st} - \Omega_p \\ &= \left(\frac{M-1}{M}\Omega_s - \Omega_p\right) - \Omega_p \\ &= \frac{M-1}{M}\Omega_s - 2\Omega_p. \end{aligned} \tag{4.69}$$

For the design of a time-interleaved ADC with the described timing mismatch identification algorithm, we are now confronted with two conflicting design objectives. The transition band of the input filter $\Delta\Omega_t$ should be as large as possible to simplify the filter design and the mismatch band should be as large as possible to improve the identification accuracy. The final choice will depend on the time-interleaved ADC specification and on the application.

We will illustrate these choices by investigating three cases. For the first case, we use a pass band frequency of Ω_p=$\frac{(M-2)}{M}\frac{\Omega_s}{2}$ and obtain the largest possible transition band

$$\begin{aligned}\Delta\Omega_t &= \frac{M-1}{M}\Omega_s - 2\frac{(M-2)}{M}\frac{\Omega_s}{2} \\ &= \frac{\Omega_s}{M}. \end{aligned} \tag{4.70}$$

Unfortunately, the bandwidth of the mismatch band reduces to

$$\begin{aligned}\Delta\varpi &= \min\left(\frac{\Omega_s}{2} - \frac{(M-2)}{M}\frac{\Omega_s}{2}, \frac{\Omega_s}{2} - \frac{M-1}{M}\Omega_s + \frac{(M-2)}{M}\frac{\Omega_s}{2}\right) \\ &= \min\left(\frac{\Omega_s}{2} - \frac{\Omega_s}{M}, \frac{\Omega_s}{2} - \frac{\Omega_s}{2}\left(\frac{2M-2-M+2}{M}\right)\right) \\ &= 0. \end{aligned} \tag{4.71}$$

Thus, we cannot identify any mismatches.

Second, we use the best case for the ideal filters, that is $\Omega_p = \frac{(M-1)}{M}\frac{\Omega_s}{2}$. Therefore, we obtain for the bandwidth of the mismatch band

$$\begin{aligned}\Delta\varpi &= \min\left(\frac{\Omega_s}{2} - \frac{(M-1)}{M}\frac{\Omega_s}{2}, \frac{\Omega_s}{2} - \frac{M-1}{M}\Omega_s + \frac{(M-1)}{M}\frac{\Omega_s}{2}\right) \\ &= \min\left(\frac{\Omega_s}{M}, \frac{\Omega_s}{M}\right) \\ &= \frac{\Omega_s}{M}, \end{aligned} \tag{4.72}$$

However, the transition band is in this case

$$\begin{aligned}\Delta\Omega_t &= \frac{M-1}{M}\Omega_s - 2\frac{(M-1)}{M}\frac{\Omega_s}{2} \\ &= 0, \end{aligned} \tag{4.73}$$

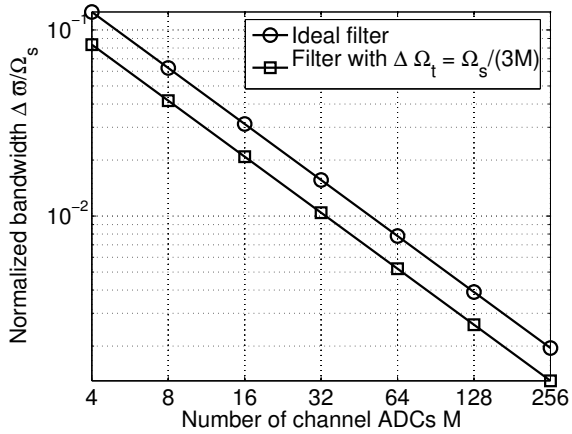

Figure 4.14: The figure shows the relation of the normalized bandwidth of the mismatch band against the number of channel ADCs. For an increasing number of channel ADCs M, the mismatch band decreases. Hence, for an increasing number of channel ADCs, we need more samples to resolve the mismatch band in order to obtain accurate timing mismatch estimates. However, with an increasing number of channels the requirements on the low-pass filter increase as well.

and cannot be implemented with real filters.

For the last case we assume $\Omega_p = \frac{(M-2)}{M}\frac{\Omega_s}{2} + \frac{\Omega_s}{3M}$ which leads to

$$\begin{aligned}\Delta\varpi &= \min\left(\frac{\Omega_s}{2} - \frac{(M-2)}{M}\frac{\Omega_s}{2} + \frac{\Omega_s}{3M}, \frac{\Omega_s}{2} - \frac{M-1}{M}\Omega_s + \frac{(M-2)}{M}\frac{\Omega_s}{2} + \frac{\Omega_s}{3M}\right) \\ &= \min\left(\frac{\Omega_s}{2}\frac{4}{3M}, \frac{\Omega_s}{2}\frac{1}{3M}\right) \\ &= \frac{\Omega_s}{3M} \end{aligned} \tag{4.74}$$

for the bandwidth of the mismatch band and

$$\begin{aligned}\Delta\Omega_t &= \frac{M-1}{M}\Omega_s - 2\left(\frac{(M-2)}{M}\frac{\Omega_s}{2} + \frac{\Omega_s}{3M}\right) \\ &= \frac{\Omega_s}{3M} \end{aligned} \tag{4.75}$$

for the transition band. This is the case where the transition band and the mismatch band have the same bandwidth. In Fig. 4.14 we have depicted the bandwidth of the normalized mismatch band for the ideal filter and the real filter, where $\Delta\varpi = \Delta\Omega_t$ (Case 3) against the number of channel ADCs. We see that, with an increasing number of channels M, the requirements on the input filter increase as well. However, even though we use real filters the mismatch band does not become much smaller than for ideal filters.

4.4.3 Simulation Results

Although background identification methods are less accurate than foreground methods, they are mandatory for many applications. In this section we show the applicability and accuracy of the introduced timing mismatch identification method.

For all simulations we use a time-interleaved ADC with eight channels ($M = 8$). Furthermore, the time-interleaved ADCs possess timing mismatches with a standard deviation from $\sigma_{\tilde{r}} = 0.1$ to $\sigma_{\tilde{r}} = 0.0001$. We use a multi-tone input signal composed of 200 sinusoidal signals with arbitrarily selected frequencies, amplitudes, and phases. The input signal is exactly bandlimited to $\Omega_p = \Omega_{st} = \frac{7\Omega_s}{16}$. From the bandlimited multi-tone input signal we take $N = 32768$ samples and identify the timing mismatches. Then we use one full-range sinusoidal input signal $A = 1$ with a frequency close to half the Nyquist frequency ($\Omega_0 = \frac{\Omega_s}{2} - 19\frac{\Omega_s}{N}$) to determine the SINAD of the time-interleaved ADC with and without timing mismatch compensation. To compensate the timing mismatches we use the perfect reconstruction method from Jenq [49].

First, we investigate the performance of the method without quantization. For each timing mismatch standard deviation we have generated 1000 time-interleaved ADCs with random timing mismatches and have determined the SINAD with and without compensation. For the first plot shown in Fig. 4.15 we have illustrated the average SINAD in ENOB against the standard deviation of the timing mismatches. We see that with a decreasing standard deviation of the timing mismatches, the SINAD of the uncompensated time-interleaved ADC increases, which conforms with our error analysis carried out in Sec. 3.5.2. For a wide range of standard deviations, the compensated curve is more than two times better than the uncompensated curve. The factor of two can be explained by the assumption we have made for the identification method, where we have only included the first two terms of the Taylor series approximation, i.e., $1 - j\Omega\Delta t_m$. Hence, the method does not consider the following term $\Omega^2 \frac{\Delta t_m^2}{2}$ of the Taylor series expansion and is therefore not fully compensated. Since this remaining uncompensated term is the square of the linear term, we can only roughly double the SINAD for the compensated case. However, we are slightly better than the factor of two, because we determine the best-fitting linear terms in the last-square sense and, therefore, we also take the higher order terms into account. Nevertheless, the compensated curve flattens for very small standard deviations, since leakage effects limit the identification accuracy. The accuracy can be improved by increasing the number of samples N. In Fig. 4.16 we plot the worst SINAD of the compensated and the uncompensated case. Thus, for all 1000 outcomes we look for the worst SINAD at each standard deviation. For a wide range of standard deviations, the compensated case is better than the uncompensated one. Only for very small standard deviations we can observe bad estimates. However, when we combine both figures as done in Fig. 4.17, we notice that the worst compensated SINAD is better than the average uncompensated SINAD for a wide frequency range. It is interesting to notice that the point where the worst-case of the compensated SINAD drops below the average uncompensated SINAD matches very well with the point where the average compensated SINAD flattens. Nevertheless, we see that for a wide range of standard deviations we do not need a detection of ill-conditioned matrices if the input signal has a uniformly distributed spectrum.

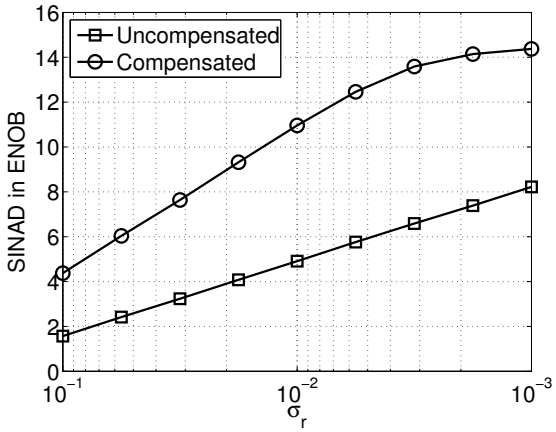

Figure 4.15: The average SINAD in ENOB against the standard deviation of the timing mismatches for compensated and uncompensated timing mismatches. The estimates for the compensation are determined by the introduced method. The compensation itself uses a perfect reconstruction method [49]. With a decreasing standard deviation of the timing mismatches, the SINAD of both the uncompensated and the compensated time-interleaved ADC increases. For a wide range of standard deviations the compensated curve is more than two times better than the uncompensated curve. Nevertheless, the compensated curve flattens for very small standard deviations, since leakage effects limit the identification accuracy. The accuracy can be improved by increasing the number of samples N.

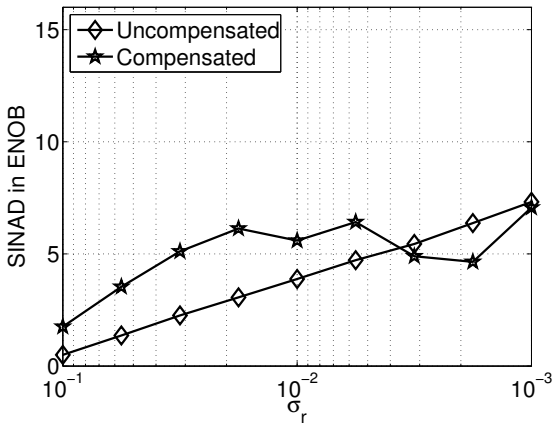

Figure 4.16: The worst SINAD in ENOB against the standard deviation of the timing mismatches for compensated and uncompensated timing mismatches. For a wide range of standard deviations, the compensated case is better than the uncompensated one. Only for very small standard deviations we can observe bad estimates, since the channel matrix is ill-conditioned.

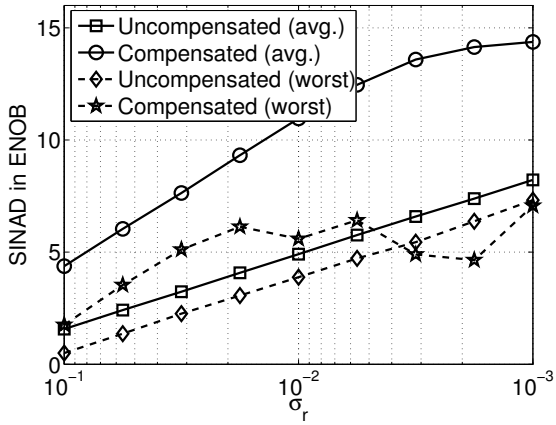

Figure 4.17: Average and worst SINAD in ENOB against the standard deviation of the timing mismatches for compensated and uncompensated timing mismatches. The worst compensated SINAD is better than the average uncompensated SINAD. The point where the worst-case of the compensated SINAD drops below the average uncompensated SINAD matches very well with the point where the average compensated SINAD flattens. Nevertheless, for a wide range of standard deviations we do not need a detection of ill-conditioned matrices if the input signal has a uniformly distributed spectrum like for this simulation.

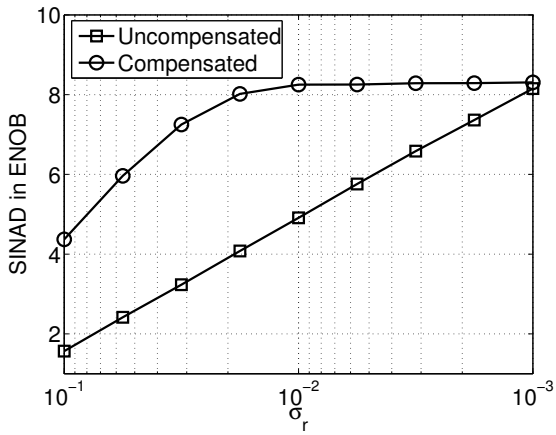

Figure 4.18: Average SINAD in ENOB of a 10-bit time-interleaved ADC against the standard deviation of timing mismatches for compensated and uncompensated timing mismatches. At a certain point, the compensated SINAD flattens. The aliased spectral components of the timing mismatches are, for the given number of samples N, in the range of the quantization noise. However, even for the sinusoidal test signal close to half the Nyquist frequency we reach a SINAD of roughly 8.2 ENOB.

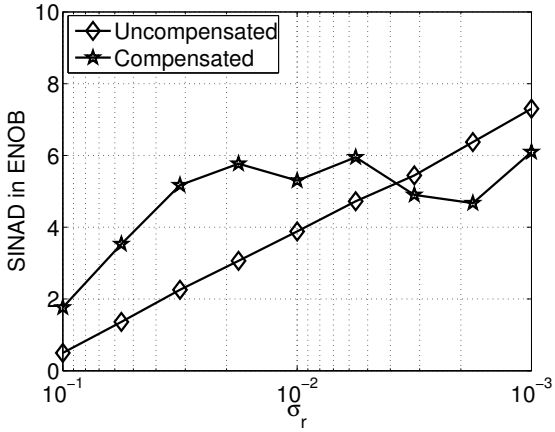

Figure 4.19: Worst SINAD in ENOB for a 10-bit time-interleaved ADC against the standard deviation of timing mismatches for compensated and uncompensated timing mismatches. Contrary to the average case, the quantization has hardly any influence on the worst-case performance of the identification method.

For the next simulation results, we use a time-interleaved ADC with quantization. All other simulation parameters remain the same. In Fig. 4.18 we see the result for the average compensated and uncompensated SINAD in ENOB. At a certain point the compensated SINAD flattens. The aliased spectral components of the timing mismatches are, for the given number of samples N, in the range of the quantization noise. Nevertheless, even for a sinusoidal test signal close to half the Nyquist frequency we reach a SINAD of roughly 8.2 ENOB. In Fig. 4.19 we see the corresponding worst compensated and uncompensated time-interleaved ADCs. Contrary to the average case, the quantization has hardly any influence on the worst-case performance of the identification method, because the accuracy problem comes from bad input signal distributions.

In Fig. 4.20 we compare the average and the worst SINAD. The curves are very similar to the ones without quantization plotted in Fig. 4.17. For this figure, we see that the curve flattens because of the 10-bit quantization, whereas for Fig. 4.17 it flattens because of leakage effects.

In Fig. 4.21 we compare the identification method with and without quantization. Quantization limits the performance but the general behavior of the method is the same.

4.5 Conclusion

The main advantage of our foreground identification method is the possibility to accurately characterize all dynamic linear mismatches, which is not possible with any other method presented in the literature. When we only consider gain and timing mismatches, we can use the additional information from different frequency points to average the results in order to obtain more accurate results. Therefore, this method can be used to determine the gain

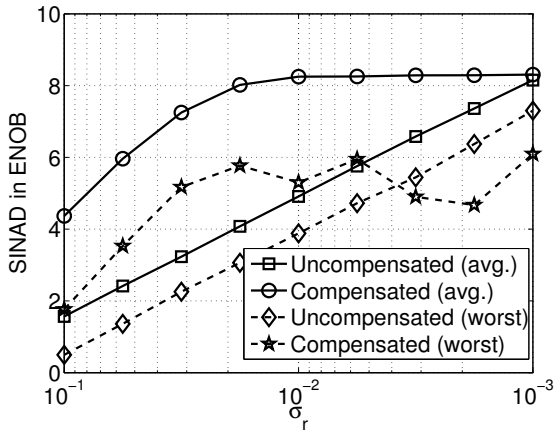

Figure 4.20: Average and worst SINAD in ENOB of a 10-bit time-interleaved ADC against the standard deviation of the timing mismatches for compensated and uncompensated timing mismatches. The curves are very similar to the ones without quantization plotted in Fig. 4.17. They only begin to flatten for different standard deviations.

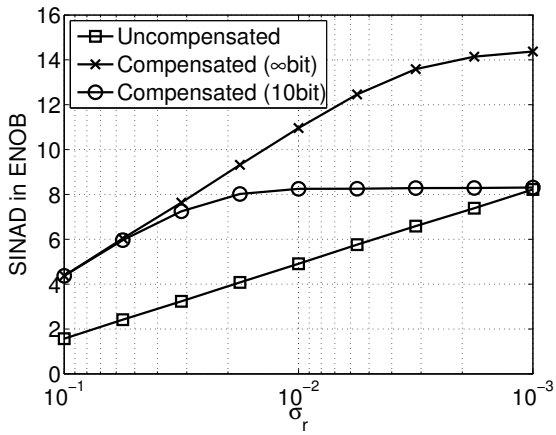

Figure 4.21: Quantization limits the performance of the identification method but its general behavior is the same with or without quantization.

and the timing mismatches for high resolution applications, where it is mandatory to have accurate estimates or to fully characterize the linear mismatches in a time-interleaved ADC. For special input signal distributions it can even be used as background calibration method as well.

Another unsolved problem was an accurate background timing mismatch identification method for broadband signals close to half the sampling frequency. With our background algorithm we can have input signals with bandwidths very close to half the sampling frequency and still obtain accurate estimation results. For practical applications, we are limited by the quantization resolution of the time-interleaved ADC; however, as simulations have shown, we obtain even for quantized samples very accurate timing mismatch estimates. A problem for the algorithm are input signals which have their signal power non-uniformly distributed over the frequency band. Then the channel mismatch matrix can become ill-conditioned and the method fails. We can detect such matrices directly by evaluating the condition number [74], which is computationally involved, or we can try to analyze the input signal power distribution, which can be done much more efficiently. While the research on this topic is far from being completed, our simulation results demonstrate the high utility of our method even under practical realization constraints.

Chapter 5

Channel Mismatch Compensation

The performance of time-interleaved ADCs is limited by channel mismatches. In the preceding chapter, we have discussed identification methods for channel mismatches, which is the first step for compensating mismatch errors. The second step, i.e, the compensation itself, can either be done on-chip or elsewhere in the signal processing chain. For that purpose, we need an extra information channel, which carries the estimated channel mismatches. With this extra information and the distorted samples we can reconstruct the original samples whenever and wherever we want, provided that the reconstruction algorithm satisfies our demands.

In many practical applications the time-interleaved ADC has to compensate for the sample distortions in order to reduce the dependency on the following signal processing components. This on-chip compensation has some implications which make the compensation of channel mismatches so difficult. First, the compensation method, e.g., a filter or an interpolation algorithm, has to run at the high-rate of Ω_s. Although, we can convert many digital algorithms to multirate counterparts running at a lower rate, we still have the problem of additional hardware, which in many cases increases the power consumption significantly. Second, we can only use algorithms, which can process the data in real-time, since otherwise we have to stop the conversion process of the time-interleaved ADCs. Third, the requirements of high-rate and high-accuracy applications are contrary to the requirement of low-power consumption.

In the following, we outline the compensation of two important channel mismatches. We introduce a nonlinearity mismatch compensation method in Sec. 5.2, which is the first of its kind, and two timing mismatch compensation methods, which have a very low power consumption compared to other methods. In Sec. 5.3 we use transfer characteristics tuning for timing mismatch compensation and in Sec. 5.4 we use spectral shaping.

5.1 Introduction

Compensation of channel mismatches reduces currently to the compensation of offset, gain, and timing mismatches. One reason are the open problems with compensating the timing mismatches. Contrary to gain and offset mismatches, which can easily be compensated by appropriate adders and multipliers in each channel ADC, timing mismatches are much more difficult to compensate. Nevertheless, new results found in the literature, e.g., [59, 60, 113], are very promising and, therefore, in the future nonlinearity errors and nonlinearity

mismatches will become the limiting factors of time-interleaved ADCs for high-resolution applications.

Since gain and offset mismatches are easy to correct most authors investigate them only in combination with their identification [33, 93, 23, 25]. Adaptive offset and gain methods are discussed in [33, 93], where the authors add randomized sequences to the input signal. In [23] the authors chop the input signal to estimate and compensate for the offset mismatch. Different gradient based adaptive algorithms for gain, offset, and timing mismatch compensation can be found in [25].

The basic theorems to cope with timing mismatches can be found in the works of Shannon [122] and Nyquist [95]. The book from Marvasti [87] covers many theoretical aspects of nonuniform sampling. However, the engineering point of view of advanced sampling theory is provided by Papoulis in [100], where he shows that a band-limited function $x_a(t)$ is uniquely determined in terms of the samples $x_s(nT_s)$ of the responses $x_m(t)$ of M linear systems with an input $x_a(t)$, sampled at $\frac{1}{M}$ the Nyquist rate. It is easy to show that the general sampling expansion (GSE) of Papoulis covers the special problem of nonuniform sampling as well. Nonuniform sampling is identical to the timing mismatch problem in time-interleaved ADCs, where the number of channels goes to infinity. In practical implementations, time-interleaved ADCs only have a finite number of channel ADCs, which can be related to a periodic nonuniformly sampled signal, which is a special case of nonuniform sampling. Furthermore, we have very small timing deviations compared to the average sampling period, which further simplify the treatment of timing mismatch compensation in time-interleaved ADCs, when compared to the general non-uniform sampling problem.

Several iterative reconstruction approaches for nonuniform sampling can be found in [86]. However, iterative algorithms are hardly applicable for the real time processing of data. As shown in chapter 2, a time-interleaved ADC is similar to a discrete-time multirate system. Hence, when we approximate the analog representatives of time-interleaved ADC components as discrete-time counterparts, we can use multi-rate reconstruction methods [139]. Although we can theoretically achieve a perfect reconstruction [31], the so far presented filter designs [91, 113] need a very large number of coefficients and still they only have a moderate accuracy.

An improvement to this approach can be found in [57, 58, 59, 82], where the authors directly work with time-interleaved ADCs represented as hybrid filter banks. By using oversampling and exploiting Farrow structure based fractional delay filters [78] the authors can compensate the timing mismatch by only adjusting M weighting coefficients, which are obtained by a matrix inversion. Thus, the used filters do not have to be redesigned, whenever the timing mismatches change. A further improvement to this method by the same authors is presented in [60, 61]. There, the authors introduce a filter design technique, which is able to directly approximate the inverse filter structure by discrete-time FIR filters. With this approach the number of coefficients and the achievable accuracy is remarkably better than the one in [91, 113].

Other proposed methods are either computationally expensive or inaccurate [49, 55]. In [49] the authors introduce a perfect reconstruction method, which works well for a finite number of samples. It can be shown that [49] is a special case of the filter design given

in [60]. The interpolation method proposed in [54, 55] either needs a large oversampling factor or is very inaccurate.

An interesting compensation method is described in [43, 44], where the authors use a correlation between two channel mismatches to compensate for offset, gain, and timing mismatches. Because they only use a two channel system, the compensation of the timing mismatch can be reduced to a filter in one channel. Unfortunately, it is not shown how this approach can be extended to more than two channel ADCs.

All these briefly discussed methods work in the digital domain. However, we can also find mixed signal solutions in the literature. Often we are not interested in compensating mismatch errors but in reducing their impact on a particular figure of merit. One example is randomization, introduced in [56]. By randomizing the order of the channel ADCs the aliased spectral components become uniformly distributed over the frequency band and, therefore, the spurious-free dynamic range (SFDR) is significantly increased compared to the non-randomized case. The signal-to-noise and distortion ratio (SINAD) is not improved in any way, since we are only distributing the error power. Further investigations on randomization can be found in [131] and in [24], where the authors propose and analyze a clock switching structure.

Another possibility used in today's high-speed ADCs are digitally adjustable delays in the clock path [112, 110]. Furthermore, we can use special sampling methods [34] to avoid timing mismatch effects.

5.2 Compensation of Nonlinearity Errors and Mismatches

In Sec. (2.5) we have modeled time-interleaved ADCs and found an input/output relation including static nonlinear effects. In this section we analyze the input/output relation to exploit the time-interleaved structure in order to find methods to reduce and compensate nonlinearity errors as well as nonlinearity mismatches.

5.2.1 Using Complementary Nonlinearities

When we consider the higher order nonlinear terms of (2.60), which are

$$T_{p,k}\left(j\Omega\right) = \frac{1}{M}\sum_{m=0}^{M-1} c_{k,m}\left(X_a\left(j\Omega\right)A_m(\Omega)e^{j\phi_m(\Omega)}\right)^{(*k)} e^{-j\Omega\Delta t_m} e^{-jpm\frac{2\pi}{M}}, \tag{5.1}$$

we see that the coefficients $c_{k,m}$ introduce error power if they are different from zero and introduce mismatch error power as soon as they differ from each other. The K coefficients $c_{k,m}$ are the coefficients of a power series describing the nonlinearity of the mth channel ADC mainly given by the smoothed transfer curve of the quantizer. In Sec. (3.3) we have shown that the linear-phase mismatches $e^{-j\Omega\Delta t_m}$ have much more impact on the time-interleaved ADC performance than nonlinear-phase mismatches $e^{j\phi_m(\Omega)}$ and magnitude mismatches $A_m(\Omega)$. Therefore, we have found a reduced input/output relation (cf. (3.42)),

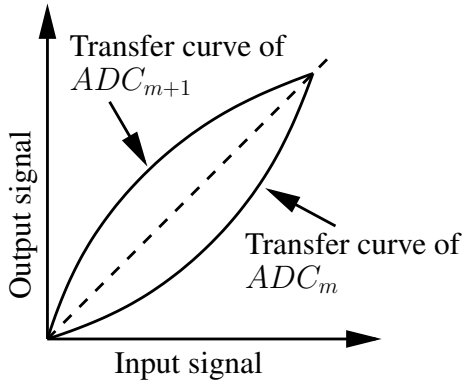

Figure 5.1: Two consecutive channel ADCs with complementary transfer curves. The dashed line represents the ideal 45° transfer curve. In this illustration the two transfer curves of the channel ADCs are ideally complementary and the average of the curves results in the ideal transfer curve. Therefore, because of interleaving the channel ADCs, nonlinearity error power becomes nonlinearity mismatch error power, which is located around $\frac{\Omega_s}{2}$. In a real environment we can only approximately achieve this ideal case.

where higher order terms are given by

$$T_{p,k}\left(j\Omega\right) = \frac{1}{M}\sum_{m=0}^{M-1} c_{k,m} e^{-j\Omega\Delta t_m} e^{-jpm\frac{2\pi}{M}}. \tag{5.2}$$

From (5.2) we see that we do not have any higher order nonlinearity errors and mismatches when the coefficients $c_{k,m}$ are zero. Due to component nonidealities, we always have to deal with nonlinear transfer curves and this ideal case cannot be achieved. However, it seems feasible to design roughly complementary transfer curve pairs [20], which are illustrated for two channel ADCs in Fig. 5.1. Thus, we design a time-interleaved ADC with an even number of channel ADCs, where two consecutive channel ADCs have complementary transfer curves. Therefore, at least the lower-ordered coefficients will fulfill $c_{k,m} \cong -c_{k,m+1}$ for $k > 1$ and $m = 0, 2, 4, ...M-2$ and we obtain vanishing nonlinearity errors, i.e., the mean over all m for a fixed k in $c_{k,m}$ tends to zero. Since the error power is not compensated in any way it is still in the system but almost shifted to half the Nyquist frequency band. These nonlinearity mismatches can be compensated by using oversampling and filtering or by an advanced randomization, which is discussed in the following section. The filtering approach has the advantage that we really compensate for the nonlinearity error and mismatches, but it has the disadvantages of a high oversampling ratio, which is given by

$$\lambda \geq 2\hat{k}, \tag{5.3}$$

where

$$\lambda = \frac{\Omega_s}{2\Omega_0}, \tag{5.4}$$

Ω_0 is the highest input frequency, and $\hat{k}$ is the highest nonlinearity, which should be filtered.

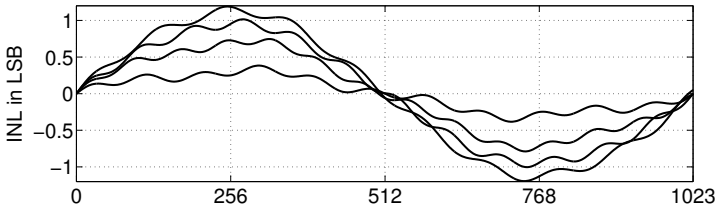

(a) Nonlinearities

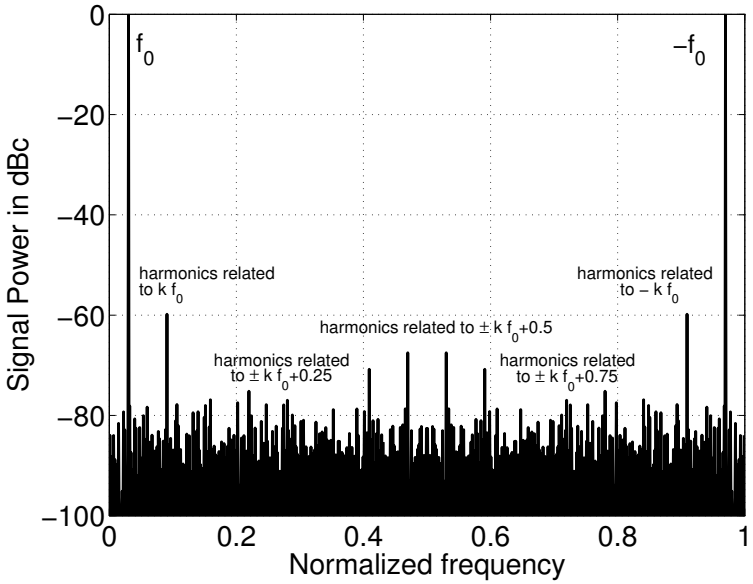

(b) Output spectrum

Figure 5.2: Time-interleaved ADC with four channels. The nonlinearities, characterized as integral nonlinearity (INL) and differential nonlinearity (DNL), of all channels are different but have similar general characteristics.

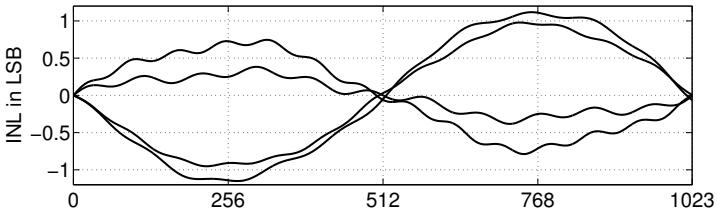

(a) Nonlinearities

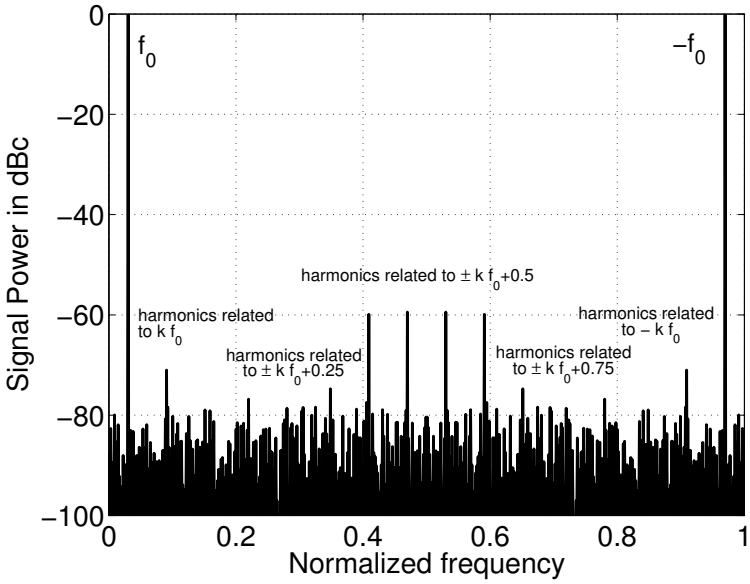

(b) Output spectrum

Figure 5.3: Time-interleaved ADC with nonlinearity mismatches and pairwise complementary nonlinearities. The nonlinearities of all channels are different but are designed to be approximately pairwise complementary ($c_{k,m} \cong -c_{k,m+1}$ for $k > 1$ and $m = 0, 2, 4, ...M-2$).

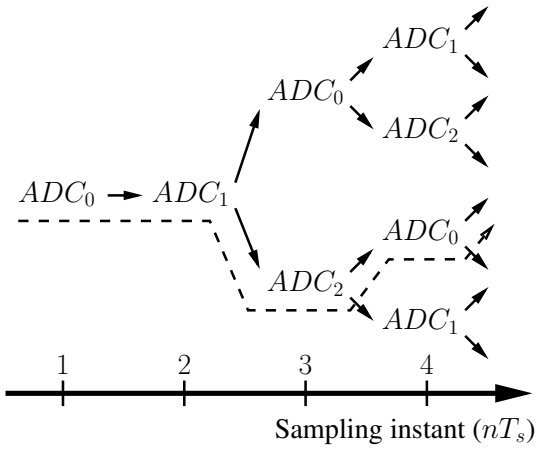

Figure 5.4: Randomization of the channel ADCs with $M = 2$ and $R = 1$. The dashed line shows one possible random sequence.

To illustrate the concept we have simulated a time-interleaved ADC with 10-bit resolution. For each simulation we have taken 1024 samples of a sinusoidal input signal and plot the output spectrum. In Fig. 5.2 we see a time-interleaved ADC with four channels and nonlinearity errors. Beside the harmonics which are related to the input signal (nonlinearity errors), we notice additional aliased harmonics centered around $p\frac{\Omega_s}{M} \pm kf_0$ = [$0 \pm kf_0$, $0.25 \pm kf_0$, $0.5 \pm kf_0$, $0.75 \pm kf_0$] (nonlinearity mismatches). In Fig. 5.3 we use pairwise complementary nonlinearities. For the simulation, we have mirrored every other transfer curve. We see that the harmonics around the input signal (case where $p = 0$) have been significantly reduced, since the average of the nonlinearity curves is close to zero, but the power of the aliased upper harmonics has increased. This error power can be easily filtered by a low-pass filter.

5.2.2 Using Randomization and Complementary Nonlinearities

Another possibility to decrease the influence of the spectral shaped nonlinearity errors is a special randomization variant.

It has been shown that channel randomization is one way to increase the SFDR in a time-interleaved ADC [56, 131]. For that purpose, we either need additional channel ADCs or we have to decrease the sampling rate. If we have a redundant array of $(M + R)$ channel ADCs, operating with a sampling interval of MT_s, and we would like to build a time-interleaved ADC with a sampling interval of T_s, we can choose at each time instant among $R + 1$ channel ADCs without violating the sampling constraints. This is illustrated in Fig. 5.4, where $M = 2$ and $R = 1$. After the first two channel ADCs (ADC_0, ADC_1) have taken a sample we can choose between ADC_0 and ADC_2, without violating our sampling constraints. After we have, for example, chosen ADC_2 we can decide between ADC_0 and ADC_1 and so forth. If we use a periodic pseudo random sequence with the period N to determine the sequence of channel ADCs, fulfilling the above requirements, where one

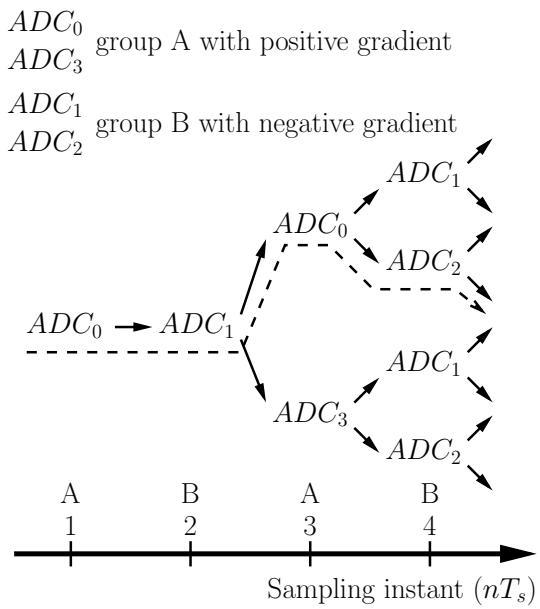

Figure 5.5: Randomization with complementary channel ADCs with $M = 2$ and $R = 2$. At each sampling instant we can choose a channel ADC from either group A or group B. The channel ADCs in group A have complementary transfer curves to the channel ADCs in group B. This could roughly be fulfilled by designing transfer curves of channel ADCs with positive and negative gradients. The selection process within each group is the same as for the conventional randomization. We can only choose channel ADCs, which have finished their conversion process, which takes at least MT_s, and are ready to take a new sample. The dashed line shows one possible random sequence.

period of the sequence is defined as $\{v_n\}_0^{N-1}$ with $v_n \in \{0, 1, ..., M + R - 1\}$, we can rewrite (5.2) as

$$T_{p,k}(j\Omega) = \frac{1}{N} \sum_{n=0}^{N-1} c_{k,v_n} e^{-j\Omega\Delta t_{v_n}} e^{-jpn\frac{2\pi}{N}}. \tag{5.5}$$

Through randomization we effectively increase the number of channels to N and, consequently, the number of aliased spectral components. Nevertheless, the amplitude of the DFT coefficients, except for $p = 0$, decreases due to the factor $\frac{1}{N}$ in (5.5) and, therefore, the distortion power is distributed more uniformly over the entire frequency band. For $p = 0$, the DFT returns the average value, which is advantageous if we only consider gain and timing mismatches, since we amplify the input spectrum by the average gain and the average timing mismatch tends to zero. However, the other harmonics caused by the common nonlinearities behave like in a single ADC. Thus, the randomization process distributes all mismatch depending harmonics over the frequency band, but harmonics related to the input frequency are still there and limit the SFDR.

In the last section we have already shown that for $p = 0$ the averaged summation over all c_{k,v_n} has to be close to zero in order to remove the harmonics related to the input fre-

quency. A solution exploiting this property is to design channel ADCs, which have pairwise complementary nonlinearities, so that in the ideal case

$$c_{k,\upsilon_n} = -c_{k,\upsilon_{n+1}} \tag{5.6}$$

holds for $k > 1$ and $n = 0, 2, 4, \ldots, N-2$. Hence, channel ADCs designed in this way and the method of randomization distribute the error power of the nonlinearities over the entire frequency band. In order to combine randomization and the idea of complementary nonlinearities, we have to modify the randomization scheme, which is illustrated in Fig. 5.5. In contrast to conventional randomization methods for time-interleaved ADCs, we need at least two additional channel ADCs or more, i.e., $R = 2, 4, 6, \ldots$, to roughly fulfill the ideal case given in (5.6). Hence, we build two groups of channel ADCs, wherefrom we can select ADCs. One group includes all channel ADCs with a transfer curve which have a positive gradient and the other group includes all channel ADCs with a transfer curve which have a negative gradient. At each sampling instant we can randomly choose a channel ADC from one group of channel ADCs. Hence, at each time instant we can choose among $\frac{R}{2} + 1$ channel ADCs.

To give an example we have simulated a time-interleaved ADC with randomization and pairwise complementary nonlinearities. We have simulated the time-interleaved ADC with 10-bit resolution in three different channel configurations. For each configuration we have taken 1024 samples of a sinusoidal input signal and plotted the output spectrum. In Fig. 5.6 we see this time-interleaved ADC with six channels. To allow randomization of the channels, we assume for each channel ADC a least possible sampling interval of MT_s, i.e., we set $M = 4$ and $R = 2$. Therefore, we can choose for each sampling instant between $R+1 = 3$ channel ADCs. From the output spectrum we notice that all mismatches are distributed over the frequency band, but the harmonics of the input signal are still there, as we would expect it from our analysis. In Fig. 5.7 we combine randomization of a six channel time-interleaved ADC with pairwise complementary nonlinearities. Hence, we can choose for each sampling instant between $\frac{R}{2}+1 = 2$ channel ADCs, without violating the sampling constraint and the constraint that a channel ADC with a negative gradient should follow a channel ADC with a positive gradient and vice versa. As a result we obtain a nearly flat noise floor. There are still small harmonics in the fundamental interval, since we have not simulated perfectly complementary pairs of nonlinearities, as this would not have reflected real ADC channels. Nevertheless, for the three configurations the SFDR has increased from 59.8 dB to 72 dB and the total harmonic distortion (THD) has decreased from -59.7 dB to -69.7 dB. However, it should be noticed that compared to the oversampling and filtering method, discussed in the last section, we do not improve the SINAD, since the amount of error power caused by nonlinearities is not influenced by this special kind of randomization.

5.3 Timing Mismatch Compensation through Transfer Characteristics Tuning

In Sec. (3.2) we have shown that there is a strong relation between aperture delay mismatches and the linear phase of the transfer characteristics of the S/H circuits in sample

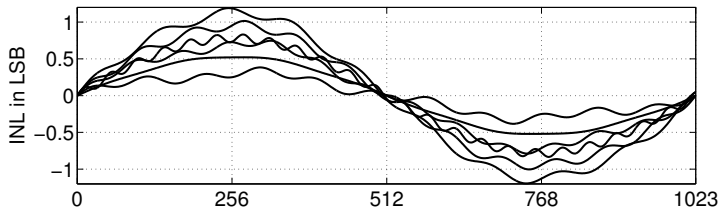

(a) Nonlinearities

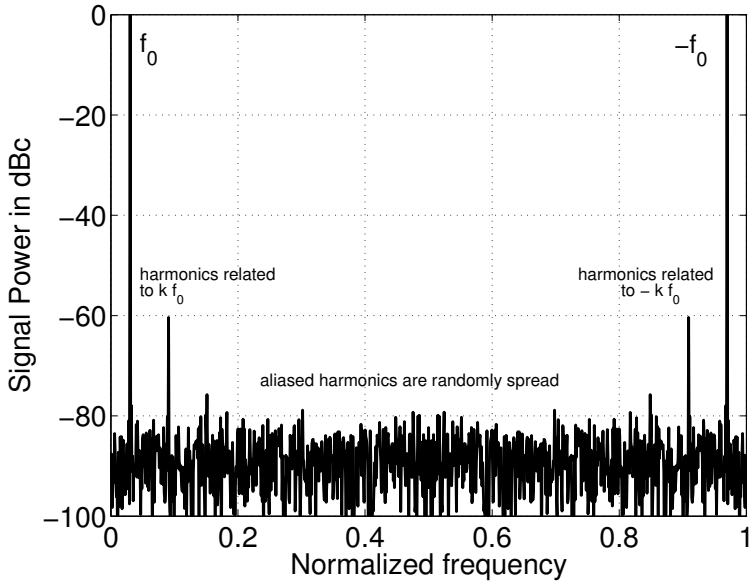

(b) Output spectrum

Figure 5.6: Time-interleaved ADC with six channels to allow randomization without decreasing the sampling rate. The aliased frequencies are randomly spread over the frequency band but the harmonics of the input signal are still there.

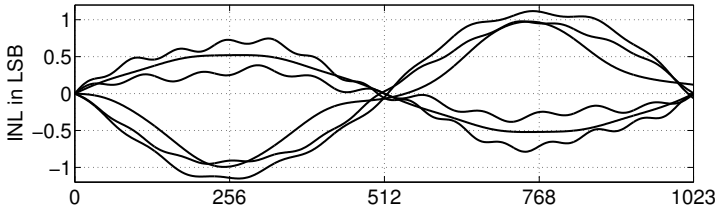

(a) Nonlinearities

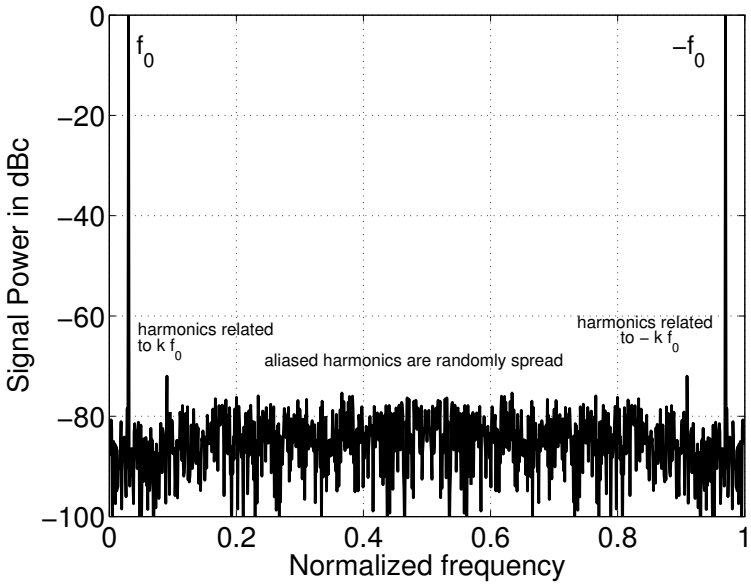

(b) Output spectrum

Figure 5.7: Time-interleaved ADC with six channels, pairwise complementary nonlinearities, and randomization. Most of the error power is distributed over the frequency band.

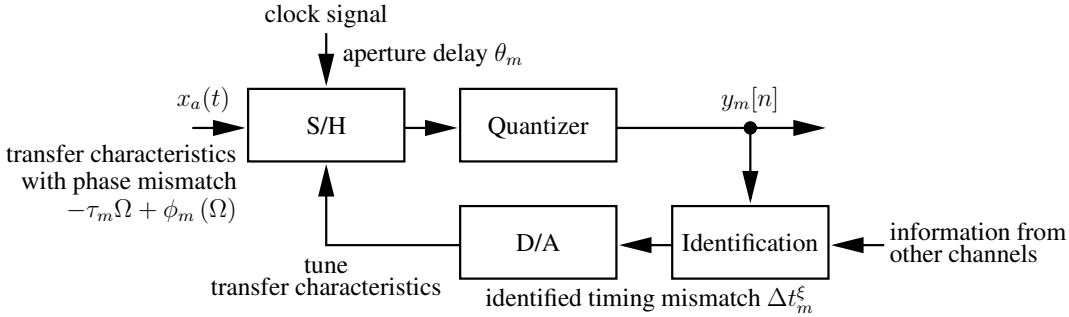

Figure 5.8: The principle of tuning the transfer characteristics is illustrated for the mth channel ADC. The timing mismatch is identified on the digital side and transformed into a corresponding analog signal, which tunes the transfer characteristics of the S/H circuit.

mode. In this section we will show how to tune the transfer characteristics in order to compensate for timing mismatches.

5.3.1 Analysis of Transfer Characteristics Tuning

Digital identification of timing mismatches and modification of aperture delays through switchable delay elements in the clock signal paths is one successful method to correct timing mismatches in high-speed time-interleaved ADCs [110]. However, we can see from our analysis that we can also modify the transfer characteristics of the S/Hs in order to compensate timing mismatches. The basic concept is shown in Fig. 5.8, where we use an adaptive system, which identifies the timing mismatch on the digital side and tunes the transfer characteristics of the S/H circuits on the analog side. Since the timing mismatch is identified, we only approximate the phase response mismatch, i.e. neglect the nonlinear phase mismatches.

In Fig. 5.9 we see the total phase response of the reference S/H (solid line without markers), which can be, for example, the average phase response of all channels, which is

$$\vartheta_R(\Omega) = -\tau_R\Omega + \phi_R(\Omega) - \theta_R\Omega \tag{5.7}$$

and the total phase response of the S/H of the mth channel (solid line with markers), which is

$$\vartheta_m(\Omega) = -\tau_m\Omega + \phi_m(\Omega) - \theta_m\Omega \tag{5.8}$$

The difference between these two phase responses is the total phase response mismatch $\Delta\vartheta_m(\Omega)$, which degrades the time-interleaved ADC performance. Taking (2.55), (2.56), (2.57), (5.7), and (5.8) into account, the phase response mismatch of the mth channel can be written as

$$\begin{aligned}
\Delta\vartheta_m(\Omega) &= \vartheta_m(\Omega) - \vartheta_R(\Omega) \\
&= -(\tau_R + \Delta\tau_m)\Omega + \tau_R\Omega - (\theta_R + \Delta\theta_m)\Omega + \theta_R\Omega + \phi_m(\Omega) - \phi_R(\Omega) \\
&= -(\Delta\tau_m + \Delta\theta_m)\Omega + \Delta\phi_m(\Omega) \\
&= -\Delta t_m\Omega + \Delta\phi_m(\Omega).
\end{aligned} \tag{5.9}$$

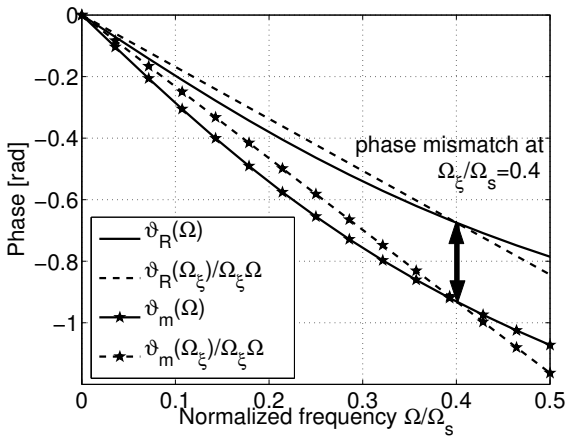

Figure 5.9: Comparison of the total phase response $\vartheta_R(\Omega)$ of the reference S/H and the total phase response $\vartheta_m(\Omega)$ of the S/H of the mth channel. The dashed lines are linear approximations of the phase responses with intersection points at 0 and Ω_ξ/Ω_s.

Hence, for small nonlinear phase response mismatches $\Delta\phi_m(\Omega)$, the identified phase response mismatch corresponds to the timing mismatch $\Delta t_m\Omega$ of the time-interleaved ADC.

When we identify the phase response mismatch with a single sinusoidal input frequency Ω_ξ (cf. Fig. 5.9) and determine the timing mismatch for that frequency from the phase response mismatch, we obtain

$$\begin{aligned}\Delta t_m^\xi &= \frac{\Delta\vartheta_m(\Omega_\xi)}{\Omega_\xi}\\ &= -\Delta t_m + \frac{\Delta\phi_m(\Omega_\xi)}{\Omega_\xi}\\ &= -(\Delta\tau_m + \Delta\theta_m) + \frac{\Delta\phi_m(\Omega_\xi)}{\Omega_\xi}.\end{aligned} \tag{5.10}$$

From (5.10) we see that in order to compensate the identified timing mismatch, i.e., forcing Δt_m^ξ to zero, we can tune the time constant τ_m, which influences Δt_m directly as well as $\Delta\phi_m(\Omega)$. However, when we compensate the identified timing mismatch we implicitly work with linear approximations of the nonlinear total phase response of the time-interleaved ADC. As we see from Fig. 5.9 the compensation for such linear approximations can be only exact for the frequency points Ω_ξ and 0. To analyze the behavior of frequencies different from Ω_ξ and 0 we assume that Δt_m^ξ of (5.10) is zero for all channels. Thus, by tuning all τ_m, we have compensated the identified timing mismatch in each channel for the frequency location Ω_ξ. From (5.10) we notice that the identified timing mismatch Δt_m^ξ is zero if the timing mismatch Δt_m equals the nonlinear phase response mismatch, which is

$$\Delta t_m = \frac{\Delta\phi_m(\Omega_\xi)}{\Omega_\xi}. \tag{5.11}$$

Hence, we can substitute (5.11) in (5.9) to obtain the remaining phase response mismatch, which results in

$$\Delta\vartheta_m^{\xi}(\Omega) = -\frac{\Delta\phi_m(\Omega_\xi)}{\Omega_\xi}\Omega + \Delta\phi_m(\Omega). \tag{5.12}$$

Finally, we can write for a time-interleaved ADC with compensated timing mismatches

$$\alpha_p = \frac{1}{M}\sum_{m=0}^{M-1} A_m^{\xi}(\Omega) e^{-j\left(\frac{\Delta\phi_m(\Omega_\xi)}{\Omega_\xi}\Omega - \Delta\phi_m(\Omega)\right)} e^{-jpm\frac{2\pi}{M}}, \tag{5.13}$$

where we also obtain modified magnitude response mismatches $A_m^{\xi}(\Omega)$, since the phase response and magnitude response mismatches are connected by (2.52). Hence, the compensation results in a remaining nonlinear-phase response mismatch $e^{-j\left(\frac{\Delta\phi_m(\Omega_\xi)}{\Omega_\xi}\Omega - \Delta\phi_m(\Omega)\right)}$ and a magnitude mismatch $A_m^{\xi}(\Omega)$. The compensation of linear-phase mismatches, i.e., timing mismatches, is for small nonlinear-phase response mismatches $\Delta\phi_m(\Omega)$ independent from the frequency Ω_ξ, where the mismatches have been identified. This is a particularly useful result, since especially in digital background identification algorithms, e.g. [26], the timing mismatch in each channel is assumed to be constant over all frequencies and, therefore, some kind of average is taken over the in fact input spectrum dependent timing mismatch estimates. Nevertheless, if the application of the time-interleaved ADC allows to use foreground calibration, e.g., [47], an exact identification and compensation of the timing mismatches close to half the Nyquist rate $\frac{\Omega_s}{2}$ would be preferable.

It should be noticed that tuning the time constant τ_m not only modifies the phase responses but also the magnitude responses $A_m^{\xi}(\Omega)$, which ultimately limits the performance of the compensation method. Nevertheless, the inherent problem of mismatching magnitudes cannot be avoided by using other compensation methods such as digital compensation methods or tuning of the clock delays, since the transfer characteristics of the channel ADCs will always mismatch. Hence, even for an ideal digital timing mismatch compensation algorithm the magnitudes still mismatch and limit its performance. At the end it depends on how much timing mismatch error power comes from the aperture delay mismatch and how much error power comes from the linear-phase transfer characteristics mismatch. When the transfer characteristics mismatch is the dominating error source, tuning the transfer characteristics results in a better performance as we then implicitly tune the magnitude mismatches, too.

The main advantage of this compensation method is its very low power consumption compared to digital methods. It only needs one backward path from the digital side to tune the transfer characteristics. In the simplest case, this can be a binary information, which increases or decreases a transfer characteristics determining component.

5.3.2 Simulation Results

For the simulations we have used a first-order low pass S/H model; nevertheless, since all S/H circuits are designed to have a close-to linear phase, the basic properties of real S/H circuits will be present even in this simple model.

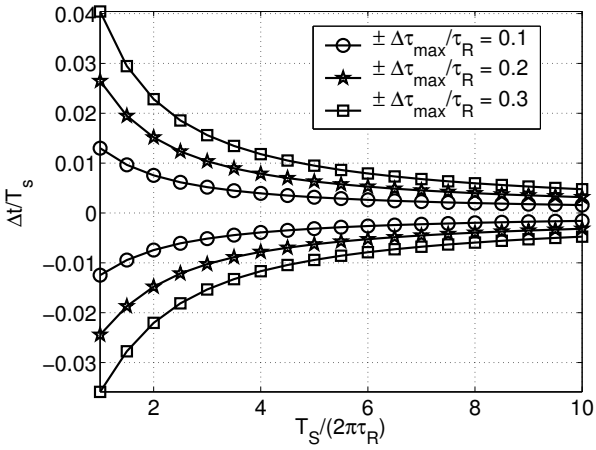

Figure 5.10: The plot shows the possible range of bandwidth independent timing deviations, which can be corrected by tuning the bandwidth when the maximal deviation from the reference time constant τ_R/T_s is ± 10, ± 20, and ± 30 percent.

The range where we can tune the transfer characteristics also determines the maximal aperture delay mismatches we can compensate for. The transfer characteristics is determined by the first-order frequency response

$$P_m(j\Omega) = \frac{1}{1 + j\Omega\tau_m}. \tag{5.14}$$

The inverse of the time constant τ_m is the angular cut-off frequency Ω_c of the mth channel, where the signal power is attenuated 3 dB below the nominal signal power. The time constant τ_m is given by

$$\tau_m = R_m C_m, \tag{5.15}$$

where R_m is the resistance and C_m is the capacitance. Hence, the phase of the transfer characteristics is given by

$$-\tau_m\Omega + \phi_m(\Omega) = -\arctan(\Omega\tau_m). \tag{5.16}$$

Accordingly, if we know the time constant τ_R and the range within we can control the time constant $\pm\Delta\tau_{\text{max}}$, we can calculate the upper and lower bounds of the maximum allowed aperture deviation $\Delta\theta_m$, we are able to compensate for. This is illustrated in Fig. 5.10, where we show the bounds for different nominal time constants τ_R and ranges.

In Fig. 5.11 the performance of the presented method is illustrated. We have numerically simulated a time-interleaved ADC with two channels, where the first channel has no aperture delay mismatch and the second one has an aperture delay mismatch of $\Delta\theta_1/T_s = \Delta t_1/T_s$, i.e., $\tau_m/T_s = 0$. The timing mismatch caused by the aperture delay mismatch is compensated with our adaptive system by using the foreground calibration method presented in Sec. 4.3. For the uncompensated case, Fig. 5.11(a), both channel

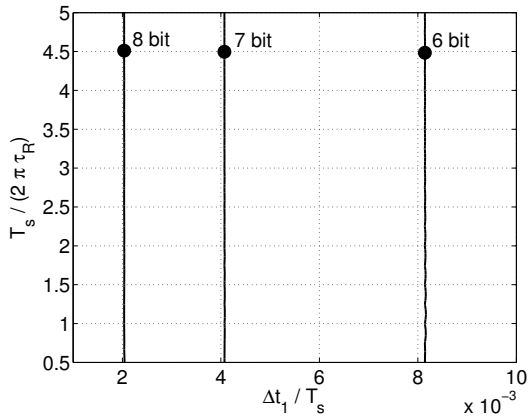

(a) Uncompensated time-interleaved ADC

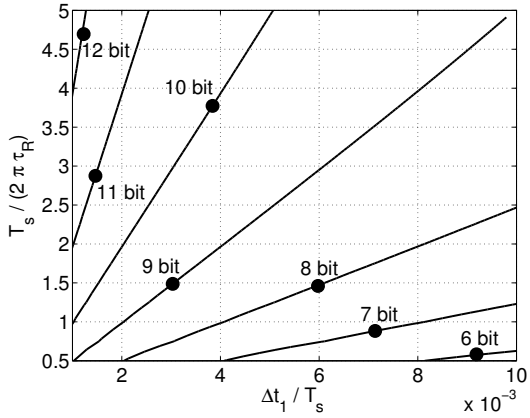

(b) Compensated time-interleaved ADC

Figure 5.11: Comparison of a simulated time-interleaved ADC with two channels ($M = 2$) before and after timing mismatch compensation. Dependence of the SINAD in ENOB (solid equipotential lines), measured for a sinusoidal input frequency close to half the Nyquist rate, on the timing mismatch $\Delta t_1/T_s$ and the normalized reference time constant $T_s/(2\pi\tau_R)$. The first channel has no aperture delay mismatch $\Delta\theta_0/T_s = 0$, whereas the second differs with $\Delta\theta_1/T_s$. For the uncompensated case both channels have the same time constants $\Delta\tau_0 = \Delta\tau_1 = \Delta\tau_R$. Thus, the timing mismatch Δt_1 is solely caused by aperture delay mismatches and $\Delta t_1/T_s = \Delta\theta_1/T_s$. Therefore, the SINAD only depends on the timing mismatches but not on the reference time constant τ_R, i.e., for decreasing Δt_1 the SINAD increases. For the compensated case, we tune the time constant $\Delta\tau_1$ and thereby change the transfer characteristics in order to compensate the timing mismatch. For the same timing mismatch $\Delta t_1/T_s$, we obtain for the compensated case a much better SINAD, which now depends on the reference time constant τ_R as well. However, the improvements of the SINAD are limited, by the introduced magnitude response mismatch.

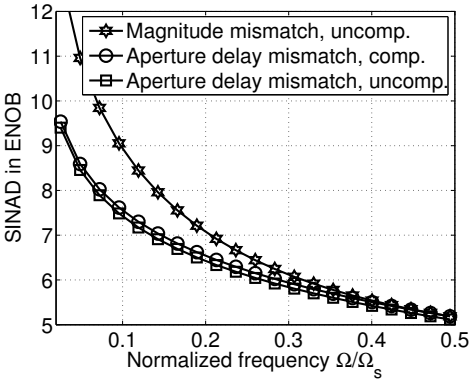

(a) $\frac{T_s}{2\pi\tau_R} = 2$

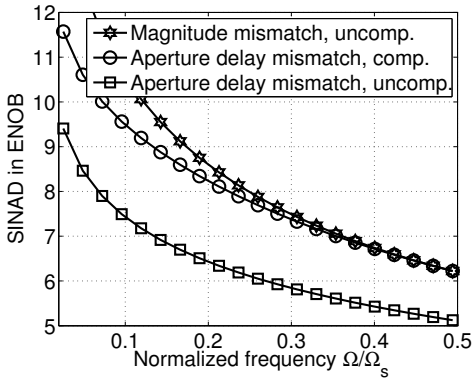

(b) $\frac{T_s}{2\pi\tau_R} = 1$

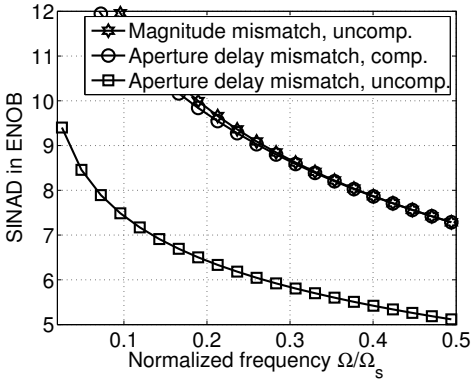

(c) $\frac{T_s}{2\pi\tau_R} = 0.5$

Figure 5.12: Analysis of the magnitude mismatch effects for time-interleaved 2-channel ADCs with transfer characteristics tuning. The aperture delay mismatches of the channel ADCs were $\Delta\theta_m = 0$ and $\Delta\theta_m = 0.0151$, respectively. For each plot we have used a different normalized reference time constant $\frac{T_s}{2\pi\tau_R}$. The first curve (squares) shows the uncompensated case. The second curve (circles) shows the compensated case, where we have tuned the transfer characteristics in order to compensate for the timing mismatch, which equals the aperture delay mismatch for this example. To show the effect of the limiting magnitude mismatches the third curve (starred) shows the time-interleaved ADC with uncompensated magnitude mismatches only, i.e., without any timing mismatches and phase mismatches. The curve with the magnitude mismatch is very close to the curve showing the compensated case, from where we can conclude that the arising magnitude mismatch is the limiting factor. We also notice that the compensation is getting better for higher reference time constants τ_R, but it should be noticed that we also need a larger deviation from this reference time constant ((a) 10%, (b) 13.1%, and (c) 25%) to compensate for the timing mismatch.

ADCs have no transfer characteristics mismatches and the SINAD is merely depending on the timing mismatch. In Fig. 5.11(b) we have compensated the timing mismatch by tuning the transfer characteristics for a frequency Ω_ξ close to half the Nyquist rate. The result is a significant improvement of the SINAD, where the limiting factor of the method is the magnitude mismatch arising from the diverging frequency responses of transfer characteristics.

This is illustrated for one particular timing mismatch configuration in Fig. 5.12. In each plot we see three cases: the uncompensated timing mismatch, the compensated timing mismatch, and the uncompensated magnitude mismatch only. For the first case we do not use any compensation. For the second case we tune the transfer characteristics in order to compensate for the timing mismatches. For the third case we tune the transfer characteristics in order to compensate for the timing mismatches as well, but after the compensation we switched off the aperture delay mismatches and also the phase response mismatches of the tuned transfer characteristics. Therefore, only the magnitude mismatches of tuned transfer characteristics remain in the simulated system. Note that this is an artificial situation which should only show the performance limiting magnitude mismatches. From the three curves we can clearly see that the magnitude mismatch limits the performance, i.e., for normalized nominal time constants $T_s/(2\pi\tau_R) \leq 1$ the compensated and the magnitude curve are very close to each other.

It should be noticed that we have chosen extreme simulation conditions, where the timing mismatch is solely caused by the aperture delay mismatch, since the transfer characteristics are assumed to match perfectly. In reality, the transfer characteristics will mismatch and will contribute to the timing mismatch as well. This contribution could be removed without the disadvantage of diverging magnitude mismatches, which would increase the efficiency of the algorithm even more.

5.4 Spectral Shaping in Time-Interleaved ADCs

Spectral shaping of error power means shifting the error power to some input signal free region in the frequency band. In order to guarantee some input signal free band, we have to oversample the input signal and have to ensure that it is bandlimited, i.e., $X_a(j\Omega) = 0$ for $|\Omega| \geq \Omega_{\text{max}}$ and $\frac{\Omega_s}{2} \geq \Omega_{\text{max}}$. Then the shifted error power can be easily filtered out.

Without any spectral shaping, we could maximally gain 3 dB for uniformly distributed error power, i.e., noise power, when we cut away half the frequency band. Unfortunately, the mismatch error power is not uniformly distributed; moreover, it tends to produce peaks in the output spectrum, which is illustrated in Fig. 5.13(a). One method to avoid such peaks is to use randomization of the channel ADCs [24, 56], which achieves an approximately uniform spectral distribution of the mismatch error power. Thereby, it is possible to gain roughly 3 dB by oversampling and filtering the input signal. In order to gain more than 3 dB we can search for better non-random channel ADC sequences, which produce a more favorable spectral shaping of the mismatches.

5.4.1 Spectral Shaping of Timing Mismatches

To understand how timing mismatch peaks appear, we analyze the output spectrum of a time-interleaved ADC with timing mismatches Δt_m, which can be written as (cf. (3.39) and (3.41))

$$Y\left(e^{j\Omega T_s}\right) = \frac{1}{T_s}\sum_{p=-\infty}^{\infty} \alpha_p\left(j\left(\Omega - p\frac{\Omega_s}{M}\right)\right) X_a\left(j\left(\Omega - p\frac{\Omega_s}{M}\right)\right), \tag{5.17}$$

where

$$\alpha_p\left(j\Omega\right) = \frac{1}{M}\sum_{m=0}^{M-1} e^{-j\Omega\Delta t_m} e^{-jpm\frac{2\pi}{M}}. \tag{5.18}$$

We see that for the pth term in (5.17) the input signal $X_a\left(j\Omega\right)$ is weighted by a frequency dependent complex weighting factor $\alpha_p\left(j\Omega\right)$ and is frequency shifted by $p\frac{\Omega_s}{M}$ afterwards. In the ideal case, this complex factor $\alpha_p\left(j\Omega\right)$ is 1 for $p = 0$ and 0 otherwise. Furthermore, we realize that $\alpha_p\left(j\Omega\right)$ is the discrete Fourier transform (DFT) of the timing mismatches. Thus, the factor $\alpha_p\left(j\Omega\right)$ is periodic in p with period M and a change of the channel sequence can influence its values. The values of $\alpha_p\left(j\Omega\right)$ determine the output spectrum and, therefore, an optimization of the channel ADC sorting sequence can achieve the desired spectral shaping of the mismatch power.

The effect of channel sequence optimization is shown in Fig. 5.13, and the required architecture is illustrated in Fig. 5.14. Without any optimization the unfiltered digital output signal appears like in Fig. 5.13(a). After the timing mismatches are identified and a new optimized channel sequence is determined (cf. Fig. 5.14) the output becomes spectrally shaped, as shown in Fig. 5.13(b). The spectrally shaped output spectrum can be simply filtered, which results in the spectrum shown in Fig. 5.13(c).

In order to describe any permutation of the channel ADC sequence, we have to find a mapping between the conventional index ordering $\langle 0, 1, 2, \ldots, M-1\rangle$ and the reordered sequence. To this end, we define the set of possible index values as $\{0, 1, \ldots, M-1\}$ from where we can choose permutations $\upsilon = \langle \upsilon_m\rangle_{m=0}^{M-1}$. The simplest permutation equals $\upsilon = \langle 0, 1, \ldots, M-1\rangle$, whereby the conventional sequence of channel ADCs, i.e., ADC_0, ADC_1, ..., ADC_{M-1}, does not change. Another example for a permutation is $\upsilon = \langle M-1, M-2, \ldots, 0\rangle$, which reverses the conventional order.

By employing these definitions we can formulate our combinatorial optimization problem as

$$\min_{\pi(\upsilon)} \frac{1}{2\pi}\int_{-\Omega_{\max}}^{\Omega_{\max}} \left|Y\left(e^{j\Omega T_s}\right) - X_a(j\Omega)\right|^2 d\Omega, \tag{5.19}$$

where $Y\left(e^{j\Omega T_s}\right)$ is as in (5.17) and

$$\alpha_p\left(j\Omega\right) = \frac{1}{M}\sum_{m=0}^{M-1} e^{-j\Omega\Delta t_{\upsilon m}} e^{-jpm\frac{2\pi}{M}}. \tag{5.20}$$

The set $\pi\left(\upsilon\right)$ contains all possible free circular permutations [161] over υ in order to minimize the mismatch error power in the region of the input signal bandwidth $[-\Omega_{\max}, \Omega_{\max}]$. From (5.19) we realize that the minimization depends on the input spectrum $X_a(j\Omega)$.

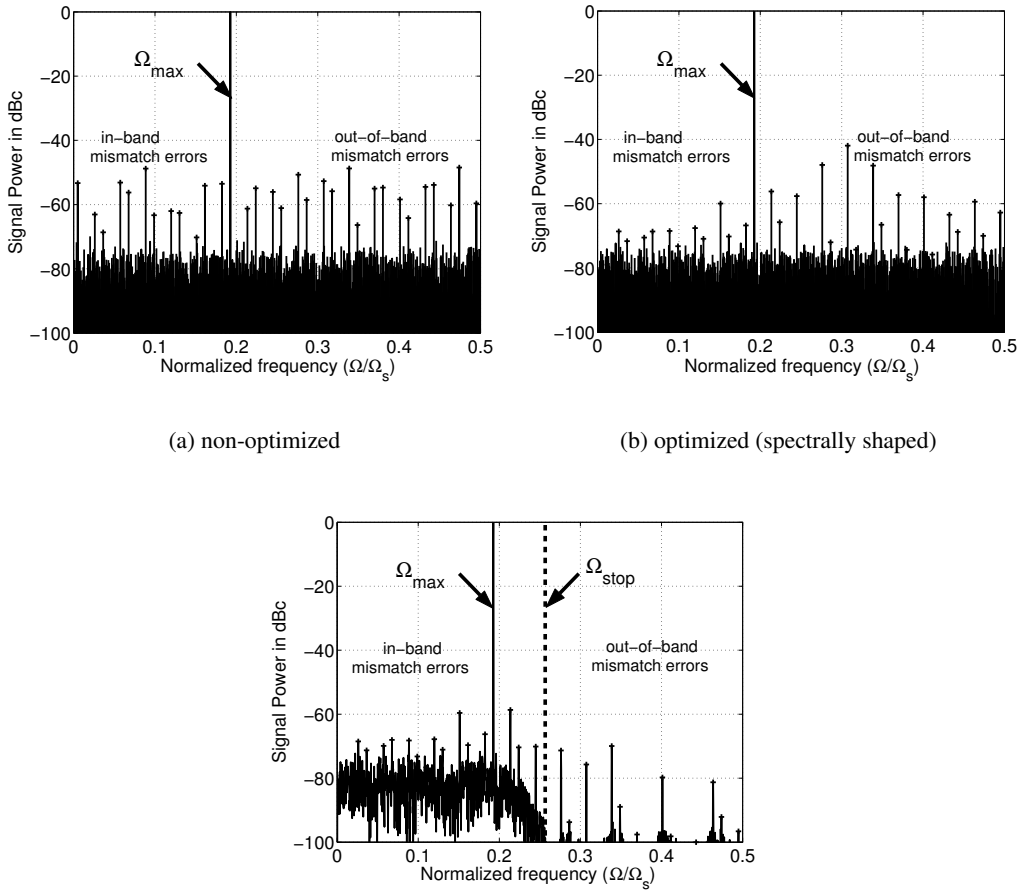

(a) non-optimized

(b) optimized (spectrally shaped)

(c) optimized and low-pass filtered

Figure 5.13: Output spectrum of a time-interleaved ADC with 32 channels ($M = 32$). All peaks in the spectrum marked with a plus are unwanted spurious peaks related to the sinusoidal input signal with frequency Ω_{max} caused by timing mismatches. In (a) the channel sequence has not been optimized. In (b) the timing mismatches have been identified and the channel sequence has been optimized according to Algorithm 1. We notice a reduction of the in-band mismatch errors. In (c) we see the low-pass filtered output (digital filter consisting of 12 coefficients and stopband edge at Ω_{stop}) of the sequence optimized time-interleaved ADC. In the band of interest we significantly reduce the mismatch error power.

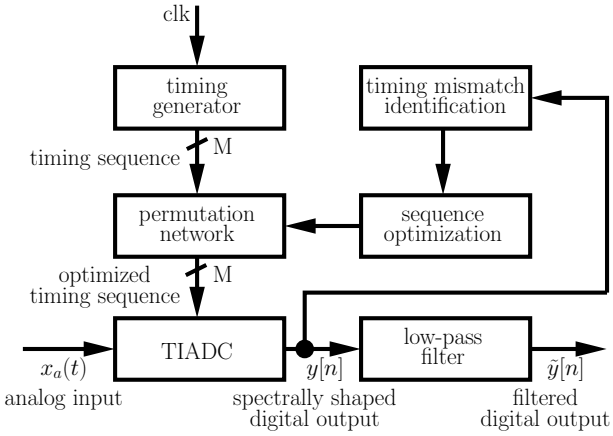

Figure 5.14: The principle of shaping timing mismatch error power. Whenever the timing mismatches are identified a new optimized permutation of the channel sequence is determined. In the permutation network, the new permutation reorders the timing information for each channel ADC. The effect of optimizing the channel ADC sequence is a spectral shaping of the timing mismatch error power towards higher frequencies (cf. Fig. 5.13(b)). This mismatch error power can be easily filtered out by a low-pass filter (cf. Fig. 5.13(c)).

We can separate the optimization problem from the input signal by formulating a less rigid optimization criterion. Therefore, we only consider spectral components $\alpha_p\left(j\left(\Omega - p\frac{\Omega_s}{M}\right)\right) X_a\left(j\left(\Omega - p\frac{\Omega_s}{M}\right)\right)$ which are completely outside the input frequency band, i.e., $P := \left\{p \mid \left(\left|\pm\Omega_{\text{max}} + p\frac{\Omega_s}{M}\right|\right) > \Omega_{\text{max}}\right\}$. Then, we apply the triangular inequality and minimize the sum of the terms which potentially contribute mismatch error power to the input frequency band $\left|\alpha_p\left(j\left(\Omega - p\frac{\Omega_s}{M}\right)\right) X_a\left(j\left(\Omega - p\frac{\Omega_s}{M}\right)\right)\right|^2$, where $p \notin P$, by maximizing the sum of the terms $\left|\alpha_p\left(j\left(\Omega - p\frac{\Omega_s}{M}\right)\right) X_a\left(j\left(\Omega - p\frac{\Omega_s}{M}\right)\right)\right)|^2$, where $p \in P$. Finally, we can write a new optimization criterion, that is

$$\max_{\pi(\upsilon)} \sum_{p\in P} \left|\alpha_p\left(j\left(\Omega - p\frac{\Omega_s}{M}\right)\right)\right|^2 \quad \text{for each } \Omega - p\frac{\Omega_s}{M} \text{ satisfying } \Omega_{\text{max}} < |\Omega - p\frac{\Omega_s}{M}| < \frac{\Omega_s}{2}, \tag{5.21}$$

where we have dropped the integration over the input signal free frequency band and the input signal $X_a(j\Omega)$, which is only valid when we can show that there is at least one permutation υ, which satisfies (5.21) for all considered $\Omega - p\frac{\Omega_s}{M}$.

To simplify matters we assume an even number of channels M for further discussion. Since a global delay causes no timing mismatches we further assume that $\sum_{m=0}^{M-1} \Delta t_m = 0$. When we only consider timing mismatches and assume that they are small enough to use the first two terms of a Taylor series expansion of $e^{-j\Omega\Delta t_{\upsilon_m}}$ around 0, which is

$$\mathcal{T}\left\{e^{-j\Omega\Delta t_{\upsilon_m}}\right\} = 1 - j\Omega\Delta t_{\upsilon_m} - \ldots, \tag{5.22}$$

we can express (5.20) as

$$\begin{aligned}\alpha_p\left(j\Omega\right) &= \delta[p_{<M>}] - j\Omega\frac{1}{M}\sum_{m=0}^{M-1}\Delta t_{\upsilon_m}e^{-jpm\frac{2\pi}{M}} \\ &= \delta[p_{<M>}] - j\Omega\Delta T_p, \end{aligned} \tag{5.23}$$

where the discrete impulse function $\delta[p_{<M>]}$ should not be confused with the Dirac delta function $\delta(\Omega)$. From the above representation we realize that $\alpha_p\left(j\Omega\right)$ is a linear function of Ω and, therefore, we can find one permutation υ satisfying (5.21) for all considered $\Omega - p\frac{\Omega_s}{M}$. We can rewrite (5.21) using (5.23) as

$$\max_{\pi(\upsilon)}\left(\sum_{p=\frac{M}{2}-W}^{\frac{M}{2}+W}|\Delta T_p|^2\right), \tag{5.24}$$

where $\frac{M}{2}-W$ and $\frac{M}{2}+W$ are the lower and the upper bounds of the considered coefficient indices in P. By introducing the index W we have fixed the range of optimization to be symmetrical around $\frac{\Omega_s}{2}$, which is favorable for implementation considerations, since we can use a simple low-pass filter to reduce the timing mismatches (cf. Fig. 5.14). We see a strong relation to discrete prolate spheroidal sequences (DPSS) analyzed in great detail by Slepian [128]. However, DPSS are arbitrary finite-length sequences maximizing the power in some frequency band of interest whereas we are searching for a permutation of a given sequence doing the same.

The more coefficients we use for the optimization the better the spectral shaping can be. We can see that there is a trade-off between the number of coefficients $(2W+1)$ we include in the maximization problem (5.24) and the maximal input signal bandwidth Ω_{max}. If we assume an ideal filter with a stopband frequency Ω_{stop} the maximal input signal bandwidth is given by

$$\Omega_{\text{max}} < \Omega_{\text{stop}} \leq \frac{1}{2}\left(\frac{\Omega_s}{2} - W\frac{\Omega_s}{M}\right). \tag{5.25}$$

5.4.1.1 A Fast Algorithm for Spectral Shaping of Timing Mismatches

Finding an optimal sequence, which maximizes (5.24), is still a difficult combinatorial optimization problem, which can be solved by using different methods such as simulated annealing and genetic algorithms. These optimization methods are computationally complex and are difficult to be implemented on a chip. Furthermore, there is no guarantee for finding the global maximum with such algorithms within a given time span. However, we have found a simple deterministic algorithm which has a very low complexity and always determines at least one suboptimal solution.

The first idea to obtain some spectral shaping is to focus the mismatch error power on the central coefficient. Hence, we seek sequences that solve

$$\max_{\pi(\upsilon)}\left|\Delta T_{\frac{M}{2}}\right|^2, \tag{5.26}$$

where we can simplify $\Delta T_{\frac{M}{2}}$ as

$$\begin{aligned}\Delta T_{\frac{M}{2}} &= \frac{1}{M}\sum_{m=0}^{M-1}\Delta t_{\upsilon_m}(-1)^{m+1} \\ &= -\frac{1}{M}\left(\sum_{m=0}^{\frac{M}{2}-1}\Delta t_{\upsilon_{2m}} - \sum_{m=0}^{\frac{M}{2}-1}\Delta t_{\upsilon_{2m+1}}\right)\end{aligned} \tag{5.27}$$

From (5.27) we see that $\Delta T_{\frac{M}{2}}$ is the negative difference of the sum of all even indexed timing mismatches and the sum of all odd indexed timing mismatches. Therefore, (5.26) is maximized if

$$\Delta t_{\upsilon_{2m}} \geq \Delta t_{\upsilon_{2n+1}}, \tag{5.28}$$

or vice versa, for all possible m and n. The ordering within the even indexed υ_{2m} and the odd indexed υ_{2m+1} channel ADCs is arbitrary. Thus, we still have additional degrees of freedom to choose the channel ADC sequence. Therefore, we can further optimize and constrain the sequence to achieve better spectral shaping or we can utilize these degrees of freedom for other purposes such as channel randomization analyzed in Sec. 5.4.2. In this section, we focus on further sequence optimization.

The next step to improve the spectral shaping is to maximize the left and the right coefficients surrounding the central one. Hence, we would like to optimize

$$\max_{\pi(\upsilon)}\left(\left|\Delta T_{\frac{M}{2}-1}\right|^2 + \left|\Delta T_{\frac{M}{2}}\right|^2 + \left|\Delta T_{\frac{M}{2}+1}\right|^2\right). \tag{5.29}$$

Since the contributions cannot be maximized independently, we are not able to provide a simple relation like for the central coefficient $\Delta T_{\frac{M}{2}}$; however, we can find at least one suboptimal sequence when we require that the central coefficient is maximized first, that is

$$\max_{\pi(\upsilon)}\left(\left|\Delta T_{\frac{M}{2}-1}\right|^2 + \max_{\pi(\upsilon)}\left(\left|\Delta T_{\frac{M}{2}}\right|^2\right) + \left|\Delta T_{\frac{M}{2}+1}\right|^2\right). \tag{5.30}$$

Hence, we further optimize only those sequences fulfilling the relation given in (5.28). For that purpose we have found the simple sorting Algorithm 1. We have compared the results from this algorithm with results from an exhaustive search, where we have determined all possible permutations of the Δt_{υ_m} sequence. In MATLAB, this comparison is feasible for time-interleaved ADCs with no more than $M = 10$ channels. We have done more than 100000 simulation examples and the Algorithm 1 has always provided the optimum solution. For more than $M = 10$ channels we have compared the results from the sorting algorithm with results from a genetic optimization algorithm. For all tests, our algorithm outperformed the genetic algorithm for the optimization criterion given by (5.30). When we use the optimization criterion given by (5.29), we have had some cases where the exhaustive search and the genetic algorithm have found better sequences than Algorithm 1. However,

Data : Non-optimized sequence of timing mismatches $\mathbf{\Delta t}$
Result : Optimized sequence of timing mismatches $\mathbf{\Delta t}_\upsilon$
$\mathbf{\Delta t}_\upsilon = \langle\rangle$;
$\mathbf{\Delta t_s}$ = sort_in_descending_order $(\mathbf{\Delta t})$;
while *forever* **do**
  $\mathbf{\Delta t}_\upsilon = \langle \mathbf{\Delta t}_\upsilon, \text{first}(\mathbf{\Delta t_s})\rangle$; $\mathbf{\Delta t_s} = \mathbf{\Delta t_s} \setminus \text{first}(\mathbf{\Delta t_s})$;
  if $|\mathbf{\Delta t_s}| = 0$ **then** return $\mathbf{\Delta t}_\upsilon$;
  $\mathbf{\Delta t}_\upsilon = \langle \text{last}(\mathbf{\Delta t_s}), \mathbf{\Delta t}_\upsilon\rangle$; $\mathbf{\Delta t_s}$=$\mathbf{\Delta t_s} \setminus \text{last}(\mathbf{\Delta t_s})$;
  if $|\mathbf{\Delta t_s}| = 0$ **then** return $\mathbf{\Delta t}_\upsilon$;
  $\mathbf{\Delta t}_\upsilon = \langle \mathbf{\Delta t}_\upsilon, \text{last}(\mathbf{\Delta t_s})\rangle$; $\mathbf{\Delta t_s}$=$\mathbf{\Delta t_s} \setminus \text{last}(\mathbf{\Delta t_s})$;
  if $|\mathbf{\Delta t_s}| = 0$ **then** return $\mathbf{\Delta t}_\upsilon$;
  $\mathbf{\Delta t}_\upsilon = \langle \text{first}(\mathbf{\Delta t_s}), \mathbf{\Delta t}_\upsilon\rangle$; $\mathbf{\Delta t_s}$=$\mathbf{\Delta t_s} \setminus \text{first}(\mathbf{\Delta t_s})$;
  if $|\mathbf{\Delta t_s}| = 0$ **then** return $\mathbf{\Delta t}_\upsilon$;

Algorithm 1: Sorting algorithm for spectral shaping of timing mismatches. Note that $|\mathbf{\Delta t_s}|$ denotes the length of the sorted sequence $\mathbf{\Delta t_s}$, first$(\mathbf{\Delta t_s})$ denotes the first element, i.e., the largest element, of the sorted sequence $\mathbf{\Delta t_s}$, and last$(\mathbf{\Delta t_s})$ denotes the last element, i.e., the smallest element, of the sorted sequence $\mathbf{\Delta t_s}$. Example: Data: $\mathbf{\Delta t} = \langle 0.18, 0.20, -0.01, 0.06, 0.03, -0.11, -0.03, -0.06\rangle$ Result: $\mathbf{\Delta t}_\upsilon = \langle 0.03, -0.03, 0.18, -0.11, 0.20, -0.06, 0.06, -0.01\rangle$, $\upsilon = \langle 5, 7, 1, 6, 2, 8, 4, 3\rangle$

the differences between the optimal solution and the suboptimal solution are small, i.e., we have obtained on average a 1 dB improvement of the SINAD.

Since we sort timing mismatches, we only have to identify their relative order, which reduces the requirements on timing identification methods. Furthermore, we only need a low-pass filter to reduce the final error mismatch power. Thus, these compensation filters can be designed independently from the number of channels and the concrete timing mismatch values.

5.4.1.2 Simulation results

In this section we show some simulation results to demonstrate the prospects of spectral shaping. We have investigated the relation between the number of channels and the performance of the sequence optimization. For all simulations we have assumed timing mismatches with a standard deviation of $0.01\ T_s$ and a sinusoidal input signal with frequency $\frac{2039}{16384}\Omega_s$, from which we have taken 16384 samples. To avoid any influence from the filter design, we have assumed an ideal filter with stopband frequency $\omega_{\text{stop}} = \frac{\Omega_s}{4}T_s = \frac{2\pi}{4}$. For each number of channel ADCs we have simulated 1000 outcomes for optimized and non-optimized channel ADC sequences. For each outcome we have measured the signal-to-noise and distortion ratio (SINAD) and the spurious free dynamic range (SFDR) [41] and have averaged both quantities over all outcomes.

In Fig. 5.15 we compare the average SINAD in effective number of bits (ENOB) [41] of the optimized and the non-optimized time-interleaved ADC when we use ideal filters. Furthermore, we see the average SINAD of non-optimized time-interleaved ADCs without

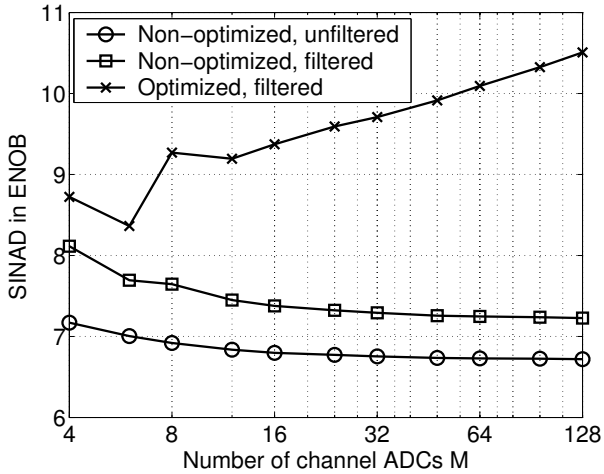

Figure 5.15: The average SINAD in ENOB for different numbers of channel ADCs (timing mismatch standard deviation 0.01 T_s).

any filtering. As expected, the unfiltered average SINAD is roughly 0.5 ENOB below the non-optimized SINAD. Compared to the non-optimized time-interleaved ADC the SINAD improvement of the optimized time-interleaved ADC is tremendous and increases with the number of channels. We can see a sharp bend of the SINAD for $M = 6$, which can be explained by considering the input frequency and the number of spectral components which are filtered out. For $M \geq 8$ all parts of the maximized spectral components are filtered out, since they are within $\frac{2\pi}{4}$ and $3\frac{2\pi}{4}$. For $M = 6$, some parts of the maximized spectral components are outside the filtered band and still contribute to the error power. For $M = 4$, we see the same effect and, therefore, we have the same gap between the filtered optimized curve and the filtered unoptimized curve as for $M = 6$. However, the filtered unoptimized curve has a better SINAD for $M = 4$, since we filter many of the aliased spectral components anyway and, therefore, it is less important if they have been optimized or not.

In Fig. 5.16 we compare the average SFDR of the optimized and the non-optimized time-interleaved ADC. We notice that the SFDR improves even for the non-optimized case with the number of channel ADCs, because the mismatch power is distributed over more coefficients and is, therefore, more uniformly distributed. However, sequence optimized time-interleaved ADCs have a significantly improved SFDR.

5.4.2 Combining Randomization and Spectral Shaping

In Sec. 5.2.2 we have already introduced the concept of channel randomization to reduce the impact of nonlinearity errors and mismatches. However, to clarify the difference between channel randomization and the combination of randomization and spectral shaping we briefly review randomization again and establish a notation for the output spectrum in the presence of timing mismatches. Then, we show how to select the channel ADCs to obtain both randomization and spectral shaping of timing mismatches.

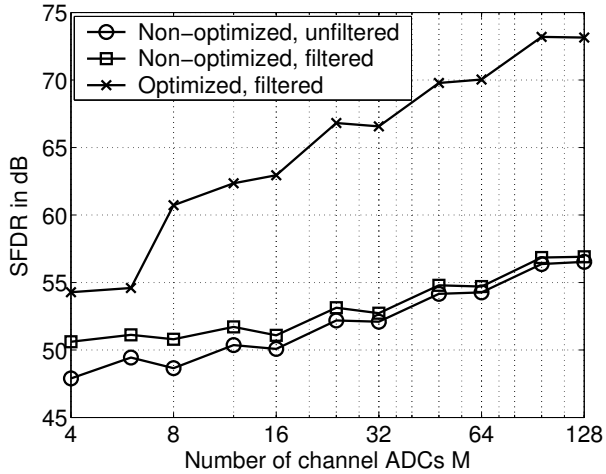

Figure 5.16: The average SFDR for different numbers of channel ADCs (timing mismatch standard deviation 0.01 T_s).

5.4.2.1 Randomized Time-Interleaved ADCs

In Fig. 5.17(a) we see the principle of a randomized time-interleaved ADC with a bandlimited input signal $x_a(t)$ For each sampling instant a new channel ADC is randomly selected, whereas we have some constraint on the selection process. If we have a redundant array of $(M + R)$ channel ADCs, operating with a minimum channel sampling period of MT_s, and we would like to build a randomized time-interleaved ADC with an overall sampling period of T_s, we can choose at each time instant among $R + 1$ channel ADCs without violating the sampling constraint, MT_s, for one channel ADC. This is illustrated in Fig. 5.17(b) for $M = 2$ and $R = 1$. Furthermore, we see from Fig. 5.17(a) that the time-interleaved ADC is followed by a low-pass filter, which filters out some portion of the uniformly shaped mismatch spectrum in order to increase the SINAD.

In order to describe randomized time-interleaved ADCs, we use the sequence $\boldsymbol{\upsilon} = \langle \upsilon_n \rangle_{n=0}^{N-1}$, where each element $\upsilon_n \in \langle 0, 1, \ldots, M + R - 1 \rangle$ stands for an index number, which maps each sampling instant to a channel ADC. The sequence has $N = (M + R)L$ elements and is repeated forever. Therefore, (5.17) and (5.18) can be rewritten as

$$Y\left(e^{j\Omega T_s}\right) = \frac{1}{T_s} \sum_{p=-\infty}^{\infty} \alpha_p \left(j\left(\Omega - p\frac{\Omega_s}{N}\right)\right) X_a \left(j\left(\Omega - p\frac{\Omega_s}{N}\right)\right), \tag{5.31}$$

where

$$\alpha_p\left(j\Omega\right) = \frac{1}{N} \sum_{n=0}^{N-1} e^{-j\Omega \Delta t_{\upsilon_n}} e^{-jpn\frac{2\pi}{N}}. \tag{5.32}$$

For a non-randomized time-interleaved ADC, i.e., to obtain (5.17) and (5.18), the sequence would be $\boldsymbol{\upsilon} = \langle 0, 1, \ldots, M - 1 \rangle_{n=0}^{N-1}$, where $R = 0$, $L = 1$ and $N = M$.

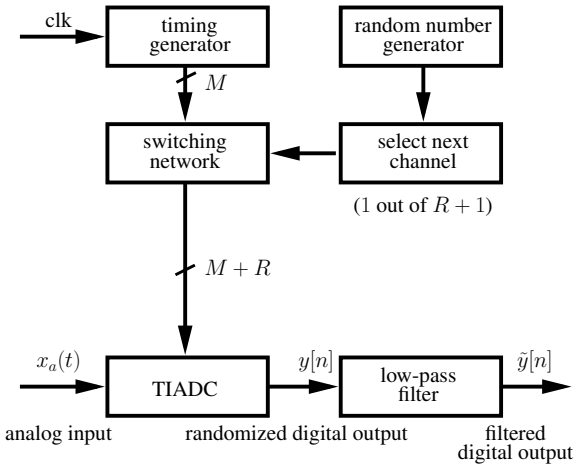

(a) Architecture

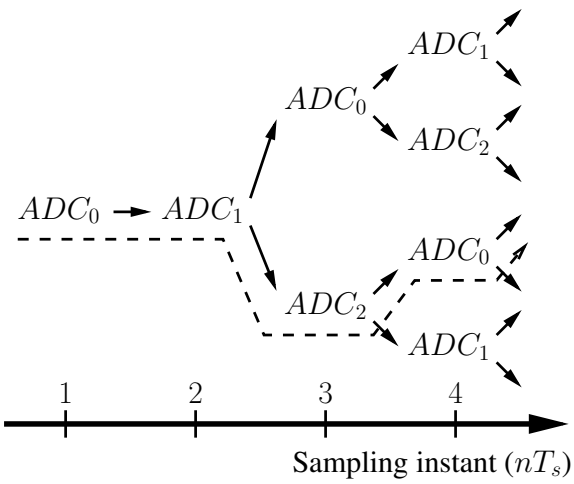

(b) Principle

Figure 5.17: The basic concept of channel randomization. (a) The channel ADC sequences are arbitrarily selected. No information about the time-interleaved ADC is used to improve the selection process. (b) Conventional randomization of channel ADCs with $M = 2$ and $R = 1$. After the first two channel ADCs (ADC_0, ADC_1) have taken a sample we can choose between ADC_0 and ADC_2, without violating our sampling constraints. After we have, for example, chosen ADC_2 we can decide between ADC_0 and ADC_1 and so forth (dashed line).

When we use a random sequence $\boldsymbol{\upsilon}$ to describe a randomized time-interleaved ADC it still has to fulfill the sampling constraints, i.e., a minimum sampling period of MT_s for all channel ADCs. Furthermore, the number of elements N of the sequence should be very large or ideally infinite. For such a sequence we see from (5.32) that we increase the number of aliased spectral components to N, whereby the power of each spectral component decreases by the factor N and the mismatch power becomes more uniformly distributed over the frequency band [29].

5.4.2.2 Spectrally Shaped and Randomized Time-Interleaved ADCs

In Fig. 5.18 we see the principle of spectrally shaped randomization. Fig. 5.18(a) shows how we can use information from identified timing mismatches to improve the channel selection process in order to achieve a spectrally shaped and randomized output spectrum. The shaped timing mismatch error power can be filtered out by a simple low-pass filter.

According to (5.17) and (5.18) timing mismatches cause weighted aliased spectral components of the input signal $\alpha_p\left(j\left(\Omega - p\frac{\Omega_s}{M}\right)\right) X_a\left(j\left(\Omega - p\frac{\Omega_s}{M}\right)\right)$, which is illustrated in Fig. 5.19. For an even number of channels M of a non-randomized time-interleaved ADC and a bandlimited input signal, i.e., $X_a(j\Omega) = 0$ for $|\Omega| \geq \frac{\Omega_s}{4}$, the central aliased spectral component ($p = \frac{M}{2}$) becomes $\alpha_{\frac{M}{2}}\left(j\left(\Omega - \frac{\Omega_s}{2}\right)\right) X_a\left(j\left(\Omega - \frac{\Omega_s}{2}\right)\right)$, where $X_a\left(j\left(\Omega - \frac{\Omega_s}{2}\right)\right)$ does not contribute to the input signal frequency band. Thus, for a non-randomized time-interleaved ADC we can shape timing mismatch power towards the central spectrum by maximizing $\alpha_{\frac{M}{2}}(j\Omega)$ (cf. Sec. 5.4.1). However, we can go one step further and combine spectral shaping and randomization. To show this, we approximate the timing mismatch by the first two terms of a Taylor series expansion and can write (5.32) as

$$\alpha_p\left(j\Omega\right) = \delta[p_{<M>}] - \frac{j\Omega}{N}\sum_{n=0}^{N-1}\Delta t_{\upsilon_n} e^{-jpn\frac{2\pi}{N}}, \tag{5.33}$$

where $\delta[p_{<M>}]$ is the discrete impulse function, and realize that the central coefficient $\alpha_{\frac{N}{2}}\left(j\Omega\right)$ of (5.33) can be further reduced to

$$\alpha_{\frac{N}{2}}\left(j\Omega\right) = -\frac{j\Omega}{N}\sum_{n=0}^{\frac{N}{2}-1}\left(\Delta t_{\upsilon_{2n}} - \Delta t_{\upsilon_{2n+1}}\right). \tag{5.34}$$

Then we build two index groups A and B out of all possible channel indices, i.e., $\langle 0, 1, \ldots, M+R-1\rangle$, with corresponding timing mismatches Δt_m^A and Δt_m^B where the size of each group is $\frac{M+R}{2}$, e.g., $A = \langle 1, 4, 5\rangle$ and $B = \langle 0, 2, 3\rangle$ for $M = 4$ and $R = 2$. We further assume that the frequency of occurrences of the elements in $\langle \upsilon_n\rangle_{n=0}^{N-1}$ is uniformly distributed, which is feasible for a fair randomization and large N, and all even indices υ_{2n} are elements from group A and all odd indices υ_{2n+1} are elements from group B. Therefore,

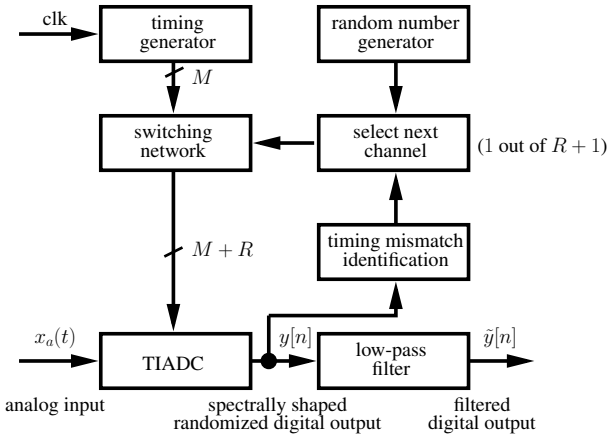

(a) Architecture

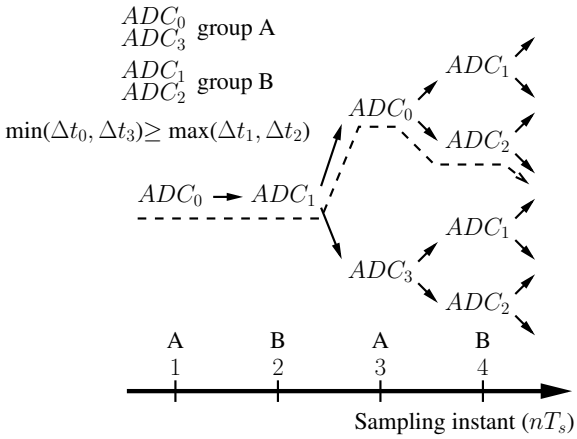

(b) Principle

Figure 5.18: The basic concept of spectrally shaped channel randomization. (a) The selection process uses information about the identified timing mismatch to achieve a spectrally shaped randomization. (b) Advanced randomization of channel ADCs with $M = 2$ and $R = 2$. For the odd samples we can choose from channel ADCs belonging to group A and for the even samples we can choose from channel ADCs belonging to group B. Therefore, at each sampling instant we can choose between two channel ADCs. All channel ADCs of Group A have timing mismatches greater than the timing mismatch of each channel ADC in group B. The dashed line shows one possible way to choose a random sequence.

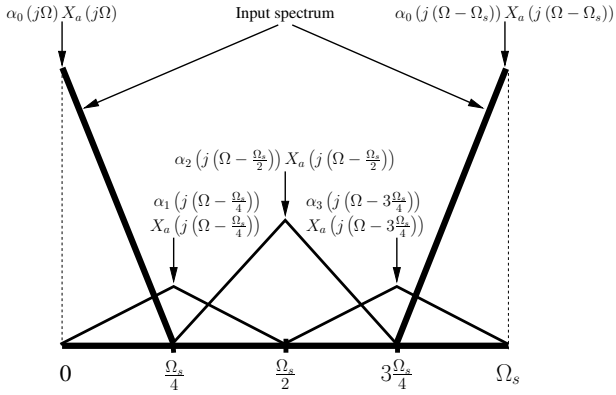

Figure 5.19: Output spectrum of a non-randomized time-interleaved ADC with four channels ($M = 4$). When the input signal is bandlimited to $\frac{\Omega_s}{4}$ the aliased spectral component at $\alpha_{\frac{M}{2}}\left(j\left(\Omega-\frac{\Omega_s}{2}\right)\right)X_a\left(j\left(\Omega-\frac{\Omega_s}{2}\right)\right)$ does not overlap with the input spectrum and can be filtered out.

we can simplify (5.34) to

$$\begin{aligned}\alpha_{\frac{N}{2}}(j\Omega) &= -\frac{j\Omega}{M+R}\sum_{m=0}^{\frac{M+R}{2}-1}\frac{1}{L}\sum_{l=0}^{L-1}\left(\Delta t_m^A-\Delta t_m^B\right)\\ &= -\frac{j\Omega}{M+R}\sum_{m=0}^{\frac{M+R}{2}-1}\left(\Delta t_m^A-\Delta t_m^B\right).\end{aligned} \tag{5.35}$$

From (5.34) and (5.35) we see that $\alpha_{\frac{N}{2}}(j\Omega)$ is the difference of the sum of all even indexed timing mismatches, i.e., all timing mismatches Δt_m^A from group A, and the sum of all odd indexed timing mismatches, i.e., all timing mismatches Δt_m^B from group B. Therefore, the magnitude of $\alpha_{\frac{N}{2}}(j\Omega)$ is maximized if

$$\Delta t_m^A \geq \Delta t_n^B, \tag{5.36}$$

or vice versa, for all possible m and n.

Thus, although we can apply an arbitrarily large random sequence $\langle \upsilon_n\rangle_{n=0}^{N-1}$ to obtain uniformly distributed timing mismatches we can maximize the central aliased spectral component, when we make sure that every $2n$th sample is taken from group A and every $(2n+1)$th sample is taken from group B. Within the groups we can still randomize, which is depicted in Fig. 5.18(b). In order to provide randomization within the two groups we need at least two additional channel ADCs ($R = 2$) to fulfill the sampling constraint of MT_s for each channel ADC. For R additional channel ADCs we can choose between $\frac{R}{2}+1$ channel ADCs for each sampling instant without violating the sampling constraint.

Because the selection of the two ADC groups is only based on the rank order of the timing mismatches, the absolute accuracy of the mismatch identification method does not

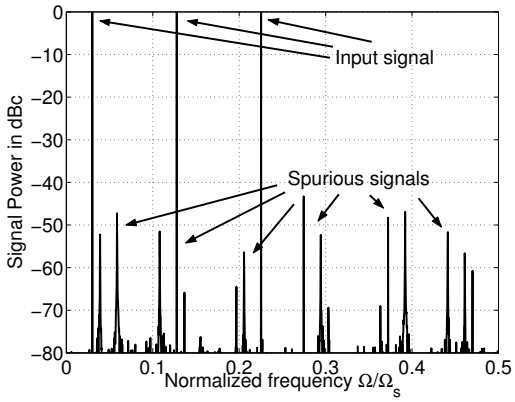

(a) Non-randomized

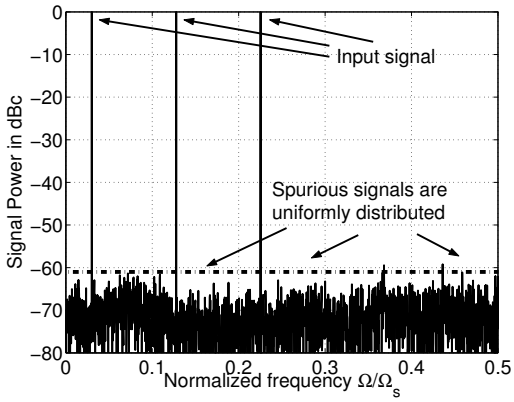

(b) Randomized

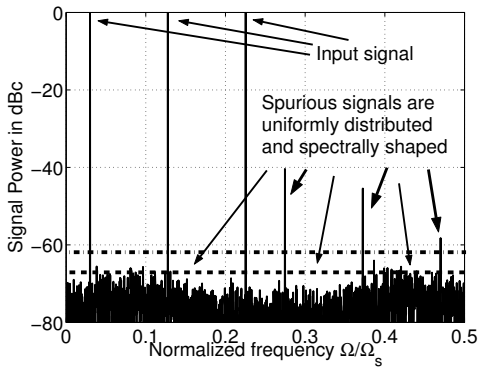

(c) Randomized and spectrally shaped

Figure 5.20: Effect of spectrally shaped randomization on a time-interleaved ADC ($M = 6$, $R = 2$) with dominating timing mismatches. In the band of interest $[0, \frac{\Omega_s}{4}]$, we remarkably reduce the mismatch noise. This is because some parts of the mismatch power have become spectrally shaped, which results in the three peaks in the band $[\frac{\Omega_s}{4}, \frac{\Omega_s}{2}]$. These peaks and the mismatch power in the band $[\frac{\Omega_s}{4}, \frac{\Omega_s}{2}]$ can be filtered by a low-pass filter.

matter and, therefore, the requirements on the timing mismatch identification are very low. Moreover, for larger numbers of channel ADCs and a typical symmetrical probability density function of the timing mismatch distribution, the difference between the mean and the median value of the timing mismatches becomes very small and we only have to determine the sign of the timing mismatches in order to divide them into the groups A and B and to obtain spectral shaping.

5.4.2.3 Simulation results

In Fig. 5.20 we illustrate the effect of combining randomization and spectral shaping. For all three plots the input signal consists of three sine waves with different frequencies. In Fig. 5.20(a) we see the output spectrum of the time-interleaved ADC ($M = 6$, $R = 2$) with timing mismatches. Additional aliased spectral components to the input signal noticeably distort the whole spectrum. In Fig. 5.20(b) we have used conventional randomization to distribute the mismatch power uniformly across all frequencies. A low-pass filter at $\frac{\Omega_s}{4}$ can increase the SINAD at most by 3 dB. Finally, in Fig. 5.20(c) we have combined randomization and spectral shaping of timing mismatches. Hence, we have maximized the central aliased spectral component by optimizing the channel selection process and still have an approximately uniformly distributed mismatch noise spectrum, which is considerably reduced (difference between dashed and dashed-dotted line of about 5 dB). With a simple low-pass filter we can filter out the spectrally shaped mismatch power and increase the SINAD and the SFDR compared to Fig. 5.20(b).

In order to compare the performance of spectrally shaped randomization and conventional randomization we have simulated time-interleaved ADCs with different numbers of channels M. For each number of channels M, we have simulated 1000 outcomes and have averaged the measured SINAD and the measured SFDR. We have assumed normally distributed timing mismatches with a standard deviation of $0.01T_s$ and a sinusoidal input signal with frequency $\Omega_0 = \frac{2039}{16384}\Omega_s$, from which we have taken 16384 samples. To allow advanced randomization we have used two additional channel ADCs ($R = 2$) for the simulation. Furthermore, we have used an ideal low-pass filter with cut-off frequency $\Omega_{\text{cut}} = \frac{\Omega_s}{4}$. For each of the following figures we have plotted three curves: the randomized unfiltered case, the randomized filtered case, and the randomized, spectrally shaped, and filtered case.

Fig. 5.21(a) shows the SINAD in effective number of bits (ENOB) [41] against the number of channel ADCs. The unfiltered average SINAD is 0.5 ENOB below the filtered SINAD. The spectrally shaped curve is 1.2 ENOB better than the unfiltered one. Therefore, we gain about 0.7 ENOB compared to the non-optimized randomization.

Fig. 5.21(b) shows the average SFDR against the number of channels. The spectrally shaped and randomized time-interleaved ADC increases the SFDR by about 5 dB compared to the non-optimized one. Furthermore, we realize that the filtered and the unfiltered time-interleaved ADC with randomization have approximately the same average SFDR. This is because, on average, there are as many peaks below as above $\frac{\Omega_s}{4}$, whereby the filtering has a minor influence on the SFDR. The SFDR decreases with the number of channels, because we have used a finite number of samples for the simulation and the ratio $\frac{R}{M}$ decreases (R

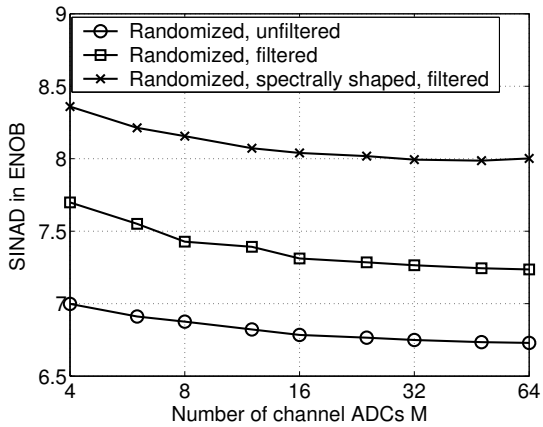

(a) The average SINAD in ENOB against the number of channels M.

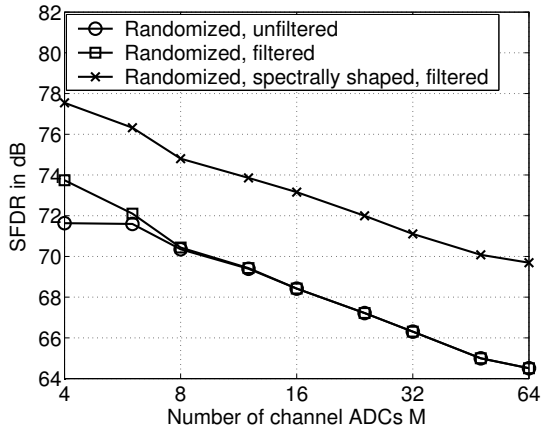

(b) The average SFDR against the number of channels M.

Figure 5.21: Performance enhancement due to spectral shaping. For each number of channels M, we have simulated 1000 outcomes and have averaged the measured SINAD and the measured SFDR. We have assumed normally distributed timing mismatches with a standard deviation of $0.01T_s$ and a sinusoidal input with frequency $\Omega_0 = \frac{2039}{16384}\Omega_s$, from which we have taken 16384 samples. To allow randomization, we use two extra channel ADCs ($R = 2$) for all simulations. The spectrally shaped and randomized algorithm performs remarkably better than pure randomization. (a) As expected, the randomized and filtered SINAD curve is roughly 0.5 ENOB above the randomized unfiltered SINAD curve. The randomized and spectrally shaped curve is about 1.2 ENOB better than the unfiltered curve. (b) Also for the SFDR we notice a significant improvement of about 5 dB.

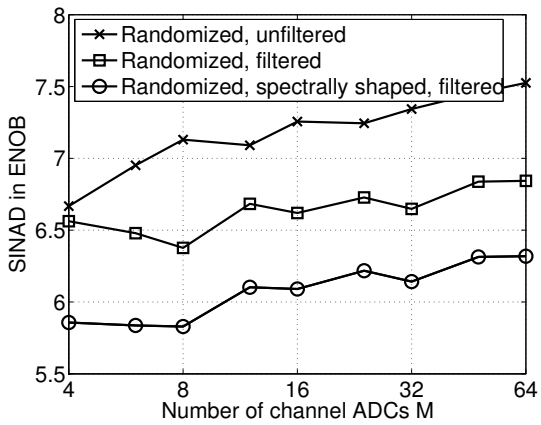

(a) The worst SINAD in ENOB against the number of channels M.

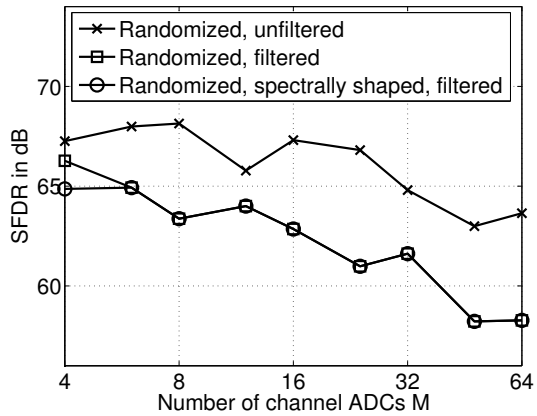

(b) The worst SFDR against the number of channels M.

Figure 5.22: Performance enhancement due to spectral shaping for the worst case. These figures show the worst cases of Fig. 5.21(a) and Fig. 5.21(b). Although the overall performance is worse, the relative performance improvements are comparable to the average case.

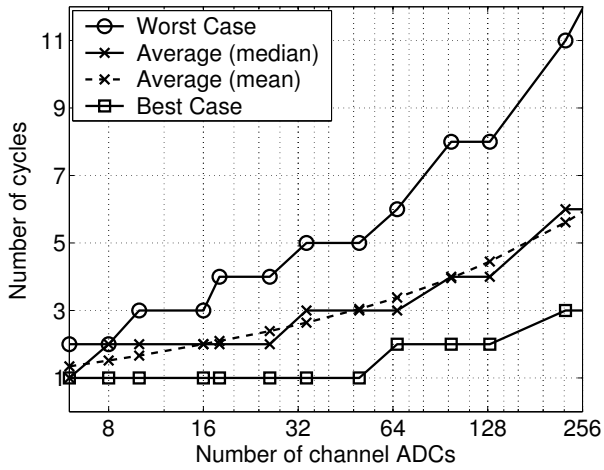

Figure 5.23: Relation between the number of ADCs M and the required number of cycles to change the group membership of the channel ADCs. We see that the change of membership should not influence the randomization.

has been constantly set equal to 2), whereby the distribution statistics of the mismatch error power become worse [29, 25].

In Fig. 5.21(a) and Fig. 5.21(b) we see the worst-case performance of spectrally shaped randomization. The relative performance improvements are comparable to the average case.

A further problem is the change of group membership within the randomization process. Each time we have new estimates for the timing mismatches (cf. Fig. 5.18(a)), which differ from the last ones, we have to change the group membership of the channel ADCs, i.e., ADCs from group A go to group B and vice versa. In order to change the membership we have to give up fair randomization because the change of membership is deterministic. Nevertheless, we still have to ensure a minimal sampling period of MT_s for each channel ADC. It is easy to show that such an algorithm, which fulfills the above requirements and halts in finite time, exists. In Fig. 5.23 we see the execution time of a group change algorithm in relation to the number of channels. The time is measured in cycles, where one cycle consists of M processed channel ADCs. For each number of ADCs we have simulated 10000 arbitrary group membership changes. Even for a large number of channel ADCs the algorithm performs very well. Hence, the change of group membership should not influence the randomization statistics significantly.

5.5 Conclusion

In this chapter we have investigated channel mismatch compensation methods with focus on nonlinearity mismatch and timing mismatch compensation.

Based on our analysis of nonlinearity mismatches in Sec. 3.2.1, we have developed a compensation method for nonlinearity errors and mismatches. By tuning the general non-

linearity behavior of the channel ADCs, i.e., by designing complementary transfer curves, we can shift nonlinearity error power to the upper frequency band. There it can be suppressed by introducing some oversampling and a low-pass filter. Another method is to combine the complementary channel ADC design with a randomization strategy for redundant time-interleaved ADCs. The methods can significantly increase the SINAD, the SFDR and the THD.

Our analyses presented in Sec. 3.2.2 show that mismatches of the S/H transfer characteristics in sample mode and aperture delay mismatches are coupled. Moreover, they reveal that we can compensate timing mismatches by tuning the transfer characteristics, i.e., the linear part of the phase responses of the S/Hs. The presented timing mismatch compensation method almost removes the timing mismatches and, as simulations show, significantly improves the performance of time-interleaved ADCs. Since we only need additional backward paths in order to tune the transfer characteristics of the S/Hs, our compensation method has a very low power consumption. Although we have analyzed the method for S/Hs with first-order characteristics, it should be applicable to more complex characteristics as well, since ADCs are designed to have a preferably linear phase.

We have also introduced spectral shaping of timing mismatch error power. We have shown that reordering the channel ADC sequence can influence the output spectrum of a time-interleaved ADC. We have provided optimization criteria in order to find such sequences for achieving spectral shaping. We have introduced a simple sorting algorithm, which always finds at least one good suboptimal solution for the optimization problem. In contrast to other timing mismatch compensation methods, we only need a permutation network in order to change the channel sequence and a simple low-pass filter at the digital output of the time-interleaved ADC to significantly reduce the impact of timing mismatches. Thus, the power consumption of our method does not considerably increase with the number of channels. Moreover, the presented algorithm does not depend on the absolute accuracy of the identification methods, because we only sort the values and do not use them for further calculations. Through our simulations we have demonstrated the excellent performance of spectral shaping in conjunction with our simple sorting algorithm for solving the timing mismatch compensation problem.

We have introduced an advanced randomization method that combines randomization and spectral shaping of timing mismatches. With a simple low-pass filter the method can, compared to conventional randomization algorithms, improve the SFDR as well as the SINAD. The method assumes a dominating mismatch source, which is given by the timing mismatch. To find optimal shaping sequences, we only have to sort the channel ADCs into two groups, where one group contains all channel ADCs with a greater timing mismatch than all channel ADCs in the other group. Because we only compare timing mismatches the absolute accuracy of the identification method does not matter and the requirements on the timing mismatch identification are very low.

When we compare spectral shaping of timing mismatches to the combination of randomization and spectral shaping of timing mismatches the former is superior to the latter in terms of SINAD. In contrast, the spectrally shaped randomization results in a better SFDR for $M \lesssim 32$ channels. For more channels, spectral shaping only results in a better SFDR

too. Furthermore, spectral shaping is easier to implement than spectrally shaped randomization.

Chapter 6

Concluding Remarks

In this thesis we have analyzed channel mismatch errors in time-interleaved ADCs and have found methods to identify and compensate them. For the first time, we have modeled time-interleaved ADCs as nonlinear hybrid filter banks. We use for each channel ADC a linear analysis filter $H_m(j\Omega)$, a static nonlinearity $f_m(x)$, and again a linear synthesis filter $G_m(e^{j\Omega T_s})$. This structure represents an LNL cascade model, which can approximate a large class of Volterra systems [138, 158]. Nevertheless, to obtain a more precise system representation, e.g., to include the entire dynamic nonlinear effects of the S/H [21, 142, 160] in each channel ADC, we have to extend the representation to a full Volterra system [158, 138]. Such an approach complicates the input/output relation but it can provide new insight into the system, which could be used for advanced mismatch compensation algorithms. Furthermore, we have not investigated any inverse system approaches to compensate for the nonlinearities of time-interleaved ADCs.

In chapter 3 we have investigated channel mismatches in time-interleaved ADCs. We have analyzed combined channel mismatch errors including timing jitter and quantization noise and clarified how offset, gain, and timing mismatches interact. For the first time, we have introduced the concept of a meta time-interleaved ADC, which allows us to consider the mutual influence of timing jitter and combined mismatch errors for an arbitrary number of channels. For individual channel mismatches we can analytically derive the worst-case for given mismatch bounds. One open issue is the worst-case for combined channel mismatches and given bounds, which would help to specify the worst-case performance of a time-interleaved ADC with given specifications.

In chapter 4 we have introduced an accurate background timing mismatch identification method for broadband signals close to half the sampling frequency. A problem of these algorithms are input signals which do not have uniformly distributed signal power over the frequency band of interest. Then the channel matrix can become ill-conditioned and the method fails. We can either detect such matrices directly, which is computationally complex, or we can analyze the input power distribution, which can be done much more efficiently. However, this is still an open research topic.

In Sec. 5.3 we have revealed how to compensate timing mismatches by tuning the transfer characteristics, i.e., the linear part of the phase responses of the S/Hs. As until now we have not manufactured any chip with this method it is unclear how accurately we can change the phase response of the S/Hs.

In Sec. 5.4 and Sec. 5.4.2 we have introduced spectral shaping of the timing mismatch error power. We have shown that reordering the channel ADC sequence can shape the output

spectrum of a time-interleaved ADC. The basic assumption is that the reordering does not influence the timing mismatches too much. In particular we assume that the rank order of the timing mismatches will remain after reordering the sequence. A manufactured chip will provide an answer to this question in the near future.

To summarize, we have found a comprehensive model for time-interleaved ADCs and have analyzed channel mismatch errors. With our foreground and background identification methods we can precisely determine the channel mismatches. Furthermore, we have found power-aware channel mismatch compensation methods, which significantly reduce the impact of channel mismatches on the time-interleaved ADC performance. Therefore, in the future high-rate time-interleaved ADCs can be used for power critical as well as for high-resolution applications.

Appendix A

Simulation Environment for Time-Interleaved ADCs

In order to understand an ADC system, the design and use of a simulation environment is an important and critical task. Being able to control the entire analog-to-digital conversion process is the main advantage of a simulation environment. Thereby, it is possible to adjust parameters to any desired level and to clarify the reason for a certain ADC behavior. The difficulty of a simulation is the abstraction level of the real world entity. If the abstraction is too coarse, some effects might never be discovered. If it is too detailed the speed of the simulation decreases. It gets even worse if the abstraction is wrong and a behavior that does not exist in real life is simulated. To sum up, we carefully have to choose the abstraction level with the trade-off between simulation precision and simulation speed.

A.1 Introduction

Two books have been written about high level simulations of ADCs [53, 89]. These books provide introductions and program codes for the most relevant ADC architectures. Many papers have been written about ADC modeling [3, 9, 115, 2, 12]. The special problem of modeling the S/H device is considered in [88, 21, 134, 135]. In [67, 125] the problems of static nonlinearities are investigated. Dynamic modeling of nonlinearity errors can be found for example in [38, 42, 90]. A simulation based on the programming language C is presented in [92].

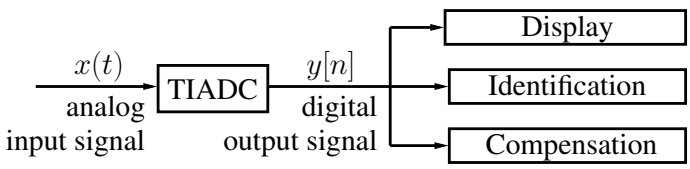

Figure A.1: Basic architecture of the time-interleaved ADC simulation.

A.2 System Modeling

In Fig. A.1 we illustrate the basic simulation architecture. The input signal $x(t)$ goes through the time-interleaved ADC which converts it to a sampled and quantized output signal $y[n]$. Afterwards, the output signal can be used for different kinds of analysis and post-processing tools. For example, we can use the output signal for system identification, system compensation, or for visualization purposes. The general time-interleaved ADC structure has to be independent of the channel ADC implementation. Thereby, it is possible to adapt the behavioral model to specific channel ADC architectures. Both the input signal and the time-interleaved ADC model must be fast and dynamically configurable in order to simulate quasi-nonstationary signals and systems. For the simulation environment, we consider the main error sources of a time-interleaved ADC, the signal generation, and the channel model.

A.2.1 Time-Interleaved ADC Model

Due to its wide range of toolboxes, we have decided to use MATLAB as a simulation environment, which allows a fast and flexible programming of the required functionality.

The simulation model should include the most important signal processing error sources of a time-interleaved ADC. The three main error sources degrading the spurious free-dynamic range (SFDR) and the signal-to-noise and distortion ratio (SINAD) of a time-interleaved ADC are offset, gain, and timing mismatches (cf. chapter 3). Gain mismatches are the differences among the gains and offset mismatches are the differences among the offsets of the channel ADCs. Timing mismatches are the deterministic deviations between the nominal sampling time and the real sampling time for each channel. Another important error source is timing jitter, which is, however, not restricted to time-interleaved ADCs. In contrast to the timing mismatch, it is the stochastic deviation from the nominal sampling period for each sample [48]. From multirate systems analyses we also find that bandwidth mismatches lower the SINAD and the SFDR [139]. Conventional ADCs have static and dynamic nonlinearities, which have to be considered in time-interleaved ADCs as well.

A.2.2 Signal Generation

The first problem, which has to be solved, is the input signal generation. It is a non-trivial task, since we want to simulate the sampling of an arbitrary continuous-time signal with a discrete computing environment. To define a general set of P input signals $x_p(t)$ we use the coefficients of the Fourier series to define each input signal as

$$x_p(t) = a_{p,0} + \sum_{k=1}^{+\infty} a_{p,k} \sin(2\pi f_p k t + \varphi_{p,k}), \tag{A.1}$$

where the total input signal is

$$x(t) = \sum_{p=0}^{P-1} x_p(t). \tag{A.2}$$

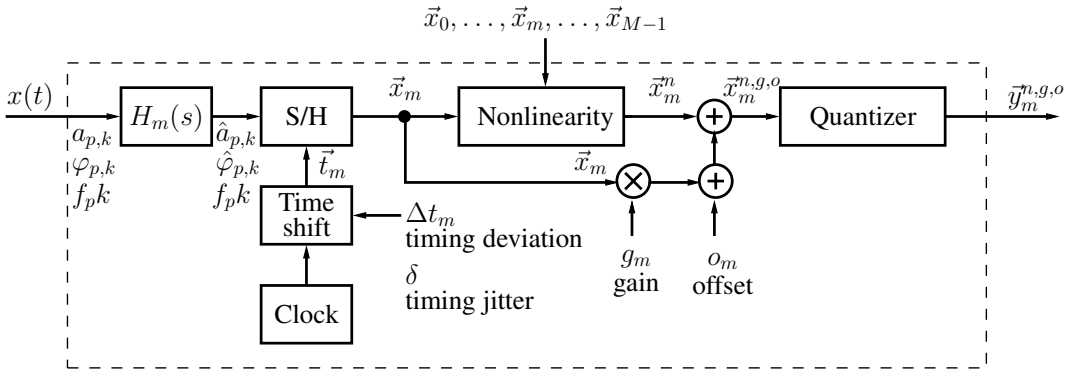

Figure A.2: Behavioral simulation model of the lth channel ADC.

This signal representation spans a sufficiently large signal space that allows us to simulate a broad class of possible input signals (including non-harmonic signals) and can easily be applied to continuous-time filter operations. Moreover, the simulation can imitate the sampling process with high calculation precision through direct calculation of the continuous-time sine functions for any specific continuous-time instant t.

A.2.3 Channel ADC Model

In order to achieve the described error effects from Sec. A.2.1 we have developed a behavioral channel model, which is presented in Fig. A.2.

A.2.3.1 Input Filter

The input signal $x(t)$ is sent through a continuous-time filter $H_m(s)$. The transfer function of the filter can be specified by its Laplace transform. An insightful example is the first-order RC-low pass. Its transfer function is

$$H_m(s) = \frac{1}{1 + s\tau_m} \tag{A.3}$$

where $\tau_m = R_m C_m$ to get the connection to a real world device. The filter operates on the amplitude coefficients $a_{p,k}$ and phase coefficients $\varphi_{p,k}$ of the Fourier series. For each given frequency component $f_p k$ these two coefficients are modified according to the transfer function and thereby become $\hat{a}_{p,k}$ and $\hat{\varphi}_{p,k}$.

A.2.3.2 Sample and Hold

In the S/H block the analog signal described by the Fourier coefficients is converted to discrete time values. Therefore, sampling instants must be generated. Through error analyses we have found out that all instants possess deterministic timing mismatches Δt_m and

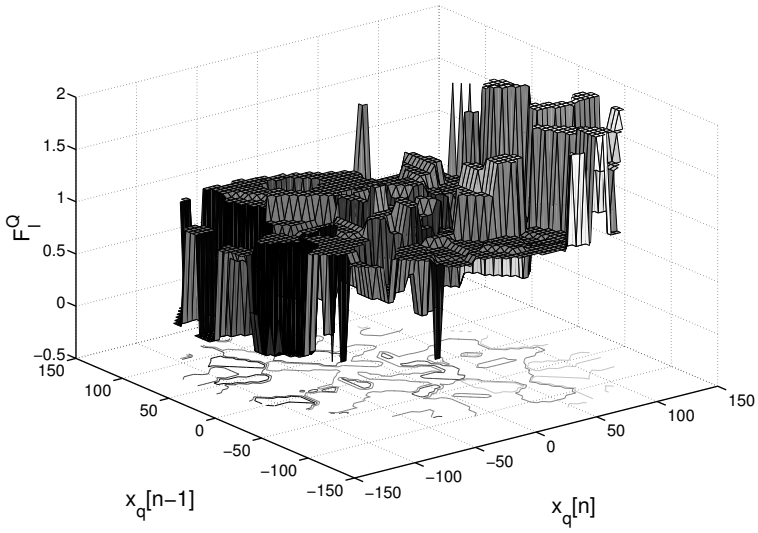

Figure A.3: Illustration of the nonlinear mapping $\mathcal{F}_m^Q$ with a memory of $J = 2$ and a quantization resolution of $Q = 8$ bits.

stochastic timing jitter δ. Hence, the time vector for the mth channel is

$$\begin{aligned}\vec{t}_m = \quad & [mT_s + \Delta t_m + \delta_{m,0}, (M+l)T_s + \Delta t_m + \delta_{m,1}, \ldots, \\ & (kM+m)T_s + \Delta t_m + \delta_{m,k}, \ldots, \\ & ((K-1)M+m)T_s + \Delta t_m + \delta_{m,K-1}]^T \end{aligned} \tag{A.4}$$

where M is the number of ADCs and K the number of samples of one channel ADC. The sampling process itself is the evaluation of the Fourier series, given by the coefficients $\hat{a}_{p,k}$, $\hat{\varphi}_{p,k}$, and $f_p k$, and the time vector $\vec{t}_m$

$$\vec{x}_m = x(\vec{t}_m). \tag{A.5}$$

A.2.3.3 Nonlinearity

In the next block, the sampled signal runs through a static or dynamic nonlinearity. The nonlinearity is realized as an arbitrary nonlinear mapping $\mathcal{F}_m$

$$\vec{x}_m^n = \mathcal{F}_m(\vec{x}_0, ..., \vec{x}_m, ..., \vec{x}_{M-1}). \tag{A.6}$$

We have to consider samples from all channels to be able to simulate the dynamic nonlinear behavior of the S/H circuits. With this approach we can easily simulate given static integral nonlinearity (INL) specifications, since the maximum of $\mathcal{F}$ is at the same time the INL as defined in [41].

In order to computationally efficiently implement the nonlinearity, we have to reduce the complexity of the nonlinear mapping $\mathcal{F}_m$. First, we rewrite the input of the mapping in a more convenient form

$$\vec{x} = \mathbf{X}(:), \tag{A.7}$$

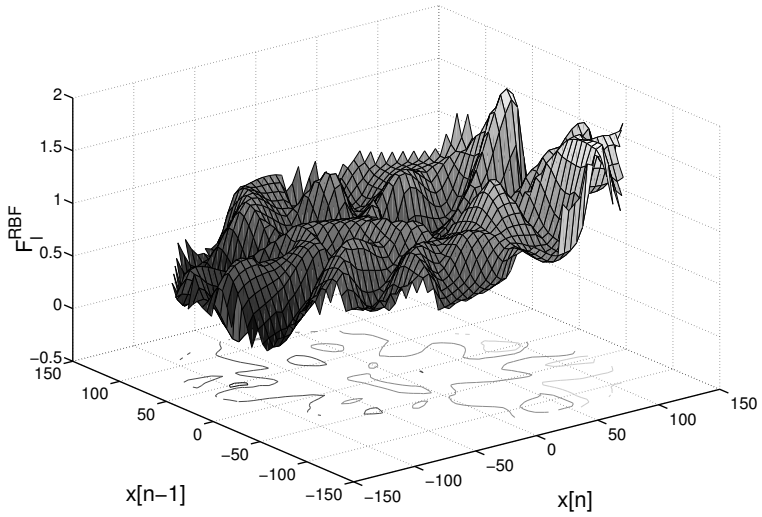

Figure A.4: RBF network approximation of the nonlinear mapping $\mathcal{F}_m$ with a memory of $J = 2$.

where

$$\mathbf{X} = [\vec{x}_0, ..., \vec{x}_m, ..., \vec{x}_{M-1}]^T . \tag{A.8}$$

Thus, the vector $\vec{x}$ contains all samples from all channel ADCs with the correct timing order. Afterwards, we assume causality and a finite memory length of J samples for the nonlinearity and, therefore, obtain the input sequence

$$\vec{x}[n]_J = \langle \vec{x}[n], \vec{x}[n-1], \ldots, \vec{x}[n-J+1] \rangle , \tag{A.9}$$

where $\vec{x}[n]_J$ is a subvector of $\vec{x}$ with length J starting at element n. To further reduce the complexity we utilize two different approaches. The first approach quantizes the input sequence, whereas the second one approximates the nonlinear mapping $\mathcal{F}_m$ with radial basis functions (RBF). The effect of the nonlinear mapping $\mathcal{F}_m^Q$ is illustrated in Fig. A.3. There we have used a finite memory of $J = 2$ and a quantization resolution of $Q = 8$ bits. In general, we need Q^J entries to implement the mapping with the help of a J-dimensional table. In the second approach the input sequences $\vec{x}[n]_J$ are mapped to scalar output samples using a weighted sum

$$\mathcal{F}_m^{RBF}(\vec{x}[n]_J) = \sum_{k=1}^{N_b} w_k \phi_k(\vec{x}[n]_J), \tag{A.10}$$

where

$$\phi_k(\vec{x}[n]_J) = \exp\left[-\frac{1}{2\sigma^2}||\vec{x}[n]_J - \vec{c}_k||^2\right] \tag{A.11}$$

and $\vec{c}_k$ is the constant center of the kth basis function $\phi_k(\vec{x}[n])$. An RBF network approximation is shown in Fig. A.4, where the relevance vector machine algorithm [133] has been used to estimate the weights w_k of the RBF network from samples of simulated nonlinear channel ADCs.

A.2.3.4 Gain and Offset

The block parallel to the nonlinearity multiplies the signal $\vec{x}_m$ with the gain g_m. Thereby a static gain mismatch can be simulated. After that, the offset o_m is added to obtain offset mismatches. To sum up, we modify the signal as

$$\vec{x}_m^{n,g,o} = \vec{x}_m \cdot g_m + o_m + \vec{x}_m^n. \tag{A.12}$$

Because of the nonlinearity the separate gain and offset block are redundant as they could be absorbed into the zeroth and first-order term of the nonlinearity, however, since the mismatches of these parameters are frequently investigated, we have used separate blocks.

A.2.3.5 Quantizer and Coder

In the next step, the signal is quantized in order to get the digital signal, i.e., a discrete-time and discrete-amplitude signal,

$$\vec{y}_m^{n,g,o} = \mathcal{Q}\left\{\vec{x}_m^{n,g,o}\right\}. \tag{A.13}$$

Finally, all channel outputs are merged into one output signal in a time-interleaved way and coded, e.g., one's complement or two's complement, afterwards.

A.3 Simulation Results

In the following we will present our simulation results of the most important error sources, which show the abilities of the environment. In Fig. A.5 we see the output spectrum of a time-interleaved ADC consisting of four channel ADCs with offset, gain, and timing mismatches. Additionally, the time-interleaved ADC produces timing jitter. Beside the input signal, i.e., a sine wave given as $x(t) = \sin(2\pi f_0 t)$, we see additional spurious lines in the spectrum. The spectral lines appear at $k\Omega_s/M$ for offset mismatches and at $\pm\Omega_0 + k\Omega_s/M$ for timing and gain mismatches. Although we use a 10-bit resolution and 1024 samples for this simulation, we see a noise floor, which is considerably above 89 dBc of an ideal 10-bit ADC [41]. This is due to the timing jitter, which increases the noise floor.

Another important error occurring in time-interleaved ADCs is the bandwidth mismatch. In order to simulate this error, we assume low-pass characteristics for the input filters and an ideal cut-off frequency (-3 dB), which is five times higher than the sampling frequency. Each input filter has a cut-off frequency that deviates randomly from the ideal one. These deviations are assumed to be Gaussian distributed with a standard deviation of 0.1. The transfer functions of the described filters are shown in Fig. A.6. In Fig. A.7 we see the output spectrum of a time-interleaved ADC with these input filters. We notice additional spectral lines similar to the case with static gain and timing mismatches.

Finally, we consider static nonlinearities. In [125] the authors show that the INL and the DNL of the time-interleaved ADC are smaller than the INL and the DNL of the worst channel ADC. In the output spectrum of a time-interleaved ADC, Fig. A.8, additional spectral lines arise due to the INL mismatch between the channels. Nevertheless, as simulations

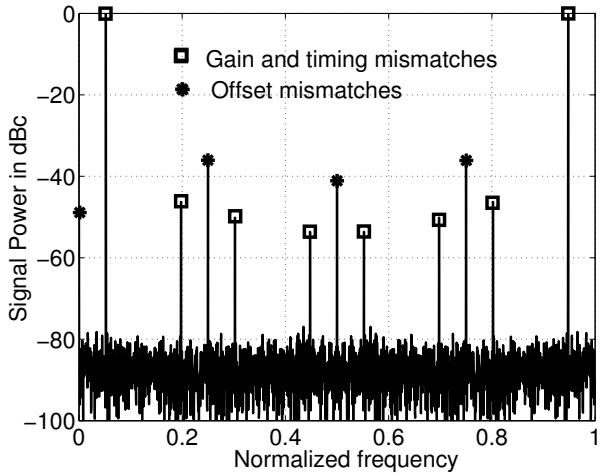

Figure A.5: Simulation with offset, gain and timing mismatches.

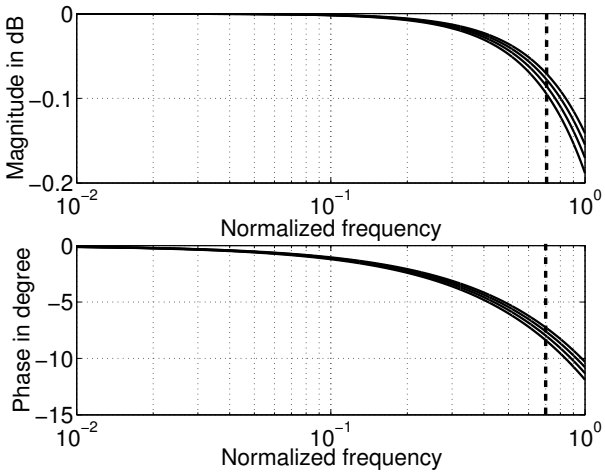

Figure A.6: Input filters used for demonstrating the bandwidth mismatch effect. The dashed line indicates half the sampling frequency.

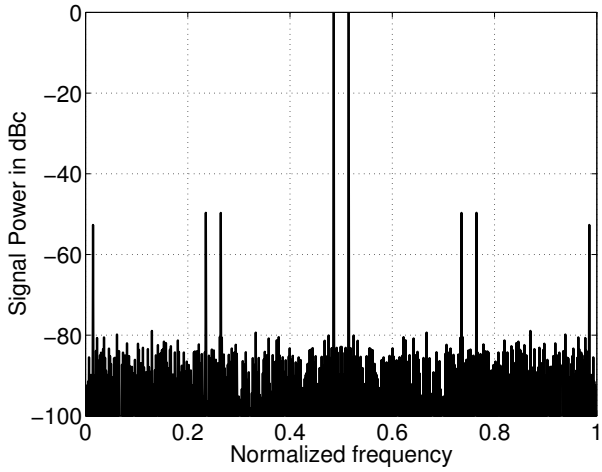

Figure A.7: The effect of bandwidth mismatches.

show, the whole noise and distortion energy decreases in a time-interleaved environment. In Fig. A.9 we see the SINAD of a time-interleaved ADC ($M = 4$) and its worst channel ADC. For each entry we have simulated 50 realizations of a time-interleaved ADC, where the channel ADCs have an INL drawn from a zero mean uniform INL distribution with a given standard deviation. We see that on the average the SINAD of the time-interleaved ADC is better than the SINAD of the worst channel ADC. In Fig. A.10 we see a comparison between the SFDR of the time-interleaved ADC and its worst channel ADC. Again, we notice the better performance of the time-interleaved ADC.

A.4 Conclusion

We have introduced a MATLAB environment for simulating the behavior of time-interleaved ADCs. We have shown how to generate continuous-time input signals and filter them with continuous-time filters. We have found a solution for the problem of sampling continuous-time signals in a non-uniform manner with high precision. Configurable parameters allow us to degrade the system performance to desired levels and characteristics. We are able to simulate the main signal processing errors in a time-interleaved ADC and can verify the results found in the literature.

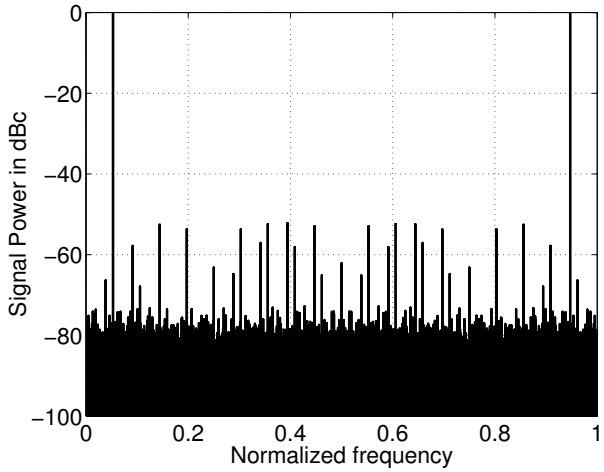

Figure A.8: Time-interleaved ADC where each channel ADC has a different INL.

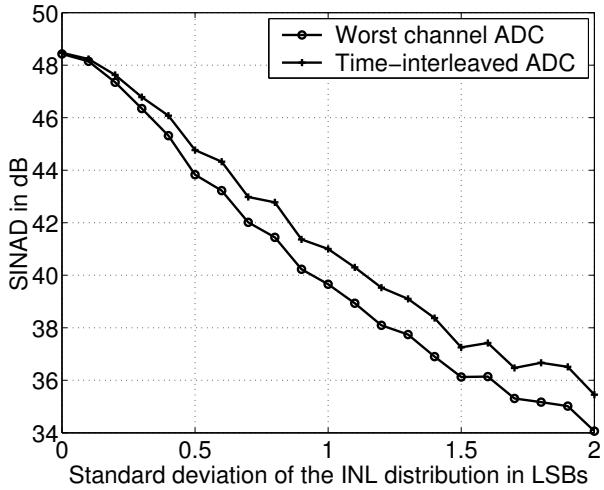

Figure A.9: Comparison between the SINAD of a time-interleaved ADC and its worst channel ADC.

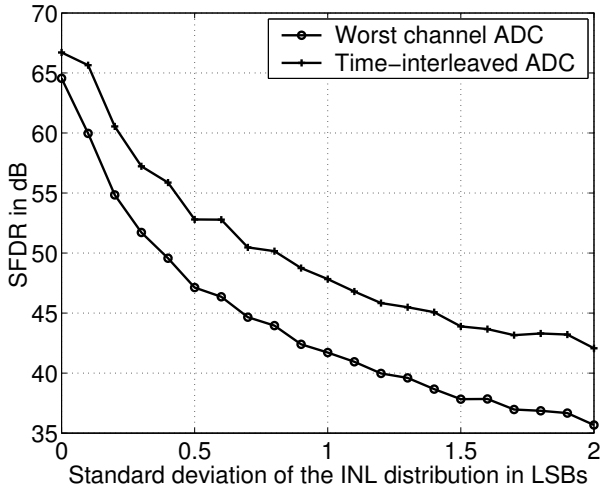

Figure A.10: Comparison between the SFDR of a time-interleaved ADC and its worst channel ADC.

Appendix B

Channel Mismatch Identification in the Time Domain

Existing time-domain channel mismatch identification algorithms are more power efficient than mismatch identification methods in the frequency domain. Unfortunately, time-domain methods are either not as accurate as frequency domain methods or they need additional analog components to identify the channel mismatches.

In the following we will introduce two principal approaches. All methods of the first approach, which are presented in Sec. B.1, work exclusively in the digital domain. Therefore, we call them purely digital methods. The quality of these digital methods depends very much on the input signal and, therefore, the quality differs with the input signal distribution. All methods of the second approach, which are presented in Sec. B.2, use an additional reference channel ADC to determine the mismatches. These methods are much more accurate than the purely digital methods; however, under some circumstances they can suffer from bad input signal distributions as well.

B.1 Purely Digital Methods

Digital methods only use the output signals of time-interleaved ADCs to determine the channel mismatches. We analyze three methods to determine offset, gain, and timing mismatches.

For further analysis, we assume that we have taken K samples with each channel of a time-interleaved ADC consisting of M channels. Thus, altogether we have taken $N = KM$ samples. To address a particular sample we either use $y_m[k]$ or $y[n]$, where both representations are connected by $n = m + kM$.

B.1.1 Offset Mismatch Identification

The basic idea of the present digital offset mismatches identification is that without any mismatches the average over all K samples $y_m[k]$ in a given channel m should be identical for all M channels and, in the ideal case, i.e., without offset errors, it should be equal to the mean value of the input signal which often will be zero. Thus, when we average the

samples of each channel ADC, which is

$$y_m^o = \frac{1}{K}\sum_{k=0}^{K-1} y_m[k], \tag{B.1}$$

and compare the result to the average of all samples,

$$\begin{aligned} y_{Ref}^o &= \frac{1}{N}\sum_{m=0}^{M-1}\sum_{k=0}^{K-1} y_m[k] \\ &= \frac{1}{N}\sum_{n=0}^{N-1} y[n], \end{aligned} \tag{B.2}$$

we obtain the offset mismatch estimates

$$\tilde{o}_m = y_m^o - y_{Ref}^o. \tag{B.3}$$

Unfortunately, the method becomes inaccurate either if there is a correlation between the input signal and the channel switching sequence of the time-interleaved ADC, i.e., the estimates depend not only on the mismatches but on the input signal as well, or if we have gain mismatches in combination with non-DC free input signals.

To find such bad input signals, i.e., signals which correlate with the channel switching sequence, we investigate the identification method in the frequency domain. The discrete Fourier transform of the output samples is given by

$$Y[l] = \sum_{n=0}^{N-1} y[n]e^{-jln\frac{2\pi}{N}}, \tag{B.4}$$

which is the output spectrum $Y\left(e^{j\Omega T_s}\right)$ of the windowed sampled output signal evaluated on discrete frequency points $\left(\Omega = l\frac{\Omega_s}{N}\right)$, that is

$$\begin{aligned} Y[l] &= \left(Y(e^{j\Omega T_s}) * W(e^{j\Omega T_s})\right)|_{\Omega = l\frac{\Omega_s}{N}} \\ &= \tilde{Y}(e^{j\Omega T_s})_{\Omega = l\frac{\Omega_s}{N}}. \end{aligned} \tag{B.5}$$

When we consider all frequency bins, where $l = p\frac{N}{M}$ and $p = [0, \ldots, M-1]$, we can write (B.4) as

$$Y\left[p\frac{N}{M}\right] = \sum_{n=0}^{N-1} y[n]e^{-jpn\frac{2\pi}{M}}. \tag{B.6}$$

We can use (B.6) to relate (B.3) to the output spectrum $\tilde{Y}\left(e^{j\Omega T_s}\right)$. Therefore we take the DFT of (B.1), which gives

$$\sum_{m=0}^{M-1} y_m^o e^{-jpm\frac{2\pi}{M}} = \frac{1}{K}\sum_{m=0}^{M-1}\sum_{k=0}^{K-1} y_m[k]e^{-jpm\frac{2\pi}{M}}. \tag{B.7}$$

Then we use the relation $n = m + kM$, which results in

$$\sum_{m=0}^{M-1} \tilde{o}_m e^{-jpm\frac{2\pi}{M}} = \frac{1}{K} \sum_{n=0}^{N-1} y[n] e^{-jpn\frac{2\pi}{M}} \tag{B.8}$$

and can express (B.8) by using (B.6) as

$$\sum_{m=0}^{M-1} y_m^o e^{-jpm\frac{2\pi}{M}} = \frac{1}{K} Y\left[p\frac{N}{M}\right]. \tag{B.9}$$

By using (B.6) we can write for (B.2)

$$y_{Ref}^o = \frac{1}{N} Y[0]. \tag{B.10}$$

Finally, we can write the offset identification given by (B.3) as

$$\tilde{o}_m = \frac{1}{K}\frac{1}{M} \sum_{p=0}^{M-1} Y\left[p\frac{N}{M}\right] e^{jpm\frac{2\pi}{M}} - \frac{1}{N} Y[0]. \tag{B.11}$$

From the frequency representation of the algorithm we see that input signals with frequencies close to $\Omega = p\frac{\Omega_s}{M}$ can influence the accuracy of the identification. Moreover, if the input signal shows significant power at those frequencies the method will fail. For broadband signals with uniform frequency distributions, the accuracy increases with the number of samples, since the signal power at $\Omega = p\frac{\Omega_s}{M}$ will decrease with N but the offset mismatch dependent contribution will stay.

To evaluate the performance of the offset mismatch identification algorithm, we have used a time-interleaved ADC with eight channel ADCs ($M = 8$) and offset mismatches. Furthermore, we have used a multitone signal, bandlimited to $0.4\Omega_s$, consisting of 200 sinusoidal tones with arbitrary selected frequencies, phases, and amplitudes. The amplitudes have been scaled in a way that the maximum amplitude of the multitone signal is within FSR=2. After we have identified the offset mismatches with this signal we have used a sinusoidal input signal close to half the Nyquist frequency to determine the SINAD with and without compensation. To obtain an average behavior for the algorithm, we have simulated 100 time-interleaved ADCs for different numbers of samples, where all ADCs had offset mismatches with a standard deviation of 0.01 FSR.

In Fig. B.1 we see the average SINAD before and after the compensation with the identified offset mismatches. We see that with an increasing number of samples the accuracy of the method increases as well. Even for the worst-case estimates, shown in Fig. B.2, we obtain good results. The SINAD increases with the number of samples, since the leakage effects decrease, i.e., the neighbor frequencies around $p\frac{\Omega_s}{M}$ contribute less power to $p\frac{\Omega_s}{M}$.

B.1.2 Gain Mismatch Identification

The gain mismatch identification is based on the assumption that without any mismatches all channel ADCs produce the same power. As soon as there are gain mismatches the power

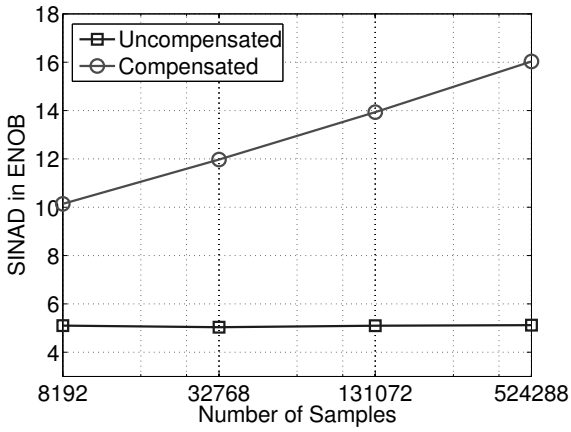

Figure B.1: Average SINAD in ENOB before and after compensation. The offset mismatches have been identified for different numbers of samples. For an increasing number of samples, the accuracy of the identification and therefore the SINAD increase as well.

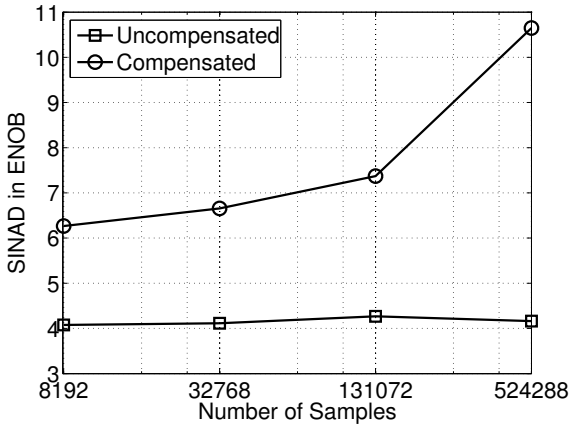

Figure B.2: Worst SINAD in ENOB before and after offset compensation. Even in the worst-case we obtain good offset identification results, which improve with the number of samples.

of the channels mismatch as well. Hence, we can determine the gain mismatch by relating the average power of each channel to the average power of the entire time-interleaved ADC, which gives

$$\tilde{g}_m = \sqrt{\frac{y_m^g}{y_{Ref}^g}} \tag{B.12}$$

where

$$y_m^g = \frac{1}{K}\sum_{k=0}^{K-1} y_m^2[k] \tag{B.13}$$

and

$$\begin{aligned} y_{Ref}^g &= \frac{1}{N}\sum_{m=0}^{M-1}\sum_{n=0}^{K-1} y_m^2[k] \\ &= \frac{1}{N}\sum_{n=0}^{N-1} y^2[n] \end{aligned} \tag{B.14}$$

Like for the purely digital offset mismatch identification, purely gain mismatch identification becomes inaccurate when the input signal correlates with the switching sequence. In contrast to offset mismatch identification, it is less obvious which frequencies can cause bad identification results. To find those frequencies, we take the DFT of (B.13), which can be written with (B.6) as

$$\begin{aligned} \sum_{m=0}^{M-1} y_m^g e^{-jpm\frac{2\pi}{M}} &= \frac{1}{K}\sum_{m=0}^{M-1}\sum_{k=0}^{K-1} y_m^2[k] e^{-jpm\frac{2\pi}{M}} \\ &= \frac{1}{K}\sum_{n=0}^{N-1} y^2[n] e^{-jpn\frac{2\pi}{M}} \\ &= \frac{1}{K} Y^{\circledast 2}\left[p\frac{N}{M}\right], \end{aligned} \tag{B.15}$$

where the operator $\circledast 2$ stands for a circular convolution of the signal $\tilde{Y}(e^{j\Omega T_s})$ (cf. (B.5)) with itself. By comparing (B.14) with (B.6) we see that we can express (B.14) as

$$\begin{aligned} y_{Ref}^g &= \frac{1}{N}\sum_{n=0}^{N-1} y^2[n] \\ &= \frac{1}{N} Y^{\circledast 2}[0]. \end{aligned} \tag{B.16}$$

With (B.15) and (B.16) we can rewrite the gain mismatch identification given by (B.12) as

$$\tilde{g}_m = \sqrt{\frac{\frac{1}{M}\sum_{p=0}^{M-1} Y^{\circledast 2}\left[p\frac{N}{M}\right] e^{jpm\frac{2\pi}{M}}}{\frac{1}{M} Y^{\circledast 2}[0]}} \tag{B.17}$$

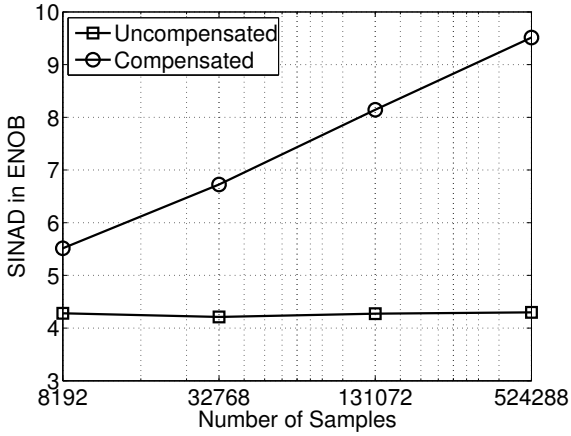

Figure B.3: We see the average SINAD in ENOB of the purely digital gain identification for different numbers of samples. With an increasing number of samples the identification quality of the algorithm increases as well.

From (B.17) we see that the gain identification algorithm is influenced by input signals with significant signal power at two arbitrary frequency locations Ω_1 and Ω_2, where either $\pm 2\Omega_1$, $\pm 2\Omega_2$, $\pm(\Omega_1 - \Omega_2)$, or $\pm(\Omega_1 + \Omega_2) = p\frac{\Omega_s}{M}$. This mixture of frequencies occurs because of the circular convolution in (B.17). Furthermore, we see from (B.17) that offset mismatches, which produce mismatch power at $\Omega = p\frac{\Omega_s}{M}$, have to be identified and compensated before the gain mismatch compensation method can be used.

For testing the method we have used a time-interleaved ADC with eight channel ADCs ($M = 8$). The input signal for the identification and the test signal for the measurement of the SINAD have been the same as for evaluating the purely digital offset mismatch identification presented in Sec. B.1.1. We have averaged the SINAD of 100 different time-interleaved ADCs with gain mismatches. The gain mismatches drawn from a Gaussian distribution with a standard deviation of 0.05 and a mean of 1. In Fig. B.3 we see the result of the simulation. The difference between the compensated and the uncompensated SINAD increases with an increasing number of samples. The picture changes when we look at the worst-case estimates shown in Fig. B.4. We see that an increased number of samples does not necessarily lead to an improved identification result. Because of the convolution of the input signal with itself, it could happen - even for a broadband signal - that too much input signal power is shifted to $p\frac{\Omega_s}{M}$.

B.1.3 Timing Mismatch Identification

In [26] a timing mismatch identification method was introduced. It is based on the assumption that if a channel ADC has a timing mismatch the difference between samples of this channel ADC and samples from its predecessor are on average larger or smaller than the average difference of all channels. In particular, in [26] the authors identify the timing

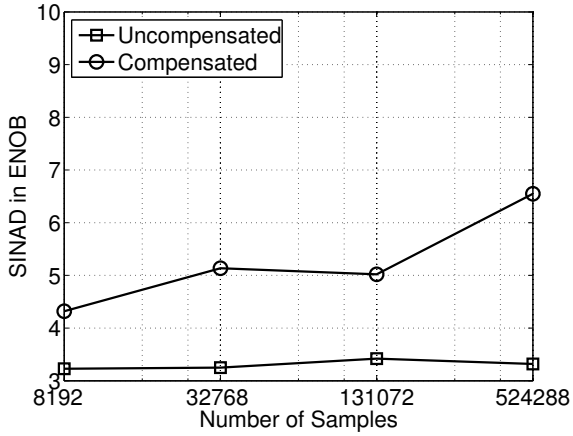

Figure B.4: We see the worst SINAD in ENOB of the purely digital gain identification for different numbers of samples. Contrary to the purely offset identification algorithm, the purely gain identification algorithm has a bad worst-case performance. An increased number of samples does not necessarily produce a better identification result.

mismatches as

$$\begin{aligned}\Delta\tilde{t}_m &= T_s \sum_{l=0}^{m} \left(\frac{\sum_{k=0}^{K-1} \left(y_l[k] - y_{l-1}[k]\right)^2}{\frac{1}{M}\sum_{n=0}^{N-1} \left(y[n] - y[n-1]\right)} - 1 \right) \\ &= T_s \sum_{l=0}^{m} \check{r}_l, \end{aligned} \tag{B.18}$$

where $y[-1] = 0$ and $y_{-1}[n] = y_{M-1}[n-1]$. The summation over $\check{r}_l$ is necessary, since we estimate the relative timing mismatch between two adjacent channels only. This relationship equals the relationship of DNL and INL errors in an ADC.

Unfortunately, if the number of samples is not huge ($N >> 10^6$) the algorithm identifies timing mismatches with a large variance. This is particularly true for input signals with a significant amount of spectral power close to half the Nyquist frequency [26]. We will use this algorithm to compare it to our results of time-domain identification with a reference channel ADC. A profound analysis of the algorithm can be found in [30, 25, 28, 27]. Like the purely digital gain and offset mismatch identification, this timing mismatch identification is vulnerable to correlations with the switching sequence as well.

To evaluate the performance of the algorithm we have once again used a time-interleaved ADC with eight channels ($M = 8$) and input signals as described in Sec. B.1.1. For different numbers of samples we have simulated 100 time-interleaved ADCs with timing mismatches. The timing mismatches of the time-interleaved ADCs have been Gaussian distributed with a standard deviation of $0.01T_s$ and zero mean. In Fig. B.5 we see the averaged SINAD for the compensated and the uncompensated time-interleaved ADCs. To avoid any influence from the reconstruction we have used a perfect reconstruction method [49]. Hence, the SINAD

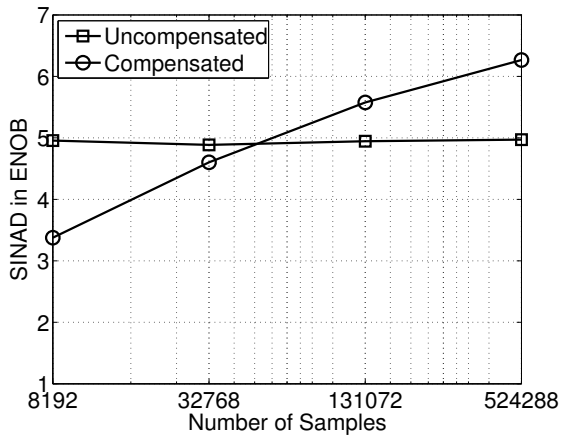

Figure B.5: Average SINAD in ENOB for compensated and uncompensated timing mismatches. The accuracy of the identification and therefore the average SINAD increase with the number of samples. However, the SINAD increases only very slowly and we need a huge number of samples to obtain good estimates.

of the compensated time-interleaved ADCs is directly related to the identification quality. We need a huge number of samples to get accurate estimates. Moreover, as we realize from Fig. B.6 the worst-case performance is even worse. Thus, to obtain acceptable identification results we need a large amount of samples.

B.2 Methods with a Reference Channel

In the last section we have seen that purely digital methods are vulnerable to input signals and switching sequence correlations, which we have investigated in the frequency domain. Moreover, we need a huge amount of samples to get good estimates. Therefore, we propose a new method, which utilizes a time-interleaved ADC with an additional channel ADC as reference. The additional channel ADC can be triggered with the same clock signal as one of the other channel ADCs. Hence, in the ideal case, i.e., without any mismatches, it takes samples at the same time instants as one of the other channel ADCs. The principle is illustrated in Fig. B.7 and the corresponding timing is shown in Fig. B.8. The method is much more robust against correlation between the switching sequence and the input signal and, compared to purely digital identification methods, it requires much shorter observation times.

The reference channel can be any channel in the time-interleaved ADC, i.e., it does not have to be calibrated. However, a calibrated reference ADC can improve the estimation results.

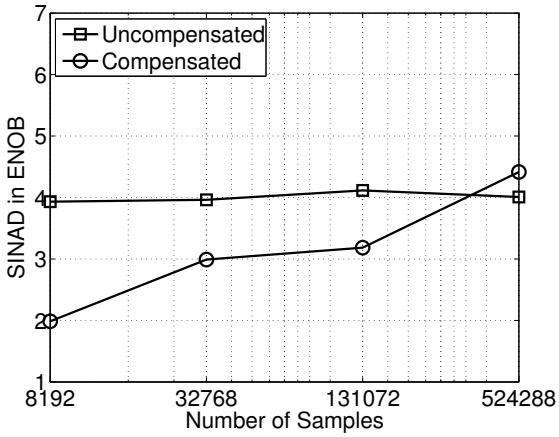

Figure B.6: Worst SINAD in ENOB for compensated and uncompensated timing mismatches. The figures show that a compensation with the identified timing mismatches can even degrade the SINAD below the uncompensated case.

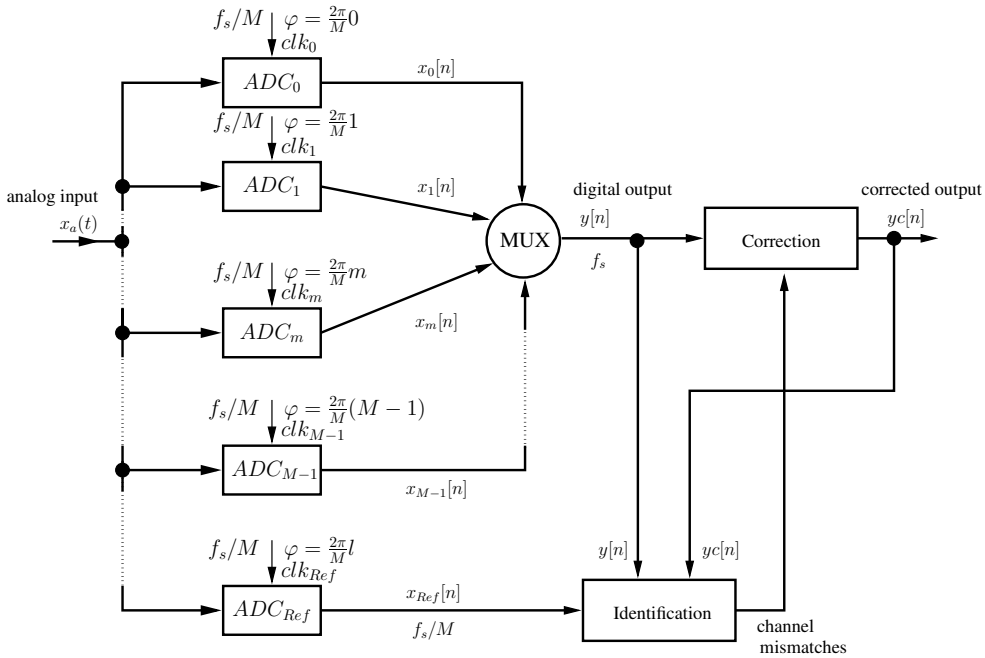

Figure B.7: We illustrate the principle architecture of a time-interleaved ADC with a reference channel ADC. The reference channel ADC samples at the same time instants as one selected channel ADC (cf. timing diagram in Fig. B.8). As soon as there are any mismatches between the reference channel and the selected channel, we obtain different sampling values. This value mismatch can be used to acquire information about the channel mismatches.

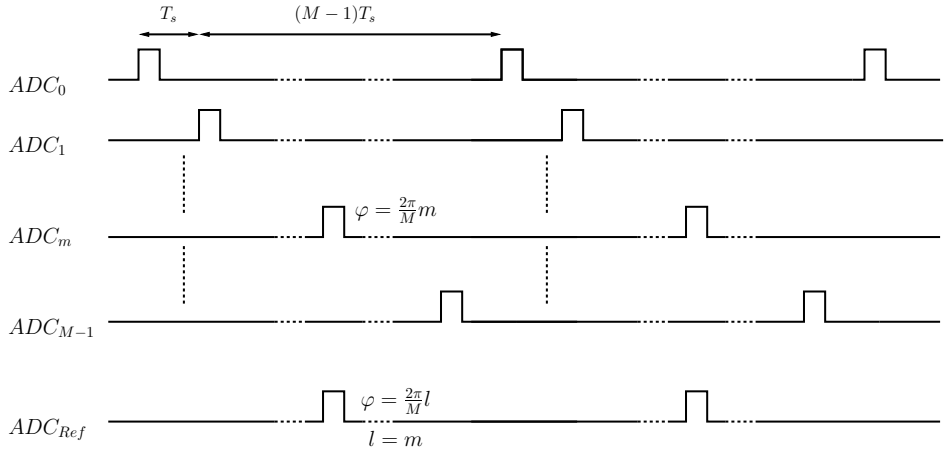

Figure B.8: Timing diagram for the identification with a reference channel ADC. In this illustration the reference channel has the same clock signal as the mth channel ADC.

B.2.1 Offset Mismatch Identification

The offset can be determined by comparing the mean value of the reference system and the mean value of the channel ADC to calibrate. The differences of the means are an estimate for the channel mismatch, which is given by

$$\tilde{o}_m = \frac{1}{K}\sum_{k=0}^{K-1}\left(y_m[k] - y_{Ref}[k]\right). \tag{B.19}$$

Without any other mismatches we exactly obtain the offset mismatch, since

$$\begin{aligned}\tilde{o}_m &= \frac{1}{K}\sum_{k=0}^{K-1}\left((x[m+kM]+o_m) - (x[m+kM]+o_{Ref})\right)\\ &= o_m - o_{Ref}.\end{aligned} \tag{B.20}$$

This method assumes a DC free input signal. Otherwise the quality of the identification is influenced by gain mismatches.

As shown in (B.20), we will identify the exact offset mismatch if we have offset mismatches only. Moreover, even for combined offset, gain and timing mismatches, we will obtain the exact estimates for long observation times as long as the input signal is DC free. However, this is only true if the input signal and the switching sequence of the channel ADCs do not correlate. If we have a correlation and combined channel mismatches, the estimates can become inaccurate.

For the following simulations we use a time-interleaved ADC with eight channel ADCs ($M = 8$) and an additional reference channel. The channel ADCs have offset and gain mismatches. The offset mismatches have a standard deviation of 0.01 FSR, where the full-scale range (FSR) is 2. The standard deviation of the gain mismatches ranges from $\sigma_{\tilde{g}} = 0.1$

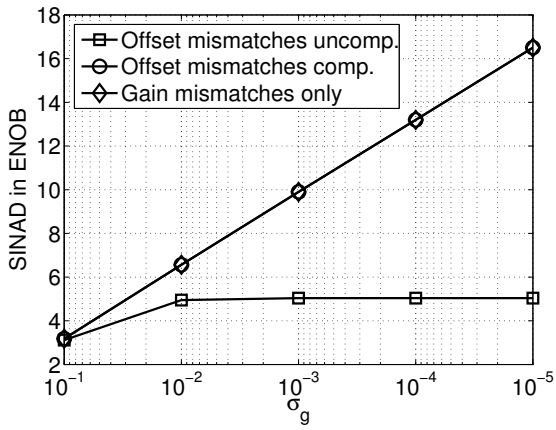

Figure B.9: The figure shows the average identification quality for different gain mismatch standard deviations and constant offset mismatches. The identified and compensated offset mismatches are only limited by the remaining gain mismatches.

to $\sigma_{\tilde{g}} = 0.00001$. For each standard deviation we simulate 100 randomly generated time-interleaved ADCs. Each generated ADC is driven by two different signals. First, we use a multitone signal, bandlimited to $0.4\Omega_s$, composed of 200 arbitrary sinusoidal signals. From this signal we take $N = 32768$ samples and determine the estimates for the offset according to (B.19). Second, we generate a single sinusoidal input signal close to half the sampling frequency to measure the SINAD. Therefore, we have taken $N = 32768$ samples with each time-interleaved ADC configuration and calculated the SINAD for uncompensated offset and gain mismatches, for compensated offset and uncompensated gain mismatches, and for gain mismatches only. To compensate the offset mismatch we use the identified offset mismatch estimates. For the measurement of the SINAD, we do not take the signal power at $\Omega = 0$ into account, since we compensate the offset mismatches and do not compensate the overall offset of the time-interleaved ADC. However, if the offset of the system is critical, the offset of the reference channel has to be calibrated by some other means. The average SINAD in ENOB over all 100 outcomes for all standard deviations is shown in Fig. B.9. The uncompensated curve is saturated for a gain mismatch standard deviation less than 0.01 because the offset mismatch limits its performance. The compensated offset curve and the curve, where we consider gain mismatches only, are very close. We obtain a very similar picture for the worst-case shown in Fig. B.10. The compensated offset curve is only limited by the uncompensated gain mismatches. Thus, the interaction of gain mismatches and offset mismatches is negligible for the presented offset identification and uniformly distributed input spectra.

B.2.2 Gain Mismatch Identification

In order to identify gain mismatches, we compare the power of the reference channel and the selected channel ADC outputs. When we first compensate offset mismatches, any deviation

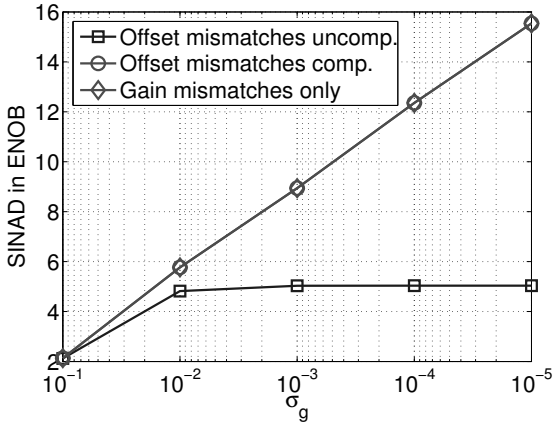

Figure B.10: The figure shows the worst-case identification quality for different gain mismatch standard deviations and constant offset mismatches. As for the average case the identification is only limited by the remaining gain mismatches.

of the channel power has to be caused by gain mismatches, since timing mismatches do not cause power variations among the channels. Thus, the gain mismatches are given by

$$\tilde{g}_m = \sqrt{\frac{\sum_{k=0}^{K-1} y_m^2[k]}{\sum_{k=0}^{K-1} y_{Ref}^2[k]}}. \tag{B.21}$$

To show the performance of the algorithm we simulate a time-interleaved ADC with eight channels ($M = 8$) and an additional reference channel. Except that the considered channel ADCs have gain and timing mismatches, the configuration and the input signal specification is identical to the offset identification simulations in Sec. B.2.1. The gain mismatches have a constant standard deviation of $\sigma_{\tilde{g}} = 0.05$. The standard deviation of the timing mismatches starts from $\sigma_{\tilde{r}} = 0.1$ and goes down to $\sigma_{\tilde{r}} = 0.00001$. In Fig. B.11 we see the average SINAD in ENOB for uncompensated gain and timing mismatches, for uncompensated gain and compensated timing mismatches, and for timing mismatches only. The uncompensated curve is saturated because the timing mismatch limits the performance and a decreasing gain mismatch standard deviation has no influence on the performance. The gain identification is only limited by the timing mismatches. Hence, although we have fully identified and compensated the gain mismatches the performance is limited by timing mismatches. This can be seen by considering the compensated curve and the curve, where we have simulated timing mismatches only.

B.2.3 Timing Mismatch Identification

The problem of the timing mismatch identification algorithm presented in [26] is its sensitivity to the input signal frequency distribution. With the reference channel approach we can improve the accuracy as well as the identification stability of the algorithm. For the method

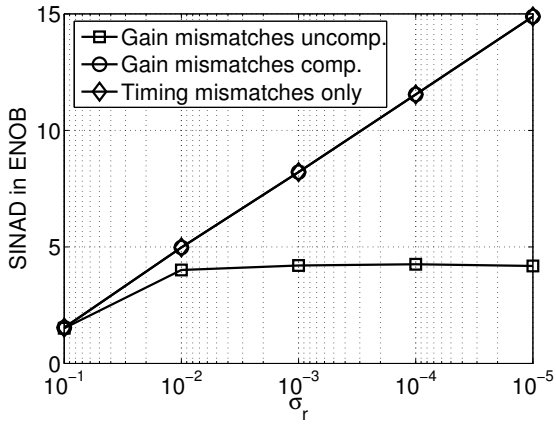

Figure B.11: The figure shows the excellent average performance of the gain mismatch identification. After we have compensated the identified gain mismatches, the performance is only limited by the remaining timing mismatches.

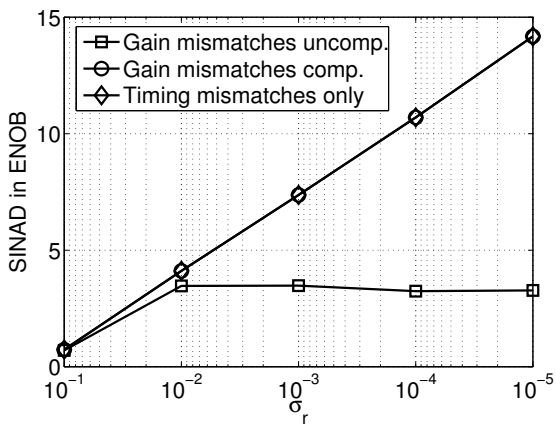

Figure B.12: Worst SINAD for the gain mismatch identification method as a function of the timing mismatch standard deviation for the compensated and the uncompensated case. Even in worst-case situations, the gain mismatch identification is accurate.

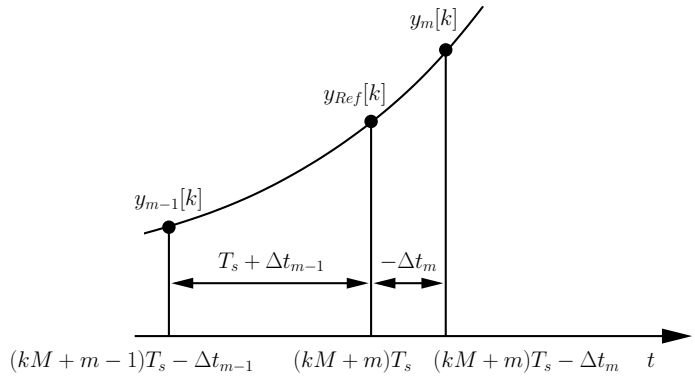

Figure B.13: The figure illustrates the identification of timing mismatches with a reference channel ADC. Without any mismatches, the difference between the reference channel and its predecessor equals the difference between the selected channel ADC and its predecessor. As soon as we have timing mismatches, the differences diverge. For negative timing mismatches Δt_m, i.e., the clock signal is delayed, the magnitude difference $y_m[k] - y_{m-1}[k]$ is on average larger than the magnitude difference of $y_{Ref}[k] - y_{m-1}[k]$ and vice versa for negative timing mismatches.

presented in [26], the reference is the average over all channel ADCs. In our case, we can use the additional channel ADC as reference. The principle is explained in Fig. B.13. Without any mismatches, the amplitude difference between the reference channel output at time $(kM+m)T_s$ and the proceeding channel ADC output at time $(kM+m-1)T_s$ equals the difference of the current channel ADC output and the proceeding channel ADC output. As soon as we have timing mismatches, these differences diverge. For negative timing mismatches, i.e., the clock signal is delayed, the magnitude difference $y_m[k] - y_{m-1}[k]$ is on average larger than the magnitude difference of $y_{Ref}[k] - y_{m-1}[k]$ and vice versa for positive timing mismatches. In Fig. B.13 we have shown an example with a positive slope. For negative slopes we obtain the same results with opposite signs. Thus we can write

$$\frac{|y_{Ref}[k] - y_{m-1}[k]|}{T_s + \Delta t_{m-1}} = \frac{|y_m[k] - y_{m-1}[k]|}{T_s + \Delta t_{m-1} - \Delta t_m}, \tag{B.22}$$

where (B.22) is only exact when the mth channel ADC has no timing mismatches, i.e., $\Delta t_m = 0$. Otherwise, (B.22) describes the best local linear approximation to the signal evolution. In this case, we can use the relation to determine the timing mismatches. To this end, we average over all slopes in an ensemble of observations. Therefore, we can write for (B.22)

$$\begin{aligned} E\left\{\frac{|\tilde{y}_{Ref} - \tilde{y}_{m-1}|}{T_s + \Delta t_{m-1}}\right\} &= E\left\{\frac{|\tilde{y}_m - \tilde{y}_{m-1}|}{T_s + \Delta t_{m-1} - \Delta t_m}\right\} \\ \frac{\Delta t_m}{T_s + \Delta t_{m-1}} &= 1 - \frac{E\left\{|\tilde{y}_m - \tilde{y}_{m-1}|\right\}}{E\left\{|\tilde{y}_{Ref} - \tilde{y}_{m-1}|\right\}}. \end{aligned} \tag{B.23}$$

When we further use the relation

$$\begin{aligned} \frac{\Delta t_m}{T_s + \Delta t_{m-1}} &\cong \frac{\Delta t_m}{T_s} \\ &\cong r_m, \end{aligned} \tag{B.24}$$

since the mismatches Δt_{m-1} are very small compared to the sampling period T_s, we can identify the relative timing mismatches as

$$r_m = 1 - \frac{E\left\{|\tilde{y}_m - \tilde{y}_{m-1}|\right\}}{E\left\{|\tilde{y}_{Ref} - \tilde{y}_{m-1}|\right\}}. \tag{B.25}$$

The basic assumption of the method was that, for a negative timing mismatch, we obtain a larger difference between the selected channel ADC and its predecessor compared to the difference of the reference channel ADC and its predecessor. There are cases where this assumption is not true. For example, when we sample a single sinusoid the first sample may occur just before its maximum amplitude and the second one after its maximum amplitude. Then, a negative timing mismatch can cause a negative slope. Nevertheless, for many cases the basic assumption is true [25]. Furthermore, we see from (B.22) and (B.25) that for compensated timing mismatches even for a single sample the identified timing mismatch becomes zero.

For a finite number of samples, we can only estimate the true mean values. For a finite number of samples K, (B.25) becomes

$$r_m = 1 - \frac{\sum_{k=0}^{K-1} |y_m[k] - y_{m-1}[k]|}{\sum_{k=0}^{K-1} |y_{Ref}[k] - y_{m-1}[k]|}. \tag{B.26}$$

For the simulation we use a time-interleaved ADC with eight channel ($M = 8$) and an additional reference channel. The basic properties of the time-interleaved ADC and the input signals are identical to the ones in Sec. B.2.1. Only the standard deviation of the timing mismatches is between $\sigma_{\tilde{r}} = 0.1T_s$ and $\sigma_{\tilde{r}} = 0.00001T_s$. In Fig. B.14 we see the average SINAD in ENOB we have achieved by using a perfect reconstruction method [49]. We compare our method with the uncompensated time-interleaved ADC and the compensated time-interleaved ADC, where we have used the purely digital timing mismatch identification introduced in Sec. B.1.3. The compensated curve scales with the standard deviation. A smaller standard deviation of the timing mismatches leads to a larger SINAD. In contrast, the purely digital method saturates very fast and for smaller standard deviations it is even worse than the uncompensated case. This is due to the limited number of samples of $N = 32768$. As discussed in Sec. B.1.3 the accuracy of the purely digital method depends on the number of samples. The compensated curve, where we have used our reference channel approach, is about 2 ENOB better than the uncompensated curve over the entire range of the standard deviation. This is illustrated in more detail in Fig. B.15, where we show the difference between the compensated and the uncompensated curve. We see that the compensated curve scales with the standard deviation. This means that we can iteratively use identification and compensation to increase the accuracy to any requirement. However, the result is influenced by the reconstruction method and in practical applications limited

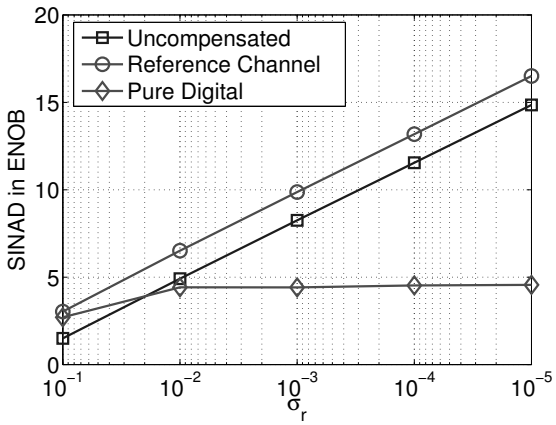

Figure B.14: The figure shows the average identification quality for different timing mismatch standard deviations. The average performance of the identification algorithm with a reference channel is significantly superior to the purely digital method. On average, we obtain timing mismatch estimates that, with a perfect reconstruction method, improve the SINAD by about 2 ENOB.

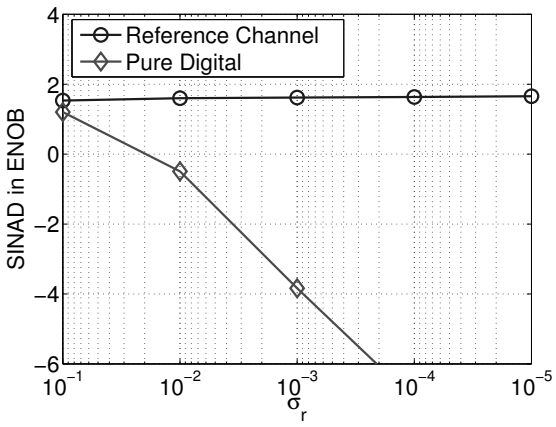

Figure B.15: The figure shows the difference between the compensated cases of Fig. B.14 and the uncompensated case. The identification quality of the reference channel method scales with the standard deviation of the timing mismatches, i.e., for smaller timing mismatches we obtain better estimates. The purely digital method fails for $\sigma_{\tilde{r}} \leq 10^{-2}$ and the limited number of samples $N = 32768$ as the resulting output is worse than the uncompensated case.

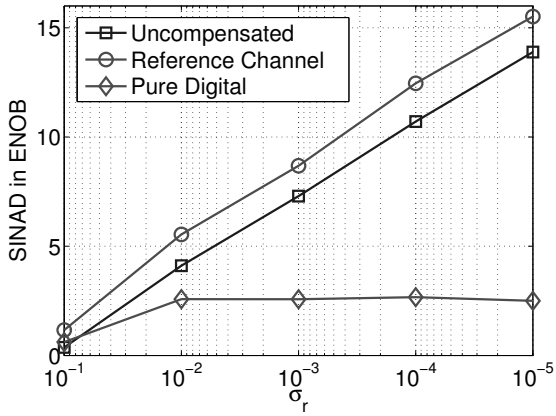

Figure B.16: The figure shows the worst-case identification quality for different timing mismatch standard deviations. Even in the worst case we can significantly improve the SINAD with our reference channel ADC method.

by the quantization noise. Fur such cases, we have to use more samples to average out the quantization noise in order to increase the identification accuracy. Even for our worst-case simulation shown in Fig. B.16 we realize the excellent identification quality, which allows us to improve the SINAD by about 2 ENOB.

B.3 Conclusion

We have investigated time-domain methods for channel mismatch identification. As simulations and calculations have shown, purely digital methods work well as long as we do not have a correlation between the input signal and the switching sequence. However, we only have investigated the methods for individual mismatches (offset, gain, and timing mismatches) and have not considered the identification of combined mismatches, i.e., cases were we identify one mismatch, e.g., offset mismatch, in the presence of other mismatches, e.g., gain and timing mismatches.

For mismatch identification with a reference channel we have also investigated cases for combined channel mismatches. The results are very promising, since the identification of individual mismatches, e.g., offset mismatches, does not seem to be influenced by other mismatches, e.g., gain and timing mismatches.

Nevertheless, we did not fully analyze the time-domain methods, especially for combined mismatches effects. Therefore, we have only included the methods in this appendix.

Appendix C

Signal and System Considerations

C.1 System Classification

A system H is linear if and only if

$$H(a_1x_1(t) + a_2x_2(t)) = a_1H(x_1(t)) + a_2H(x_2(t)) \tag{C.1}$$

for any arbitrary input signals $x_1(t)$ and $x_2(t)$, and any arbitrary constants a_1 and a_2. If this superposition principle does not hold the system is nonlinear [114].

A system H is static or memoryless if its output at any time instant t depends only on the current input at a time t, but not on any past or future inputs. In any other case, the system is said to be dynamic or to have memory [114].

A system H is time-invariant if and only if

$$H(x(t)) = y(t), \tag{C.2}$$

implies that

$$H(x(t - \Delta t)) = y(t - \Delta t) \tag{C.3}$$

for every input signal $x(t)$ and every time shift Δt [114].

C.2 Signal Classification

A continuous-time signal is defined over an uncountable ordered set of points in time represented by a continuous independent variable. Discrete-time signals are defined over a countable ordered set of points in time and denoted by a discrete independent variable. Equivalently, we can define the amplitude either to be continuous or to be discrete. We define analog signals as continuous-time signals with a continuous amplitude. We define a digital signal as discrete-time signal with discrete amplitudes accordingly. Without additional notes a continuous-time signal is assumed to have a continuous-amplitude. Therefore, it is an analog signal. A discrete-time signal is also often assumed to have a continuous amplitude. With the given definition a discrete-time signal is different from a digital signal. Therefore, in this thesis mostly we deal with analog to discrete-time conversion instead of analog-to-digital conversion.

C.3 Signal Transforms

To operate with signals and filters we often transfer them to an eigenspace, where signals are decomposed in independent eigenfunctions weighted by eigenvalues. This greatly simplifies the computation with such signals and filter systems. For continuous-time systems we use the Laplace transform given by [99]

$$X(s) = \int_{-\infty}^{\infty} x(t)e^{-st}dt \tag{C.4}$$

$$x(t) = \frac{1}{2\pi j}\int_{\sigma-j\infty}^{\sigma+j\infty} X(s)e^{st}d\Omega \tag{C.5}$$

The continuous-time Fourier transform (CTFT) is the Laplace transform evaluated along the $s = j\Omega$ frequency axis. The CTFT and its inverse is given by [99]

$$X(j\Omega) = \int_{-\infty}^{\infty} x(t)e^{-j\Omega t}dt \tag{C.6}$$

$$x(t) = \frac{1}{2\pi}\int_{-\infty}^{\infty} X(j\Omega)e^{j\Omega t}d\Omega \tag{C.7}$$

For discrete-time signals we use the z-transform to project systems in an eigenspace. The z-transform pair is [99]

$$X(z) = \sum_{n=-\infty}^{\infty} x[n]z^{-n} \tag{C.8}$$

$$x[n] = \frac{1}{j2\pi}\oint_{\gamma} X(z)z^{n-1}dz \tag{C.9}$$

where γ is a closed contour surrounding the origin of the complex plane in the domain of analyticity of $X(z)$. The discrete-time Fourier transform (DTFT) is the z-transform evaluated for $|z| = 1$, i.e., $z = e^{j\omega}$. We define the DTFT and its inverse as [98]

$$X(e^{j\omega}) = \sum_{n=-\infty}^{\infty} x[n]e^{-j\omega n} \tag{C.10}$$

$$x[n] = \frac{1}{2\pi}\int_{-\pi}^{\pi} X(e^{j\omega})e^{j\omega n}d\omega \tag{C.11}$$

The Fourier representation of finite-duration sequences is given by the discrete Fourier transform (DFT), which is [98]

$$X[k] = \sum_{n=0}^{N-1} x[n]e^{-jnk\frac{2\pi}{N}} \tag{C.12}$$

$$x[n] = \frac{1}{N}\sum_{k=0}^{N-1} X[k]e^{jnk\frac{2\pi}{N}} \tag{C.13}$$

where N is the number of samples.

C.4 Special Signals

The continuous-time impulse $\delta(t)$ is a linear functional with some mathematical subtleties, which are not discussed in detail here. The Dirac delta impulse $\delta(t)$ is defined with a continuously differentiable function $\phi(t)$ as [52]

$$\int_{-\infty}^{\infty} \phi(t)\delta(t-\tau)dt = \phi(\tau), \tag{C.14}$$

which implies that

$$\int_{-\infty}^{\infty} \delta(t)dt = 1. \tag{C.15}$$

The Dirac delta impulse can only be used under an integral. Nevertheless, for convenience we often use the Dirac delta impulse simply as a regular signal and drop the integral. One special application of the Dirac delta impulse is known as periodic impulse train denoted by [99]

$$x_s(t) = \sum_{n=-\infty}^{\infty} \delta(t - nT_s). \tag{C.16}$$

The Kronecker delta discrete-time impulse is the discrete version of the Dirac delta impulse and is defined as

$$\delta[i-j] = \begin{cases} 0 & \text{for } i \neq j \\ 1 & \text{for } i = j. \end{cases} \tag{C.17}$$

We will refer to the Kronecker delta as discrete-time impulse or simple impulse and to the continuous-time impulse as Dirac delta impulse. Note that the discrete-time impulse is a well-defined function and does not need distribution theory for its handling.

C.5 Relation between Sampled Continuous-Time Signals and Discrete-Time Signals

When we deal with hybrid filter banks we have to consider analog signal processing as well as digital signal processing. Moreover, we have to combine both worlds and find an adequate notation. In the following we show the relation between sampled analog signals and discrete-time signals. In the time domain we can represent the process of sampling through the modulation of a continuous-time signal with a periodic impulse train provided in (C.16). The sampled signal can be expressed as [98]

$$x_s(t) = \sum_{n=-\infty}^{\infty} x_a(t)\delta(t - nT_s). \tag{C.18}$$

The CTFT, (C.6), of the sampled signal is

$$X_s(j\Omega) = \sum_{p=-\infty}^{\infty} x_a(pT_s)e^{-j\Omega T_s p}. \tag{C.19}$$

When we compare the sampled and Fourier transformed signal with the discrete-time Fourier transform (DTFT), (C.10), we recognize that the relation between these two transforms is only a frequency scaling factor $\omega = \Omega T_s$. Hence, we can mix both representations and write

$$X_s(j\Omega) = X(e^{j\omega})|_{\omega=\Omega T_s} = X(e^{j\Omega T_s}). \tag{C.20}$$

In discrete-time signal processing it is well known that we obtain periodic spectra with a fundamental interval ranging from $-\pi$ to π. For sampled continuous-time signals this periodic spectra behavior is difficult to deduce from (C.19). By developing the term $\delta(t - nT_s)$ of (C.18) into Fourier series we can find another representation for the CTFT of (C.18), which is

$$X_s(j\Omega) = X(e^{j\Omega T_s}) = \frac{1}{T_s} \sum_{p=-\infty}^{\infty} X_a\left(j\left(\Omega - p\Omega_s\right)\right). \tag{C.21}$$

This representation clearly indicates the periodic repetition of the continuous-time signal spectrum $X_a(j\Omega)$. If $X_a(j\Omega)$ is bandlimited to $|\Omega| < \frac{\Omega_s}{2}$ the fundamental interval, i.e., $p = 0$, of the sampled signal spectrum $X(e^{j\Omega T_s})$ equals $\frac{1}{T_s}X_a(j\Omega)$. As soon as the bandlimitation fails, aliasing occurs and the sampled spectrum is different from the continuous-time spectrum and we are not able to perfectly reconstruct $X_a(j\Omega)$ from $X(e^{j\Omega T_s})$.

C.6 Finding the Coefficients of a Static Nonlinearity

We discuss two methods for finding the coefficients of a polynomial in order to approximate a static nonlinearity.

When we search for a method to find the coefficients we realize that we have to impose further restrictions on our nonlinearity. If we use, for example, a Taylor Series expansion we have to restrict the nonlinearity to the class of analytic functions, which are functions that are differentiable at all points of a given domain D. The Taylor series expansion for a real analytic function, with center of the series at $x_0 = 0$, is

$$f(x) = \sum_{k=0}^{\infty} \frac{f^{(k)}(0)}{k!} x^k. \tag{C.22}$$

This kind of series is also known as Maclaurin Series. The relation to power series, (2.15), is given by

$$c_k = \frac{f^{(k)}(0)}{k!}. \tag{C.23}$$

A different and often more fruitful approach towards finding the coefficients of the approximation polynomial $p(x)$ is to use classes of orthogonal polynomials. Two orthogonal polynomials $p_m(x)$ and $p_n(x)$ over the range $[a, b]$ of such a class have the property that the inner product results in

$$\int_a^b p_m(x)p_n(x)w(x)dx = \delta[m-n]c_k, \tag{C.24}$$

where c_k is an arbitrary constant and $\delta[n]$ is the discrete-time impulse. If $c_k = 1$ the polynomials are not only orthogonal, but orthonormal. The advantage of an orthogonal basis is the spectral decomposition of the input signals as long as they belong to a special signal class [136]. This means that there is a one-to-one relation between a component c_k of the series representation and the corresponding spectrum. Thus, we completely remove one unwanted spectral component by canceling the appropriate component c_k [136].

For example, we can use Chebyshev polynomials $T_k(x)$, which are orthogonal on the interval $[-1, 1]$, to represent a nonlinearity $f(x)$ with

$$p(x) = \sum_{k=0}^{K-1} c_k T_k(x). \tag{C.25}$$

The basis is given by [74]

$$T_{k+1}(x) = 2xT_k(x) - T_{k-1}(x), \tag{C.26}$$

where $T_0 = 1$ and $T_1 = 1$ and the coefficients c_k can be found for the given nonlinearity $f(x)$ by

$$c_k = \int_{-1}^{1} f(x)T_k(x)\frac{1}{\sqrt{1-x^2}}. \tag{C.27}$$

Chebyshev polynomials have the property of spectral decomposition for sinusoidal input signals.

To illustrate both the Taylor series representation and the representation through orthogonal polynomials, we consider the function

$$f(x) = 3x^3 + 4x^2 + 1. \tag{C.28}$$

By substituting (C.28) in (C.23) we obtain

$$\begin{aligned} c_0 = 1, c_1 = 0, c_2 = 4, c_3 = 3, \\ c_k \equiv 0 \quad \text{for all } k \geq 4 \end{aligned} \tag{C.29}$$

Since $f(x)$ is already in a polynomial representation we directly get the result for the Taylor series. For the Chebyshev polynomial the coefficients are given by evaluating (C.27), which results in

$$\begin{aligned} c_0 = 3\pi, c_1 = \frac{9}{8}\pi, c_2 = \pi, c_3 = \frac{3}{8}\pi, \\ c_k \equiv 0 \quad \text{for all } k \geq 4 \end{aligned} \tag{C.30}$$

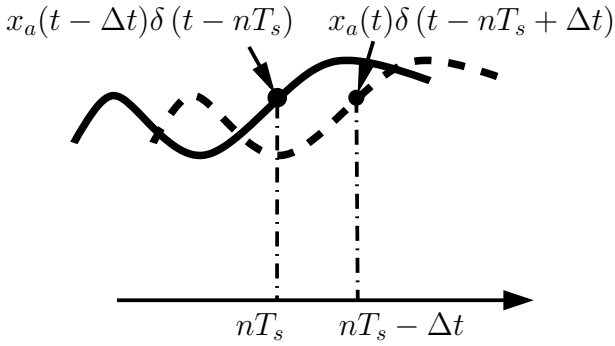

Figure C.1: A time delay in the delta distribution can be expressed as time advance in the signal and vice versa.

C.7 Representations of Sampling Time Errors

When we talk about sampling a signal we normally assume uniform sampling instants. Such a system is described by the relations found in Sec. C.5. When we face the problem of nonuniform sampling we have to modify (C.18) by a time delay Δt, which gives

$$x_s(t) = \sum_{n=-\infty}^{\infty} x_a(t)\delta\left(t - nT_s + \Delta t\right). \tag{C.31}$$

Hence, for each sample we delay or advance the delta impulse distribution compared to the uniform case. For modeling time-interleaved ADCs it is useful to shift the delay Δt into the signal path. Therefore, we obtain

$$x_s(t) = \sum_{n=-\infty}^{\infty} x_a(t-\Delta t)\delta(t - nT_s), \tag{C.32}$$

where the sign of Δt has changed. The reason for that is illustrated in Fig. C.1. We see the ideal sampling instant and a shifted sampling instant. The dashed line represents the ideal analog signal $x_a(t)$ sampled at the wrong sampling instant, i.e., the Dirac-delta impulse is delayed. When we now assume that we have ideal sampling, we have to advance the input signal $x_a(t)$ (solid line) to obtain the same sampling value as for the non-ideal sampling case. For this reason, i.e., a delay in the sampling path is an advance in the signal path and vice versa, we have to change the signs when we move the delays from one signal path to the other.

List of Abbreviations and Symbols

Abbreviations

ADC	Analog-to-digital converter
CMOS	Complementary metal oxide semiconductor
CT	Continuous time
CTFT	Continuous-time Fourier transform
dBc	DeciBels (below) carrier measures the relative signal strength between main lobe and spurs
DFT	Discrete Fourier transform
DT	Discrete time
DTFT	Discrete-time Fourier transform
ENOB	Effective number of bits
FSR	Full-scale range
GSE	Generalized Sampling Expansion
HFB	Hybrid filter bank
DNL	Differential nonlinearity
INL	Integral nonlinearity
LHFB	Linear hybrid filter bank
LSB	Least significant bit
MUX	Multiplexer
NHFB	Nonlinear hybrid filter bank
QMF	Quadrature mirror filter
SFDR	Spurious-free dynamic range

S/H	Sample-and-hold
SINAD	Signal-to-noise and distortion ratio
THD	Total harmonic distortion

Symbols

$A_m(\Omega)$	Magnitude response of the mth S/H
$\alpha_p(j\Omega)$	Weighting factor corresponding to the DFT of linear mismatches
$\mathbf{A}\left(\check{\mathbf{\Omega}}\right)$	Channel mismatch matrix
$\beta_p(j\Omega)$	Weighting factor corresponding to the DFT of offset mismatches
δ_n	Relative time-dependent timing mismatch (timing jitter)
$\tilde{\delta}$	Random variable corresponding to the time-dependent relative timing mismatch δ
f	Function to model continuous deviations from the ideal tranfer curve.
f_s	Overall sampling rate of the time-interleaved ADC
$\tilde{f}_s$	Sampling rate of the channel ADCs
$G_m(e^{j\Omega T_s})$	Discrete-time synthesis filter
g_m	Gain of the mth channel ADC
$\tilde{g}$	Random variable corresponding to the gain mismatch g
$H_m(j\Omega)$	Continuous-time analysis filter
K	Number of samples of one channel in a time-interleaved ADC
M	Number of channels in a time-interleaved ADC
$\mu_{\tilde{g}}$	Mean of the random variable $\tilde{g}$
$\mu_{\tilde{o}}$	Mean of the random variable $\tilde{o}$
$\mu_{\tilde{\delta}}$	Mean of the random variable $\tilde{\delta}$
$\mu_{\tilde{r}}$	Mean of the random variable $\tilde{r}$
N	Number of samples
Ω	Continuous-time angular frequency given by $\frac{2\pi}{T_s} = 2\pi f_s$
ω	Discrete-time angular frequency
o_m	Offset of the mth channel ADC

$\tilde{o}$	Random variable corresponding to the offset mismatch o
$\Phi_{\tilde{r}}(\omega)$	Characteristic function of the relative timing mismatch $\tilde{r}$
$\Phi_{\tilde{\delta}}(\omega)$	Characteristic function of the time-dependent relative timing mismatch $\tilde{\delta}$
$\phi_m(\Omega)$	Nonlinear-phase response of the mth S/H
P_N	Total noise power
P_S	Total signal power
$P_m(j\Omega)$	Frequency response of the mth S/H
r	Relative timing mismatch of the mth channel ADC
$\tilde{r}$	Random variable corresponding to the relative timing mismatch r
$\sigma_{\tilde{g}}$	Standard deviation of the random variable $\tilde{g}$
$\sigma_{\tilde{g}}$	Standard deviation of the random variable $\tilde{o}$
$\sigma_{\tilde{r}}$	Standard deviation of the random variable $\tilde{\delta}$
$\sigma_{\tilde{r}}$	Standard deviation of the random variable $\tilde{r}$
$\Delta\theta_m$	Aperture delay mismatch of the mth channel ADC
θ_m	Aperture delay of the mth channel ADC
θ_R	Aperture delay of the reference channel ADC
$\Delta\tau_m$	Constant corresponding to the linear-phase response mismatch $-\Delta\tau_m\Omega$ of the mth S/H
τ_m	Constant corresponding to the linear-phase response $-\tau_m\Omega$ of the mth S/H
τ_R	Constant corresponding to the linear-phase response $-\tau_R\Omega$ of the reference S/H
$\Delta\vartheta\,(\Omega)$	Total phase response mismatch of the mth channel ADC
$\vartheta_m\,(\Omega)$	Total phase response of the mth channel ADC
$\vartheta_R\,(\Omega)$	Total phase response of the reference channel ADC
$T_{p,k}\,(j\Omega)$	Weighting factor corresponding to the DFT of the kth order nonlinearity mismatches
T_s	Overall sampling period of the time-interleaved ADC
$\tilde{T}_s$	Sampling period of the channel ADCs
Δt_m	Timing mismatch of the mth channel ADC

t_m	Timing deviation of the mth channel ADC
t_R	Timing deviation of the reference channel ADC
$\Upsilon_m(\Omega)$	Total magnitude response of the mth channel ADC
$x_a(t)$	Analog input signal
$X_a(j\Omega)$	Fourier transform of the analog input signal $x_a(t)$
$\mathbf{x}(\boldsymbol{\Omega})$	Input vector of the channel mismatch matrix $\mathbf{A}\left(\check{\boldsymbol{\Omega}}\right)$
$x_s(t)$	Sampled analog input signal
$X_s(j\Omega)$	Fourier transform of the sampled analog input signal $x_s(t)$
$\mathbf{y}(\boldsymbol{\Omega})$	Output vector of the channel mismatch matrix $\mathbf{A}\left(\check{\boldsymbol{\Omega}}\right)$
$\zeta(\Omega)$	Frequency transformation

Bibliography

[1] M. Anderson, J. Elbornsson, J. Eklund, J. Alvbrant, and H. Fredriksson, "Verification of a blind mismatch error equalization method for randomly interleaved ADCs using a 2.5V/12b/30MSs PSAADC," in *Conference on European Solid-State Circuits, ESSCIRC*, September 2003, pp. 473– 476. 4.1

[2] P. Arpaia, P. Daponte, and L. Michaeli, "Influence of the architecture on ADC error modeling," *IEEE Transactions on Instrumentation and Measurement*, vol. 48, no. 5, pp. 956–966, October 1999. 1.3, A.1

[3] A. Baccigalupi, P. Daponte, and M. D'Apuzzo, "An improved error model of data acquisition systems," *IEEE Transactions on Instrumentation and Measurement*, vol. 43, no. 2, pp. 220–225, April 1994. 1.3, A.1

[4] R. D. Batten, A. Eshraghi, and T. S. Fiez, "Calibration of parallel $\Delta\Sigma$ ADCs," *IEEE Transactions on Circuits and Systems II: Analog and Digital Signal Processing*, vol. 49, no. 6, pp. 390–399, June 2002. 1.3

[5] D. Bellan, A. Brandolini, and A. Gandelli, "Quantization theory in electrical and electronic measurements," in *Proceedings of the IEEE Instrumentation and Measurement Technology Conference, IMTC*, April 1995, pp. 494–499. 2.1, 3.2.1.3

[6] D. Bellan, A. Brandolini, and A. Gandelli, "Quantization theory-a deterministic approach," *IEEE Transactions on Instrumentation and Measurement*, vol. 48, no. 1, pp. 18–25, February 1999. 2.1, 3.2.1.3

[7] W. C. Black Jr., "High speed CMOS A/D conversion techniques," Ph.D. Dissertation, University of California, Berkeley, November 1980. 1.1.1, 1.1.3, 1.3, 2.1, 3.1

[8] W. C. Black Jr. and D. A. Hodges, "Time-interleaved converter arrays," *IEEE Journal of Solid State Circuits*, vol. 15, no. 6, pp. 1024–1029, December 1980. 1.1.1, 1.1.3, 1.3, 2.1, 3.1

[9] S. Brigati, V. Liberali, and F. Maloberti, "Precision behavioural modelling of circuit components for data converters," in *Second International Conference on Advanced A-D and D-A Conversion Techniques and their Applications*, July 1994, pp. 110–115. 1.3, A.1

[10] J. J. Brown, "Multi-channel sampling of low-pass signals," *IEEE Transactions on Circuits and Systems*, vol. 28, no. 2, pp. 101–106, February 1981. 2.1

[11] J. Brown, "Generalized sampling and the perfect reconstruction problem for maximally decimated filter banks," in *1989 International Conference on Acoustics, Speech, and Signal Processing, ICASSP*, vol. 2, May 1989, pp. 1195–1198. 2.1

[12] J. Compiet, P. de Jong, P. Wambacq, G. Vandersteen, S. Donnay, D. Engels, and I. Bolsens, "High-level modeling of a high-speed flash A/D converter for mixed-signal simulations of digital telecommunication front-ends," in *Symposium on Mixed-Signal Design, SSMSD*, February 2000, pp. 135–140. 1.3, A.1

[13] C. S. G. Conroy, D. W. Cline, and P. R. Gray, "A high-speed parallel pipelined ADC technique in CMOS," in *1992 Symposium on VLSI Circuits, Digest of Technical Papers*, June 1992, pp. 96–97. 1.1.3

[14] C. S. G. Conroy, D. W. Cline, and P. R. Gray, "An 8-b 85-MS/s parallel pipeline A/D converter in 1-μm CMOS," *IEEE Journal of Solid-State Circuits*, vol. 28, no. 4, pp. 447–454, April 1993. 1.1.3

[15] J. Corcoran, K. Poulton, and T. Hornak, "A 1-GHz 6-bit ADC system," in *1987 IEEE International Solid-State Circuits Conference, Digest of Technical Papers*, February 1987, pp. 102– 103. 1.1.3

[16] M. Demler, *High-Speed Analog-to-Digital Conversion*. Academic Press, 1991. 3.2.2

[17] A. Devices, "Data sheet AD12400," http://www.analog.com/, 2003, revision 0. 2.1

[18] D. Draxelmayr, "A 6b 600MHz 10mW ADC array in digital 90nm CMOS," in *2004 IEEE International Solid-State Circuits Conference*, vol. 1, February 2004, pp. 45–48. 1.1.1, 1.1.3

[19] D. Draxelmayr, F. Kuttner, and C. Vogel, "Delay equalization in converter arrays," German patent application 102 004 009 612.9, February 27, 2004. 1.3

[20] D. Draxelmayr, C. Vogel, and F. Kuttner, "Compensation of nonlinearity mismatches in time-interleaved ADCs," German patent application 102 004 009 613.9, February 27, 2004. 1.3, 5.2.1

[21] M. Duppils, J. E. Eklund, and C. Svensson, "A study of the non-ideal properties of sample-and-hold circuits with respect to the analog bandwidth," in *Third International Conference on Advanced A/D and D/A Conversion Techniques and their Applications*, Glasgow UK, July 1999, pp. 119–121. 3.3, 6, A.1

[22] K. Dyer, F. Daihong, S. Lewis, and P. Hurst, "An analog background calibration technique for time-interleaved analog-to-digital converters," *IEEE Journal of Solid-State Circuits*, vol. 33, no. 12, pp. 1912–1919, December 1998. 4.1

[23] J. E. Eklund and F. Gustafsson, "Digital offset compensation of time-interleaved ADC using random chopper sampling," in *Proceedings of the 2000 IEEE International Symposium on Circuits and Systems, ISCAS*, vol. 3, May 2000, pp. 447–450. 5.1

[24] K. El-Sankary, A. Assi, and M. Sawan, "New sampling method to improve the SFDR of time-interleaved ADCs," in *Proceedings of the 2003 International Symposium on Circuits and Systems, ISCAS*, vol. 1, May 2003, pp. 833– 836. 5.1, 5.4

[25] J. Elbornsson, "Analysis, estimation and compensation of mismatch effects in A/D converters," Ph.D. dissertation, Linköpings universitet, 2003. 2.1, 3.1, 4.1, 5.1, 5.4.2.3, B.1.3, B.2.3

[26] J. Elbornsson and J. Eklund, "Blind estimation of timing errors in interleaved AD converters," in *Proceedings of the 2001 IEEE International Conference on Acoustics, Speech, and Signal Processing, ICASSP*, vol. 6, May 2001, pp. 3913–3916. 4.1, 5.3.1, B.1.3, B.1.3, B.2.3

[27] J. Elbornsson, K. Folkesson, and J. Eklund, "Measurement verification of estimation method for time errors in a time-interleaved A/D converter system," in *Proceedings of the 2002 IEEE International Symposium on Circuits and Systems, ISCAS*, vol. 3, May 2002, pp. 129–132. 4.1, B.1.3

[28] J. Elbornsson, F. Gustafsson, and J. Eklund, "Amplitude and gain error influence on time error estimation algorithm for time interleaved A/D converter system," in *Proceedings of the 2002 IEEE International Conference on Acoustics, Speech, and Signal Processing, ICASSP*, vol. 2, May 2002, pp. 1281–1284. 4.1, B.1.3

[29] J. Elbornsson, F. Gustafsson, and J.-E. Eklund, "Analysis of mismatch noise in randomly interleaved ADC system," in *Proceedings of the 2003 IEEE International Conference on Acoustics, Speech, and Signal Processing, ICASSP*, vol. 6, April 2003, pp. 277–280. 5.4.2.1, 5.4.2.3

[30] J. Elbornsson, F. Gustafsson, and J. E. Eklund, "Blind adaptive equalization of mismatch errors in a time-interleaved A/D converter system," *IEEE Transactions on Circuits and Systems I: Regular Papers*, vol. 51, no. 1, pp. 151–158, January 2004. 4.1, B.1.3

[31] Y. C. Eldar and A. V. Oppenheim, "Filterbank reconstruction of bandlimited signals from nonuniform and generalized samples," *IEEE Transactions on Signal Processing*, vol. 48, no. 10, pp. 2864–2875, October 2000. 2.1, 5.1

[32] J. Franca, A. Petraglia, and S. Mitra, "Multirate analog-digital systems for signal processing and conversion," *Proceedings of the IEEE*, vol. 85, no. 2, pp. 242–262, February 1997. 2.1

[33] D. Fu, K. C. Dyer, S. H. Lewis, and P. J. Hurst, "A digital background calibration technique for time-interleaved analog-to-digital converters," *IEEE Journal of Solid-State Circuits*, vol. 33, no. 12, pp. 1904–1911, December 1998. 4.1, 5.1

[34] M. Gustavsson and N. N. Tan, "A global passive sampling technique for high-speed switched-capacitor time-interleaved ADCs," *IEEE Transactions on Circuits and Systems II: Analog and Digital Signal Processing*, vol. 47, no. 9, pp. 821–831, September 2000. 5.1

[35] M. Gustavsson, J. J. Wikner, and N. Tan, *CMOS Data Converters for Communications*. Kluwer Academic Publishers, 2000. 2.1, 3.1, 3.5.2, 3.5.2

[36] F. J. Harris, "On the use of windows for harmonic analysis with the discrete Fourier transform," *Proceedings of the IEEE*, vol. 66, no. 1, pp. 51–82, January 1978. 4.3.2, 1

[37] D. F. Hoeschele, *Analog-to-Digital and Digital-to-Analog Conversion Techniques*, 2nd ed. Wiley-Interscience, 1994. 3.2.2

[38] D. M. Hummels, J. J. McDonald II, and F. H. Irons, "Distortion compensation for time-interleaved analog to digital converters," in *Proceedings of the IEEE Instrumentation and Measurement Technology Conference, IMTC*, vol. 1, June 1996, pp. 728–731. 2.1, A.1

[39] D. Hummels, W. Ahmed, and F. Irons, "Measurement of random sample time jitter for ADCs," in *Proceedings of the 1995 IEEE International Symposium on Circuits and Systems, ISCAS*, vol. 1, April 1995, pp. 708–711. 3.1

[40] "IEEE standard for digitizing waveform recorders," IEEE Std 1057-1994, December 1994. 1.1.2

[41] "IEEE standard for terminology and test methods for analog-to-digital converters," IEEE Std 1241-2000, June 2001. 1.1.2, 2.5, 2.5, 3.1, 3.21, 3.4.1, 3.4.2, 5.4.1.2, 5.4.1.2, 5.4.2.3, A.2.3.3, A.3

[42] F. H. Irons, D. M. Hummels, and S. Lasmin, "The use of the triangle functions to model analog-to-digital converter dynamic errors," in *Proceedings of the 35th Midwest Symposium on Circuits and Systems, MWSCAS*, vol. 2, August 1992, pp. 1473–1476. A.1

[43] S. M. Jamal, F. Daihong, P. J. Hurst, and S. H. Lewis, "A 10b 120Msample/s time-interleaved analog-to-digital converter with digital background calibration," in *2002 IEEE International Solid-State Circuits Conference, Digest of Technical Papers, ISSCC*, vol. 2, February 2002, pp. 132–436. 1.1.3, 4.1, 5.1

[44] S. Jamal, F. Daihong, N. Chang, P. Hurst, and S. Lewis, "A 10-b 120-Msample/s time-interleaved analog-to-digital converter with digital background calibration," *IEEE Journal of Solid-State Circuits*, vol. 37, no. 12, pp. 1618–1627, December 2002. 1.1.3, 4.1, 5.1

[45] J.-M. Janik, D. Bloyet, and B. Guyot, "Measurement of timing jitter contributions in a dynamic test setup for A/D converters," *IEEE Transactions on Instrumentation and Measurement*, vol. 50, no. 3, pp. 786–791, June 2001. 3.1

[46] Y. C. Jenq, "Digital spectra of nonuniformly sampled signals: Fundamentals and high-speed waveform digitizers," *IEEE Transactions on Instrumentation and Measurement*, vol. 37, no. 2, pp. 245–251, June 1988. 1.3, 2.1, 3.1, 3.4, 3.5.1, 3.5.2

[47] Y. C. Jenq, "Digital spectra of nonuniformly sampled signals: A robust sampling time offset estimation algorithm for ultra high-speed waveform digitizers using interleaving," *IEEE Transactions on Instrumentation and Measurement*, vol. 39, no. 1, pp. 71–75, February 1990. 4.1, 5.3.1

[48] Y. C. Jenq, "Digital spectra of nonuniformly sampled signals: Theories and applications-measuring clock/aperture jitter of an A/D system," *IEEE Transactions on Instrumentation and Measurement*, vol. 39, no. 6, pp. 969–971, December 1990. 1.3, 3.1, 3.2.2.2, 3.2.2.2, A.2.1

[49] Y. C. Jenq, "Perfect reconstruction of digital spectrum from nonuniformly sampled signals," *IEEE Transactions on Instrumentation and Measurement*, vol. 46, no. 7, pp. 649 – 652, June 1997. 4.2, 1, 1, 4.7, 4.8, 4.10, 2, 4.4.3, 4.15, 5.1, B.1.3, B.2.3

[50] Y. Jenq, "Digital-to-analog (D/A) converters with nonuniformly sampled signals," *IEEE Transactions on Instrumentation and Measurement*, vol. 45, no. 1, pp. 56–59, February 1996. 3.1

[51] A. J. Jerri, "The Shannon sampling theorem its various extensions and applications: A tutorial review," *Proceedings of the IEEE*, vol. 65, no. 11, pp. 1565–1596, November 1977. 2.1

[52] A. J. Jerri, *Integral and Discrete Transforms With Applications and Error Analysis*. Marcel Dekker, 1992. C.4

[53] P. G. A. Jespers, *Integrated Converters: D to A and A to D Architectures, Analysis and Simulation*. Oxford University Press, 2001. 1.3, A.1

[54] H. Jin and E. K. F. Lee, "A digital technique for reducing clock jitter effects in time-interleaved A/D converter," in *Proceedings of the 1999 IEEE International Symposium on Circuits and Systems, ISCAS*, vol. 2, May 1999, pp. 330–333. 4.1, 5.1

[55] H. Jin and E. K. F. Lee, "A digital-background calibration technique for minimizing timing-error effects in time-interleaved ADCs," *IEEE Transactions on Circuits and Systems II: Analog and Digital Signal Processing*, vol. 47, no. 7, pp. 603–613, July 2000. 2.1, 4.1, 5.1

[56] H. Jin, E. K. F. Lee, and M. Hassoun, "Time-interleaved A/D converter with channel randomization," in *Proceedings of 1997 IEEE International Symposium on Circuits and Systems, ISCAS*, vol. 1, June 1997, pp. 425–428. 5.1, 5.2.2, 5.4

[57] H. Johansson and P. Löwenborg, "Reconstruction of nonuniform sampled bandlimited signals using digital fractional filters," in *Proceedings of the 2001 IEEE International Symposium on Circuits and Systems, ISCAS*, vol. 2, 2001, pp. 593–596. 5.1

[58] H. Johansson and P. Löwenborg, "Reconstruction of a class of nonuniformly sampled and decimated bandlimited signals," in *Proceedings of the 2002 IEEE International Symposium on Circuits and Systems, ISCAS*, vol. 2, May 2002, pp. 604–607. 5.1

[59] H. Johansson and P. Löwenborg, "Reconstruction of nonuniformly sampled bandlimited signals by means of digital fractional delay filters," *IEEE Transactions on Signal Processing*, vol. 50, no. 11, pp. 2757– 2767, November 2002. 5.1

[60] H. Johansson and P. Löwenborg, "Reconstruction of nonuniformly sampled bandlimited signals using time-varying discrete-time FIR filters," in *Proceedings of the XII European Signal Processing Conference, EUSIPCO*, September 2004. 5.1

[61] H. Johansson and P. Löwenborg, "Reconstruction of nonuniformly sampled bandlimited signals by means of time-varying discrete-time FIR filters," *J. Applied Signal Processing – Special Issue on Frames and Overcomplete Representations in Signal Processing, Communications, and Information Theory*, 2005, accepted for publication. 5.1

[62] K. Ju-Hyung, H. Sung-Wook, L. Seung-Hoon, and J. Yong, "An 8b 52MHz double-channel CMOS A/D converter for high-speed data communications," in *Proceedings of the Asia and South Pacific Design Automation Conference, ASP-DAC*, vol. 1, January 1999, pp. 25–28. 1.1.3

[63] S. M. Kay, *Fundamentals of Statistical Signal Processing: Estimation Theory*. Prentice Hall, 1993. 3.4.2

[64] R. Khoini-Poorfard and D. A. Johns, "Time-interleaved oversampling convertors," *Electronics Letters*, vol. 29, no. 19, pp. 1673–1674, September 1993. 1, 1.3

[65] R. Khoini-Poorfard and D. A. Johns, "Mismatch effects in time-interleaved oversampling converters," in *Proceedings of the 1994 IEEE International Symposium on Circuits and Systems, ISCAS*, vol. 5, May 1994, pp. 429–432. 1.3, 3.1

[66] R. Khoini-Poorfard, L. B. Lim, and D. A. Johns, "Time-interleaved oversampling A/D converters: Theory and practice," *IEEE Transactions on Circuits and Systems II: Analog and Digital Signal Processing*, vol. 44, no. 8, pp. 634–645, August 1997. 1, 1.3

[67] K. Kim, "Analog-to-digital conversion and harmonic noises due to the integral nonlinearity," *IEEE Transactions on Instrumentation and Measurement*, vol. 43, no. 2, pp. 151–156, April 1994. A.1

[68] H. Kobayashi, M. Morimura, K. Kobayashi, and Y. Onaya, "Aperture jitter effects in wideband sampling systems," in *Proceedings of the 16th IEEE Instrumentation and*

Measurement Technology Conference, IMTC, vol. 2, May 1999, pp. 880–884. 3.1, 3.4.2

[69] H. Kopmann, "Comprehensive model-based error analysis of multiple concurrent, time-interleaved, and hybrid ultra-wideband analogue-to-digital conversion," *EURASIP J. Signal Processing*, vol. 84, no. 10, pp. 1837–1859, 2004. 2.1, 2.5

[70] M. Kozak and I. Kale, "Novel topologies for time-interleaved delta-sigma modulators," *IEEE Transactions on Circuits and Systems II: Analog and Digital Signal Processing*, vol. 47, no. 7, pp. 639–654, July 2000. 1.3

[71] M. Kozak and I. Kale, "Time-interleaved delta-sigma modulators using zero-insertion interpolation," in *Proceedings of the 43rd IEEE Midwest Symposium on Circuits and Systems, MWSCAS*, vol. 3, August 2000, pp. 1406–1409. 1.3

[72] M. Kozak and I. Kale, *Oversampled Delta-Sigma Modulators: Analysis, Applications and Novel Topologies*. Kluwer Academic Publishers, 2003. 1.3

[73] M. Kozak, M. Karaman, and I. Kale, "Efficient architectures for time-interleaved oversampling delta-sigma converters," *IEEE Transactions on Circuits and Systems II: Analog and Digital Signal Processing*, vol. 47, no. 8, pp. 802–810, August 2000. 1.3

[74] E. Kreyszig, *Advanced Engineering Mathematics*, 8th ed. John Wiley & Sons, 1998. 2.3.1, 2.3.1, 3.10, 4.5, C.6

[75] N. Kurosawa, H. Kobayashi, and K. Kobayashi, "Channel linearity mismatch effects in time-interleaved ADC systems," in *Proceedings of the 2001 IEEE International Symposium on Circuits and Systems, ISCAS*, vol. 1, May 2001, pp. 420–423. 1.3, 2.1, 3.1

[76] N. Kurosawa, H. Kobayashi, K. Maruyama, H. Sugawara, and K. Kobayashi, "Explicit analysis of channel mismatch effects in time-interleaved ADC systems," *IEEE Transactions on Circuits and Systems I: Fundamental Theory and Applications*, vol. 48, no. 3, pp. 261–271, March 2001. 1.3, 2.1, 3.1, 3.2.2.1, 3.4.1, 3.6

[77] N. Kurosawa, K. Maruyama, H. Kobayashi, H. Sugawara, and K. Kobayashi, "Explicit formula for channel mismatch effects in time-interleaved ADC systems," in *Proceedings of the 17th IEEE Instrumentation and Measurement Technology Conference, IMTC*, vol. 2, May 2000, pp. 763–768. 2.1, 3.1

[78] T. Laakso, V. Valimaki, M. Karjalainen, and U. Laine, "Splitting the unit delay," *IEEE Signal Processing Magazine*, vol. 13, no. 1, pp. 30–60, January 1996. 5.1

[79] G. Leger, E. Peralias, and A. Rueda, "SNR probability in time-interleaved ADCs with random channel mismatches," in *Proceedings of the 2002 IEEE International Symposium on Circuits and Systems, ISCAS*, vol. 2, May 2002, pp. 380–383. 1.3, 3.1

[80] G. Leger, E. Peralias, and A. Rueda, "SFDR probability in time-interleaved ADCs with random channel mismatches," in *IX Workshop IBERCHIP*, March 2003. 3.1

[81] G. Leger, E. J. Peralias, A. Rueda, and J. Huertas, "Impact of random channel mismatch on the SNR and SFDR of time-interleaved ADCs," *IEEE Transactions on Circuits and Systems I: Regular Papers*, vol. 51, no. 1, pp. 140–150, January 2004. 3.1

[82] P. Löwenborg, "Asymmetric filter banks for mitigation of mismatch errors in high-speed analog-to-digital converters," Ph.D. dissertation, Linköpings universitet, 2002. 2.1, 2.2, 2.2, 2.3, 2.3.2, 2.3.2, 2.4.1, 4.2, 5.1

[83] P. Löwenborg, H. Johansson, and L. Wanhammar, "On the frequency-response of M-channel mixed analog and digital maximally decimated filter banks," in *Proc. European Conf. Circuit Theory Design*, August 1999. 2.1, 2.2.1, 2.2.1, 2.4.1

[84] P. Löwenborg, H. Johansson, and L. Wanhammar, "Analysis of gain and time-skew errors in filter bank based A/D converters," in *Proceedings of the 44th IEEE 2001 Midwest Symposium on Circuits and Systems, MWSCAS*, vol. 1, 2001, pp. 263–266. 3.1

[85] P. Löwenborg, H. Johansson, and L. Wanhammar, "Two-channel digital and hybrid analog/digital multirate filter banks with very low-complexity analysis or synthesis filters," *IEEE Transactions on Circuits and Systems II: Analog and Digital Signal Processing*, vol. 50, no. 7, pp. 355– 367, July 2003. 2.1, 2.2

[86] F. Marvasti, M. Analoui, and M. Gamshadzahi, "Recovery of signals from nonuniform samples using iterative methods," *IEEE Transactions on Signal Processing*, vol. 39, no. 4, pp. 872–878, April 1991. 5.1

[87] F. A. Marvasti, Ed., *Nonuniform Sampling: Theory and Practice*. Kluwer Academic/Plenum Pub Corp, 2001. 5.1

[88] D. Mirri, G. Luculano, F. Filicori, G. Pasini, and G. Vannini, "Modeling of non ideal dynamic characteristics in S/H-ADC devices," in *Proceedings of the IEEE Instrumentation and Measurement Technology Conference, IMTC*, April 1995, pp. 27–32. A.1

[89] A. Moscovici, *High Speed A/D Converters - Understanding Data Converters Through SPICE*, ser. The Kluwer International Series in Engineering and Computer Science. Kluwer Academic Publishers, 2001. 1.3, A.1

[90] D. Moulin, "Real-time equalization of A/D converter nonlinearities," in *IEEE International Symposium on Circuits and Systems*, vol. 1, May 1989, pp. 262–267. A.1

[91] W. Namgoong, "Finite-length synthesis filters for non-uniformly time-interleaved analog-to-digital converter," in *Proceedings of the 2002 IEEE International Symposium on Circuits and Systems, ISCAS*, vol. 4, May 2002, pp. 815–818. 5.1

[92] V. K. Navin, T. Ray, M. M. Hassoun, W. Black, E. Lee, E. Soenen, and R. Geiger, "A simulation environment for pipelined analog-to-digital converters," in *Proceedings of 1997 IEEE International Symposium on Circuits and Systems, ISCAS*, vol. 3, June 1997, pp. 1620–1623. 1.3, A.1

[93] T. Ndjountche and R. Unbehauen, "Adaptive calibration techniques for time-interleaved ADCs," *Electronics Letters*, vol. 37, no. 7, pp. 412–414, March 2001. 4.1, 5.1

[94] V. T. Nguyen, P. Loumeau, and J. F. Naviner, "Analysis of time-interleaved delta-sigma analog to digital converter," in *Proceedings of the IEEE 55th Vehicular Technology Conference, VTC*, vol. 4, May 2002, pp. 1594–1597. 1.3

[95] H. Nyquist, "Certain topics in telegraph transmission theory," *Reprinted in Proceedings of the IEEE*, vol. 90, no. 2, pp. 280–305, February 2002. 2.1, 5.1

[96] O. Oliaei, "Asymptotically perfect reconstruction in hybrid filter banks," in *Proceedings of the 1998 IEEE International Conference on Acoustics, Speech, and Signal Processing, ICASSP*, vol. 3, May 1998, pp. 1829–1832. 2.1

[97] O. Oliaei, "High-speed A/D and D/A converters using hybrid filter banks," in *IEEE International Conference on Electronics, Circuits and Systems*, 1998. 2.1

[98] A. V. Oppenheim, R. W. Schafer, and J. R. Buck, *Discrete-Time Signal Processing*. Prentice Hall, 1999. 2.2, 2.2.1, 2.2.1, 2.2.1, 2.2.1, 2.2.1, 3.2.1.1, C.3, C.3, C.5

[99] A. V. Oppenheim and A. Willsky, *Signals and Systems*. Prentice-Hall, 1983. 2.1, 3.2.1.1, 3.2.2.1, C.3, C.3, C.3, C.4

[100] A. Papoulis, "Generalized sampling expansion," *IEEE Transactions on Circuits and Systems*, vol. 23, no. 11, pp. 652– 654, November 1977. 1.1, 2.1, 5.1

[101] A. Papoulis and U. Pillai, *Probability, Random Variables and Stochastic Processes*, 4th ed., ser. McGraw-Hill series in electrical engineering : Communications and signal processing. McGraw-Hill, 2002. 3.4.2, 3.4.2, 3.4.2

[102] J. C. Pedro and N. B. Carvalho, *Intermodulation Distortion in Microwave and Wireless Circuits*. Artech House, 2003. 2.3.1

[103] J. Pereira, P. Girao, and A. Serra, "An FFT-based method to evaluate and compensate gain and offset errors of interleaved ADC systems," *IEEE Transactions on Instrumentation and Measurement*, vol. 53, no. 2, pp. 423–430, April 2004. 4.1

[104] A. Petraglia, F. Maloberti, and S. K. Mitra, "QMF-based A/D converters: Overview and new results," in *International Conference on Analogue to Digital and Digital to Analogue Conversion*, September 1991, pp. 112–117. 2.1

[105] A. Petraglia and S. K. Mitra, "High speed A/D conversion using QMF banks," in *IEEE International Symposium on Circuits and Systems, ISCAS*, vol. 4, May 1990, pp. 2797–2800. 2, 2.1

[106] A. Petraglia and S. K. Mitra, "High-speed A/D conversion incorporating a QMF bank," *IEEE Transactions on Instrumentation and Measurement*, vol. 41, no. 3, pp. 427–431, June 1992. 1.3, 2.1, 2.2

[107] A. Petraglia and S. Mitra, "Analysis of mismatch effects among A/D converters in a time-interleaved waveform digitizer," *IEEE Transactions on Instrumentation and Measurement*, vol. 40, no. 5, pp. 831–835, October 1991. 1.3, 2.1, 3.1, 3.4, 3.5.2, 3.5.2

[108] M. A. A. Pinheiro, P. B. Batalheiro, A. Petraglia, and M. R. Petraglia, "Improving the near-perfect hybrid filter bank performance in the presence of realization errors," in *Proceedings of the 2001 IEEE International Conference on Acoustics, Speech, and Signal Processing, ICASSP*, vol. 2, 2001, pp. 1069–1072. 2.1

[109] K. Poulton, J. Corcoran, and T. Hornak, "A 1-GHz 6-bit ADC system," *IEEE Journal of Solid-State Circuits*, vol. 22, no. 6, pp. 962– 970, December 1987. 1.1.3

[110] K. Poulton, K. L. Knudsen, J. Kerley, J. Kang, J. Tani, E. Cornish, and M. VanGrouw, "An 8-GSa/s 8-bit ADC system," in *1997 Symposium on VLSI Circuits, Digest of Technical Papers*, June 1997, pp. 23–24. 1.1.3, 5.1, 5.3.1

[111] K. Poulton, R. Neff, A. Muto, W. Liu, A. Burstein, and M. Heshami, "A 4GSample/s 8b ADC in 0.35μm CMOS," in *2002 IEEE International Solid-State Circuits Conference, Digest of Technical Papers, ISSCC*, vol. 2, Feb 2002, pp. 126 – 434. 1.1.3

[112] K. Poulton, R. Neff, B. Setterberg, B. Wuppermann, T. Kopley, R. Jewett, J. Pernillo, C. Tan, and A. Montijo, "A 20 GS/s 8 b ADC with a 1 MB memory in 0.18 μm CMOS," in *2003 IEEE International Solid-State Circuits Conference*, vol. 1, February 2003, pp. 318–496. 1, 1.1.1, 1.1.3, 5.1

[113] R. Prendergast, B. Levy, and P. Hurst, "Reconstruction of band-limited periodic nonuniformly sampled signals through multirate filter banks," *IEEE Transactions on Circuits and Systems I: Regular Papers*, vol. 51, no. 8, pp. 1612–1622, August 2004. 5.1

[114] J. G. Proakis and D. G. Manolakis, *Digital Signal Processing: Principles, Algorithms and Applications*, 3rd ed., ser. McGraw-Hill series in electrical engineering : Communications and signal processing. Prentice Hall, 1995. 2.2, 3.2.1.1, C.1, C.1

[115] G. Ruan, "A behavioral model of A/D converters using a mixed-mode simulator," *IEEE Journal of Solid-State Circuits*, vol. 26, no. 3, pp. 283–290, March 1991. 1.3, A.1

[116] S. Sai-Weng, U. Seng-Pan, R. P. Martins, and J. E. Franca, "Timing-mismatch analysis in high-speed analog front-end with nonuniformly holding output," in *Proceedings of the 2003 International Symposium on Circuits and Systems, ISCAS*, vol. 1, May 2003, pp. 129 –132. 3.1

[117] M. Schetzen, "Theory of the pth-order inverses of nonlinear systems," *IEEE Transactions on Circuits and Systems*, vol. CAS-23, pp. 285–291, May 1976. 2.4.2

[118] M. Schetzen, *The Volterra and Wiener Theories of Nonlinear Systems*. John Wiley and Sons, 1980. 2.3, 2.4.2

[119] C. Schiller and P. Byrne, "A 4-GHz 8-b ADC system," *IEEE Journal of Solid-State Circuits*, vol. 26, no. 12, pp. 1781–1789, December 1991. 1.1.3

[120] D. Schwingshackl, G. Kubin, and G. Paoli, "Causality considerations for the identification of continuous-time Volterra system," *Proceedings IEEE Workshop on Nonlinear Dynamics of Electronic Systems, NDES*, pp. 241–244, 2003. 2.11, 2.3.2

[121] U. Seng-Pan, R. Martins, and J. Franca, "Design and analysis of low timing-skew clock generation for time-interleaved sampled-data systems," in *Proceedings of the 2002 IEEE International Symposium on Circuits and Systems, ISCAS*, vol. 4, May 2002, pp. 441–444. 3.1

[122] C. E. Shannon, "Communication in the presence of noise," *Reprinted in Proceedings of the IEEE*, vol. 86, no. 2, pp. 447–457, February 1998. 2.1, 5.1

[123] M. Shinagawa, Y. Akazawa, and T. Wakimoto, "Jitter analysis of high-speed sampling systems," *IEEE Journal of Solid-State Circuits*, vol. 25, no. 1, pp. 220–224, February 1990. 3.1, 3.4.2

[124] H. Shu, T. Chen, and B. Francis, "Minimax design of hybrid multirate filter banks," *IEEE Transactions on Circuits and Systems II: Analog and Digital Signal Processing*, vol. 44, no. 2, pp. 1057–7130, February 1997. 2.1

[125] J. B. Simões, J. Landeck, and C. M. B. A. Correia, "Nonlinearity of a data-acquisition system with interleaving/multiplexing," *IEEE Transactions on Instrumentation and Measurement*, vol. 46, no. 6, pp. 1274–1279, December 1997. 1.3, 2.1, 3.1, A.1, A.3

[126] P. Singerl and C. Vogel, "An analysis of a low complexity received signal strength indicator for wireless applications," in *Proceedings of the Austrochip 2004*, October 2004, pp. 57–60. 1.3

[127] P. Singerl and C. Vogel, "A fast and accurate automatic gain control for a wireless local area network receiver," in *Proceedings of 2005 Global Mobile Congress*, October 2005, accepted for publication. 1.3

[128] D. Slepian, "Prolate spheroidal wave functions, Fourier analysis, and uncertainty – V: The discrete case," *Bell System Technical Journal*, vol. 57, no. 5, pp. 1371–1430, May-June 1978. 5.4.1

[129] T. M. Souders, D. R. Flach, C. Hagwood, and G. L. Yang, "The effects of timing jitter in sampling systems," *IEEE Transactions on Instrumentation and Measurement*, vol. 39, no. 1, pp. 80–85, February 1990. 3.1

[130] L. Sumanen, M. Waltari, and K. A. I. Halonen, "A 10-bit 200-MS/s CMOS parallel pipeline A/D converter," *IEEE Journal of Solid-State Circuits*, vol. 36, no. 7, pp. 1048–1055, July 2001. 1.1.3

[131] M. Tamba, A. Shimizu, H. Munakata, and T. Komuro, "A method to improve SFDR with random interleaved sampling method," in *Proceedings of the International Test Conference*, October 2001, pp. 512–520. 5.1, 5.2.2

[132] R. Tangelder, H. de Vries, R. Rosing, H. Kerkhoff, and M. Sachdev, "Jitter and decision-level noise separation in A/D converters," in *Proceedings of the 16th IEEE Instrumentation and Measurement Technology Conference, IMTC*, vol. 3, May 1999, pp. 1558–1562. 3.1

[133] M. E. Tipping, "Sparse Bayesian learning and the relevance vector machine," *Journal of Machine Learning Research*, vol. 1, pp. 211–244, June 2001. A.2.3.3

[134] P. A. Traverso, D. Mirri, G. Pasini, and F. Filicori, "A non-linear dynamic S/H-ADC device model based on a modified Volterra series: Identification procedure and commercial CAD tool implementation," in *Proceedings of the 19th IEEE Instrumentation and Measurement Technology Conference, IMTC*, vol. 1, May 2002, pp. 195–200. A.1

[135] J. Tsimbinos and K. V. Lever, "Applications of higher-order statistics to modelling, identification and cancellation of nonlinear distortion in high-speed samplers and analogue-to-digital converters using the Volterra and Wiener models," in *IEEE Signal Processing Workshop on Higher-Order Statistics*, June 1993, pp. 379–383. A.1

[136] J. Tsimbinos and K. V. Lever, "Nonlinear system compensation based on orthogonal polynomial inverses," *IEEE Transactions on Circuits and Systems I: Fundamental Theory and Applications*, vol. 48, no. 4, pp. 406–417, 2001. 2.4.2, 3.10, C.6

[137] M. Unser, "Sampling-50 years after Shannon," *Proceedings of the IEEE*, vol. 88, no. 4, pp. 569–587, April 2000. 2.1

[138] G. L. S. V. J. Mathews, *Polynomial Signal Processing*. John Wiley & Sons, Inc., 2000. 2.3, 2.6, 6

[139] P. P. Vaidyanathan, *Multirate Systems and Filter Banks*. Prentice Hall, 1993. 2.1, 2.2, 2.2, 2.4.1, 5.1, A.2.1

[140] P. P. Vaidyanathan, "Generalizations of the sampling theorem: Seven decades after Nyquist," *IEEE Transactions on Circuits and Systems I: Fundamental Theory and Applications*, vol. 48, no. 9, pp. 1094–1109, September 2001. 2.1

[141] P. Vaidyanathan, "Multirate digital filters, filter banks, polyphase networks, and applications: A tutorial," *Proceedings of the IEEE*, vol. 78, no. 1, pp. 56–93, January 1990. 2.1, 2.2.1, 2.4.1, 2.4.1, 2.5

[142] R. Van De Plassche, *CMOS Integrated Analog-To-Digital and Digital-To-Analog Converters*, 2nd ed. Kluwer Academic Publishers, 2003. 1.1.3, 3.2.1.2, 3.2.1.3, 3.2.2, 3.3, 6

[143] S. R. Velazquez, T. Q. Nguyen, and S. R. Broadstone, "Design of hybrid filter banks for analog/digital conversion," *IEEE Transactions on Signal Processing*, vol. 46, no. 4, pp. 956–967, April 1998. 2.1, 2.2, 2.3, 2.3.2

[144] S. Velazquez, "Hybrid filter banks for analog/digital conversion," Ph.D. dissertation, Massachusetts Institute of Technology, 1997. 2.1

[145] S. Velazquez, T. Nguyen, S. Broadstone, and J. Roberge, "A hybrid filter bank approach to analog-to-digital conversion," in *Proceedings of the IEEE-SP International Symposium on Time-Frequency and Time-Scale Analysis*, October 1994, pp. 116–119. 2.1

[146] C. Vogel, "Comprehensive error analysis of combined channel mismatch effects in time-interleaved ADCs," in *Proceedings of the 20th IEEE Instrumentation and Measurement Technology Conference, IMTC*, vol. 1, May 2003, pp. 733–738. 1.3, 3.1

[147] C. Vogel, "Work report on the project digital correction of analog signal processing errors in fast analog-to-digital converters," Christian Doppler Laboratory for Nonlinear Signal Processing, Graz University of Technology, Austria, Tech. Rep. TR: 2003 - 0001, 2003. 1.3

[148] C. Vogel, "Work report on the project digital correction of analog signal processing errors in fast analog-to-digital converters," Christian Doppler Laboratory for Nonlinear Signal Processing, Graz University of Technology, Austria, Tech. Rep. TR: 2004 - 0001, 2004. 1.3

[149] C. Vogel, "The impact of combined channel mismatch effects in time-interleaved ADCs," *IEEE Transactions on Instrumentation and Measurement*, vol. 54, no. 1, pp. 415–427, February 2005. 1.3, 2.5, 3.1, 3.2.2.2

[150] C. Vogel, D. Draxelmayr, and G. Kubin, "Spectral shaping of timing mismatches in time-interleaved analog-to-digital converters," in *Proceedings of the 2005 IEEE International Symposium on Circuits and Systems, ISCAS*, May 2005, pp. 1394–1397. 1.3

[151] C. Vogel, D. Draxelmayr, and F. Kuttner, "Compensation of timing mismatches in time-interleaved analog-to-digital converters through transfer characteristics tuning," in *Proceedings of the 47th IEEE International Midwest Symposium On Circuits and Systems, MWSCAS*, vol. 1, July 2004, pp. 341–344. 1.3, 2.1, 2.5, 3.2.2.1

[152] C. Vogel and H. Koeppl, "Behavioral modeling of time-interleaved ADCs using MATLAB," in *Austrochip 2003*, October 2003, pp. 45–48. 1.3, 3.4.4, 3.5.3

[153] C. Vogel and G. Kubin, "Analysis and compensation of nonlinearity mismatches in time-interleaved ADC arrays," in *Proceedings of the 2004 IEEE International Symposium on Circuits and Systems, ISCAS*, vol. 1, May 2004, pp. 593–596. 1.3, 2.1, 2.3, 2.3.1, 2.3.1, 3.2.1.3

[154] C. Vogel and G. Kubin, "Time-interleaved ADCs in the context of hybrid filter banks," in *Proceedings International Symposium on Signals, Systems, and Electronics, ISSSE*, August 2004, pp. 214–217. 1.3, 2.1

[155] C. Vogel, V. Pammer, and G. Kubin, "A novel channel randomization method for time-interleaved ADCs," in *Proceedings of the 2005 IEEE International Measurement and Instrumentation Conference, IMTC*, vol. 1, May 2005, pp. 150–155. 1.3

[156] C. Vogel, D. Draxelmayr, and G. Kubin, "Channel sequence optimization in converter arrays," German patent application 102 004 049 161.5, October 8, 2004. 1.3

[157] C. Vogel and G. Kubin, "Modeling of time-interleaved ADCs with nonlinear hybrid filter banks," *AEÜ-International Journal of Electronics and Communications*, vol. 05, 2005, accepted for publication. 1.3, 2.1, 3.1

[158] V. Volterra, *Theory of Functionals*. Blackie and Sons Limited, 1930. 2.3, 2.6, 6

[159] R. Walden, "Analog-to-digital converter survey and analysis," *IEEE Journal on Selected Areas in Communications*, vol. 17, no. 4, pp. 539–550, April 1999. 3.2.2.2

[160] M. E. Waltari and K. A. Halonen, *Circuit Techniques for Low-Voltage and High-Speed A/D Converters*. Kluwer Academic Publishers, 2002. 3.2.2, 6

[161] E. W. Weisstein, "Circular permutation," From MathWorld–A Wolfram Web Resource. http://mathworld.wolfram.com/CircularPermutation.html, last visit 30.9. 2004. 5.4.1

[162] B. Widrow, I. Kollar, and L. Ming-Chang, "Statistical theory of quantization," *IEEE Transactions on Instrumentation and Measurement*, vol. 45, no. 2, pp. 353–361, April 1996. 2.1, 3.2.1.3

[163] B. Yu and W. J. Black, "A 900 MS/s 6b interleaved CMOS flash ADC," in *IEEE Conference on Custom Integrated Circuits*, May 2001, pp. 149–152. 1.1.3

[164] B. Yu and W. C. Black Jr., "Error analysis for time-interleaved analog channels," in *Proceedings of the 2001 IEEE International Symposium on Circuits and Systems, ISCAS*, vol. 1, May 2001, pp. 468–471. 1.1.3, 1.3, 2.1, 3.1, 3.5.2, 3.5.2